Modal approach to the dynamics of optical frequency combs and applications

Matthieu Ansquer

To cite this version:

Matthieu Ansquer. Modal approach to the dynamics of optical frequency combs and applications. Optics [physics.optics]. Sorbonne Université, 2022. English. NNT : 2022SORUS033 . tel-03640545

HAL Id: tel-03640545
https://theses.hal.science/tel-03640545

Submitted on 13 Apr 2022

Thèse de Doctorat de
Sorbonne Université

présentée par

Matthieu ANSQUER

le 02/02/2022

pour obtenir le grade de Docteur de Sorbonne Université
sur le sujet:

APPROCHE MODALE DE LA DYNAMIQUE DES PEIGNES DE FRÉQUENCES ET APPLICATIONS

Modal approach to the dynamics of optical frequency combs and applications

Laboratoire Kastler Brossel
Physique quantique et applications

Membres du jury :

Alfredo De Rossi	Rapporteur
Daniele Fausti	Rapporteur
Agnès Maitre	Membre du jury
Simon Pigeon	Membre du jury
Valentina PARIGI	Membre invité
Fabien Bretenaker	Membre invité
Nicolas TREPS	Directeur de thèse

A mon père avec qui, parmi tant d'autres, j'aurais aimé partager cette aventure.

Abstract

The main focus of this manuscript is the investigation of the dynamics of optical frequency combs. Based on a spectral modal decomposition of the electric field, a full characterization of the laser dynamics is achieved by measuring the fluctuations on the four main laser parameters: the intensity, the carrier-envelope offset (CEO), the central frequency and the repetition rate. Two different experimental schemes are investigated and compared in terms of sensitivity. The intensity related dynamics is also studied. Based on a simple model, we demonstrate that the main source of noise is the pump laser via its intensity fluctuations. This noise induces phase noise, and especially CEO noise, via the fluctuations of the center of the spectrum. The coupling parameter between both quantities is the residual group velocity dispersion of the laser which has been evaluated experimentally. In a second time a machine learning protocol, called reservoir computing, is investigated. Such protocol is used as a tool for studying the laser dynamics. In addition, the optical frequency comb, studied in the first parts, is used as a hardware for the implementation of a photonic reservoir computing. The long term objective of the experiment is to go toward quantum reservoir computing. Consequently, a source of quantum states is developed. Based on a PPKTP waveguide, multimode squeezed states are produced at the scale of the laser pulses. Such states can be implemented in the reservoir computing protocol to test the capacity of such configuration compared to the classical approach.

L'objectif principal de ce manuscrit est l'étude de la dynamique des peignes de fréquence optiques. Sur la base d'une décomposition modale spectrale du champ électrique, une caractérisation complète de la dynamique du laser est réalisée en mesurant les fluctuations des quatre principaux paramètres du laser : l'intensité, le décalage porteuse-enveloppe (CEO), la fréquence centrale et le taux de répétition. Deux schémas expérimentaux sont étudiés et comparés en termes de sensibilité. La dynamique liée à l'intensité est également étudiée. Sur la base d'un modèle simple, nous démontrons que la principale source de bruit est le laser de pompe via ses fluctuations d'intensité. Ce bruit induit un bruit de phase, et surtout un bruit CEO, via les fluctuations du cen-

tre du spectre. Le paramètre de couplage entre ces deux quantités est la dispersion de la vitesse de groupe résiduelle du laser qui a été évaluée expérimentalement. Dans un deuxième temps, un protocole d'apprentissage automatique, appelé "reservoir computing", est étudié. Ce protocole est utilisé comme outil pour étudier la dynamique du laser. En outre, le peigne de fréquence optique, étudié dans les premières parties, est utilisé comme support pour la mise en œuvre d'un réservoir photonique. L'objectif à long terme de l'expérience est d'aller vers un réservoir quantique. Par conséquent, une source d'états quantiques est développée. Sur la base d'un guide d'ondes PPKTP, des états comprimés multimodes sont produits à l'échelle des impulsions du laser. Ces états peuvent être utilisés dans le protocole de réservoir computing afin de tester la capacité d'une telle configuration par rapport à l'approche classique.

Remerciements

Quelques semaines se sont écoulées depuis la soutenance qui a conclu trois ans et demi de travail. Par ces quelques lignes, je voudrais remercier toutes les personnes qui y ont contribué et m'ont apporté soutien ainsi que conseils.

Je tiens en premier lieu à remercier mon jury de thèse qui a accepté d'évaluer mon travail. Dans un second temps, je voulais remercier l'ensemble des personnes que j'ai croisées au LKB. Collègues thésards, post-doc, administration ainsi que le personnels techniques, tous ont contribué à m'offrir un environnement de travail idéal. Je tiens surtout à remercier Bérangère Argence qui m'a grandement aidé, notamment pendant mon stage de M2 et le début de ma thèse. Ce travail n'aurait pas été possible sans son aide et ses connaissances précieuses.

Au sein du laboratoire, je souhaite en particulier remercier mon équipe, le groupe d'optique quantique multimode. Les anciens, Tiphaine, Luca, Syamsundar, Thibault, Adrien, qui m'ont énormément appris, mais aussi tous les autres, Claude, Mattia, Alex, Ganaël, David B., Ilya, Clémentine, David F., ainsi que les derniers arrivés, Johan, Niels et Guilherme.

Bien évidemment je ne pouvais pas écrire de remerciements sans dédier une section à mes deux acolytes, Paul et Francesca. Paul, merci d'avoir été là pour partager toutes ces galères pendant de longues heures en salle de manip. Merci pour ta (relative) bonne humeur (ça va...) et ton sens de l'humour. Francesca, ce fut un très grand plaisir de travailler avec toi. Tes élans optimistes ont su à merveille contrebalancer mon pessimisme, et c'était toujours un plaisir de te rendre la pareille dans tes périodes de démotivation (0.6 dB de squeezing ce n'est pas rien, et on passera sous silence les problèmes d'orientation de lentilles...). Merci à tous les deux d'avoir animé mes journées de vos "disputes".

Je tenais également à remercier toutes les personnes avec qui j'ai eu la chance de collaborer durant cette thèse. Vincent et Loïc, merci de m'avoir accueilli à Thales et de m'avoir consacré du temps bien que vous n'en n'ayez pas beaucoup. Un grand merci aussi à toi Fabien. J'ai énormément apprécié travailler avec toi, merci pour ton temps, ta bonne humeur, et ces repas partagés à Terronia. J'espère réussir à garder contact avec toi maintenant que moi aussi j'ai rejoint les contrées lointaines du plateau de Saclay. Enfin, je ne saurais exprimer à quel point je vous suis reconnaissant, Nicolas et Valentina.

Travailler avec vous a été un réel plaisir. J'ai énormément appris à votre contact. J'admire à quel point vous arrivez à jongler entre toutes vos casquettes, chercheur, encadrant, enseignant, et cela toujours dans la bonne humeur et la bienveillance. Grâce à vous, j'ai passé trois excellentes années dans cette équipe.

Une thèse, c'est un travail qu'il est impossible de mener sans l'aide de collègues formidables, mais c'est aussi une aventure personnelle que je n'aurais accomplie sans mes proches. Ainsi, je tiens également à les remercier de leur soutien. De manière générale je tenais à remercier ma famille, grands parents, oncles, tantes, cousins et cousines, de même que mes amis pour ces moments passés à se changer les idées autour d'une pizza ou d'une bière. Merci aussi à ma belle famille, qui m'a toujours apporté beaucoup de soutien et m'a même hébergé pour la rédaction de ce manuscrit (merci Maryvonne).

Plus particulièrement, j'aimerais remercier certaines personnes qui ont été très importantes durant ce doctorat et dans ma vie.

Alexis, merci beaucoup d'avoir été là pour moi, merci pour les petites parties de basket, tes histoires de mouches mais aussi ton aide dans les moments de panique à deux semaines de la soutenance. Plus qu'un ami je te considère comme un frère.

Marine, Mathilde, Martin, mes frère et sœurs sur qui je suis certain de toujours pouvoir compter quoi qu'il arrive. Merci de m'avoir supporté bien que je sois grumpy. Ça n'a pas toujours été facile dans la vie mais maintenant on forme une équipe soudée, et ce travail vous est aussi dédié.

Maman, merci déjà de m'avoir appris à lire. Sans toi il est évident que je n'en serais pas là. Merci pour tout ce que tu as fait pour nous, et merci d'avoir fait de moi la personne que je suis aujourd'hui. Bien évidemment cette thèse je te la dois à toi aussi.

Enfin, ces derniers mots sont dédiés à Hannah, ma compagne de vie depuis déjà dix ans et ma future femme. La palme de la patience te revient sans conteste. Merci de me supporter au quotidien, d'écouter mes angoisses et de me rassurer. Ta présence m'apaise et rien n'aurait été possible sans toi. Je suis heureux et chanceux de partager ma vie avec toi et j'espère passer de nombreuses années à tes côtés. Je t'aime.

Contents

Introduction 1

I CHARACTERIZING, PRODUCING AND MEASURING LIGHT PULSES FROM AN OPTICAL FREQUENCY COMB 5

1 Multimode description of the state of light 7
- 1.1 The classical electromagnetic field 8
  - 1.1.1 Wave equation and plane-wave solution 8
  - 1.1.2 Fourier transform 8
- 1.2 Modal description of the electric field 9
  - 1.2.1 Definition of a mode of light 9
  - 1.2.2 Envelope modes 9
  - 1.2.3 Quadratures of the field 12
  - 1.2.4 Energy, intensity and optical power 12
- 1.3 Quantum counterpart of the electric field 13
  - 1.3.1 Quantization of the electric field 13
  - 1.3.2 The coherent, or quasi-classical, state 14
  - 1.3.3 Continuous operators 15
  - 1.3.4 Wigner function 16
- 1.4 Noise and fundamental limits 17
  - 1.4.1 Power spectral density 17
  - 1.4.2 Fundamental limits in parameter estimation 20

2 Optical frequency comb 25
- 2.1 Description of an optical frequency comb 25
  - 2.1.1 Naive description of a frequency comb 26
  - 2.1.2 Mathematical description of the comb electric field 28
- 2.2 Kerr-lens mode-locking 32
  - 2.2.1 Kerr-lens effect 32
  - 2.2.2 Master equation for Kerr-lens mode-locking 33

2.2.3 Resolution of the master equation and intracavity dispersion . . 36
2.3 Dispersion of an optical pulse 37
2.3.1 Fourier transform pulses 38
2.3.2 Propagation through a dispersive medium 39
2.3.3 Numerical application 40

3 Measuring quadratures of light **43**
3.1 Heterodyne detection 44
3.2 Self-heterodyne detection 45
3.2.1 Self-heterodyne beat signal 47
3.2.2 Transfer function 48
3.3 Homodyne detection 49
3.3.1 Temporal representation 49
3.3.2 Spectral representation 50
3.3.3 Variation of the homodyne detection 51
3.4 Sensitivity of the measurements 53
3.4.1 Fisher information of the detection schemes 53
3.4.2 Experimental sensitivity of the self-heterodyne 58
3.4.3 Phase sensitivity as a function of the analysis frequency 64

II CHARACTERIZATION OF THE DYNAMICS OF OPTICAL FREQUENCY COMBS **67**

4 Modal investigation of the dynamics **71**
4.1 Modal description of the dynamics 72
4.1.1 Single pulse fluctuations 72
4.1.2 Field quadrature fluctuations 73
4.2 Measuring the multimode field 74
4.2.1 Reference beam 75
4.2.2 Spectral phase compensation 77
4.2.3 Multipixel homodyne detection 81
4.3 Extracting the noise spectra 88
4.3.1 Measuring the noise spectrum: the sideband picture 88
4.3.2 Normalization of the measurements 92
4.4 Results 94
4.4.1 Covariance matrices 94
4.4.2 Noise spectra 95
4.4.3 RIN of the laser 97

5 Harnessing noises correlations 101
5.1 Amplitude-phases correlation matrices . . . 101
5.2 Fixed point model . . . 102
5.2.1 General idea of the model . . . 103
5.2.2 Fixed point for laser pump noise . . . 104
5.3 Unveiling the dynamics from XP correlations . . . 109
5.3.1 Singular value decomposition of the correlation matrix . . . 110
5.3.2 Intensity related dynamics: Model from J. Ye . . . 111

6 Menlo noise analysis 119
6.1 Unbalanced Mach-Zehnder for amplitude and phase measurement . . . 120
6.1.1 Reminder on self-heterodyne detection . . . 120
6.1.2 Amplitude and phase extraction . . . 122
6.1.3 Recovering the noise on the parameters . . . 124
6.2 Experimental setup . . . 125
6.3 Results . . . 126
6.3.1 Phase measurement . . . 126
6.3.2 Noise floors . . . 129

III PULSED APPROACH TO RESERVOIR COMPUTING 133

7 Time series processing with neural networks 137
7.1 Reservoir computing . . . 137
7.1.1 General principle . . . 138
7.1.2 Application of RC to noise analysis . . . 141
7.2 Delayed-feedback reservoir computing . . . 142
7.2.1 General description: memory and links . . . 145
7.2.2 Experimental implementation . . . 148
7.2.3 Capacity . . . 153

8 Toward quantum reservoir computing 161
8.1 Single mode squeezing . . . 161
8.1.1 Parametric down conversion . . . 162
8.1.2 Quantum correlations . . . 163
8.2 Multimode squeezing . . . 165
8.3 Single pass squeezing . . . 166
8.3.1 Experimental scheme . . . 166
8.3.2 Results . . . 168

Conclusion 175

References **177**

Introduction

Light is a widely spread and powerful tool in experimental physics. It has been recently confirmed with the Nobel prize in optics in 2017, for the observation of gravitational waves with the gravitational interferometers LIGO and VIRGO [1], as well as in 2018[1], for the development of optical tweezers [2]. One field of predilection of light is metrology. Light is particularly adapted for the measurement of lengths or distances as illustrated by the precise measurement of the distance earth-moon down to a millimeter [3]. Many of the milestones in metrology have been achieved thanks to the development of one particular light source: the laser [4]. In metrology, lasers are used in many different ways. For example, the coherence of this source of light can be used to perform interferometric measurements, such as in the gravitational interferometers. Lasers can also serve as frequency reference in spectroscopy experiments [5]. Additionally, pulsed lasers can be used to perform time-of-flight measurements in ranging experiments, as it is the case with the measurement of the distance between the earth and the moon.

Various laser architectures, including pulsed lasers, have been developed depending on the applications. In particular, among other pulsed laser sources, mode-locked femtosecond lasers, or optical frequency combs (OFCs), illustrated themselves as an ubiquitous tool in metrology for the past 20 years. Those lasers are composed of many equally spaced individual frequency lines, forming the teeth of the comb. In the temporal domain, this particular structure leads to the production of ultra-short pulses of the order of a few femtoseconds [6]. They were originally used to transfer the excellent spectral properties of the optical atomic clocks to the microwave frequency domain [7, 8]. Since then, they have found applications in numerous fields, such as tests of fundamental physics [9, 10, 11, 12], atomic and molecular spectroscopy [13, 14], time or frequency transfer [15, 16, 17], ranging measurements [18, 19] or astrophysics [20].

Since frequency combs are widely employed as tools in experiments, understanding their dynamics, i.e. the noises affecting their properties, is essential. It contributes to the development of ultra-stable sources which are necessary to prevent the laser stability from limiting the precision of the measurements. To fully characterize the laser dynamics, the investigation of the noise sources as well as the coupling mechanisms between

---

[1] By coincidence, I am writing those lines the precise day of the announcement of the Nobel prize in physics 2021. Too bad its not for quantum optics, another time.

those sources and the different laser parameters is critical. Such investigation allows for the understanding of the noise path through the laser and thus the identification of the physical knobs to act on in order to improve the light source. However, this study can be cumbersome as, most of the time, a specific setup must be employed to characterize each laser parameter individually, leading to bulky and complicated experimental setups.

In this thesis, an analysis technique to characterize the dynamics of optical frequency combs with a single setup is presented. By the mean of tools borrowed from the field of quantum optics, interferometric measurements are developed to fully characterize the fluctuations of the laser parameters. In a detection scheme, the ultimate precision on the measurement of those laser parameters is limited by the quantum nature of light. Such limit is called standard quantum limit. In this work, two different interferometer configurations are considered, based either on a homodyne or on a heterodyne detection. Both configurations are compared in terms of sensitivity. As will be demonstrated, under certain conditions, the ultimate sensitivity can be reached.
The analysis technique is applied to two different lasers, a Titanium-Sapphire based femtosecond oscillator and a fiber-based optical frequency comb. The aim is to demonstrate the versatility of our technique which can be applied to various sources of light pulses.
Furthermore, the correlations between the Titanium-Sapphire laser noises are studied, in particular the amplitude and phase ones. This experiment permits the understanding of the intensity related dynamics, one of the fundamental mechanisms that governs mode-locking.

Investigating the intensity related dynamics allows to understand how the pump laser noise affects the laser parameters. Consequently, the knowledge gathered in the previous experiment is put into practice in an attempt to predict the laser dynamics from the pump laser fluctuations. This prediction relies on a machine learning protocol, simulated on a computer, known as reservoir computing [21]. This protocol is particularly well suited for the processing of time series [22] and has many advantages. In particular, the simplicity of its design makes it a good candidate for hardware implementation and especially in photonics [23, 24]. Therefore, in this work is also presented an experimental implementation of an optical reservoir computing protocol using a frequency comb as a hardware. This architecture is based on the same tools as the ones used for investigating the laser dynamics and borrowed from quantum optics. Its performances are evaluated via the information processing capacity [25].
The long term perspective of this experiment is to implement quantum resources in the machine learning protocol. As a matter of fact, optical frequency combs can also be used in quantum optics to produce, for example, highly multimode entangled states

[26]. Using such quantum resources in a reservoir computing protocol allows to move toward quantum machine learning [27] and explore the capability of such architecture. To this aim, a source of quantum states based on a parametric process is presented. The objective is to produce squeezed-states of light in a single pass configuration to exploit quantum correlations at the level of the laser pulses. It is worth mentioning that the investigation of the stability of the laser is also critical for this type of applications. Indeed, the production of quantum states can be deteriorated by classical noise, hence the need to characterize the laser source.

Outline of the manuscript

The first part of this thesis introduces the notations, the mathematical tools and the basic concepts needed along this work.

The first chapter is dedicated to the definitions of the notations needed to conduct our investigation. In particular, the modal description of the field, a fundamental concept in this study, is presented. Noises and fundamental limits in parameter estimation are also discussed.

The second chapter focuses on the description of the physics behind optical frequency combs. The master equation, describing the evolution of the pulses inside the laser cavity, is derived. It aims at identifying the different processes at stake in the mode-locking mechanism, at the origin of optical frequency combs. In addition, the effects of ultrashort pulses propagation in materials are discussed.

The third chapter concentrates on the experimental techniques allowing to measure the electric field of an optical frequency comb. Particularly, two techniques are considered and their sensitivity compared.

The second part of this manuscript presents some experimental results obtained during this thesis. Some of those results have been published in [28].

The fourth chapter presents the modal decomposition of the laser dynamics. Each parameter of the laser is associated to a particular spectral mode. Using a spectrally resolved detection, those detection modes are addressed and the laser dynamics retrieved with a single setup.

The fifth chapter analyzes the results found in the previous chapter. It exploits the correlations between the laser parameters, as well as the noise sources, in order to understand the coupling mechanisms in the laser cavity. A simple model allows to understand how the noise propagates from the sources to the laser parameters.

In the sixth chapter is presented an application of the analysis previously described to a different laser source and a different experimental setup. The results presented are preliminary and were obtained during a collaboration with Thales Research and Technology.

Finally, the last part of this thesis is dedicated to an application of optical frequency combs for a machine learning protocol.
Chapter seven introduces the machine learning protocol, called reservoir computing, and its experimental implementation. Preliminary results are presented and compared to simulations.
The last chapter focuses on the experimental development of a source of quantum states. The aim is to produce quantum correlations at the level of the laser pulses in order to implement such source in the machine learning protocol presented in the previous chapter.

Part I

Characterizing, producing and measuring light pulses from an Optical Frequency Comb

Chapter 1

Multimode description of the state of light

Contents

1.1 The classical electromagnetic field 8
1.1.1 Wave equation and plane-wave solution 8
1.1.2 Fourier transform 8
1.2 Modal description of the electric field 9
1.2.1 Definition of a mode of light 9
1.2.2 Envelope modes 9
1.2.3 Quadratures of the field 12
1.2.4 Energy, intensity and optical power 12
1.3 Quantum counterpart of the electric field 13
1.3.1 Quantization of the electric field 13
1.3.2 The coherent, or quasi-classical, state 14
1.3.3 Continuous operators 15
1.3.4 Wigner function 16
1.4 Noise and fundamental limits 17
1.4.1 Power spectral density 17
1.4.2 Fundamental limits in parameter estimation 20

This chapter aims at introducing the basic mathematical tools to describe the electromagnetic field and to characterize the fluctuations affecting its parameters, such as its amplitude or its phase. We start by giving the mathematical expression of the electromagnetic field and its representations in terms of field quadratures, a notation that will be used throughout this manuscript. We then present the modal description of the electromagnetic field. This description is the cornerstone of this work as those modes are used to conduct investigations all along this thesis. The quantum description of the electromagnetic field is also presented. This description will be useful to compare the sensitivity of our measurements to the fundamental limits fixed by the quantum properties of the light. Finally, we present the mathematical tools used to describe the noise of the electromagnetic field. This work is based on the measurement and the manipulation of the noise. Hence, mathematical tools are needed to characterize and quantify it.

1.1 The classical electromagnetic field

1.1.1 Wave equation and plane-wave solution

The propagation of light in vacuum can be described by Maxwell's equations from which the wave equation can be derived. For an electric field $\mathbf{E}(\mathbf{r}, t)$ it is given by

$$\mathbf{\Delta}\mathbf{E}(\mathbf{r}, t) - \frac{1}{c^2}\frac{\partial^2 \mathbf{E}(\mathbf{r}, t)}{\partial t^2} = 0, \tag{1.1}$$

where $\mathbf{\Delta}$ stands for the three dimensional Laplacian operator. Note that all along this thesis, the vectors will be represented by bold letters.
A typical solution of this equation is the so-called plane-wave solution

$$\mathbf{E}(\mathbf{r}, t) = \mathbf{E}_0 e^{i(\mathbf{k}\cdot\mathbf{r} - \omega_0 t + \phi)} + cc, \tag{1.2}$$

where $\mathbf{E}_0$ is a constant vector, $\mathbf{k}$ is the propagation vector, ω_0 is the pulsation of the field, ϕ an arbitrary phase and cc stands for complex conjugate.

1.1.2 Fourier transform

At many occasions, it will be useful to describe the electric field in the frequency domain rather than in the time domain. Both are related by the Fourier transform (FT)

$$\tilde{\mathbf{E}}(\mathbf{r}, \omega) = \frac{1}{\sqrt{2\pi}} \int_{-\infty}^{+\infty} e^{i\omega t}\mathbf{E}(\mathbf{r}, t)\ \mathrm{d}t. \tag{1.3}$$

It can be noted that $\mathbf{E}(\mathbf{r}, t)$ is a real quantity, thus

$$\left[\tilde{\mathbf{E}}(\mathbf{r}, \omega)\right]^{\star} = \tilde{\mathbf{E}}(\mathbf{r}, -\omega). \tag{1.4}$$

Therefore, it is possible to describe the electric field only by its positive frequency component, the analytic electric field defined by

$$\mathbf{E}^{(+)}(\mathbf{r}, t) = \frac{1}{\sqrt{2\pi}} \int_{0}^{+\infty} e^{-i\omega t}\tilde{\mathbf{E}}(\mathbf{r}, \omega)\ \mathrm{d}\omega. \tag{1.5}$$

The analytic signal is a complex quantity and is related to the real electric field by

$$\mathbf{E}(\mathbf{r},t) = \mathbf{E}^{(+)}(\mathbf{r},t) + \mathbf{E}^{(-)}(\mathbf{r},t), \tag{1.6}$$

where $\left[\mathbf{E}^{(+)}(\mathbf{r},t)\right]^{\star} = \mathbf{E}^{(-)}(\mathbf{r},t)$. Finally, the analytic signal in the frequency domain is defined by taking the Fourier transform of the analytic signal in the time domain

$$\tilde{\mathbf{E}}^{(+)}(\mathbf{r},\omega) = \frac{1}{\sqrt{2\pi}} \int_{-\infty}^{+\infty} e^{i\omega t} \mathbf{E}^{(+)}(\mathbf{r},t)\ \mathrm{d}t. \tag{1.7}$$

1.2 Modal description of the electric field

In this section, we introduce the modal representation of the electric field. The light is composed of many properties such as the polarization of the electric field, its frequency or its spatial distribution. Each of those degrees of freedom can be associated to a mode of the electric field.

1.2.1 Definition of a mode of light

A mode can be defined as a normalized solution of Maxwell equations. Because the wave equation is linear, any linear superposition of solutions is also solution of the wave equation. Hence, orthonormal basis can be formed using a set of optical modes $\{\mathbf{f_l}(\mathbf{r},t)\}$. Those modes must satisfy the orthonormality and completeness relations at any time t

$$\frac{1}{V}\int_V \mathbf{f_l}^{\star}(\mathbf{r},t)\cdot\mathbf{f_{l'}}(\mathbf{r},t)\ \mathrm{d}\mathbf{r} = \delta_{ll'}, \quad \text{and} \quad \frac{1}{V}\int_V \mathbf{f_l}^{\star}(\mathbf{r'},t)\cdot\mathbf{f_l}(\mathbf{r},t)\ \mathrm{d}\mathbf{r} = \delta^{(3)}(\mathbf{r}-\mathbf{r'}), \tag{1.8}$$

V being the large volume containing the physical system, $\delta_{ll'}$ being the Kronecker delta function, and $\delta^{(3)}(\mathbf{r}-\mathbf{r'})$ the delta function in a three dimensional space. With this decomposition, any analytic field can be written

$$\mathbf{E}^{(+)}(\mathbf{r},t) = \sum_l \mathcal{F}_l\ \mathbf{f_l}(\mathbf{r},t), \tag{1.9}$$

with $\mathcal{F}_l$ the complex amplitude of each mode $\mathbf{f_l}(\mathbf{r},t)$.

1.2.2 Envelope modes

In this study, we wish to describe the propagation of optical fields corresponding to the light emitted by a laser. In such systems, the field propagates in only one direction, has a narrow spectrum around a central frequency ω_0, and is slowly diverging in space. Consequently, we model the field by a superposition of plane waves, as defined in equation (1.2), and use the paraxial and narrow-band approximations. The paraxial approximation implies that the wavevector is the same for all the individual waves, noted $\mathbf{k}_0$. We set the direction of propagation along the z axis so that $\mathbf{k}_0 = k_0\mathbf{u}_z$. The narrow-band approximation implies that all the frequencies are close to a central frequency ω_0. Besides, we consider a single polarization component, and thus a linear polarization, so that all the fields are scalar quantities. With those approximations, and by factorizing the field (1.9) by a carrier plane wave, the electric field can be decomposed on a new set of modes $f_l(\mathbf{r}, t)$, called the envelope modes [29], according to

$$E^{(+)}(\mathbf{r}, t) = \mathcal{E}_0\ e^{i(k_0 z - \omega_0 t)} \sum_l a_l\ f_l(\mathbf{r}, t), \tag{1.10}$$

with $e^{i(k_0 z - \omega_0 t)}$ the carrier plane wave. The envelope modes $f_l(\mathbf{r}, t)$ are slowly varying functions of time at the scale of the optical period $2\pi/\omega_0$, and space at the scale of the wavelength $\lambda = 2\pi/k_0$. $\mathcal{E}_0$ is a normalization constant. It is defined such as a_l, the amplitude of the field in the mode $f_l(\mathbf{r}, t)$, has the dimension of the square-root of a photon number. This will be relevant later for the quantum description of the electric field. Thus, $\mathcal{E}_0$ is defined as

$$\mathcal{E}_0 = \sqrt{\frac{\hbar\omega_0}{2nc\epsilon_0 V}}. \tag{1.11}$$

To further simplify, we restrict ourselves to a family of modes that can be factorized in transverse and longitudinal modes. Thus, the mode basis is decomposed as follow

$$f_l(\mathbf{r}, t) = g_l(\mathbf{r}) \times u_l(z, t), \tag{1.12}$$

where the $g_l(\mathbf{r})$ are the transverse (or spatial) modes and $u_l(z, t)$ the longitudinal (or temporal) ones.

The light emitted by a solid state laser has a Gaussian spatial distribution. Hence, the family of transverse electromagnetic mode (TEM) can be used to describe the spatial profile of the laser beam. In this work, as we are not interested in spatial effects, we only use the first transverse electromagnetic mode (TEM_{00}) to describe the spatial profile of the beam. Its expression is given by

$$g_0(\mathbf{r} = (\boldsymbol{\rho}, z)) = \frac{w_0}{w(z)} e^{-\boldsymbol{\rho}^2/w^2(z)} e^{-ik_0\boldsymbol{\rho}^2/2R(z)} e^{i\phi(z)}, \tag{1.13}$$

where $R(z)$ is the radius of curvature of the beam, $\phi(z)$ the Gouy phase, w_0 its waist and $w(z)$ its width at a position z. They are given by

$$\begin{aligned} R(z) &= z + \frac{z_R^2}{z}, && (1.14a) \\ w(z) &= w_0\sqrt{1 + \frac{z^2}{z_R^2}}, && (1.14b) \\ \phi(z) &= \arctan\left(\frac{z}{z_R}\right), && (1.14c) \end{aligned}$$

where z_R is the Rayleigh length defined as

$$z_R = \pi \frac{w_0^2}{\lambda}. \tag{1.15}$$

On the other hand, the temporal modes, which are slowly varying envelope, can be written $u_l(z,t) = u_l(\tau = t - z/c)$, describing the propagation of the undistorded envelope at the speed of light in the direction z. For simplicity we set $z = 0$, which corresponds, for instance, to the position of a detector, so that $\tau = t$. Consequently, the electric field writes

$$E^{(+)}(\mathbf{r}, t) = \mathcal{E}_0 g_0(\mathbf{r}) e^{-i\omega_0 t} \sum_l a_l \ u_l(t). \tag{1.16}$$

From this expression the longitudinal electric field, representing only the propagation in time, can be written

$$E_L^{(+)}(t) = \mathcal{E}_0 e^{-i\omega_0 t} \sum_l a_l \ u_l(t) = \mathcal{E}_0 e^{-i\omega_0 t} a_L(t), \tag{1.17}$$

where we defined $a_L(t) = \sum_l a_l \ u_l(t)$. The temporal modes $u_l(t)$ are suitable for the description of pulses of light as it will be the case later in the manuscript. The Fourier transform of this field is given by

$$\tilde{E}_L^{(+)}(\Omega) = \mathcal{E}_0 \sum_l a_l \ \tilde{u}_l(\Omega) = \mathcal{E}_0 \tilde{a}_L(\Omega), \tag{1.18}$$

where $\Omega = \omega - \omega_0$. In the rest of the manuscript, we will mainly consider this longitudinal field and not the transverse one. Thus, we will drop the index L and refer to it as $E^{(+)}(t)$. Note that if the variable $\mathbf{r}$ is present we refer to the total field $E^{(+)}(\mathbf{r}, t)$ given by equation (1.16).

1.2.3 Quadratures of the field

Because $E^{(+)}(t)$ is a complex quantity, it can be separated in a real part and an imaginary one. Those quantities are called the quadratures of the electric field and are defined by

$$E^{(+)}(t) = \mathcal{E}_0 e^{-i\omega_0 t} a(t) = \frac{\mathcal{E}_0}{2}\left[x(t) + ip(t)\right] e^{-i\omega_0 t}, \tag{1.19}$$

with

$$x(t) = a(t) + a^*(t), \quad \text{and} \quad p(t) = i(a^*(t) - a(t)). \tag{1.20}$$

Thus the total electric field can be re-written

$$E(t) = \mathcal{E}_0 e^{-i\omega_0 t} a(t) + cc = \mathcal{E}_0\left[x(t)\cos(\omega_0 t) + p(t)\sin(\omega_0 t)\right] \tag{1.21}$$

From the expression above it is clear that the two quantities $x(t)$ and $p(t)$ are in quadrature hence the name quadratures of the electric field.

1.2.4 Energy, intensity and optical power

We conclude this section by presenting the expressions of the energy as well as the optical intensity and the optical power. Those quantities are of prime interest as they are easily accessible experimentally.
The optical intensity in $\mathrm{W/m^2}$ is related to the field amplitude by

$$I(\mathbf{r}, t) = 2\epsilon_0 nc|\mathbf{E}^{(+)}(\mathbf{r}, t)|^2, \tag{1.22}$$

with n the optical index and ϵ_0 the vacuum permittivity. The optical power in W is found by integrating the intensity over a surface S. We remind that we are considering a field propagating along the z axis. Hence the integration over the detector surface is made on the coordinates $\boldsymbol{\rho} = (x, y)$ so that

$$P(z, t) = \int_S I(\mathbf{r}, t)\ \mathrm{d}\boldsymbol{\rho}. \tag{1.23}$$

Finally, the energy, in J, contained in the electric field is obtained by integrating the optical power over a detection time T

$$U(z) = \int_T P(z, t)\ \mathrm{d}t. \tag{1.24}$$

We will use those quantities all along this manuscript to describe the result of measurements performed on the electric field.

1.3 Quantum counterpart of the electric field

So far, all the quantities defined are classical quantities. However, in this manuscript, it will be necessary to compare the sensitivity of our measurements to the ultimate bound given by the quantum description of the electric field. Because of the normalization (1.11) defined in the previous section, a straightforward way to do so is to replace the quantities previously defined by quantum operators.

1.3.1 Quantization of the electric field

We start by replacing the quantities a_l and their conjugates $a_l^\star$, introduced in the previous section, by the annihilation $\hat{a}_l$ and creation $\hat{a}_l^\dagger$ operators. Due to the normalization (1.11), those operators obey the commutation relations [30]

$$\left[\hat{a}_l, \hat{a}_k^\dagger\right] = \delta_{lk}, \quad \text{and} \quad [\hat{a}_l, \hat{a}_k] = 0. \tag{1.25}$$

It follows that the quantum electric field can be written as

$$\hat{E}^{(+)}(\mathbf{r}, t) = \mathcal{E}_0 e^{-i\omega_0 t} \sum_l \hat{a}_l \; u_l(t). \tag{1.26}$$

It can be noted that the classical description given by equation (1.17) can be retrieved by taking the average value of the electric field above.

In the quantum framework, light is best describe by an assembly of harmonic oscillators. The excitations of these oscillators are the photons. Within this framework, the total energy of the field is given by the Hamiltonian composed of the sum of the contribution of each mode [30]

$$\hat{H} = \sum_l \hat{H}_l = \sum_l \hbar\omega_l \left(\hat{N}_l + \frac{1}{2}\right), \tag{1.27}$$

with $\hat{N}_l = \hat{a}_l^\dagger \hat{a}_l$ the photon-number operator of the mode l. The eigenstates of this photon number operator are the so called Fock states $|N_l\rangle$ so that $\hat{N}_l|N_l\rangle = N_l|N_l\rangle$ with N_l the number of photons in the mode l. Hence, the eigenstates of the Hamiltonian (1.27) are the multimode Fock states $|N_1, \ldots, N_l, \ldots\rangle$.
The annihilation $\hat{a}_l$ and creation $\hat{a}_l^\dagger$ operators are so called as they remove or create a photon in the mode l. Thus, the action of those operators on the multimode Fock state is

$$\begin{aligned} \hat{a}_l|N_1, \ldots, N_l, \ldots\rangle &= \sqrt{N_l}|N_1, \ldots, N_l - 1, \ldots\rangle, \\ \hat{a}_l^\dagger|N_1, \ldots, N_l, \ldots\rangle &= \sqrt{N_l + 1}|N_1, \ldots, N_l + 1, \ldots\rangle. \end{aligned}$$

The quadratures operators $\hat{x}$ and $\hat{p}$ can also be defined similarly to (1.20). Those operators are hermitian operators, thus correspond to observables. They are given by

$$\hat{x}_l = \hat{a}_l + \hat{a}_l^\dagger, \quad \text{and} \quad \hat{p}_l = i(\hat{a}_l^\dagger - \hat{a}_l). \tag{1.28}$$

The quadrature operators satisfy the commutation relation $[\hat{x}_l, \hat{p}_l] = 2i$. The normalization has been chosen so their variances, defined by $\mathrm{Var}\,[\hat{q}_l] = \langle \hat{q}_l^2 \rangle - \langle \hat{q}_l \rangle^2$, ($\hat{q} = \hat{x}$ or $\hat{p}$), follow the Heisenberg inequality

$$\mathrm{Var}\,[\hat{x}_l]\,\mathrm{Var}\,[\hat{p}_l] \geq 1. \tag{1.29}$$

This inequality can be saturated for some specific quantum states. In the next section we present a family of such states, the coherent states, used in this work.

1.3.2 The coherent, or quasi-classical, state

The coherent states are the quantum states that best represent the state of light emitted by a laser well above threshold. They are also called quasi-classical states for that particular reason. They can be obtained by applying the displacement operator $\hat{D}(\alpha_l)$ on a vacuum state [31] so that

$$|\alpha_l\rangle = \hat{D}(\alpha_l)|0\rangle = e^{\alpha_l \hat{a_l}^\dagger - \alpha_l^\star \hat{a}_l}|0\rangle. \tag{1.30}$$

The coherent states are eigenvectors of the annihilation operator:

$$\hat{a}_l|\alpha_l\rangle = \alpha_l|\alpha_l\rangle, \tag{1.31}$$

with $\langle \hat{N}_l \rangle = N_l = |\alpha_l|^2$, the average photon number of the coherent state. From equations (1.28) and (1.31) it follows that

$$\mathrm{Var}\,[\hat{x}_l] = \mathrm{Var}\,[\hat{p}_l] = 1. \tag{1.32}$$

Consequently, the coherent states saturate the inequality (1.29).

Another property we wish to present is the photon number distribution of a coherent state. We saw earlier that the average photon number of a coherent state is given by $\langle \hat{N}_l \rangle = |\alpha_l|^2$. On the other hand, its variance is given by

$$\mathrm{Var}\left[\hat{N}_l\right] = \langle \hat{N}_l^2 \rangle - \langle \hat{N}_l \rangle^2 = \langle \hat{N}_l \rangle = |\alpha_l|^2. \tag{1.33}$$

We see that the variance of the photon-number operator is equal to its mean value. This property is characteristic of a Poisson distribution.

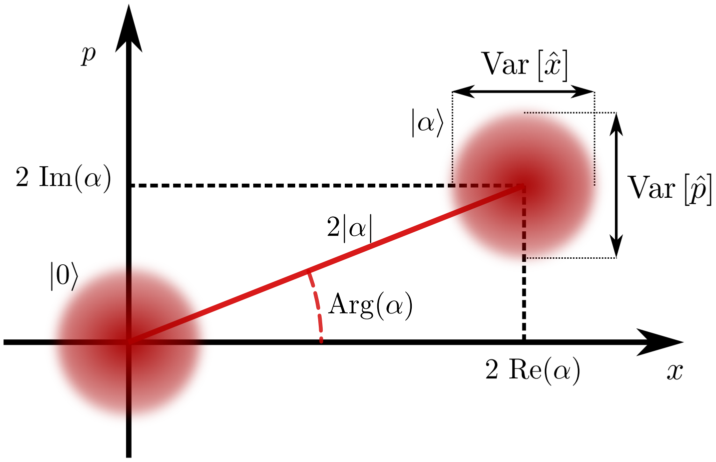

Figure 1.1 – **Phasor representation of a coherent state.** A coherent state can be represented in a 2D space. Its coordinates in this basis are the quadratures $\hat{x}$ and $\hat{p}$. For a coherent state $\mathrm{Var}\,[x] = \mathrm{Var}\,[x] = 1$

A more general coherent state can be obtained by considering a coherent superposition of coherent states $|\alpha_l\rangle$

$$|\psi\rangle = |\alpha_1\rangle \otimes \cdots \otimes |\alpha_l\rangle \otimes \cdots . \tag{1.34}$$

It can be shown that this state is intrinsically single mode [32]. It implies that there always exist a basis in which the coherent state $|\psi\rangle$ can be written as a coherent state $|\alpha\rangle$ in one mode and vacuum in all the others:

$$|\psi\rangle = |\alpha\rangle \otimes |0, \ldots, 0, \ldots\rangle. \tag{1.35}$$

From the definition above, the total photon number in the electric field N is given by

$$N = |\alpha|^2 = \sum_l |\alpha_l|^2 = \sum_l N_l \tag{1.36}$$

For convenience, the coherent states can be represented on a two dimensional space called a phasor as represented in Figure 1.1. This representation corresponds to a coherent state of mean photon number $|\alpha|^2$ obtained from the vacuum state $|0\rangle$ by applying the displacement $D(\alpha)$.

1.3.3 Continuous operators

Another notation that needs to be introduced is the representation in terms of continuous operators [33]. They are defined by

$$\hat{a}(t) = \sum_l \hat{a}_l\ u_l(t). \tag{1.37}$$

Those operators are, down to a constant, equal to the electric field (1.26). Hence, from equations (1.25) and (1.37), the commutation relation between the continuous annihilation and creation operators is given by

$$\left[\hat{a}(t), \hat{a}^\dagger(t')\right] = \delta(t - t') \tag{1.38}$$

We can use the same time and frequency decomposition as introduced in the classical case so that

$$\hat{a}(t) = \frac{1}{\sqrt{2\pi}} \int \mathrm{d}\omega \hat{a}(\omega) e^{-i\omega t}. \tag{1.39}$$

With this notation, the commutation relation in the frequency domain is given by

$$\left[\hat{a}(\omega), \hat{a}^\dagger(\omega')\right] = \delta(\omega - \omega'). \tag{1.40}$$

Finally, the continuous quadrature operators can be defined according to

$$\hat{x}(t) = \hat{a}(t) + \hat{a}^\dagger(t), \quad \text{and} \quad \hat{p}(t) = i(\hat{a}^\dagger(t) - \hat{a}(t)). \tag{1.41}$$

1.3.4 Wigner function

The electric field can also be represented in terms of quadratures using the Wigner function $W(\mathbf{x}, \mathbf{p})$ [34]. In the classical framework, the Wigner function would give the probability to measure a set of quadratures $\mathbf{x}$ and $\mathbf{p}$. However, in the quantum framework, the quadratures operators do not commute. Thus, the Wigner function is a quasi-probability distribution. The projection of $W(\mathbf{x}, \mathbf{p})$ on all quadratures except one leads to the probability to measure it. This function is normalized such that the integral over all quadratures is equal to 1:

$$\int \mathrm{d}^n\mathbf{x}\ \mathrm{d}^n\mathbf{p}\ W(\mathbf{x}, \mathbf{p}) = 1. \tag{1.42}$$

Another important property of the Wigner function is that it can be negative [35] which, even though not necessary, is a signature of the quantum nature of a state.

Gaussian states: In this thesis, we will only work with the so-called Gaussian states. They correspond to states whose Wigner function is Gaussian. Coherent states introduced in section 1.3.2 are part of the Gaussian states.
For a set of quadratures, their Wigner function is given by[1] [36]

$$W_p\left(\hat{\mathbf{Q}}\right) = \frac{1}{(2\pi)^M} \exp\left[\frac{1}{2}\left(\hat{\mathbf{Q}} - \langle\hat{\mathbf{Q}}\rangle\right)^T \Gamma^{-1}\left(\hat{\mathbf{Q}} - \langle\hat{\mathbf{Q}}\rangle\right)\right], \tag{1.43}$$

where $\hat{\mathbf{Q}} = (\hat{x}_1, \ldots, \hat{x}_M, \hat{p}_1, \ldots, \hat{p}_M)$ is the vector of $2M$ quadratures, and Γ is the real $2M \times 2M$ covariance matrix such that $\Gamma = \frac{1}{2}\langle\hat{\mathbf{Q}}\hat{\mathbf{Q}}^T + \left(\hat{\mathbf{Q}}\hat{\mathbf{Q}}^T\right)^T\rangle$.

---

[1] This definition is valid for a pure state.

Covariance matrix: The covariance matrix can be expressed in terms of operators fluctuations $\delta\hat{q}_i = \hat{q}_i - \langle\hat{q}_i\rangle$. We define the x covariance matrix $\hat{\Gamma}_x$, and the p covariance matrix $\hat{\Gamma}_p$ as

$$\left[\hat{\Gamma}_x\right]_{ij} = \langle\delta\hat{x}_i\delta\hat{x}_j\rangle \qquad \left[\hat{\Gamma}_p\right]_{ij} = \langle\delta\hat{p}_i\delta\hat{p}_j\rangle \tag{1.44}$$

The diagonal elements correspond to the variance of each individual quadrature. The off-diagonal elements correspond to the correlations between the different quadratures. The total matrix $\hat{\Gamma}$, is given by the x and p covariance matrices as well as their correlation matrix

$$\left[\hat{C}\right]_{ij} = \langle\delta\hat{x}_i\delta\hat{p}_j\rangle. \tag{1.45}$$

Thus we have

$$\hat{\Gamma} = \begin{pmatrix} \hat{\Gamma}_x & \hat{C} \\ \hat{C}^T & \hat{\Gamma}_p \end{pmatrix} \tag{1.46}$$

The covariance matrix contains all the second moments of the quadrature operators. Consequently, for gaussian states, this matrix contains all the information about the state. This tool will be very useful in this work as it allows to characterize simultaneously the fluctuations of each quadrature from a given basis as well as their correlations.

1.4 Noise and fundamental limits

Now that the notations to describe the electric field have been presented, we introduce the mathematical tools to describe the noise affecting its parameters. The most common way to characterize the fluctuations of a given quantity is to measure its power spectral density. It corresponds to the distribution of the signal power over the frequencies composing this signal. Then, we have a closer look at the fundamental limits imposed by the presence of noise, i.e the smallest quantities that can be measured experimentally.

1.4.1 Power spectral density

Let us consider a signal $i(t)$, of zero mean for simplicity, observed during a time T. This signal can be, for example, a fluctuating parameter of the electric field we wish to characterize. The total average power of the signal over all time is given by the time average

$$P = \lim_{T\to+\infty} \frac{1}{T} \int_{-T/2}^{T/2} |i(t)|^2 \, \mathrm{d}t \tag{1.47}$$

To pursue the derivation, we introduce the windowed signal $i_T(t)$ according to

$$i_T(t) = \begin{cases} i(t) & \text{if } t \in [-T/2 : T/2]\,, \\ 0 & \text{otherwise.} \end{cases} \tag{1.48}$$

With this notation, equation (1.47) can be written

$$P = \lim_{T\to+\infty} \frac{1}{T} \int_{-\infty}^{+\infty} |i_T(t)|^2 \ \mathrm{d}t. \tag{1.49}$$

According to the Parseval-Plancherel theorem, the same definition can be written in the frequency domain:

$$P = \lim_{T\to+\infty} \frac{1}{T} \int_{-\infty}^{+\infty} |i_T(t)|^2 \ \mathrm{d}t = \lim_{T\to+\infty} \frac{1}{T} \int_{-\infty}^{+\infty} |\tilde{i}_T(f)|^2 \ \mathrm{d}f. \tag{1.50}$$

The power spectral density (PSD) $W_i(f)$ is defined as the integrand of the right part of the expression above, so that

$$W_i(f) = \lim_{T\to+\infty} \frac{1}{T} |\tilde{i}_T(f)|^2 \tag{1.51}$$

This definition is not practical to use experimentally for data processing. Consequently, we derive another expression relating the PSD to the variance of the signal, which is easier to compute.
The first step is to rewrite $|\tilde{i}_T(f)|^2$ in terms of the Fourier transform of a time convolution. Hence, equation (1.51) can be rewritten

$$\begin{aligned} \lim_{T\to+\infty} \frac{1}{T} |\tilde{i}_T(f)|^2 &= \lim_{T\to+\infty} \frac{1}{T} \mathrm{FT}\left\{ i_T^\star(t) * i_T(t) \right\} \\ &= \int_{-\infty}^{+\infty} \left\{ \lim_{T\to+\infty} \frac{1}{T} \int_{-\infty}^{\infty} i_T^\star(t-\tau) i_T(t) \ \mathrm{d}t \right\} e^{2i\pi f\tau} \ \mathrm{d}\tau. \end{aligned} \tag{1.52}$$

To go further, the ergodic hypothesis needs to be used. It implies that the time evolution of a random signal observed for a sufficiently long time carry the same information as many realization of this signal. Hence, the statistical properties of this signal can be derived from its time evolution. The consequence is that the time average, as presented in equation (1.47), can be identified to the statistical average, noted $\langle \cdot \rangle$. Thus, the time average in equation (1.52) can be replaced by the statistical average. The PSD is then written

$$\begin{aligned} W_i(f) &= \int_{-\infty}^{+\infty} \langle i^\star(t-\tau) i(t) \rangle e^{2i\pi f\tau} \ \mathrm{d}\tau \\ &= \int_{-\infty}^{+\infty} R_i(\tau) e^{2i\pi f\tau} \ \mathrm{d}\tau \\ &= \tilde{R}_i(f), \end{aligned} \tag{1.53}$$

where $R_i(\tau) = \langle i^\star(t-\tau) i(\tau) \rangle$ is the auto-correlation function of $i(t)$. This relation, known as the Wiener-Khinchin theorem, states that the PSD is the Fourier transform

of the auto-correlation function.
Still, the auto-correlation is not always easy to compute experimentally. To go further, we take the inverse Fourier transform of both sides which leads to

$$R_i(\tau) = \int_{-\infty}^{+\infty} W_i(f) e^{-2i\pi f\tau} \, \mathrm{d}f. \tag{1.54}$$

Finally, using the fact that the auto-correlation is equal to the variance for $\tau = 0$ we have

$$R_i(\tau = 0) = \langle |i(t)|^2 \rangle = \int_{-\infty}^{+\infty} W_i(f) \, \mathrm{d}f. \tag{1.55}$$

This expression shows how the PSD is related to the variance of a signal. To really be practical in an experiment, a spectral link between the variance and the PSD is needed. To this aim, the variance is calculated for a fixed frequency interval $[f : f + \Delta f]$. This can be achieved by different means but the most common is to use a swept radio-frequency signal mixed with the signal measured and to filter the resulting signal with a bandwidth Δf. It corresponds to the measurement of a spectrum analyzer. A different implementation of this procedure will also be detailed in Chapter 4.
Using equation (1.55), the variance over the frequency interval Δf is related to the PSD according to

$$\langle |i(t)|^2 \rangle_{[f:f+\Delta f]} = \int_{f}^{f+\Delta f} W_i(f) \, \mathrm{d}f. \tag{1.56}$$

For a sufficiently small interval Δf, the PSD can be considered constant over the detection bandwidth. Consequently, the PSD can be directly related to the variance calculated over a frequency range according to

$$W_i(f) = \frac{\langle |i(t)|^2 \rangle_{[f:f+\Delta f]}}{\Delta f} \tag{1.57}$$

Note that $W_i(f)$ is defined for both positive and negative frequency values. However, in practice, the signal measured are real. Thus, the negative frequencies do not contain additional information. Hence, we define the single-sided PSD, $S_i(f) = 2W_i(f)$. This quantity is defined for positive frequencies only and contains the same power as the double-sided PSD $W_i(f)$.

White Gaussian noise : We take a moment here to discuss a particular class of noises called white Gaussian noises. Up to now, the equations have been derived without specifying anything about the signal $i(t)$. However, we will encounter in this thesis noises that can be classified as white Gaussian noises. Gaussian means that the probability density function describing the noise statistic is a normal distribution of mean μ and variance σ^2. White means that there is no correlations between realizations of the signal taken at different times . A well known example of white Gaussian noise is the shot noise of a field containing many photons[2], due to the random time of arrival of the photons on a detector. We will see that the definitions above allow to calculate the PSD associated to that particular class of noises.

We keep the assumption that $i(t)$ is a signal with zero mean. As seen in equation (1.53), the PSD is given by the Fourier transform of the auto-correlation function. We remind that the auto-correlation function is given by

$$R_i(\tau) = \langle i^\star(t-\tau) i(\tau) \rangle. \tag{1.58}$$

If $i(t)$ is a white Gaussian noise, there is no correlations between realization of the signal at two different times, thus the auto-correlation is given by

$$R_i(\tau) = \langle |i(t)|^2 \rangle \delta(\tau) = \sigma^2 \delta(\tau), \tag{1.59}$$

where $\delta(\tau)$ is the Dirac function. Inserting this result in equation (1.53) leads to

$$W_i(f) = \int_{-\infty}^{+\infty} \sigma^2 \delta(\tau) e^{2i\pi f \tau} \, \mathrm{d}\tau = \sigma^2, \tag{1.60}$$

where we used the fact that the Fourier transform of a Dirac function is equal to one. We find the well-known result that the PSD of a white noise is constant and equal to the variance of the signal in case of a Gaussian noise. This expression will be useful later in the manuscript.

1.4.2 Fundamental limits in parameter estimation

The previous section presents the tools to characterize noises. The question that can now be asked is: what is the smallest quantity that can be theoretically measured in the presence of noise? In this section we first present a simplified approach to determine the lower bound for the estimation of the phase and the amplitude of the electric field. Secondly, we introduce the Fisher information which allows to properly quantify the smallest accessible value of a parameter measured with a given experimental setup. Finally, we apply the calculation of the Fisher information to the determination of a phase shift. We will see that, in the case of Gaussian states, the same result as the first derivation can be found.

---

[2] In the low photon regime, the statistic is given by the Poisson distribution.

1.4.2.1 Amplitude and phase fundamental limits

In order to estimate the smallest phase and amplitude variation measurable, let us start by writing the expression of the electric field whose amplitude and phase are slightly deviated from their average values:

$$\hat{E}^{(+)}(t) = \mathcal{E}_0 e^{-i\omega_0 t}\hat{a}(t)(1+\delta\epsilon(t))e^{i\delta\varphi(t)}, \tag{1.61}$$

where $\delta\epsilon(t)$ stands for the amplitude deviation and $\delta\varphi(t)$ the phase one. In this expression, $a(t)$ is taken to be real. In section 1.2.3 we introduced the quadratures of the electric field which are observables. Consequently, we assume that the electric field (1.61) is measured via its quadratures. This can be achieved using, e.g a homodyne detection as will be explained in section 3.3.
As the deviations are small, expression (1.61) can be expanded at first order. Taking only the deviation from the mean value, i.e $\delta\hat{E}^{(+)}(t) = \hat{E}^{(+)}(t) - \left\langle \hat{E}^{(+)}(t) \right\rangle$ and using equation (1.19) we have

$$\delta\hat{E}^{(+)}(t) = \mathcal{E}_0 e^{-i\omega_0 t}\hat{a}(t)(\delta\epsilon(t) + i\delta\varphi(t)) = \frac{\mathcal{E}_0}{2}\left[\delta\hat{x}(t) + i\delta\hat{p}(t)\right]e^{-i\omega_0 t}, \tag{1.62}$$

with $\delta\hat{x}(t) = \hat{x}(t) - \langle\hat{x}(t)\rangle$ and the same for $\delta\hat{p}(t)$. Thus the amplitude and phase deviations induce deviations of the quadratures according to

$$\delta\hat{x}(t) = 2\hat{a}(t)\delta\epsilon(t), \quad \text{and} \quad \delta\hat{p}(t) = 2\hat{a}(t)\delta\varphi(t). \tag{1.63}$$

In order to determine the minimal measurable deviation, the signal to noise ratio (SNR) needs to be calculated. Experimentally, the quadratures $\hat{x}(t)$ and $\hat{p}(t)$ are affected by noise coming from various sources. This noise is characterized by the variance of the quadratures. Hence, the SNR, e.g for a measurement of the quadrature $\hat{x}(t)$, is given by

$$\mathrm{SNR} = \frac{\langle\delta\hat{x}(t)\rangle}{\sqrt{\mathrm{Var}\left[\hat{x}(t)\right]}}. \tag{1.64}$$

The smallest measurable quantity corresponds to a SNR equals to one, that is when the noise is as strong as the signal. Hence, using equations (1.63) and (1.64), we have

$$\delta\epsilon_{min} = \frac{\sqrt{\mathrm{Var}\left[\hat{x}(t)\right]}}{2\langle\hat{a}(t)\rangle}, \quad \text{and} \quad \delta\varphi_{min} = \frac{\sqrt{\mathrm{Var}\left[\hat{p}(t)\right]}}{2\langle\hat{a}(t)\rangle}, \tag{1.65}$$

where $\delta\epsilon_{min}$ and $\delta\varphi_{min}$ are the smallest amplitude a phase deviations measurable in the presence of noise $\sqrt{\mathrm{Var}\left[\hat{q}(t)\right]}$.

We are interested in determining the smallest phase and amplitude deviations measurable. As can be seen from the expressions above, the limit is fixed by the noise of the electric field via its quadratures. Consequently, the fundamental limit is set by the quantum noise of the field. Therefore, to find this limit, we calculate the noise for a coherent state of same power as the laser studied. The properties of the coherent states introduced in section 1.3.2 combined to the definition of the continuous modes (1.37) leads to $\mathrm{Var}\left[\hat{q}(t)\right] = 1$ and $\langle \hat{a}(t) \rangle = |\alpha| = \sqrt{N}$. Hence, from (1.63) the minimal measurable amplitude and phase deviations are given by

$$\delta\epsilon_{min} = \frac{1}{2\sqrt{N}}, \quad \text{and} \quad \delta\varphi_{min} = \frac{1}{2\sqrt{N}}. \tag{1.66}$$

Note that some states of light allow to go beyond this limit. This is the case for the so called squeezed states. As they are not used to perform any measurement in this work we do not wish to go into more details.

1.4.2.2 Fisher information

The previous derivation has been made for a specific scenario. More generally ,the Fisher information can be used to quantify the amount of information that can be extracted from an observable, called estimator, about a parameter p. Knowing the probability $P_p(X)$ to get a given measurement result X when measuring the estimator depending on p, the Fisher information is given by

$$I_{Fisher} = -\int \frac{\partial^2 \log(P_p(X))}{\partial p^2} P_p(X) dX. \tag{1.67}$$

The lower bound on the estimation of the parameter p for an unbiased[3] estimator is given by

$$p_{CRB} = \frac{1}{\sqrt{I_{Fisher}}}. \tag{1.68}$$

This bound is called the Cramèr-Rao bound (CRB) [37]. An estimator allowing to reach that bound is called optimal. In Chapter 3, we will investigate two measurement strategies and compare them with the mean of this optimal bound.

1.4.2.3 Parameter estimation

In this section we apply the Fisher information to the estimation of a parameter encoded in the electromagnetic field. We will see that, in the case of Gaussian states, it allows to find the same result for the estimation of a phase deviation as in section 1.4.2.1.

---

[3] Meaning that its expectation value is equal to the parameter p.

We start by making the assumption that the most general scenario is the measurement of the quadratures of the electric field. As stated previously, the Wigner function (1.43) can be used to describe such measurement. Hence, we apply the Fisher information formula (1.67) to this quasi-probability distribution:

$$I_{Fisher} = -\int \frac{\partial^2 \log\left[W_p\left(\hat{\mathbf{Q}}\right)\right]}{\partial p^2} W_p\left(\hat{\mathbf{Q}}\right) d\hat{\mathbf{Q}}, \tag{1.69}$$

where p is the parameter we want to estimate, $\hat{\mathbf{Q}}$ is the vector of $2M$ measured quadratures. After calculation, and under some assumptions, it can be shown [38] that equation (1.69) can be simplified into

$$I_{Fisher} = \left(\left.\frac{\partial\langle\hat{\mathbf{Q}}\rangle}{\partial p}\right|_0\right)^T \Gamma^{-1} \left(\left.\frac{\partial\langle\hat{\mathbf{Q}}\rangle}{\partial p}\right|_0\right). \tag{1.70}$$

We remind that the annihilation operator can be written as $\hat{a}(t) = \sum_l \hat{a}_l \, u_l(t)$ where the $u_l(t)$ form an othonormal basis. In this basis, the quadratures are written $q_l = \hat{a}_l + \hat{a}_l^\dagger$ and $q_{l+M} = i(\hat{a}_l^\dagger - \hat{a}_l)$. In order to simplify the expression (1.70), we introduce a new basis whose first element $w_1(t)$ is given by

$$w_1(t) = \left.\frac{\partial\overline{a}_p(t)}{\partial p}\right|_0 \left|\left|\left.\frac{\partial\overline{a}_p(t)}{\partial p}\right|_0\right|\right|^{-1}, \tag{1.71}$$

where $\overline{a}_p(t) = \langle\psi_p|a(t)|\psi_p\rangle$ is the mean field, with $|\psi_p\rangle$ the state of the electric field in which the parameter p is encoded. $\left|\left|\left.\frac{\partial\overline{a}_p(t)}{\partial p}\right|_0\right|\right|$ is the L^2 norm:

$$\left|\left|\left.\frac{\partial\overline{a}_p(t)}{\partial p}\right|_0\right|\right|^2 = \int_{\mathbb{R}} \mathrm{d}t \left|\left.\frac{\partial\overline{a}_p(t)}{\partial p}\right|_0\right|^2. \tag{1.72}$$

The mode $w_1(t)$ is called detection mode. The basis is completed with modes $w_{j>1}(t)$ orthonormal to $w_1(t)$. In this basis the annihilation operators writes

$$\hat{a}(t) = \sum_j \hat{b}_j w_j(t) \quad \text{with} \quad \hat{b}_j = \int_{\mathbb{R}} \mathrm{d}t \; w_j^\star(t)\hat{a}(t). \tag{1.73}$$

Using this new basis to write the quadrature operators, it can be shown [39] that the Fisher information of a Gaussian state is given by

$$I_{Fisher} = 4\left[\Gamma^{-1}\right]_{1,1} \left|\left|\left.\frac{\partial\overline{a}_p(t)}{\partial p}\right|_0\right|\right|^2, \tag{1.74}$$

where $\left[\Gamma^{-1}\right]_{1,1}$ is the first diagonal element of the inverse covariance matrix in the basis $\{w_j(t)\}$.

We can now apply this treatment to the determination of phase a shift $\delta\varphi$. As in section 1.4.2.1 we assimilate the field to a coherent state $|\alpha\rangle$. We apply a phase shift $\delta\varphi$ on this field such that the perturbed field is given by

$$|\alpha_{\delta\varphi}\rangle = \hat{D}(\alpha_{\delta\varphi})|0\rangle = \exp\left[\alpha e^{i\delta\varphi}\hat{a}^{\dagger}(t) - \alpha^{\star}e^{-i\delta\varphi}\hat{a}(t)\right]|0\rangle. \tag{1.75}$$

Thus, the mean field is given by

$$\overline{a}_{\delta\varphi}(t) = \langle\alpha_{\delta\varphi}|a(t)|\alpha_{\delta\varphi}\rangle = \alpha(t)e^{i\delta\varphi}, \tag{1.76}$$

with $\alpha(t) = \sum_l \alpha_l u_l(t)$. Because a coherent state is intrinsically single mode, it can also be written $\alpha(t) = \alpha u_0(t)$, where $u_0(t)$ is the mean field temporal mode. Applying equation (1.74), taking into account the fact that for a coherent state $\Gamma = Id$, where Id is the identity matrix, we find $I_{Fisher} = 4N$, where $N = |\alpha|^2$ is the number of photons in the incident field. Thus the smallest phase shift that can be measured is

$$\delta\varphi_{SQL} = \frac{1}{\sqrt{I_{Fisher}}} = \frac{1}{2\sqrt{N}}. \tag{1.77}$$

This bound corresponds the ultimate limit for phase measurement and corresponds to the result found in section 1.4.2.1. It is usually referred as standard quantum limit (SQL) [40, 41]

Chapter 2

Optical frequency comb

Contents

2.1 Description of an optical frequency comb 25
2.1.1 Naive description of a frequency comb 26
2.1.2 Mathematical description of the comb electric field 28
2.2 Kerr-lens mode-locking 32
2.2.1 Kerr-lens effect 32
2.2.2 Master equation for Kerr-lens mode-locking 33
2.2.3 Resolution of the master equation and intracavity dispersion . 36
2.3 Dispersion of an optical pulse 37
2.3.1 Fourier transform pulses 38
2.3.2 Propagation through a dispersive medium 39
2.3.3 Numerical application 40

In the previous chapter we presented the mathematical tools to describe the electric field. It was expressed in terms of envelope modes. In this chapter we will see how those modes can be used to model optical pulses. This description is applied to the specific case of optical frequency combs (OFCs). This particular class of lasers produces train of ultra-short pulses. In the frequency domain, a succession of such pulses is composed of numerous individual frequency lines which represent the teeth of the comb. We present the physical process behind the generation of such ultrashort pulses. We restrict ourselves to the so called Kerr-lens mode-locking corresponding to the laser used in this work. Finally, we present some effects related to the propagation of pulses in materials.

2.1 Description of an optical frequency comb

In this section we first present a simplified description of the optical frequency comb. The aim is to understand the physical process of mode-locking responsible for the generation of ultrashort pulses in OFCs. We then derive the mathematical expression of the electric field describing the light emitted by an OFC.

2.1.1 Naive description of a frequency comb

2.1.1.1 Continuous wave laser

A laser is essentially composed of two elements: a cavity, or resonator, and a gain medium. The gain medium coherently amplifies the light passing through it. The cavity allows the light to go back and forth along the same path every time. One of the mirrors from the cavity is slightly transmissive, allowing light to escape it. This mirror is called the output-coupler (OC). Steady state lasing is obtained when the gain per round trip in the resonator is equal to the losses (introduced e.g by the OC). Besides, steady state can only be achieved for certain frequency ω_m of the electric field. Those particular frequencies correspond to the electric field forming a standing wave inside the resonator. Boundary conditions at the mirror interfaces impose that the resonating frequencies are of the form

$$\omega_m = m\frac{2\pi c}{L}, \tag{2.1}$$

where L is the cavity round-trip optical path length[1]. The laser can thus oscillate only at those frequencies called optical modes of the cavity. The separation between two frequencies $\Delta f = \frac{1}{2\pi}(\omega_m - \omega_{m-1}) = \frac{c}{L}$ is called the free spectral range (FSR).
Finally, the frequency at which the laser actually operates is given by the loss and gain spectral profiles. For example, if the spectral region for which the gain overtakes the losses is really narrow compared to the FSR, only one frequency will be emitted leading to a monochromatic wave as illustrated in Figure 2.1.

2.1.1.2 Optical frequency comb

On the other hand, if the gain and loss profiles are such that many modes can oscillate in the cavity at the same time, pulsed operation can be achieved under a certain condition. This condition is called mode-locking. We present here a textbook explanation of this process and how it leads to the production of ultrashort pulses. Note that other processes allow to produce (usually longer) pulses of light, such as Q-switching, but are not studied in this thesis.

If we consider that N optical modes, of equal amplitude E_0, separated by the FSR of the cavity, oscillate inside the laser, the total electric field at the laser output can be

---

[1] We consider a ring cavity for the calculations in this chapter. Note that we specified optical path because the length depends on the optical index of the cavity elements.

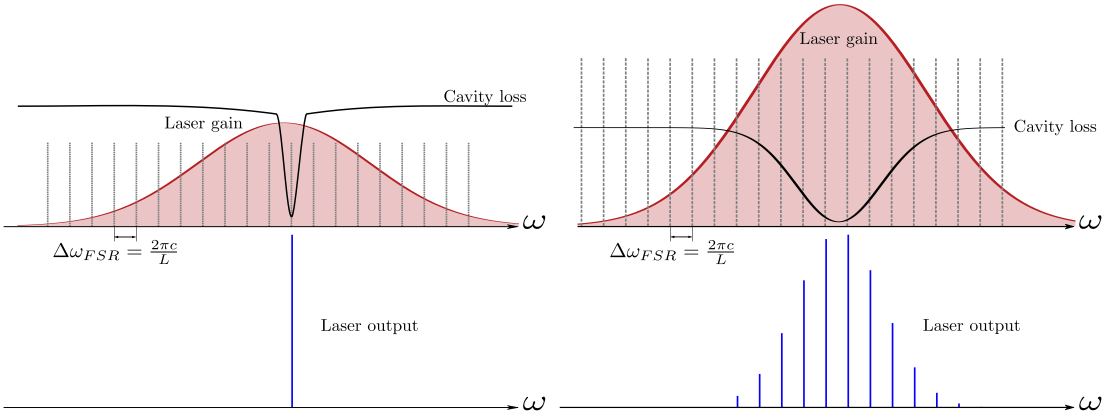

Figure 2.1 – **Spectra of two different laser losses and gain conditions.** The optical modes of the cavity (in dashed grey) are separated by the FSR, $\Delta\omega_{FSR} = \frac{2\pi c}{L}$. The gain profile of the active medium is represented in red. The loss profile is represented as a black line. The configuration on the left corresponds to a single frequency operation. The region for which the losses are lower than the gain is really narrow. Thus only one mode can oscillate. The configuration on the right has a broader loss profile. Hence many modes can oscillate at the same time in the laser cavity.

written

$$E^{(+)}(t) = E_0 \sum_{m=-(N-1)/2}^{(N-1)/2} e^{i\phi_m} e^{-i(\omega_0+\omega_m)t}, \tag{2.2}$$

were ϕ_m is the phase of each optical mode and ω_0 is an offset frequency, also called carrier frequency (this designation will be justified later). If no assumption is made on the phases ϕ_m, it can be shown [42] that the intensity $I(t)$ randomly fluctuates around the average intensity $I(t) \propto N|E_0|^2$. On the other hand, if all the phases of the modes are fixed so that $\phi_m = \phi$, the intensity is given by

$$I(t) \propto |E_0|^2 \frac{\sin^2(N\pi t\Delta f)}{\sin^2(\pi t\Delta f)}. \tag{2.3}$$

With this simple but explicit picture, it is possible to understand how ultrashort pulses can be produced. By taking a discrete superposition of frequency modes, a periodic train of pulses can be formed as illustrated by equation (2.3). This is true provided that a constant phase relation exists between the modes. It is the mode-locking condition. We will later present one of those mode-locking process, based on the Kerr effect. The discrete frequency modes form the teeth of the optical frequency comb. In the time domain, individual pulses of approximate duration $\Delta t = 1/(N\Delta f)$ are evenly separated in time by $T_r = 1/\Delta f = L/c$. This period corresponds to the repetition rate of the laser and is sometimes given in frequency according to $f_r = 1/T_r$.

The intensity at the top of each pulse is of the order of $N^2|E_0|^2$ which corresponds to an enhancement of a factor N of the average intensity. It can be noted that the more modes oscillate in phase, the shorter and more intense the pulses produced.

2.1.2 Mathematical description of the comb electric field

The previous section introduced a simplified description of the optical frequency comb. In this section, we derive the equations to properly characterize the OFC. We start by the expression of the spectral modes forming the teeth of the comb. Then, based on equation (2.2), we derive the field associated to the OFC. Finally, we discuss the representation of a single pulse.

2.1.2.1 Spectral modes of the optical frequency comb

As seen previously, if the gain and losses conditions are suitable, many spectral modes (or spectral lines) can oscillate in the cavity at the same time. Each of those modes ω_m will acquire a phase shift $\phi(\omega_m)$ due to the round trip in the laser cavity. The condition for the modes to oscillate, is that their phase shift must be a multiple of 2π i.e

$$\phi(\omega_m) = 2\pi m, \quad m \in \mathbb{Z}. \tag{2.4}$$

This resonating condition is identical to equation (2.1). However, to describe a real comb, the chromatic dispersion inside the cavity must be taken into account.

Dispersion: Dispersion comes from the frequency dependent refractive index $n(\omega)$ of some of the cavity components[2]. To witness the effect of this dispersion, the round trip phase, written

$$\phi(\omega) = Lk(\omega) = L\frac{\omega}{c}n(\omega), \tag{2.5}$$

with L the cavity length and $k(\omega)$ the wavenumber, can be Taylor expanded around the carrier frequency ω_0, according to

$$\begin{aligned}\phi(\omega) &\simeq \phi(\omega_0) + (\omega-\omega_0)\left.\frac{\partial\phi(\omega)}{\partial\omega}\right|_{\omega_0} + (\omega-\omega_0)^2\left.\frac{\partial^2\phi(\omega)}{\partial\omega^2}\right|_{\omega_0} \\ &= \phi^{(0)} + (\omega-\omega_0)\phi^{(1)} + (\omega-\omega_0)^2\phi^{(2)},\end{aligned} \tag{2.6}$$

At first, only the two first terms will be considered as they are the most important contributions. The quadratic term will be investigated later in section 2.3.

---

[2] This can be the case of the mirror, the crystal or other passive elements used for dispersion compensation. Sometimes, even the dispersion of the air must be taken into account.

Repetition rate and carrier-envelope offset: In equation (2.6), we have defined a constant phase term $\phi^{(0)}$ and a linear one $\phi^{(1)}$. They are given by

$$\phi^{(0)} = \phi(\omega_0) = \frac{\omega_0}{c} n(\omega_0) L = \frac{\omega_0 L}{v_\phi}, \tag{2.7a}$$

$$\phi^{(1)} = \frac{L}{c}\left(n(\omega_0) + \omega_0 \left.\frac{\partial n(\omega)}{\partial \omega}\right|_{\omega_0} \right) = \frac{L}{v_g}, \tag{2.7b}$$

were v_g and v_ϕ are respectively the group and phase velocity at the carrier frequency ω_0[3]. The group velocity corresponds to the velocity at which the envelope of the pulse propagates in a medium. On the other hand, the phase velocity corresponds to the velocity of the carrier phase front at the frequency ω_0. With those notations, the two first terms of equation (2.6) can be rewritten

$$\phi(\omega) \simeq -\omega_0 L \left(\frac{1}{v_g} - \frac{1}{v_\phi} \right) + \frac{\omega L}{v_g} = -\Delta\phi_{CEO} + \frac{\omega L}{v_g}, \tag{2.8}$$

were $\Delta\phi_{CEO}$ corresponds to a phase shift induced by the difference between group and phase velocity due to chromatic dispersion. We will see in the next section, that this term is responsible for a phase shift between the envelope and the carrier from pulse to pulse, hence the name carrier-envelope offset (CEO).

Using equations (2.7) and (2.8), the resonating condition (2.4) can be written

$$-\Delta\phi_{CEO} + \frac{\omega_m L}{v_g} = 2\pi m \quad \Rightarrow \quad \omega_m = \frac{v_g}{L}(2\pi m + \Delta\phi_{CEO}) = m\omega_r + \omega_{CEO}, \tag{2.9}$$

were ω_m is the frequency of each spectral line, $\omega_r = 2\pi \frac{v_g}{L}$ corresponds to the FSR of the laser and $\omega_{CEO} = \frac{v_g}{L}\Delta\phi_{CEO}$ is the CEO frequency. This frequency is sometimes called f_0 as it corresponds to the frequency of the first tooth of the comb.

2.1.2.2 Electric field of the optical frequency comb

To write the electric field of the optical frequency comb, the expression of the spectral modes ω_m, given by equation (2.9), can be injected in equation (2.2). However, in equation (2.2), we assumed that all the modes have the same amplitude. In principle this is not true. Each mode ω_m has a given spectral amplitude $E^{(+)}(\omega_m)$. In addition, we assume that the mode-locking condition is satisfied, that is $\phi_m = \phi$. For simplicity we take $\phi = 0$. Thus the electric field of the comb is given by

$$E^{(+)}_{\text{comb}}(t) = \sum_{m=-(N-1)/2}^{(N-1)/2} E^{(+)}(\omega_m) e^{-i(\omega_0+\omega_m)t}, \tag{2.10}$$

---

[3] Note that this is valid in the narrow-band approximation so that all the frequencies are close to the central one ω_0.

The spectrum of the laser field is given by the Fourier transform of the expression above. Hence, the electric field of the comb in the spectral domain can be written

$$\tilde{E}^{(+)}_{\text{comb}}(\omega) = \tilde{E}^{(+)}(\Omega) \sum_m \delta(\Omega - (m\omega_r + \omega_{CEO})), \tag{2.11}$$

with $\Omega = \omega - \omega_0$ and were $\sum_m \delta(\Omega - (m\omega_r + \omega_{CEO}))$ is the Dirac comb. This field corresponds to a set of evenly separated spectral lines, modulated by a spectral amplitude centered around the frequency ω_0, as represented in Figure 2.2. Note that, in this expression, the spectral amplitude, $\tilde{E}^{(+)}(\Omega)$ is a continuous function, while it was discrete in equation (2.10). However, because the Dirac function is null except at the frequencies ω_m, this notation is equivalent.
We recover the field of the comb in the time domain by taking the inverse Fourier transform of the expression above. It can be shown that

$$\begin{aligned} E^{(+)}_{\text{comb}}(t) &\propto E^{(+)}(t) * \sum_k \delta(t - kT_r) e^{-ik\Delta\phi_{CEO}} \\ &\propto \mathcal{E}_0 \sum_k a(t - kT_r) e^{-i\omega_0(t-kT_r)} e^{-ik\Delta\phi_{CEO}}, \end{aligned} \tag{2.12}$$

with $T_r = 2\pi/\omega_r$ and $\Delta\phi_{CEO} = \frac{2\pi}{\omega_r}\omega_{CEO}$. The symbol $*$ represent the convolution product. In addition, we wrote the amplitude as $E^{(+)}(t) = \mathcal{E}_0 a(t) e^{-i\omega_0 t}$ to be consistent with the notations introduced in the first Chapter. Equation (2.12) indicates that the field of the comb can be expressed as a field $E^{(+)}(t)$, representing the field of an isolated pulse, convolved with a Dirac comb $\sum_k \delta(t - kT_r)$. It implies that this pulse is replicated many times separated by T_r which is the repetition rate of the laser. In the rest of this thesis, the field associated to a single pulse will be noted $E^{(+)}_{\text{pulse}}(t)$.

In conclusion, the same result as in section 2.1.1 is found. The superposition of discrete frequency lines at the frequencies $\omega_m = m\omega_r + \omega_{CEO}$, corresponding to the teeth of the comb, allows to generate pulses if the mode-locking condition is satisfied. In the time domain, the laser emits a train of pulses separated in time by $T_r = 2\pi/\omega_r$, the repetition rate of the laser. Due to dispersion, the phase velocity, v_ϕ is different from the group one, v_g. Hence, each pulse accumulates a phase shift $\Delta\phi_{CEO}$. This is illustrated in Figure 2.2.

2.1.2.3 Pulse shape

In the previous section, we saw that the field of the OFC can be describe as the convolution of a single pulse $E^{(+)}_{\text{pulse}}(t)$, with a Dirac comb. Each pulse is composed of an envelope $a(t)$ and a carrier oscillating at the frequency ω_0. Their expression is given by

$$E^{(+)}_{\text{pulse}}(t) = \mathcal{E}_0 a(t) e^{-i\omega_0 t}. \tag{2.13}$$

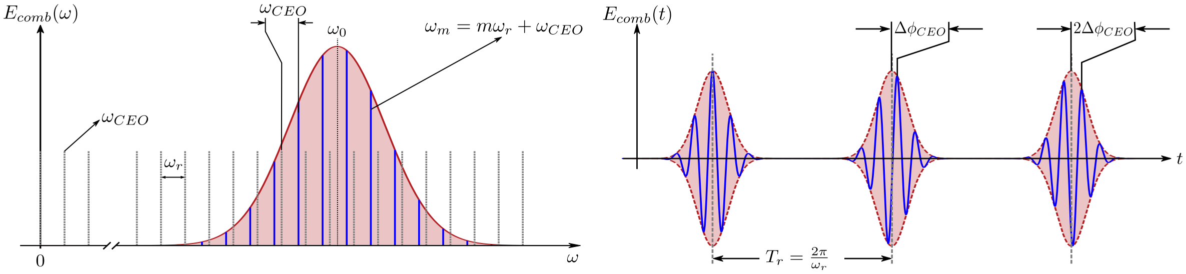

Figure 2.2 – **Representation of the optical frequency comb in the frequency domain and the train of pulses in the time domain.** In the frequency domain (left) the comb is composed of many individual frequency lines separated by the FSR of the laser ω_r. Due to chromatic dispersion, the lasing frequencies (in blue) are shifted from the resonating modes of the cavity (in dashed grey) by the CEO frequency ω_{CEO}. In the time domain (right), the field is composed of a succession of individual pulses separated by the repetition rate of the laser $T_r = 2\pi/\omega_r$. The carrier oscillation (in blue) is shifted from pulse to pulse by $\Delta\phi_{CEO} = \frac{\omega_r}{2\pi}\omega_{CEO}$.

This expression is similar to equation (1.17). Consequently, the description of the electric field in terms of envelope modes is particularly well suited for the description of optical pulses. In this framework, $a(t)$ is the envelope mode, slowly varying in time compared to the carrier frequency ω_0. In principle, this mode can have any shapes. The most commons are the Gaussian or the hyperbolic secant, which approximate the best the shape of the pulses emitted by a mode-locked laser.
The Fourier Transform of this pulse is given by

$$E^{(+)}_{\text{pulse}}(\Omega) = \mathcal{E}_0 \tilde{a}(\Omega), \tag{2.14}$$

this envelope mode in the frequency domain is the optical spectrum of the laser.

This decomposition in single pulses periodically repeated will be important in the second part of this manuscript. Indeed, because the field of the comb is related to the field of a single pulse according to equation (2.11) (or equation (2.12)), characterizing one impulsion is enough to fully characterize the optical frequency comb. By making this assumption, and looking only at $E^{(+)}_{\text{pulse}}(t)$ and $E^{(+)}_{\text{pulse}}(\Omega)$, we restrict our investigation to the effects affecting all the pulses in a same way.

2.1.2.4 Peak power

We use the opportunity of the definition of the laser pulse parameters to introduce a new quantity, the peak optical power P_{peak}. This quantity corresponds to the power at the top of the pulse. It is related to average optical power P_{avg} defined in equation 1.23

according to

$$P_{peak} = \frac{0.88}{f_r \Delta t} P_{avg}, \tag{2.15}$$

where $f_r = 1/T_r$ is the repetition rate of the laser, Δt is the full width at half maximum (FWHM) duration of the pulse. This power depends on the shape of the pulses. The factor 0.88 is valid for pulses with a temporal shape close to a sech^2. For Gaussian shaped pulses, this factor is 0.94.

2.2 Kerr-lens mode-locking

Now that the mathematical description of the electric field of an OFC has been introduced, we take a deeper look into the mode-locking process allowing to create ultrashort pulses. We restrict ourselves to a specific type of mode-locking. Our study concerns passive mode-locking for which the locking between the modes is ensured by a saturable absorber. Saturable absorber are passive nonlinear optical components whose absorption decreases as the optical intensity increases. Thus, when an ultrashort pulse circulates inside the laser cavity, the intracavity losses are modulated synchronously with this pulse. Such modulation of losses synchronized with the pulses allows the optical modes to be locked [42]. Interestingly, some optical components can behave like saturable absorber, even though no real absorption occurs. This is the case in some nonlinear medium subject to the Kerr effect. In this section, we first present the Kerr effect and how it can behave as a saturable absorber. This physical process, known as Kerr-lens effect, is at the origin of mode-locking in the laser studied in the second part of this manuscript. Secondly, the equation describing the propagation of a pulse in the laser cavity is introduced. This equation is called the master equation and has been derived in [43].

2.2.1 Kerr-lens effect

Kerr effect: The optical Kerr effect is a third order nonlinear effect. It can be described by a change of the nonlinear refractive index of a medium depending on the laser pulse intensity. In a laser, this effect usually occurs in the active medium, the laser crystal, used for the amplification. Formally, it can be written

$$n(\mathbf{r}, t) = n_0 + n_2 I(\mathbf{r}, t), \tag{2.16}$$

where $I(\mathbf{r}, t)$ is the intensity as defined in equation (1.22). In most cases, $n_2 < 0$, therefore an increase in optical intensity induces an increase of refractive index proportional to the instantaneous intensity. Due to this change of refractive index, the field acquires a phase shift $\Delta\phi(t)$ after propagation in a medium of length L_a, given by

$$\Delta\phi(t) = \frac{\omega}{c} n_2 I(t) L_a, \tag{2.17}$$

where we made the assumption that the medium is small enough so that the intensity does not change when propagating through it. In solid-states lasers, such as the titanium:sapphire (Ti:Sa), this effect is used to achieve mode-locking. The Kerr effect can be used as artificial saturable absorber via the Kerr-lens effect.

Kerr-lens effect: As explained previously, mode-locking occurs when a periodic modulation of the laser losses is synchronized with the laser pulses. In frequency combs based on the Kerr effect, this amplitude modulation can be achieved via a lensing effect known as Kerr-lens mode-locking (KLM)[4]. As seen in equation (2.16), the Kerr effect locally (in time and space) changes the refractive index of the medium. Hence, the medium acts as a lens and leads to self-focusing in the laser cavity. To mitigate the losses, different strategies can be applied. Among others, a slit can be used to introduce losses for the un-focalized beam. This technique is called hard aperture KLM. The spatial overlap between the lasing mode and the pump spatial profile can also be used. This configuration is called soft-aperture KLM and corresponds to the laser investigated in this work. The combination of the self-focusing and the mitigation of the losses leads to intensity dependent losses. This process is called self-amplitude modulation and is similar to the effect of a saturable absorber.

It can be noted that the Kerr effect leads to other effects such as self-phase modulation (SPM) which, associated to group velocity dispersion (GVD), plays an important role in the mode-locking process as will be seen later.

2.2.2 Master equation for Kerr-lens mode-locking

In this section, we introduce the equation describing the evolution of a pulse inside the laser cavity, known as master equation. To keep it as concise as possible, we will proceed by reviewing the different effects modifying the pulse during its propagation in the laser cavity. All those effects will then be added up to write the master equation as introduced in [42, 43]. Such perturbation approach can be understood as follows: we start by rewriting the expression of the electric field

$$E(t) = E^{(+)}(t) + cc = A(t)e^{-i\omega_0 t} + cc, \tag{2.18}$$

where the constant $\mathcal{E}_0$, from equation (1.11), has been integrated in $A(t)$, the envelope. Only the longitudinal field is considered to simplify the expressions.
Each component from the cavity is described by a transfer operator $\mathcal{T}_j$ so that the

---

[4] Other process can be used such as additive pulse mode-locking (APM) or nonlinear polarization rotation (NPR)

envelope after one round trip of duration T_r can be written

$$A(t+T_r) = \left(\prod_j \mathcal{T}_j\right) A(t). \tag{2.19}$$

Assuming that the action of each element is an infinitesimal perturbation, we can write $\mathcal{T}_j \simeq 1 + \mathrm{d}\mathcal{T}_j$. Besides, if we assume that the evolution over one round trip is small, expression (2.19) can be developed, leading to

$$A(t+T_r) = A(t) + T_r \frac{\mathrm{d}A(t)}{\mathrm{d}t} \simeq \left(\prod_j (1+\mathrm{d}\mathcal{T}_j)\right) A(t) \quad \Rightarrow \quad T_r \frac{\mathrm{d}A(t)}{\mathrm{d}t} \simeq A(t) \sum_j \mathrm{d}\mathcal{T}_j. \tag{2.20}$$

With the above expression, the master equation can be determine from the infinitesimal operators $\mathrm{d}\mathcal{T}_j$ of each element of the laser cavity which we derive now.

2.2.2.1 Laser amplification

The first element that needs to be taken into account is the gain from the laser amplifier of length L_a. This amplifier can have many forms. In our study, the gain medium is a crystal of titanium:sapphire, optically pumped by a continuous laser at 532 nm. This gain, $G(\omega)$, depends on the frequency and can be modeled by [42]

$$G(\omega) = \frac{g}{1 - i\frac{\omega-\omega_0}{\delta\omega_a}}, \tag{2.21}$$

where $\delta\omega_a$ is the gain bandwidth, and g the maximum gain reached at the frequency ω_0. The effect of the gain is to amplify the field as it propagates in the amplifier so that the In and Out relation is

$$A\left(t + \frac{L_a}{c} n\right) = A(t) e^{G(\omega) L_a}, \tag{2.22}$$

with n the index of the optical medium. Consequently, after one trip across the amplifier, assuming a small gain, we can write

$$e^{G(\omega)L_a} \simeq 1 + g_0 \left(1 + i\frac{\omega-\omega_0}{\delta\omega_a} - \left(\frac{\omega-\omega_0}{\delta\omega_a}\right)^2\right), \tag{2.23}$$

were $g_0 = gL_a$. Thus, the infinitesimal operator, in the time domain[5], associated to the amplification is given by

$$\mathrm{d}\mathcal{T}_{amp} = g_0 \left(1 - \frac{1}{\delta\omega_a}\frac{\mathrm{d}}{\mathrm{d}t} + \frac{D_g}{g_0}\frac{\mathrm{d}^2}{\mathrm{d}t^2}\right), \tag{2.24}$$

where we defined $D_g = g_0/(\delta\omega_a)^2$.

---

[5] From the definition of the Fourier transform of the field (1.5) we have the relation $-i(\omega-\omega_0) = \mathrm{d}/\mathrm{d}t$

2.2.2.2 Intracavity dispersion

As already discussed in section 2.1.2.1, the dispersion introduced by the elements in the cavity can be taken into account by Taylor expansion of the round trip phase $\phi(\omega)$ according to

$$e^{i\phi(\omega)} \simeq e^{i\phi^{(0)}+i(\omega-\omega_0)\phi^{(1)}+\frac{i}{2}(\omega-\omega_0)^2\phi^{(2)}}. \tag{2.25}$$

The first term is a constant term, it can be taken equal to one assuming that ω_0 is a cavity resonance frequency. Consequently, the infinitesimal operator associated to dispersion is given by

$$\mathrm{d}\mathcal{T}_{disp} = -\phi^{(1)}\frac{\mathrm{d}}{\mathrm{d}t} - iD\frac{\mathrm{d}^2}{\mathrm{d}t^2}, \tag{2.26}$$

where $\phi^{(1)} = L/v_g$ is the group delay experienced by the pulse due to dispersion. $D = \phi^{(2)}/2 = \frac{1}{2}\frac{\partial}{\partial\omega}\left(\frac{L}{v_g}\right)$ is called group delay dispersion (GDD). Note that this quantity is related to group velocity dispersion (GVD) according to $GVD = \beta_2 = 2D/L$. The effect of this dispersion on the pulse will be investigated in details in the section 2.3.

2.2.2.3 Self-amplitude modulation

In the laser used in this work, the Kerr-lens effect is responsible for the mode-locking. As explained before, this effect can be assimilate to a fast[6] saturable absorber. Such modulation of the losses depending on the laser intensity is called self-amplitude modulation. The absorption due to the propagation inside the saturable absorber of length L_{abs} can be modeled by

$$e^{-l\left(1+\frac{I(t)}{I_{sat}}\right)^{-1}L_{abs}} \simeq 1 - l\left(1-\frac{I(t)}{I_{sat}}\right)L_{abs}, \tag{2.27}$$

where $I(t)$ is the intensity proportional to $|A(t)|^2$ and I_{sat} the saturation intensity. l corresponds to the losses when the intensity inside the medium is null. When the intensity increases, the losses drop to $l/2$ at the saturation intensity I_{sat}. The In and Out relation of the losses due to self-amplitude modulation is similar to the gain one. Hence, the transfer operator accounting for self-amplitude modulation can be written

$$\mathrm{d}\mathcal{T}_{SAM} = -l_0 + \gamma|A(t)|^2 \tag{2.28}$$

where $l_0 = lL_{abs}$ is a linear loss term, and γ is the self-amplitude modulation coefficient which depends on the laser geometry. Note that in addition to the linear losses induced by the saturable absorption, we also include all the other losses from the cavity, such as the one introduced by the output coupler, inside l_0.

---

[6] Fast means that the recovery time of the saturable absorber is smaller than the duration of the pulse.

2.2.2.4 Self-phase modulation

As seen in equation (2.17), the Kerr effect also induces a time varying nonlinear phase shift. This phase shift is known as self-phase modulation. The effect of this phase shift is given by

$$e^{i\Delta\phi(t)} \simeq 1 + i\Delta\phi(t). \tag{2.29}$$

Hence, the operator accounting for the Self-phase modulation effect can be written

$$\mathrm{d}\mathcal{T}_{SPM} = i\delta|A(t)|^2, \tag{2.30}$$

where δ is the Self-phase modulation coefficient which depends on the laser geometry.

2.2.2.5 Master equation

The master equation can finally be obtained by summing the contributions from the amplification, the dispersion, the self-amplitude modulation and the self-phase modulation in equation (2.20). If the laser operates in a stationary regime, we have $A(t+T_r) = A(t)$. Consequently, all the first derivatives of the field are null, leading to

$$\left[(D_g - iD)\frac{\mathrm{d}^2}{\mathrm{d}t^2} + (g_0 - l_0) + (\gamma + i\delta)|A(t)|^2\right] A(t) = 0, \tag{2.31}$$

where $D_g = g_0/(\delta\omega_a)^2$, with g_0 the linear gain and $\delta\omega_a$ the gain bandwidth. $D = \phi^{(2)}/2 = \frac{1}{2}\frac{\partial}{\partial\omega}\left(\frac{L}{v_g}\right)$ is the group delay dispersion. l_0 represents the linear losses. γ is the self-amplitude coefficient and δ the self-phase modulation coefficient.

This equation allows to describe the propagation of a pulse in the laser cavity for a Kerr-lens mode-locked laser. We will present a solution of this equation in the next section. From that solution, the effects of intra-cavity dispersion on the pulse propagating inside the cavity will be investigated.

2.2.3 Resolution of the master equation and intracavity dispersion

The effects of the dispersion have already been studied in section 2.1.2.1 for the two first order of the development of the round trip phase $\phi(\omega)$. We now concentrate our study on how the quadratic term, the group delay dispersion, D, affects the pulse while propagating in the cavity. To proceed, we introduce into equation (2.31) the ansatz

$$A(t) = a_0\left[\mathrm{sech}\left(\frac{t}{t_p}\right)\right]^{1+i\beta_0} = a_0\mathrm{sech}\left(\frac{t}{t_p}\right)e^{i\beta_0\ln(\mathrm{sech}(t/t_p))}, \tag{2.32}$$

where t_p is the duration of the pulse. This solution corresponds to a chirped hyperbolic secant of chirp parameter β_0. The term chirp becomes explicit by computing the frequency of the pulse $\omega(t) = \omega_0 - \Delta\omega(t)$, where $\Delta\omega(t)$ is the instantaneous frequency shift induced by the phase term $\phi(t) = \beta_0 \ln(\mathrm{sech}(t/t_p))$. It is given by

$$\Delta\omega(t) = \frac{\partial\phi(t)}{\partial t} = -\frac{\beta_0}{t_p}\tanh\left(\frac{t}{t_p}\right). \tag{2.33}$$

Thus, if $\beta_0 > 0$, the frequency increase along the pulse, it is up-chirped. On the contrary, if $\beta_0 < 0$ the pulse is down-chirped.
By injecting (2.32) into (2.31), the following relation can be found:

$$(D_g - iD)\,\frac{2 + 3i\beta_0 - \beta_0^2}{t_p^2} = (\gamma + i\delta)\, a_0^2. \tag{2.34}$$

For simplicity we introduced the normalized quantities $D_n = \frac{D}{D_g}$, $t_{pn} = \frac{a_0^2 t_p^2}{D_g}$. By multiplying equation (2.34) by t_p^2/D_g and identifying the real and imaginary part, we find

$$\begin{cases} 2 - \beta_0^2 + 3\beta_0 D_n = \gamma t_{pn} \\ -3\beta_0 + 2D_n - \beta_0^2 D_n = -\delta t_{pn} \end{cases} \tag{2.35}$$

Using the above expressions, we can find influence of the cavity GDD, $D = D_n \times D_g$, on the chirp parameter β_0 and the duration of the pulse t_p. The variation of those two parameters as a function of the GDD are reproduced in Figure 2.3. We calculated those quantities using self-phase modulation (δ) and self-amplitude modulation (γ) coefficients close to the experimental conditions of the second part of the manuscript. In both cases it can be seen that the chirp and the pulse duration strongly depend on the intracavity dispersion. Interestingly, it can be noted that both curves are asymmetric. The evolution of the chirp and pulse duration is steeper for positive GDD. Thus it is often advantageous to design cavity with negative residual GDD by using anomalous dispersion to limit the effect of the GDD. To give an example, we will calculate in Chapter 5 the value of the intracavity dispersion of the laser studied. The GDD is found to be $D = -280$ fs^2.

2.3 Dispersion of an optical pulse

To conclude this chapter, we study the evolution of an initially chirped pulse through a dispersive medium. Up to now, we only focused our investigations on the effects arising inside the laser cavity. In particular, we saw that the group velocity dispersion (GVD), due to the frequency dependent refractive index of some of the cavity elements, has a significant impact on the duration and the chirp of the pulse. Because those

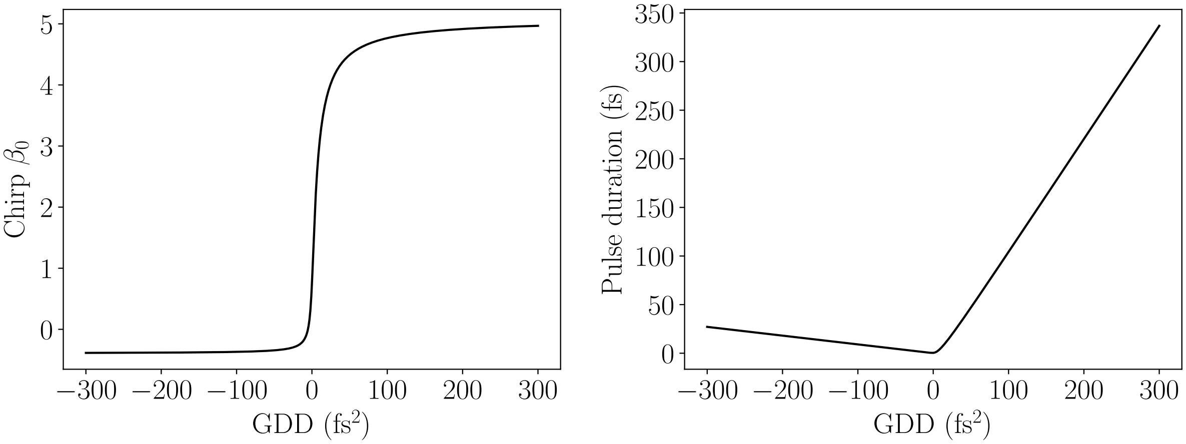

Figure 2.3 – **Chirp parameter and pulse duration as a function of the GDD.** The chirp parameter β_0 and the pulse duration are calculated from equations (2.35) as a function of the intracavity dispersion D in fs^2. The pulse duration is given as FWHM in intensity. We used $\delta = 3 \times 10^{-6}$ rad/W, for the self-phase modulation coefficient, $\gamma = 2 \times 10^{-6}$ W^{-1} for the self-amplitude modulation coefficient, $2a_0^2 t_p = 23$ nJ the pulse energy and $D_g = 2.4 \times 10^{-30}$ s^2 related to the gain bandwidth. Those values correspond to the laser investigated in the second part of the manuscript.

dispersive elements are distributed along the cavity, the duration and the chirp of the pulse continuously evolve during the round-trip. Cavities are usually designed such that the pulse is the shortest inside the active medium to increase the nonlinear effect. Consequently, the pulse exiting the laser cavity can be chirped. In experimental conditions, chirped pulses are often not desired. To remediate to that issue, dispersive elements can be used after the laser to remove the chirp.

2.3.1 Fourier transform pulses

In section 2.2.3, we saw that a pulse produced by a laser can present a chirp β_0. This chirp creates a frequency shift along the pulse, which in the case of an hyperbolic secant pulse, is given by equation (2.33). In this section, we will see that this chirp plays a role in the pulse duration and its spectral width.

For convenience the following calculations are performed assuming a Gaussian profile for the pulse. This shape is very close to the hyperbolic secant used in section 2.2.3, but the Gaussian profile facilitates the calculations [44]. Hence, the electric field of the chirped pulse at the output of the cavity is written

$$E^{(+)}(t) = A(t)e^{-i\omega_0 t} = a_0 \exp\left(-(1+i\beta_0)\frac{t^2}{2\Delta t_0^2}\right) \exp\left(-i\omega_0 t\right), \qquad (2.36)$$

which gives, in the frequency domain,

$$E^{(+)}(\omega) = \tilde{A}(\omega) = \tilde{a}_0 \exp\left(-\frac{\Delta t_0^2}{2(1+i\beta_0)}(\omega-\omega_0)^2\right). \tag{2.37}$$

Both fields are relate by the Fourier transform. Hence, the pulse duration[7], given by Δt_0 and its spectral width (also called bandwidth), given by $\Delta\omega = \sqrt{1+\beta_0^2}/\Delta t_0$ are related by the time-bandwidth product

$$\Delta t_0 \times \Delta\omega = \sqrt{1+\beta_0^2}. \tag{2.38}$$

This product is minimal when the pulse is not chirped, meaning that $\beta_0 = 0$. In this condition, the time-bandwidth product, $\Delta t_0 \times \Delta\omega = 1$, corresponds to the so-called Fourier transform limited pulse [45], which corresponds to a pulse of minimal duration given a fixed spectrum $\Delta\omega$.

2.3.2 Propagation through a dispersive medium

In the previous section we saw that a chirped pulse has a spectral width $\Delta\omega = \sqrt{1+\beta_0^2}/\Delta t_0$ and a duration Δt_0. In this section, we will see that this pulse duration is not the shortest given the spectral width $\Delta\omega$. Indeed, when a chirped pulse propagates in a dispersive medium, under certain conditions, the pulse initial chirp can be suppressed, leading to a pulse of minimal duration. This effect is known as pulse compression.

Dispersive elements have a non-zero GVD β_2. We saw in section 2.1.2.1 that the dispersion can be taken into account by developing the spectral phase according to

$$e^{i\phi(\omega)} \simeq e^{i\phi^{(0)}+i(\omega-\omega_0)\phi^{(1)}+\frac{i}{2}(\omega-\omega_0)^2\phi^{(2)}} = e^{i\phi(\omega_0)+i(\omega-\omega_0)\frac{z}{v_g}+\frac{i}{2}(\omega-\omega_0)^2\beta_2 z}, \tag{2.39}$$

where z is the length of the dispersive medium. We remind that the GVD is related to the GDD according to $\beta_2 = 2D/z$. The two first terms in the development can be ignored, as they only represent a constant phase and a delay. Hence, the evolution of $E^{(+)}(\omega)$ from equation (2.37), when propagating in a dispersive medium of length z and GVD β_2 is given by

$$\begin{aligned} E^{(+)}(z,\omega) &\propto E^{(+)}(\omega) \times \exp\left(\frac{i}{2}(\omega-\omega_0)^2\beta_2 z\right) \\ &\propto \tilde{a}_0 \exp\left(-\left(\frac{\Delta t_0^2}{2(1+i\beta_0)} - \frac{i}{2}\beta_2 z\right)(\omega-\omega_0)^2\right). \end{aligned} \tag{2.40}$$

---

[7] Here the duration is given as the σ of the Gaussian which for the field is related to the FWHM by $\Delta t_{FWHM} = 2\Delta t_0\sqrt{2\ln 2}$.

The field in the time domain is found by taking the inverse Fourier transform of the expression above. It can be shown that the field writes

$$E^{(+)}(z,t) \propto a_0 \exp\left(-\frac{\left(t-\frac{z}{v_g}\right)^2}{4}\left(\frac{\Delta t_0^2}{2(1+i\beta_0)}-\frac{i}{2}\beta_2 z\right)^{-1}\right). \tag{2.41}$$

Consequently, the evolution of the duration and chirp of a chirped pulse going through z mm of a dispersive medium of dispersion β_2 is given by

$$\Delta t(z) = \Delta t_0\sqrt{\left(1+\frac{\beta_2 z\beta_0}{\Delta t_0^2}\right)^2+\left(\frac{\beta_2 z}{\Delta t_0^2}\right)^2}, \tag{2.42}$$

$$\beta(z) = \beta_0+\frac{\beta_2 z\beta_0^2}{\Delta t_0^2}+\frac{\beta_2 z}{\Delta t_0^2}. \tag{2.43}$$

From equations (2.42) and (2.43) it can be seen that a pulse propagating through a dispersive medium will experience a change of duration and chirp parameter. Interestingly, if $\beta_0\beta_2 < 0$, a minimal value of pulse duration can be found for $z > 0$. The minimal duration of the pulse is reached for

$$z_{min} = -\frac{\beta_0}{1+\beta_0^2}\frac{\Delta t_0^2}{\beta_2}. \tag{2.44}$$

Using this expression in equation (2.42), we find a minimal pulse duration of

$$\Delta t_{min} = \frac{\Delta t}{\sqrt{1+\beta_0^2}}. \tag{2.45}$$

We see that for a given spectral width $\Delta\omega = \sqrt{1+\beta_0^2}/\Delta t_0$, the minimal temporal width is $\Delta t_{min} = \frac{\Delta t_0}{\sqrt{1+\beta_0^2}}$. Consequently, the time-bandwidth product is $\Delta t_{min} \times \Delta\omega = 1$ which corresponds to a Fourier transform limited pulse. Consequently, if the GVD β_2, has the opposite sign of the chirp of the pulse β_0, the pulse can be compressed to its Fourier transform limit by propagating through a dispersive medium of length z_{min}. For long z, the pulse duration as well as the chirp parameter increase. It can be noted that even if the pulse is initially not chirped, i.e $\beta_0 = 0$, it still acquires a chirp during its propagation.

2.3.3 Numerical application

To illustrate this section, we consider the experimental conditions corresponding to the laser studied in the second part of the manuscript. As mentioned in section 2.2.3, the

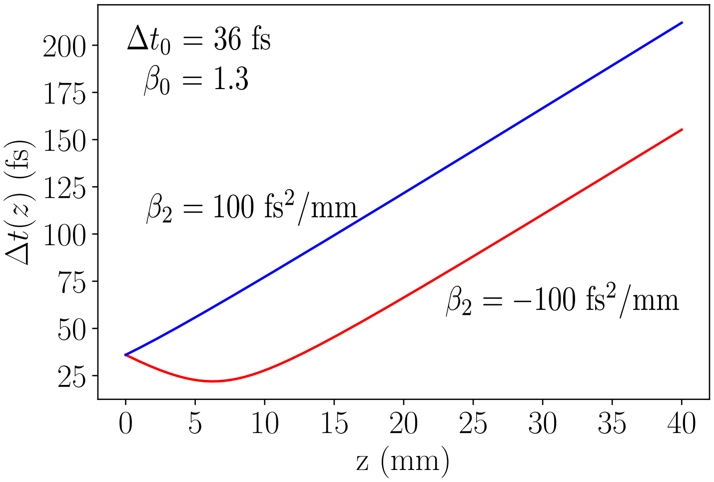

Figure 2.4 – **Evolution of the duration of a chirped pulse in a dispersive medium.** The duration of an initially chirped pulse of chirp parameter $\beta_0 = 1.3$ and initial duration $\Delta t_0 = 36$ fs is affected by the propagation in a dispersive medium. If the GVD in fs^2/mm is negative, the pulse can be compressed (red curve) to reach the Fourier transform limit of $\Delta t_{min} = 22$ fs.

laser cavity presents a residual GDD of -280 fs^2. Hence, the pulse leaving the laser cavity is chirped. The chirp parameter β_0 can be determined from the duration of the pulse measured at the output of the cavity and its Fourier transform limited duration given by its spectral width. Our laser has a spectrum of approximately 40 nm FWHM. Thus, the corresponding Fourier transform duration is $\Delta t_{min} = 22$ fs FWHM. Using an auto-correlation measurement [46], the duration of the pulse at the output of the cavity was found to be $\Delta t_0 = 36$ fs FWHM. Using equation (2.45) the chirp parameter is given by

$$|\beta_0| = \sqrt{\left(\frac{36}{22}\right) - 1} \simeq 1.3. \tag{2.46}$$

Note that the equation above does not give information on the sign of the chirp. To determine this sign, it is common to add positive chirp in the path of the laser beam, using a piece of glass for example. If the duration of the pulse increases, it implies that more dispersion has been introduced which means that the pulse was already positively chirped. On the contrary, if the pulse duration is reduced, dispersion has been removed, the pulse was negatively chirped.

The evolution of the pulse duration depending on the propagation length z through two media of different dispersions β_2 is represented in Figure 2.4. It can be seen that, if negative dispersion is introduced in the optical path of the laser, its duration can be compressed to reach the Fourier transform limited duration of $\Delta t_{min} = 22$ fs. In the experiment, negatively chirped mirror are placed after the laser to achieve this configuration.

Chapter 3

Measuring quadratures of light

Contents

3.1 Heterodyne detection 44
3.2 Self-heterodyne detection 45
3.2.1 Self-heterodyne beat signal 47
3.2.2 Transfer function 48
3.3 Homodyne detection 49
3.3.1 Temporal representation 49
3.3.2 Spectral representation 50
3.3.3 Variation of the homodyne detection 51
3.4 Sensitivity of the measurements 53
3.4.1 Fisher information of the detection schemes 53
3.4.2 Experimental sensitivity of the self-heterodyne 58
3.4.3 Phase sensitivity as a function of the analysis frequency . . . 64

In the previous chapters, we introduced the formal description of the electric field, and in particular the field of an optical frequency comb. Measuring this electric field is a crucial step in this thesis. The objective is to access the information encoded either in the amplitude or the phase of this electric field. Hence, detection schemes are needed to access those quantities. The detection of the amplitude of the electric field is an easy task as a simple photodiode is sufficient. However, as it is an intensity measurement, no phase information can be extracted from this detection. Consequently, more sophisticated methods must be employed to measure the phase of an electric field. It usually consists in interferometric measurements. As most of the time those measures give also access to a measure of the intensity, we concentrate our investigations on the measurement of the phase only. In this chapter, we present two of those detection techniques. The first one, the heterodyne detection, is based on the interference between two laser fields at two different frequencies. We will see that this technique can also be refined into a self-heterodyne detection scheme. Then, the homodyne detection is presented. This scheme is commonly used in quantum optics. It is based on the interference of two laser fields at the same frequency, usually coming from the same source. It allows to access directly to the amplitude and the phase of the electric field by measuring the field quadratures introduced in section 1.2.3. Finally, we compare both techniques in terms of sensitivity. The aim is to determine the smallest quantity measurable with each scheme.

3.1 Heterodyne detection

A heterodyne detection is an interferometric measurement where two beams interfere on a beam-splitter (BS). A scheme of such detection is represented in Figure 3.1. One of the field, called local oscillator (LO), is stronger than the other one, called signal. Those two fields have different frequencies. They can either come from different laser sources or from the same laser source but one field is shifted in frequency compared to the other. Each field is given by

$$\begin{aligned} E_{LO}^{(+)}(t) &= \mathcal{E}_0 a_{LO}(t) e^{-i\omega_{LO} t}, \\ E_s^{(+)}(t) &= \mathcal{E}_0 a_s(t) e^{-i\omega_s t}. \end{aligned} \tag{3.1}$$

After mixing on the BS, the fields $E_\pm^{(+)}$ at each output can be expressed as

$$E_\pm^{(+)}(t) = \frac{E_{LO}^{(+)}(t) \pm E_s^{(+)}(t)}{\sqrt{2}}. \tag{3.2}$$

In the above expression we assumed that the BS perfectly splits the intensity in two. The optical power at each output port, $P_\pm$, given according to[1] $P_j(t) = 2\epsilon_0 nc|E_j^{(+)}(t)|^2$ in (W), is

$$P_\pm(t) = \frac{P_{LO}(t)}{2} + \frac{P_s(t)}{2} \pm nc\epsilon_0\{E_{LO}^{(+)}(t)E_s^{(-)}(t) + E_{LO}^{(-)}(t)E_s^{(+)}(t)\} \tag{3.3}$$

This field is detected by a square-law detector, usually a photodiode. The physical quantity measured by a photodiode is the integral of the optical power during an integration time T. Those devices are characterized by their optical responsivity, $\mathcal{R}$, in (A/W). This quantity corresponds to the efficiency of the conversion of photons hitting the detector into electrons. Assuming that the beam size is smaller than the detector size and that both beams have the same spatial mode, the photo-current $\mathcal{I}_\pm(t)$ is given by

$$\mathcal{I}_\pm(t) = \mathcal{R} \int_t^{t+T} P_\pm(t')\ \mathrm{d}t', \tag{3.4}$$

---

[1] Here, the integral on the detector surface is not included in the definition as we are considering longitudinal electric fields only. We assume that all the light is measured by the detector so that this integral over the transverse field is equal to one.

Thus, the total photo-current, in Ampère, can be rewritten

$$\begin{aligned}\mathcal{I}_{\pm}(t) &= \frac{\mathcal{I}_{LO}(t)}{2} + \frac{\mathcal{I}_{s}(t)}{2} \pm \mathcal{R}nc\epsilon_0 \int_t^{t+T} \{E_{LO}^{(+)}(t')E_s^{(-)}(t') + E_{LO}^{(-)}(t')E_s^{(+)}(t')\}\,\mathrm{d}t', \\ &= \frac{\mathcal{I}_{LO}(t)}{2} + \frac{\mathcal{I}_{s}(t)}{2} \pm \mathcal{R}nc\epsilon_0\mathcal{E}_0^2 \int_t^{t+T} \{a_{LO}(t')a_s^{\star}(t')e^{-i(\omega_{LO}-\omega_s)t'} + cc\}\,\mathrm{d}t'. \qquad (3.5)\end{aligned}$$

The two first terms are proportional to the LO and signal optical power respectively. Those components can be considered as constant and represent the DC part of the signal. In principle this DC component can still fluctuates if the optical power fluctuates. However, those variations are slow compared to the integration time T. The last term is oscillating at the difference frequency $\omega_{beat} = \omega_{LO} - \omega_s$, between the LO and the signal. The amplitude of this signal is proportional to the product of the electric field of the two beams. Such signal is commonly known as a beat-note. The interest of this method is to bring the information, encoded e.g in the signal field, from the optical domain (at the frequency ω_s), to the radio-frequency (RF) one (at the frequency ω_{beat}). Off the shelf electronics can then be used to detect this signal. It can be isolated using electronic filtering and post-processing methods to recover information. A typical application of such detection scheme is coherent Doppler LIDAR [47, 48]. In this technique, a signal field is sent to a target, which can be a moving vehicle or air particles in movement due to the wind. Part of this signal will be reflected and detected via a heterodyne detection by mixing with a strong LO beam. Thanks to the LO, the signal reflected is amplified. Information such as the speed of the target is encoded in the Doppler shift of the reflected signal and can thus be read from the beat note.

3.2 Self-heterodyne detection

Even though heterodyne detection has found many applications, this detection is not the most convenient for the characterization of light sources. For example, to measure the frequency noise of a laser using a heterodyne detection, the standard method is to use another laser, usually stabilized. Its noise must be perfectly known and lower than the noise of the laser investigated [49, 50]. This is not always possible, especially for the design of ultra-stable sources. Alternatively, two identical lasers can be built and compared. The noise measured corresponds to twice the noise of a single laser. Nevertheless, this is only feasible to characterize the light source and cannot be used to measure the absolute phase of one of the lasers. To circumvent this limitation a different scheme can be used, known as self-heterodyne [51].

The idea of self-heterodyne, is to use a single light source as a self reference to measure its phase. To achieve this measure, the light is split in two paths and a long time

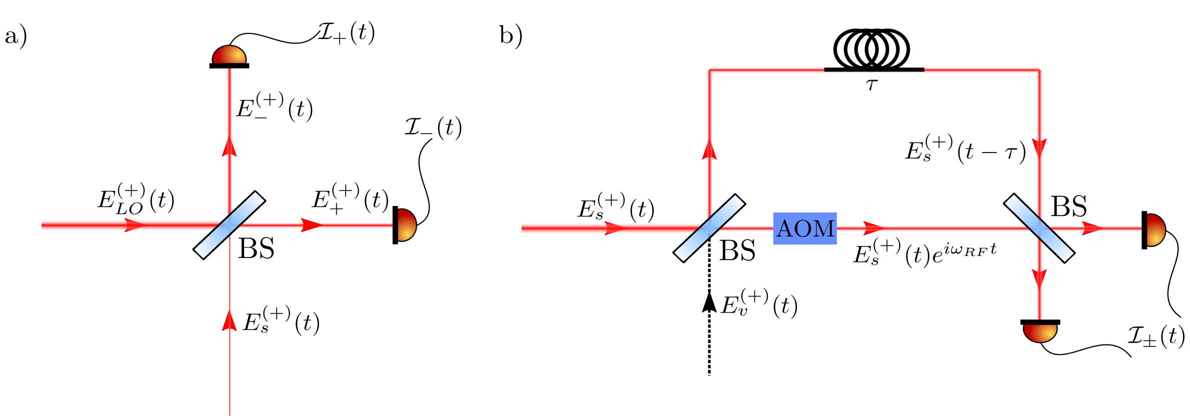

Figure 3.1 – **Experimental detection schemes:** a) Experimental scheme of a heterodyne or a homodyne detection. A strong field interfere on a 50-50 BS and is measured by photodetectors. For a heterodyne detection, both fields have different frequencies. For a homodyne detection, the fields have the same frequency. b) Experimental scheme of a self-heterodyne detection. After being split in two, one arm of the interferometer is delayed and the other one is shifted in frequency by an acousto-optic modulator (AOM). The beams are recombined on a 50-50 BS to form the UMZI.

delay is introduced on one of the arms using, for instance, a long optical fiber. At first glance, one would expect that the delay introduced must be long enough to decouple the phase fluctuations of both arms. It can be achieved with a delay longer than the coherence length of the laser. However, for low noise lasers, this length can be very important and thus kilometers of fibers would be needed. Fortunately, we will see in this section that the delay does not need to be longer than the coherence length of the laser. Modulo a transfer function, the phase fluctuations of the laser can be retrieved from the measurement of the relative phase fluctuations between both arms.
To perform the measure, the arm not delayed of the interferometer is shifted in frequency using an acousto-optic modulator (AOM). The purpose is, as in the heterodyne configuration, to bring the information in the RF domain to detect it with simple photodiodes. The interferometer is closed by a 50-50 BS which combines the two arms. A typical experimental setup is represented in Figure 3.1b. This interferometer is similar to a Mach-Zehnder interferometer. However, as one arm is delayed, it is commonly referred as unbalanced Mach-Zehnder interferometer (UMZI). In this section, we present how such experimental scheme allows to access the phase and hence the instantaneous frequency of a laser.

3.2.1 Self-heterodyne beat signal

We start by considering the electric field

$$E_s^{(+)}(t) = \mathcal{E}_0 a_s(t) e^{-i(\omega_s t + \varphi_s(t))}, \tag{3.6}$$

where ω_s, is the optical frequency and $\varphi_s(t)$ is the phase of the field. Due to the presence of phase noise, $\varphi_s(t)$ fluctuates in time (with zero mean value for simplicity). Those fluctuations can be related to frequency fluctuations, $\Delta\omega_s(t)$, using the relation

$$\Delta\omega_s(t) = \frac{\mathrm{d}\varphi_s(t)}{\mathrm{d}t}, \tag{3.7}$$

so that the instantaneous frequency is $\omega(t) = \omega_s + \Delta\omega_s(t)$.
After separation by a first 50-50 BS, the delay τ is introduced in one arm. A frequency shift ω_{RF} is applied on the other arm. Hence, the fields at the input ports of the recombining BS are given by

$$\begin{aligned} E_0^{(+)}(t) &= \frac{\mathcal{E}_0}{\sqrt{2}} a_s(t-\tau) \exp\left[-i\left(\omega_s(t-\tau) + \varphi(t-\tau)\right)\right], && \text{(3.8a)} \\ E_1^{(+)}(t) &= \frac{\mathcal{E}_0}{\sqrt{2}} a_s(t) \exp\left[-i\left((\omega_s - \omega_{RF})t + \varphi(t)\right)\right]. && \text{(3.8b)} \end{aligned}$$

The two beams are recombined at the output of the interferometer. The optical powers after the BS $P_\pm(t)$ are given by

$$P_\pm(t) = \frac{P_s(t-\tau)}{4} + \frac{P_s(t)}{4} \pm \frac{1}{2} n c \epsilon_0 \mathcal{E}_0^2 \left[a_s(t) a_s^\star(t-\tau) e^{i(\omega_s\tau - \omega_{RF}t + \varphi(t) - \varphi(t-\tau))} + cc\right] \tag{3.9}$$

Those optical powers are detected by photodiodes. The photo-current is similar to the one derived in equation (3.5) for the heterodyne detection. It reads

$$\begin{aligned} \mathcal{I}_\pm(t) &= \frac{\mathcal{I}_s(t-\tau)}{4} + \frac{\mathcal{I}_s(t)}{4} \pm \mathcal{R} n c \epsilon_0 \mathcal{E}_0^2 \int_t^{t+T} |a_s(t')|^2 \cos\left[\omega_s\tau - \omega_{RF}t' + \varphi(t') - \varphi(t'-\tau)\right] \mathrm{d}t' \\ &= \frac{\mathcal{I}_s(t)}{2} \pm \frac{\mathcal{I}_s(t)}{2} \int_t^{t+T} \cos\left[\omega_s\tau - \omega_{RF}t' + \Delta\varphi(t',\tau)\right] \mathrm{d}t', \end{aligned} \tag{3.10}$$

where we assumed that the amplitude of the field is constant during the delay time τ so that $a_s(t-\tau) = a_s(t)$. We also made the assumption that the amplitude varies slowly compared to the integration time T. In addition we introduced the notation

$$\Delta\varphi(t,\tau) = \varphi(t) - \varphi(t-\tau). \tag{3.11}$$

It can be seen that the self-heterodyne detection allows to access to information on the phase (and the amplitude) of the laser using a single laser, which can then be related to the field quadratures as seen in section 1.4.2.1. The treatment to extract this information will be presented in Chapter 6.
It should be noted that this scheme gives access to the phase difference $\Delta\varphi(t,\tau)$ and not directly to $\varphi(t)$. Thus, to go from one to the other, the transfer function of the interferometer must be applied.

3.2.2 Transfer function

The transfer function of the interferometer, h_{UMZI}, can be obtained by taking the Fourier transform of equation (3.11). It leads to

$$\Delta\varphi(f,\tau) = \left(1 - \mathrm{e}^{-2i\pi\tau f}\right)\varphi(f) = \frac{1}{h_{UMZI}(f)}\varphi(f), \tag{3.12}$$

with $h_{UMZI}(f) = 1/\left(1 - \mathrm{e}^{-2i\pi\tau f}\right)$ and where f is the measurement frequency. This transfer function depends on the the delay τ introduced in the interferometer. An example of this function is represented in Figure 3.2 for two different values of delay. It can be noted that the gain and the bandwidth of the detection critically depend on τ. Indeed, for short delays, i.e $\tau \ll 1/f$, the transfer function can be approximated by

$$h_{UMZI}(f) \simeq \frac{1}{2i\pi\tau f}. \tag{3.13}$$

Thus, the gain, corresponding to the absolute value of the inverse transfer function, is given by $1/|h_{UMZI}(f)| \simeq 2\pi\tau f$. Therefore, the longer the delay the higher the gain. This gain amplifies the phase noise and allows to rise its level above other technical noises such as the one associated to the photo-detection. On the other hand, the transfer function presents blind spots. Those blind spots, corresponding to the peaks in Figure 3.2, are frequencies for which the phase cannot be measured. The frequency of the first one, $f = 1/\tau$, gives the bandwidth of the detection. After this frequency, the phase cannot be accurately determined due to all the blind spots. Hence, the longer the delay the smaller the bandwidth. As a consequence, a trade-off between gain and bandwidth needs to be found for each measurement. To characterize a source displaying very low phase noise, a long delay needs to be used. On the other hand, to characterize the noise at very high frequencies (a few gigahertz typically) short delays should be preferred at the expanse of the gain.

Additionally, a transfer function to relate phase noise to frequency noise can be derived in a similar way. Indeed, the Fourier transform of equation (3.7) gives

$$\Delta\nu_s(f) = 2\pi\Delta\omega_s(f) = if\varphi(f). \tag{3.14}$$

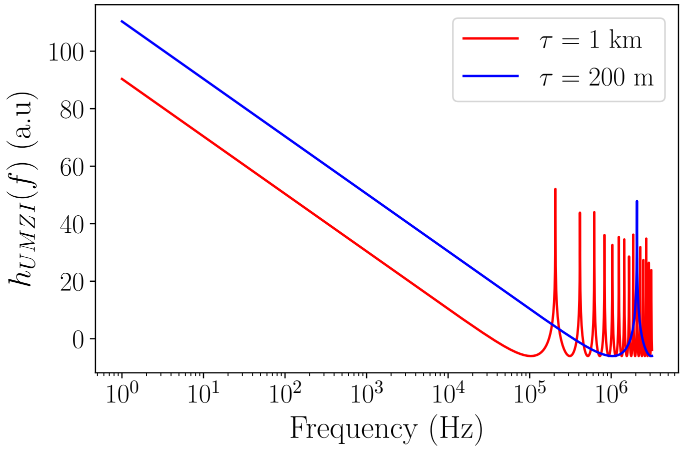

Figure 3.2 – **Transfer function as a function of the frequency.** Transfer function according to equation (3.12) for two different delays $\tau = 200$ m and $\tau = 1$ km. The smaller delay leads to a higher bandwidth but to a smaller gain for the phase given by the inverse of transfer function.

Thus, the transfer function of the UMZI defined by $H_{UMZI}(f) = \Delta\nu(f)/\Delta\varphi(f,\tau)$ reads

$$H_{UMZI}(f) = \frac{if}{1 - \mathrm{e}^{-2i\pi\tau f}}. \tag{3.15}$$

3.3 Homodyne detection

The previous method is widely spread for the characterization of lasers phase and frequency noise [52, 53]. In this work, we will also use a scheme were both beams in the interferometer come from the same source and have exactly the same frequency. This scheme is called homodyne detection [54]. It is widely used in quantum optics and allows to measure the quadratures $x(t)$ and $p(t)$ of the electric field. The main difference between self-heterodyne and homodyne detection is that the homodyne detection performs a lossless measurement which is not the case of the self-heterodyne detection. As will be seen later in this chapter, the first beam-splitter of the UMZI introduces losses which reduces the sensitivity of the measurement.

3.3.1 Temporal representation

We begin, similarly to the heterodyne case, with a strong field, the LO, combined on a 50-50 BS with a weaker one, the signal. In the homodyne detection, both fields have the same frequency ω_0. Thus the photo-currents detected at both outputs of the BS read

$$\mathcal{I}_{\pm}(t) = \frac{\mathcal{I}_{LO}(t)}{2} + \frac{\mathcal{I}_s(t)}{2} \pm \mathcal{R}nc\epsilon_0\mathcal{E}_0^2 \int_t^{t+T} \{a_{LO}(t')a_s^\star(t') + a_{LO}^\star(t')a_s(t')\}\,\mathrm{d}t'. \tag{3.16}$$

Taking the difference of the photo-currents leads to the standard homodyne signal

$$i_-(t) = \mathcal{I}_+(t) - \mathcal{I}_-(t) \propto \int_t^{t+T} \{a_{LO}(t')a_s^\star(t') + a_{LO}^\star(t')a_s(t')\}\, \mathrm{d}t'. \tag{3.17}$$

3.3.2 Spectral representation

In this work we will essentially work in the spectral domain rather than in the temporal domain. We are mainly interested in resolving the spectrum of the OFC and not resolving temporally the pulses. Hence, we derive a spectral representation of the homodyne. Starting from equation (3.16), with the definition of the FT given by equation (1.3), the intensity at each output can be written

$$\mathcal{I}_\pm = \frac{\mathcal{I}_{LO}}{2} + \frac{\mathcal{I}_s}{2} \pm \frac{\mathcal{R}nc\epsilon_0\mathcal{E}_0^2}{2\pi} \int_t^{t+T} \mathrm{d}t' \int_{\mathbb{R}}\int_{\mathbb{R}} \{\tilde{a}_{LO}(\Omega')\tilde{a}_s^\star(\Omega)e^{i(\Omega-\Omega')t'} + cc\,\}\, \mathrm{d}\Omega\mathrm{d}\Omega', \tag{3.18}$$

were $\Omega = \omega - \omega_0$ (and $\Omega' = \omega' - \omega_0$). The temporal integration is made over a time T, corresponding to the bandwidth of the detector, $BW = 1/T$. In this thesis we will mainly deal with detectors whose bandwidth is low and thus with long integration time. In particular, this integration time is a lot longer than the duration of the pulses. Thus we can make the approximation that the boundaries of the time integration tend to infinity. This assumption allows to approximate the temporal integral of the exponential $e^{i(\Omega-\Omega')t'}$, by a Dirac function $\delta(\Omega-\Omega')$. Hence, equation (3.18) can be rewritten

$$\mathcal{I}_\pm = \frac{\mathcal{I}_{LO}}{2} + \frac{\mathcal{I}_s}{2} \pm \mathcal{R}nc\epsilon_0\mathcal{E}_0^2 \int_{\mathbb{R}} \{\tilde{a}_{LO}(\Omega)\tilde{a}_s^\star(\Omega) + \tilde{a}_{LO}^\star(\Omega)\tilde{a}_s(\Omega)\}\, \mathrm{d}\Omega. \tag{3.19}$$

To further simplify this expression, we write each field as a single spectral mode according to

$$\tilde{a}_{LO}(\Omega) = a_{LO}\tilde{u}_{LO}(\Omega) = \alpha_{LO}e^{i\varphi_{LO}}\tilde{u}_{LO}(\Omega), \tag{3.20a}$$
$$\tilde{a}_s(\Omega) = a_s\tilde{u}_s(\Omega), \tag{3.20b}$$

where $\alpha_{LO} = |a_{LO}| = \sqrt{N_{LO}}$, with N_{LO} the mean photon number of the LO, by analogy with the quantum treatment. a_s is the complex amplitude of the signal field. $\tilde{u}_j(\Omega)$ is the spectral mode of the LO (or signal) and corresponds to its optical spectrum. With those definitions, equation (3.19) reads

$$\mathcal{I}_\pm = \frac{\mathcal{I}_{LO}}{2} + \frac{\mathcal{I}_s}{2} \pm \mathcal{R}nc\epsilon_0\mathcal{E}_0^2 \left[\alpha_{LO}a_s^\star e^{i\varphi_{LO}}\mathcal{O}_{LO,s} + cc\,\right], \tag{3.21}$$

where we introduced the spectral overlap between the LO and the signal: $\mathcal{O}_{LO,s} = \int_{\mathbb{R}}\{\tilde{u}_{LO}(\Omega)\tilde{u}_s^\star(\Omega)\}\, \mathrm{d}\Omega$. Due to this overlap, the homodyne detection is a projective measurement as will be seen in section 3.4.1.1. This quantity is maximal when both spectrum perfectly overlap so that $\mathcal{O}_{LO,s} = 1$ which we assume to be the case in this derivation.

Similarly to equation (3.17), taking the difference of the photo-currents (3.21) leads to the standard homodyne signal

$$i_- \propto \alpha_{LO}\left(a_s^\star e^{i\varphi_{LO}} + a_s e^{-i\varphi_{LO}}\right), \tag{3.22}$$

$$i_- \propto \sqrt{N_{LO}}\, x_s^{\varphi_{LO}} \tag{3.23}$$

where we defined

$$x_s^{\varphi_{LO}} = a_s^\star e^{i\varphi_{LO}} + a_s e^{-i\varphi_{LO}} = x_s \cos\varphi_{LO} + p_s \sin\varphi_{LO}, \tag{3.24}$$

with x_s and p_s the quadratures of the signal field defined according to equations (1.20). Hence, the homodyne detection allows to measure the quadrature of a signal beam in phase with the LO. Changing the phase of the LO allows to go from one quadrature to the other.

3.3.3 Variation of the homodyne detection

The self-heterodyne detection gives access to a measurement of the amplitude and the phase of the field simultaneously. The procedure to retrieve those quantities will be described in chapter 6. On the other hand, the homodyne detection gives access to only one quadrature at the time, depending on the LO phase. Consequently the phase and the amplitude of the field are not measured simultaneously. As one of the aims of this study is to investigate the amplitude and phase correlations from the laser fluctuations, a slightly different approach is used. Our aim here is to demonstrate that, using a different configuration of the homodyne detection, it is possible to measure the phase fluctuations of the fields as well as the amplitude fluctuations of the LO simultaneously. This configuration corresponds to the one used in the second part of this manuscript.

The first step is to assume, similarly to section 1.4.2.1, that the signal and LO fields, from equation (3.22), undergo amplitude and phase fluctuations according to

$$a_j(t_n) = \alpha_j(1 + \delta\epsilon_j(t_n))e^{i(\varphi_j + \delta\varphi_j(t_n))}. \tag{3.25}$$

To differentiate the different time scales, we introduced the notation t_n for the laser parameters fluctuations, while the notation t stands for the fluctuations at the scale of the laser pulse, thus much faster. We define the fluctuations of the fields as $\delta a_j(t_n) = a_j(t_n) - \langle a_j(t_n)\rangle_{t_n}$, where $\langle\rangle_{t_n}$ stands for the time average. Assuming that the phase and amplitude fluctuations are small, we have

$$\delta a_j(t_n) = \alpha_j e^{i\varphi_j}(\delta\epsilon(t_n) + i\delta\varphi_j(t_n)). \tag{3.26}$$

The phase fluctuations can be retrieved from the differential photo-current (3.22)[2], that is $i_-(t_n) = a_{LO}(t_n)a_s^\star(t_n) + a_s(t_n)a_{LO}^\star(t_n)$. Because the signal and LO are fluctuating, the photo-current is also affected by fluctuations. We define the fluctuations of the differential photo-current as $\delta i_-(t_n) = i_-(t_n) - \langle i_-(t_n)\rangle_{t_n}$. Using the expressions of the signal and the LO, given by equation (3.25), the fluctuations of the differential photo-current can be written

$$\begin{aligned}\delta i_-(t_n) &= \langle a_{LO}(t_n)\rangle_{t_n}\delta a_s^\star(t_n) + \langle a_s(t_n)\rangle_{t_n}\delta a_{LO}^\star(t_n) + cc \\ &= \alpha_{LO}e^{i\varphi_{LO}}\alpha_s e^{-i\varphi_s}(\delta\epsilon_s(t_n) - i\delta\varphi_s(t_n)) + \alpha_{LO}e^{-i\varphi_{LO}}\alpha_s e^{i\varphi_s}(\delta\epsilon_{LO}(t_n) - i\delta\varphi_{LO}(t_n)) + cc \\ &= 2\alpha_{LO}\alpha_s(\delta\epsilon_{LO}(t_n) + \delta\epsilon_s(t_n))\cos(\varphi_{LO} - \varphi_s) + 2\alpha_{LO}\alpha_s(\delta\varphi_{LO}(t_n) - \delta\varphi_s(t_n))\sin(\varphi_{LO} - \varphi_s).\end{aligned} \tag{3.27}$$

It can be seen that, if the relative phase between the LO and the signal, $\varphi_{LO} - \varphi_s$ is set to $\pm\frac{\pi}{2}$, the differential photo-current leads to a measurement of the difference of the phase fluctuations

$$\delta i_-(t_n) = 2\alpha_{LO}\alpha_s(\delta\varphi_{LO}(t_n) - \delta\varphi_s(t_n)) \tag{3.28}$$

On the other hand, in order to access to information on the amplitude of the field, the sum of the photo-currents (3.21), $i_+ = \mathcal{I}_+ + \mathcal{I}_-$, is calculated. This signal reads

$$\begin{aligned}i_+(t_n) &= \mathcal{I}_{LO}(t_n) + \mathcal{I}_s(t_n) \\ &\propto |a_{LO}(t_n)|^2 + |a_s(t_n)|^2.\end{aligned} \tag{3.29}$$

As the LO is stronger than the signal, i.e $|\alpha_s|^2 \ll |\alpha_{LO}|^2$, this photo-current mainly measures the LO intensity so that[3]

$$i_+(t_n) = |a_{LO}(t_n)|^2. \tag{3.30}$$

Computing the fluctuations of this photo-current leads to

$$\begin{aligned}\delta i_+(t_n) &\simeq 2\alpha_{LO}^2\delta\epsilon_{LO}(t_n), && \text{(3.31a)}\\ &\simeq \alpha_{LO}\delta x_{LO}(t_n), && \text{(3.31b)}\end{aligned}$$

where we used the result derived in section 1.4.2.1, the amplitude fluctuations are proportional to the x quadrature fluctuations.

---

[2] Note that i_- is renormalized to get rid of the proportional sign

[3] with renormalization to get rid of the proportional sign.

In this section we demonstrated that, using a modified homodyne detection, it is possible to measure simultaneously phase and amplitude fluctuations. This is achieved by measuring both $\mathcal{I}_+$ and $\mathcal{I}_-$ at the same time and taking their sum and difference. It is important to note that the amplitude fluctuations, measured via equations (3.31), correspond to the fluctuations of the LO. However, the phase fluctuations, given by equation (3.28), correspond to a relative measure between the fluctuations of the LO and the signal phases. This nuance and its consequences will be discussed in more details in section 4.3.2 in the next chapter.

3.4 Sensitivity of the measurements

In this chapter, we presented two experimental schemes to measure the phase of an electric field. As we will use both schemes in this thesis, it is interesting to compare the self-heterodyne and the homodyne detections in terms of sensitivity. The idea is to determine the smallest phase variation that can be measured with each setup. Note that, up to now, all the calculations have been made in the classical framework. However, all the equations are compatible with the quantum description by replacing, as before, all the quantities by operators. Hence, we use a semi-classical description in order to compare the sensitivity to the limit fixed by the quantum properties of the light, derived in section 1.4.2.1.

As previously mentioned, the main difference between the two detection schemes comes from losses. As a matter of fact, the homodyne detection allows a lossless measure of the quadratures of the field. Consequently, using the same approach as the one developed in section 1.4.2.3, we will see that, because the homodyne measurement is a projective measurement, it allows to reach the standard quantum limit. On the other hand, the heterodyne detection introduces losses due to the first beam-splitter of the interferometer. This first beam-splitter allows vacuum to enter the system, adding noise onto the measurement. In the semi-classical framework, the intensity measurement performed at the output of the interferometer, assuming that the signal is a coherent state, follows a Poissonian statistic. Using this probability distribution, the Fischer information (FI), as defined in equation (1.67), can be calculated and the bound on the sensitivity determined. Then, we will look at the experimental sensitivity of the self-heterodyne scheme. Indeed, we will see that, because the optimal estimator is not accessible, an experimental sensitivity needs to be derived.

3.4.1 Fisher information of the detection schemes

3.4.1.1 Homodyne sensitivity

To begin with, we assume that a phase shifted $\delta\varphi_s$ is encoded in the signal field, such that $E_s^{(+)}(t) = \mathcal{E}_0 a_s(t) e^{-i\omega_s t} e^{-i\delta\varphi_s}$, with $a_s(t) = \alpha_s u_s(t)$, where $u_s(t)$ is the envelope mode of the field[4]. This phase shift can be coming from a dephasing element on the signal path. It can also be the classical phase noise of the laser. Both configurations are similar, the point is to measure phase variations from an initial state. To compute the sensitivity, we make the assumption that the signal field is a coherent state. Thus, we are trying to determine what is the smallest measurable phase shift encoded in a coherent state, in the presence of the intrinsic noise of the coherent state[5]. If this phase shift is small, the field $E_s^{(+)}(t)$ can be developed at first order:

$$E_s^{(+)}(t) \simeq \mathcal{E}_0 e^{-i\omega_s t}\left(a_s(t) - i a_s(t)\delta\varphi_s\right) = \mathcal{E}_0 \alpha_s e^{-i\omega_s t}\left(u_s(t) - \delta\varphi_s\ w(t)\right), \tag{3.32}$$

where we introduced the normalized mode $w(t) = i u_s(t)$. Using equation (3.17), taking (3.32) for the signal field, the differential photocurrent reads[6]

$$i_- \propto 2\alpha_{LO}\alpha_s \ \mathrm{Re}\left[\int_{\mathbb{R}} \mathrm{d}t\ u_{LO}(t)(u_s(t) - \delta\varphi_s\ w(t))^\star\right], \tag{3.33}$$

where the LO is written as a single temporal mode $E_{LO}^{(+)}(t) = \mathcal{E}_0\alpha_{LO}u_{LO}(t)e^{-i\omega_s t}$. It is clear that if the LO is set in the mode $w(t)$, the signal can be reduced to

$$i_- \propto 2\alpha_{LO}\alpha_s\delta\varphi_s = 2\sqrt{N_{LO}N_s}\ \delta\varphi_s. \tag{3.34}$$

It can be seen that, because homodyne detection is a projective measurement, it allows to retrieve information encoded in the mode defined by the temporal (or spectral) mode of the LO. A technique to control this mode will be presented in section 4.2.2.

To determine the sensitivity of the measurement, similarly to section 1.4.2.1, we need to compute the signal to noise ratio (SNR) of the measurement. To do so, the variance of the homodyne signal must be calculated. We saw in equation (3.24) that the homodyne signal, when no phase shift is applied on the signal field, is proportional to the signal quadrature in the direction of the LO $x_s^{\varphi_{LO}}(t)$ multiplied by the square-root of the the number of photons in the LO field α_{LO}. We stated that the signal field without any phase shift is a coherent state. Knowing that the variance of the quadratures of such states is given by $\mathrm{Var}\left[x_s^{\varphi_{LO}}\right] = 1$ as seen in section 1.3.2, the detection noise is given by

$$\mathrm{Var}\left[i_-\right] = N_{LO}. \tag{3.35}$$

---

[4] We also took $\varphi_s = 0$ for simplicity

[5] Note that we are using here the semi-classical approach where we introduce by hand the noise coming from the vacuum fluctuations.

[6] Here also we made the approximation that the integration time is slow compared to the time scale of the pulses shape, so that the boundaries of the integral are extended to infinity.

The sensitivity, that is the smallest phase variation measurable with a homodyne detection $\varphi_{min,hom}$, is achieved for a SNR equals to one:

$$\text{SNR} = \frac{\langle i_- \rangle}{\sqrt{\text{Var}\left[i_-\right]}} = \frac{2\sqrt{N_{LO}N_s}\;\varphi_{min,hom}}{\sqrt{N_{LO}}} = 1 \quad \Rightarrow \quad \varphi_{min,hom} = \frac{1}{2\sqrt{N_s}}. \tag{3.36}$$

As expected, this calculation gives the same sensitivity as the one derived in section 1.4.2.3 which corresponds to the standard quantum limit (SQL). It can be concluded that the homodyne detection is an optimal measurement. Note that we derived all the expressions in the particular case where the parameter under investigation is a phase. This treatment can be generalized to any parameter.

3.4.1.2 Self-heterodyne sensitivity

In the self heterodyne scheme, bucket detectors are used to measure the intensity of the fields at the outputs of the BS. In addition, the interferometer measures the phase difference $\Delta\varphi(t,\tau)$ given by

$$\Delta\varphi(t,\tau) = \varphi(t) - \varphi(t-\tau), \tag{3.37}$$

and not directly the phase $\varphi(t)$. Hence, we need first to determine the sensitivity on the measurement of $\Delta\varphi(t,\tau)$ before determining the one on $\varphi(t)$ via the transfer function defined in equation (3.12). To that end, as explained in section 1.4.2.2, the Fisher information associated to the experimental conditions needs to be calculated.

To calculate the Fisher information associated to the self-heterodyne detection, the probability distribution associated to the measurement needs to be determined. In the semi-classical framework, the intensity measurement of the outputs of the BS, $\hat{i}_{1,2}(t)$, can be modeled by a Poissonian distribution. As the two outputs are uncorrelated, the probability to measure n_1 photons from one measurement at output 1 and n_2 at output 2 is given by

$$\begin{aligned} P(n_1,n_1) &= P_1(n_1)P_2(n_2) \\ &= \left(\frac{\langle i_1(t)\rangle^{n_1}}{n_1!}e^{-\langle i_1(t)\rangle^{n_1}}\right)\left(\frac{\langle i_2(t)\rangle^{n_2}}{n!}e^{-\langle i_2(t)\rangle^{n_2}}\right). \end{aligned} \tag{3.38}$$

Thus, to explicit this probability law, we need to determine the average photocurrent, $\langle\hat{i}_{1,2}(t)\rangle$, for each output.

Photo-currents: For a complete treatment, the vacuum entering the system must be considered. Indeed, as shown in Figure 3.1, one of the input of the first BS is fed with the signal state $\hat{E}_s^{(+)}(t)$, while the other one is fed with vacuum $\hat{E}_v^{(+)}(t)$. However, the vacuum terms do not play any role in the mean values. Hence, the calculation can be done using classical fields. The noise coming from the vacuum is added by hand by considering that the probability distribution associated to the intensity measurement is a Poissonian distribution, as stated in equation (3.38). Nonetheless, we chose to introduce the expressions using both the signal and the vacuum fields before calculating the mean values. The final result in the semi-classical approach could be retrieved by using equations (3.39) to determine the variance of the signal assuming a Gaussian distribution for the noise on the measurement.

The signal and vacuum fields are given by

$$\hat{E}_s^{(+)}(t) = \mathcal{E}_0 e^{-i(\omega_s t+\varphi_s(t))}\hat{a}_s(t) \tag{3.39a}$$
$$\hat{E}_v^{(+)}(t) = \mathcal{E}_0 e^{-i\omega_s t}\hat{a}_v(t). \tag{3.39b}$$

The input state of the interferometer can be written as $|\psi\rangle = (D(\alpha)|0\rangle_s)\otimes|0\rangle_v$ with $D(\alpha) = e^{\alpha\hat{a}^\dagger(t_0)-\alpha^\star\hat{a}(t_0)}$. After the first BS, the fields in both arms read

$$\hat{E}_{1,2}(t) = \frac{1}{\sqrt{2}}\left[\hat{E}_s(t) \pm \hat{E}_v(t)\right]. \tag{3.40}$$

Similarly to the treatment of section 3.2.1, the upper arm experiences a delay τ before being recombined with the lower arm at the second BS, forming two outputs whose electrical fields are given by

$$\hat{E}_{out1,2}(t) = \frac{1}{\sqrt{2}}\left[\hat{E}_1(t-\tau_d) \pm \hat{E}_2(t)\right]. \tag{3.41}$$

Note that, as a first step, the frequency shift ω_{RF} is not included in the description as in equation (3.10). It allows to keep the expressions as simple as possible. The effect of this frequency shift will be discussed later.
From equation (3.41), the field at the output 1 of the BS is given by

$$\begin{aligned}\hat{E}_{out1}(t) &= \frac{1}{2}\left[\hat{a}_s(t-\tau)e^{-i(\omega_s(t-\tau)+\varphi_s(t-\tau))} + \hat{a}_s(t)e^{-i(\omega_s t+\varphi_s(t))}\right.\\ &+ \left.\hat{a}_v(t-\tau)e^{-i\omega_s(t-\tau)} - \hat{a}_v(t)e^{-i\omega_s t}\right]. \end{aligned} \tag{3.42}$$

The photo-current is proportional to $\hat{i}_j = \hat{E}^\dagger_{outj}\hat{E}_{outj}$. The average photo-current can be thus written as

$$\begin{aligned}\langle\hat{i}_1(t)\rangle &= \langle\hat{E}^{\dagger}_{out1}(t)\hat{E}_{out1}(t)\rangle\\ &= \frac{1}{4}\left[\langle\hat{a}^{\dagger}_s(t-\tau)\hat{a}_s(t-\tau)\rangle + \langle\hat{a}^{\dagger}_s(t)\hat{a}_s(t)\rangle\right.\\ &\quad +\langle\hat{a}^{\dagger}_s(t-\tau)\hat{a}_s(t)\rangle e^{i(\omega_s\tau+\Delta\varphi_s(t,\tau))}\\ &\quad \left.+\langle\hat{a}^{\dagger}_s(t)\hat{a}_s(t-\tau)\rangle e^{-i(\omega_s\tau+\Delta\varphi_s(t,\tau))}\right]. \end{aligned} \tag{3.43}$$

It can be seen that the vacuum does not contribute to the photo-current mean value. However, its contribution needs to be taken into account if one wants to calculate the variance of this photo-current.
Given that $\langle\psi|\hat{a}_s(t)|\psi\rangle = \langle\psi|\hat{a}_s(t-\tau)|\psi\rangle = \alpha_s$ with $|\alpha_s|^2 = N_s$ the photon number, the average photo-current is given by

$$\langle\hat{i}_1(t)\rangle = \frac{N_s}{2}\left[1+\cos\left(\omega_s\tau+\Delta\varphi_s(t,\tau)\right)\right]. \tag{3.44}$$

A similar calculation using $\hat{E}_{out2}$ gives the average photo-current at the second output of the interferometer:

$$\langle\hat{i}_2(t)\rangle = \frac{N_s}{2}\left[1-\cos\left(\omega_s\tau+\Delta\varphi_s(t,\tau)\right)\right]. \tag{3.45}$$

Sensitivity: The maximum information that can be extracted by measuring the intensity at the output 1 is calculated by injecting equation (3.44) in $P_1(n_1)$ from equation (3.38) and using it in the Fisher information formula given by equation (1.67). Thus, the Fisher information FI_1 is given by

$$\mathrm{FI}_1 = \frac{N_s}{2}\left[1-\cos\left(\omega_s\tau+\Delta\varphi_s(t,\tau)\right)\right]. \tag{3.46}$$

A similar calculation gives the Fisher information for the measurement of the photo-current at the output 2:

$$\mathrm{FI}_2 = \frac{N_s}{2}\left[1+\cos\left(\omega_s\tau+\Delta\varphi_s(t,\tau)\right)\right]. \tag{3.47}$$

As both measurements are independent, the total information can be written as

$$\mathrm{FI}_{tot} = \mathrm{FI}_1 + \mathrm{FI}_2 = N_s. \tag{3.48}$$

Therefore, the minimal phase difference that can be measured using the information from both outputs of the UMZI is

$$\Delta\varphi_{min,het} = \frac{1}{\sqrt{N_s}}. \tag{3.49}$$

It should be noted that, if only one output is measured as it is often the case, the Fisher information depends on the delay τ.
This sensitivity represents the smallest phase difference $\Delta\varphi(t,\tau)$ that can be measured experimentally. It can be seen that, due to the vacuum noise introduced via the first beam-splitter, this phase sensitivity is twice the one of the homodyne detection given by equation (3.36). Nevertheless, as explained previously, it does not correspond yet to the sensitivity on the measurement of the phase $\varphi(t,\tau)$. It will be obtained by applying the transfer function (3.12) in section 3.4.2.2 and compared to the bound found in section 3.4.1.1.

3.4.2 Experimental sensitivity of the self-heterodyne

3.4.2.1 Optimal estimator

Equation (3.49) corresponds to the maximal information that can be extracted from the intensity measurement at the output of the UMZI. However, maximal information on the phase difference $\Delta\varphi(t,\tau)$, from equation (3.37), can only be extracted from an optimal estimator. We remind that the estimator is a physical quantity, in our case it can be a photo-current, from which a value of the parameter can be estimated. Not all estimator are optimal. It is thus interesting to determine the optimal estimator and to see whether it is experimentally reachable. To find the optimal estimator, the method of moments can be used [55].

Let $i_{est}(t)$ be our estimator for the phase difference $\Delta\varphi(t,\tau)$. Its variance is given by $\mathrm{Var}\left[i_{est}\right] = \langle i_{est}(t)^2\rangle - \langle i_{est}(t)\rangle^2$. The sensitivity achieved via this estimator is defined as

$$\Delta\varphi_{est}^2 = \frac{\mathrm{Var}\left[i_{est}(t)\right]}{|\frac{\partial}{\partial\Delta\varphi}\langle i_{est}(t)\rangle|^2} \tag{3.50}$$

This estimator can be based on several observables. In the present case we have two: the intensities measured at both outputs of the interferometer $i_1(t)$ and $i_2(t)$. Thus we write $i_{est}(t)$ as a linear combination of those observables

$$i_{est}(t) = \overrightarrow{m} \cdot \begin{pmatrix} i_1(t) \\ i_2(t) \end{pmatrix}, \tag{3.51}$$

where $\overrightarrow{m}$ is the vector containing the weights for each observable. The optimal estimator can be found by solving

$$\begin{aligned}\Delta\varphi^2_{opt} &= \min_{\overrightarrow{m}}\left[\frac{\mathrm{Var}\left[i_{est}(t)\right]}{|\frac{\partial}{\partial\Delta\varphi}\langle i_{est}(t)\rangle|^2}\right] \\ &= \min_{\overrightarrow{m}}\left[\frac{\overrightarrow{m}^T\cdot\Gamma\cdot\overrightarrow{m}}{\left(\overrightarrow{m}^T\cdot\overrightarrow{D}\right)^2}\right],\end{aligned} \tag{3.52}$$

where Γ is the covariance matrix defined by

$$\Gamma_{ij} = \langle i_i(t)i_j(t)\rangle - \langle i_i(t)\rangle\langle i_j(t)\rangle, \tag{3.53}$$

and $\overrightarrow{D}$ is the vector of the derivative of the average values

$$D_i = \frac{\partial}{\partial\Delta\varphi}\langle i_i(t)\rangle. \tag{3.54}$$

It can be shown [55] that the weights to achieve the minimal phase sensitivity are given by

$$\overrightarrow{m}_{min} = c\,\Gamma^{-1}\cdot\overrightarrow{D}, \tag{3.55}$$

where c is a constant. Inserting this expression in equation (3.52) leads to the expression of the sensitivity as a function of the covariance matrix Γ and the vector $\overrightarrow{D}$:

$$\Delta\varphi^2_{opt} = \left[\overrightarrow{D}^T\cdot\Gamma^{-1}\cdot\overrightarrow{D}\right]^{-1}. \tag{3.56}$$

Using equations (3.44) and (3.45), it is straightforward to show that

$$\overrightarrow{D} = \frac{N_s}{2}\sin\left(\omega_s\tau + \Delta\varphi_s(t,\tau)\right)\begin{pmatrix}-1\\1\end{pmatrix}. \tag{3.57}$$

The calculation of the covariance matrix, although tedious, is predictable. The intensity measurements are described by a Poissonian distribution. Consequently, the variance of each photo-current $i_j(t)$ is equal to its average value $\langle i_j(t)\rangle$. In addition, it can be shown that the off-diagonal elements of the covariance matrix are null. This is consistent with the fact that the two outputs of the interferometer are independent. Thus, the covariance matrix is given by

$$\Gamma = \begin{pmatrix}\mathrm{Var}(i_1(t)) & 0\\ 0 & \mathrm{Var}(i_2(t))\end{pmatrix}. \tag{3.58}$$

Using equations (3.57) and (3.58) into equations (3.55) and (3.56), the optimal weights and the phase sensitivity are given by

$$\overrightarrow{m}_{min} = \frac{N_s}{2\mathrm{Var}(i_1)\mathrm{Var}(i_2)}\sin\left(\omega_s\tau + \Delta\varphi_s(t,\tau)\right)\begin{pmatrix}-\mathrm{Var}(i_2)\\ \mathrm{Var}(i_1)\end{pmatrix}, \tag{3.59}$$

and

$$\Delta\varphi_{opt} = \frac{1}{\sqrt{N_s}} \tag{3.60}$$

Note that the constant in front of the vector in equation (3.59) are not needed to define the optimal estimator as it is common to both $i_1(t)$ and $i_2(t)$. However, we keep them in order to simplify equation (3.63). One can see that the optimal estimator is independent of $\omega_s\tau$ and, as expected, reaches the minimal bound $\Delta\varphi_{min,het}$, estimated from the Fischer information in the self-heterodyne configuration given by equation (3.49).
From equations (3.51) and (3.59), the optimal estimator can be written as

$$i_{opt}(t) = \frac{N_s}{2}\sin\left(\omega_s\tau + \Delta\varphi_s(t,\tau)\right)\left[\frac{i_1(t)}{\langle i_1(t)\rangle} - \frac{i_2(t)}{\langle i_2(t)\rangle}\right]. \tag{3.61}$$

In equation (3.61), $i_1(t)$ and $i_2(t)$ have weights that depend on their average values given by equations (3.44) and (3.45), and thus on the total phase $\omega_s\tau + \Delta\varphi_s(t,\tau)$. However, in practice, the weights for each photo-current are determined before starting the experiment. Thus, we separate the phase in two components:

$$\omega_s\tau + \Delta\varphi_s(t,\tau) = \theta + \delta\theta(t), \tag{3.62}$$

where θ is the mean phase, also called working point of the interferometer, given by $\theta = \omega_s\tau + \Delta\varphi_s(0,\tau)$. It corresponds to the initial value of the phase at the beginning of the experiment from which the weights are calculated. $\delta\theta(t)$ is the phase variation around that working point and is the quantity we wish to measure. Thus the average of the optimal estimator (3.61) can be written as

$$\langle i_{opt}(t)\rangle = \frac{N_s}{2}\sin\left(\theta\right)\left[\frac{1+\cos\left(\theta+\delta\theta(t)\right)}{1+\cos\left(\theta\right)} - \frac{1-\cos\left(\theta+\delta\theta(t)\right)}{1-\cos\left(\theta\right)}\right]. \tag{3.63}$$

After calculation, with the approximation that $\delta\theta(t)$ is a relatively small deviation from the working point, one can find

$$\langle i_{opt}(t)\rangle = N_s\delta\theta(t). \tag{3.64}$$

It is clear that, for small deviations, the optimal estimator is directly proportional to the phase shift $\delta\theta(t)$.

3.4.2.2 Experimental sensitivity

The optimal estimator (3.61) relies on a particular linear combination of the photo-currents $i_1(t)$ and $i_2(t)$. This combination requires an a priori knowledge of the working point of the interferometer θ. A characterization of the phase sensitivity of an UMZI based on different estimators depending on the working point can be found in [56]. However such investigation necessitates a calibration procedure to determine the working point depending on the data measured. In addition, up to now, we did not take into account the frequency shift ω_{RF} introduced by the AOM as seen in section 3.2.1. This frequency shift, even though very convenient to shift the beat signal in the RF domain, adds a difficulty to the experiment. Due to the frequency shift, the working point is given by $\omega_{RF}t + \theta$, which is time dependent. Consequently, the working point of the interferometer depends on the time at which each measurement is realized. It can easily be understood that the optimal estimator is not reachable in this condition. Therefore, in this section, we consider a different, easily measurable estimator and calculate the corresponding effective sensitivity.

As an estimator of the phase difference $\Delta\varphi(t,\tau)$, we choose the differential photo-current $i_-(t) = i_1(t) - i_2(t)$. Other estimators such as in [56] could be investigated but the treatment is the same for all of them. Using the same treatment as in section 3.2.1 as well as equations (3.44) and (3.45), the average differential photo-current reads

$$\begin{aligned} \langle i_-(t)\rangle &= N_s \cos\left[\omega_s\tau - \omega_{RF}t + \Delta\varphi(t,\tau)\right] && (3.65)\\ &= N_s \cos\left[\omega_{RF}t - \theta - \delta\theta(t)\right], && (3.66) \end{aligned}$$

where, this time, we included the term $\omega_{RF}t$.
To derive the sensitivity associated to this estimator, equation (3.50) is applied to the photo-current $\langle i_-(t)\rangle$ [57]. To this end, the variance of the differential photo-current needs to be calculated. After calculation, it can be shown that $\mathrm{Var}(i_-(t)) = N_s$. Thus the sensitivity is given by

$$\Delta\varphi_{est} = \frac{1}{|\sqrt{N_s}\sin\left(\omega_{RF}t - \theta - \delta\theta(t)\right)|}. \tag{3.67}$$

According to the expression above, the sensitivity depends on θ as well as on $\omega_{RF}t$. This sensitivity is thus constantly changing. The minimal bound, $\Delta\varphi_{min,het} = 1/\sqrt{N_s}$ given by equation (3.49), can be reached for certain times but the sensitivity can also diverge. Experimentally this divergence has no physical meaning as, whatever the sensitivity, the measurement still gives a finite photo-current value. Hence, a different approach needs to be employed to determine the effective sensitivity of the experiment.

Determining the smallest measurable phase shift, $\delta\theta_{min}$, implies to find the smallest phase shift inducing a change in the measured signal, bigger than the noise of the measurement. This idea is illustrated in Figure 3.3. To characterize the change in the signal due to a phase shift $\delta\theta(t)$, we consider the difference between the signal with no

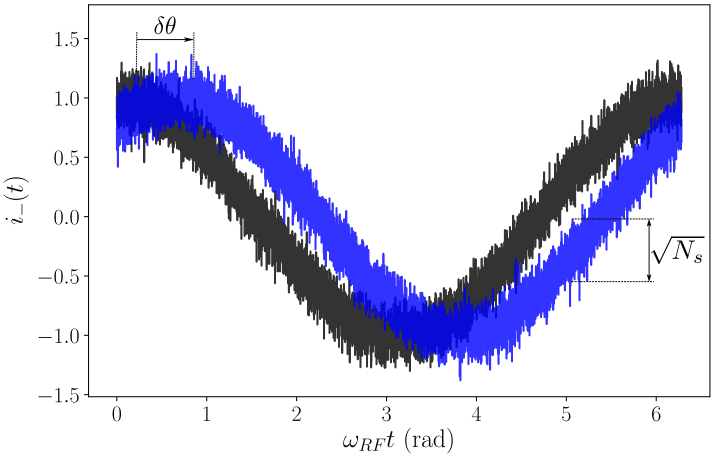

Figure 3.3 – **Noisy photo-current.** Photo-current $i_-(t)$ as a function of $\omega_{RF}t$. In the semi-classical approach the photo-current is defined by its mean value (3.66) plus its variance given by $\sqrt{\mathrm{Var}(i_-(t))} = \sqrt{N_s}$. In black the signal without phase shift and in blue the signal shifted by a phase $\delta\theta$. Our aim is to determine the smallest phase shift $\delta\theta_{min}$ as a function of $\omega_{RF}t$ for which the two curves are distinguishable.

shift and the one shifted in phase due to $\delta\theta(t)$. For simplicity and without any loss of generality, we take $\theta = 0$. The difference between the signals is thus given by

$$s(t) = N_s |\cos[\omega_{RF}t - \delta\theta(t)] - \cos[\omega_{RF}t]|. \tag{3.68}$$

The smallest phase shift, $\delta\theta_{min}$, is measured when the difference $s(t)$ starts to be bigger than the detection noise. This noise is given by the variance of the differential photo-current $\sqrt{\mathrm{Var}(i_-(t))} = \sqrt{N_s}$. Hence, the smallest phase shift $\delta\theta_{min}$ is measured for $s(t) = \sqrt{N_s}$. As the signal is constantly changing in time, we decided to use a graphical resolution. The difference $s(t)$ is calculated for different values of the time varying phase $\omega_{RF}t$. The minimal phase shift is found when the curve representing $s(t)$ crosses the detection noise level given by $\sqrt{N_s}$. An example of such graphical resolution for different values of $\omega_{RF}t$ is represented in Figure 3.4.

This resolution is applied for different values of the time varying phase $\omega_{RF}t$ from which the corresponding minimal phase $\delta\theta_{min}$ is extracted. Figure 3.5 shows $\delta\theta_{min}$ as a function of $\omega_{RF}t$ for $\omega_{RF}t \in [0, 2\pi]$. It can clearly be seen that the sensitivity reaches the optimal bound, in black, for some values of $\omega_{RF}t$ but changes rapidly with it. In an experiment, measurements are taken at different times. As the sensitivity is periodic with the time, averaging over $\omega_{RF}t \in [0, 2\pi]$ allows to determine the effective sensitivity associated to this experiment. Thus, averaging the sensitivity represented in Figure 3.5 over one period of $\omega_{RF}t$ leads to an effective sensitivity given by

$$\Delta\varphi_{eff} = \langle \delta\theta_{min} \rangle_{\omega_{RF}t} \simeq \frac{8}{\sqrt{N_s}}. \tag{3.69}$$

We see that $\Delta\varphi_{eff} \simeq 8\Delta\varphi_{min,het}$ so the effective sensitivity is height times worse than the optimal one, thus the optimal bound cannot be reached. The same analysis

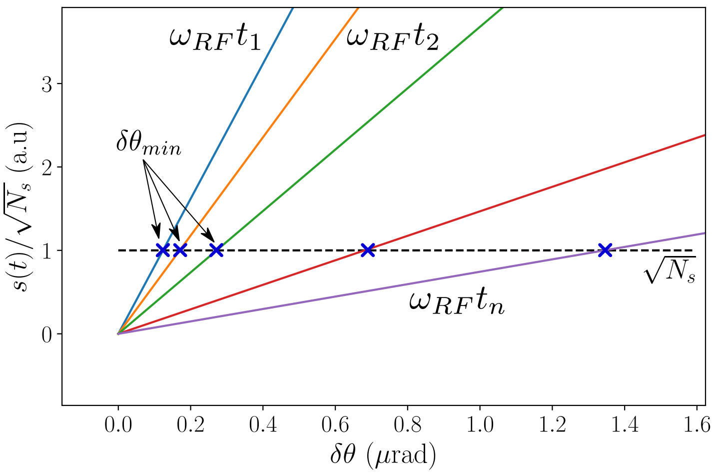

Figure 3.4 – **Graphical resolution of the sensitivity.** The signal $s(t)$ from equation (3.68) as a function of $\delta\theta(t)$. Each plain colored curve is a function $s(t)$ for a different value of $\omega_{RF}t$. It corresponds to realizations of the experiment at different times. In dashed black, the noise of the photo-detection $\sqrt{\mathrm{Var}(i_-(t))} = \sqrt{N_s}$. The signals are normalized by $\sqrt{N_s}$ for visibility. The minimal phase shift $\delta\theta_{min}$ for a given value of $\omega_{RF}t$ is given by the intersection of the plain curves with the noise.

can be conducted using a single output of the interferometer instead of the differential photo-current. The sensitivity as a function of $\omega_{RF}t$ is reproduced for this photo-current in Figure 3.5. Interestingly, even though the differential configuration is often preferred, the single output leads to the same effective sensitivity. Indeed, the curves in Figure 3.5 are different but the average sensitivity is roughly the same, leading to similar sensitivities.

The sensitivity calculated is not yet the one on the phase measurement. We derive it in the following section.

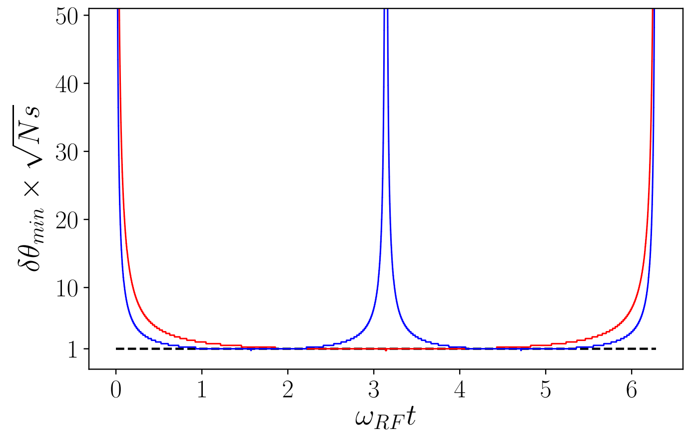

Figure 3.5 – **Determination of the experimental sensitivity.** Minimum phase fluctuation $\delta\theta_{min}$ as a function of $\omega_{RF}t$ for $N \simeq 10^{15}$. In black the optimal estimator bound $1/\sqrt{N_s}$. In blue the sensitivity for the differential photo-current. In red the sensitivity for the single photo-current measurement.

3.4.3 Phase sensitivity as a function of the analysis frequency

As said previously, the sensitivity on the phase φ can be retrieved by applying the transfer function of the UMZI (3.12) to the sensitivity on the phase difference $\Delta\varphi(f,\tau)$. This transfer function depends on the frequency analysis f at which the frequency shift is characterized. It implies that the phase sensitivity depends on the analysis frequency. If we consider the configuration where the phase shift is induced by the laser phase noise, applying the transfer function to the phase sensitivity leads to the minimal measurable phase fluctuations as a function of the analysis frequency, which can be assimilated to the minimal measurable power spectral density $S^{min}(f)$. Consequenlty, we will express this sensitivity in terms of power spectral density. From the definition of the PSD given by equation (1.51) and using the transfer function defined in equation (3.12), the PSD of the phase $S_\varphi(f)$ is related to the one of the phase difference $S_{\Delta\varphi}(f)$ according to

$$S_\varphi(f) = |h_{UMZI}(f)|^2 S_{\Delta\varphi}(f). \tag{3.70}$$

We are interested in the limit in sensitivity for a phase measurement. In an experiment, this ultimate sensitivity is set by the shot noise which is a white Gaussian noise. Hence, we assume that the noise on the phase difference $\Delta\varphi$, when looking at the limit in sensitivity, is a white Gaussian noise, which leads to $S^{min}_{\Delta\varphi_{est}}(f) = \Delta\varphi^2_{est}$, where $\Delta\varphi^2_{est}$ is the minimal phase variation that can be measured with a given estimator. Consequently, the power spectral density associated to the minimal phase is given by

$$S^{min}_{\varphi_{est}}(f) \quad = \quad \left|\frac{1}{1-e^{-2i\pi\tau f}}\right|^2 \Delta\varphi^2_{est}. \tag{3.71}$$

The minimal phase PSD as a function of the frequency is reproduced in Figure 3.6. It is represented for the optimal estimator given by equation (3.60) as well as the effective one given by (3.69). It can be seen that the optimal estimator reaches the SQL bound around 500 kHz for a delay of 200 m. On the other hand, because the effective sensitivity is eight times bigger than the optimal one, the minimal sensitivity that can be achieved experimentally is approximately 19 dB above the SQL.

A last interesting point to look at is the delay allowing to reach the best phase sensitivity (the standard quantum limit in the case of the optimal estimator) at a given frequency. In the case of the optimal estimator, the frequency at which the SQL is reached, is given as a function of the delay τ by

$$f_{SQL} = \frac{1}{2\tau}. \tag{3.72}$$

Figure 3.7 represents the variation of f_{SQL} as a function of the delay in meter introduced in the interferometer. It can be seen that if one wants to achieve the best sensitivity at a high frequency, small delays must be employed. On the other hand, to achieve the best sensitivity at low frequency, very long delays must be used.

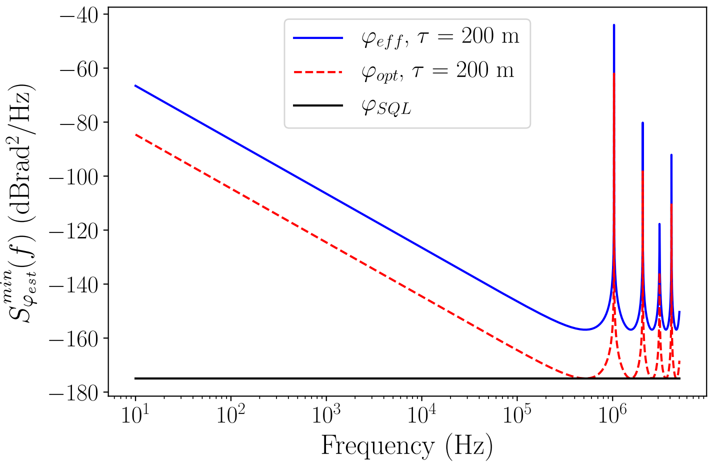

Figure 3.6 – **Minimal phase noise power spectral density.** Minimal phase noise PSD from (3.71) for the optimal estimator of the phase difference in dashed red as well as the effective one in plain blue, given by equations (3.60) and (3.69). The standard quantum limit (SQL), reached by the homodyne detection and defined in section 1.4.2.3 is also represented in black. Those limits are calculated with $P = 1$ mW, the optical power and $T = 0.1$ μs the integration time for each point.

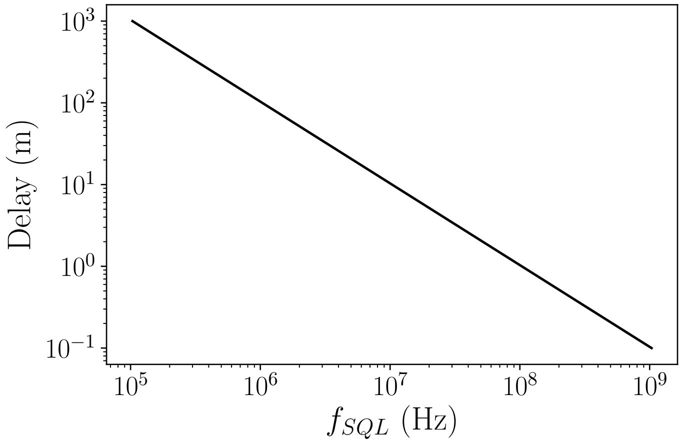

Figure 3.7 – **Delay allowing to reach the best sensitivity.** In order to achieve the best sensitivity given by equation (3.72) at the frequency f_{SQL} different delays must be employed. The delay is given by $d = \tau \times v$ where $v = c/1.45$ is the speed of light in a silica optical fiber.

Summary

In this chapter, we presented two techniques to measure the quadratures of an electric field. Since intensity measurements are easy to implement, we focused on phase measurements. The first technique, the self-heterodyne detection, is based on an unbalanced Mach-Zehnder interferometer. It allows to retrieve the information on the phase of an electric field from the beat signal with a delayed replica of this field. The second one, the homodyne detection, uses a strong field, the local oscillator, to measure the fluctuations of a weaker one at the same frequency, the signal. Both schemes will be used later to characterize the dynamics of an optical frequency comb. Consequently, we compared their sensitivity. The homodyne detection is a lossless measurement and allows to reach the standard quantum limit derived in chapter 1. On the other hand, the self-heterodyne configuration allows vacuum to enter the interferometer, degrading the sensitivity of the measurement. Even though the SQL can still be reached at certain analysis frequency using an optimal estimator, the later is not reachable experimentally. Therefore, we derived an effective bound on the phase sensitivity for an experimentally accessible observable, using a graphical resolution. This sensitivity was found to be height times higher than the SQL.

Part II

CHARACTERIZATION OF THE DYNAMICS OF OPTICAL FREQUENCY COMBS

Introduction

In the previous part we introduced the mathematical tools used to describe the electric field generated by an optical frequency comb (OFC) as well as the experimental techniques to measure it. The aim of this part is to use those tools and techniques to investigate the dynamics of OFCs. Laser dynamics refers to the temporal evolution of the laser parameters such as its mean power or its central frequency. Regarding continuous wave lasers, characterizing this dynamics is straightforward since, to some extend, it can be reduced to the study of its mean power and its frequency. However, for an optical frequency comb (OFC) the task has proven to be cumbersome due to the 10^5 individual spectral lines composing its spectrum. Yet, Haus et. al. demonstrated that the main dynamics of the OFC can be reduced to four distinct parameters: the pulse energy, the carrier envelope offset (CEO), the repetition rate and the central wavelength [58, 59]. As a consequence, the dynamics of OFCs and thus the noise affecting those main parameters, has been extensively studied in the literature. Various models have been developed to describe the noise in passively mode-locked lasers [59, 60, 61, 62]. The noise on the parameters has also been measured in the literature as in [49]. In addition, the intensity related dynamics of OFCs has drawn a lot of attention as in [63, 64, 65] where the pump laser is presented as the main source of noise. However, in those studies, a specific setup is required to measure each parameter separately. For example, a single photodiode is sufficient to measure the intensity noise of the laser. The CEO noise is usually characterized via a f-2f interferometer which will be presented later in section 4.2.1.1. The timing-jitter, meaning the noise on the repetition rate, can be measured by heterodyne beat with a stable laser. Thus, the full characterization of the dynamics requires bulky setups which are not always easy to put into practice.

In this work, a different approach to noise measurement is investigated. As introduced in [58], each noise can be associated to a specific time/frequency mode of the electric field. Thus, an experiment enabling the simultaneous measurement of the four modes of the electric field allows a characterization of the laser dynamics with a single setup. In this part, we pursue the work presented in [66, 67]. Building on the idea that each parameter can be associated to a frequency mode, an experiment to access those modes has been built. It relies on a multipixel detection allowing the measurement of separated frequency bands. Combined to an homodyne detection, the modes can be accessed and the noise extracted. The noise spectra of the parameters of a Titanium-Sapphire based femtosecond oscillator have already been measured thanks to this setup. However, in this work we go one step further. We translate our measurements in units that can be compared to other studies. In addition, we harness the correlations between noises to gain insight on the noise sources and develop a simple model to explain our measurements. Finally, we apply our analysis technique to a new source of light: the dynamics of a fiber-based frequency comb at telecom wavelength is investigated. The aim is to demonstrate that the analysis technique developed can be applied to various sources of pulses of light. Furthermore, this experiment relies on a different experimental setup from the previous one. This new setup, based on off-the-shelf optical components, is more compact and thus easier to implement.

Chapter 4

Modal investigation of the dynamics

Contents

4.1 Modal description of the dynamics 72
4.1.1 Single pulse fluctuations 72
4.1.2 Field quadrature fluctuations 73
4.2 Measuring the multimode field 74
4.2.1 Reference beam 75
4.2.2 Spectral phase compensation 77
4.2.3 Multipixel homodyne detection 81
4.3 Extracting the noise spectra 88
4.3.1 Measuring the noise spectrum: the sideband picture 88
4.3.2 Normalization of the measurements 92
4.4 Results 94
4.4.1 Covariance matrices 94
4.4.2 Noise spectra 95
4.4.3 RIN of the laser 97

In this chapter, the decomposition of the electric field in noise spectral modes is presented. The basic idea is to study a single pulse from the frequency comb undergoing intensity and phase noises. The perturbed electric field can be decomposed into noise modes each associated to a specific parameter of the laser. The fluctuations of those parameters are imprinted in the amplitude and phase covariance matrices which are measured experimentally. We describe the setup needed to achieve this measure and present the noise spectra for each parameter extracted from the measurements. This experiment allows for a complete characterization of the laser dynamics with a single setup.

4.1 Modal description of the dynamics

In this section, the mathematical tools presented in the first part of the manuscript are used to characterize the laser dynamics. In particular, the decomposition of the electric field in envelope modes is at the center of this work. We will see that a noisy laser field can be decomposed in spectral modes, each associated to a parameter of the laser.

4.1.1 Single pulse fluctuations

The starting point of the analysis is the expression of the electric field of a single pulse from the frequency comb. As seen in section 2.1.2, the complex electric field of a single pulse can be written in terms of slowly-varying envelope mode $u(t)$ according to

$$E^{(+)}_{\text{pulse}}(t) = \mathcal{E}_0 a(t)\mathrm{e}^{-i\omega_0 t} = \mathcal{E}_0 \alpha_0 u(t)\mathrm{e}^{-i\omega_0 t}, \tag{4.1}$$

where $\mathcal{E}_0$ is the single photon field amplitude [30], ω_0 is the carrier frequency, and α_0 is the (real) field amplitude so that $\alpha_0 = \sqrt{N_0}$ with N_0 the mean photon number. This expression can be related to the full train of pulses according to

$$E^{(+)}_{\text{comb}}(t) = \mathcal{E}_0 \sum_m \alpha_0 u(t - m\tau_r) e^{-i\omega_0(t-m\tau_r)} e^{-im\Delta\phi_{ceo}} \tag{4.2}$$

where τ_r is the repetition rate of the laser and $\Delta\phi_{ceo}$ is the carrier envelope offset (CEO) phase.

Due to various noise sources, such as pump laser intensity fluctuations, vibrations or temperatures fluctuations, the laser experience intensity and phase noise. The resulting dynamics can be reduced to the study of the four main parameters of the lasers regrouped in a single vector $\overrightarrow{p} = (\delta\epsilon,\ \delta\omega_0,\ \delta\tau_{ceo},\ \delta\tau_r)$ where $\delta\epsilon$ stands for amplitude fluctuations, $\delta\omega_0$ for carrier frequency fluctuations, $\delta\phi_{ceo} = \omega_0\delta\tau_{ceo}$ for CEO phase fluctuations and $\delta\tau_r$ for timing jitter. Note that $\delta\phi_{ceo}$ represents the fluctuations of the carrier envelope offset phase and should formally be noted $\delta\Delta\phi_{ceo}$. For simplicity we will keep the notation $\delta\phi_{ceo}$ in the rest of the manuscript.

As discussed in section 2.1.2, we assume that the study of a single pulse is sufficient to fully characterize the optical frequency comb. In doing so, we limit our study to effects affecting all pulses in the same way. Consequently, if we apply the perturbation $\overrightarrow{p}$ on the single pulse (4.1), we have

$$E^{(+)}_{\text{pulse}}(t, \overrightarrow{p}) = \mathcal{E}_0\alpha_0 \left(1 + \delta\epsilon\right) u\left(t - \delta\tau_r\right) \mathrm{e}^{-i(\omega_0 - \delta\omega_0)(t - \delta\tau_{ceo})}. \tag{4.3}$$

From expression (4.3), temporal modes can be associated to each parameter. However, experimentally we chose to use a spectrally resolved detection. Hence, the representation in the spectral domain is more suitable. The Fourier transform of (4.3) leads to

$$\tilde{E}^{(+)}_{\text{pulse}}(\Omega,\overrightarrow{p}) = \mathcal{E}_0\alpha_0\,(1+\delta\epsilon)\,\tilde{u}\,(\Omega-\delta\omega_0)\,\mathrm{e}^{i(\omega_0\delta\tau_{ceo}+\Omega\delta\tau_r)}, \tag{4.4}$$

where $\Omega=\omega-\omega_0$. In expression (4.4), we used the notation $\tilde{u}(\Omega)$ which corresponds the spectrum of the laser and can be found by taking the Fourier transform of (4.1) so that

$$\tilde{E}^{(+)}_{\text{pulse}}(\Omega) = \mathcal{E}_0\alpha_0\tilde{u}(\Omega) = \mathcal{E}_0\alpha_0|\tilde{u}(\Omega)|e^{i\varphi(\Omega)}, \tag{4.5}$$

where $\tilde{u}(\Omega)$ is the mean field mode normalized as $\int \mathrm{d}\Omega|\tilde{u}(\Omega)|^2=1$ and $\varphi(\Omega)$ the spectral phase. This phase is assumed to be constant over Ω. This condition is necessary to properly perform the experiment as discussed in section 4.2.2. In addition, for simplicity, we choose to work with real spectral modes by taking the phase equal to zero, i.e. $\mathrm{e}^{i\varphi(\Omega)}=\mathrm{e}^{i\varphi}=1$.

As the perturbations are small, the expression (4.4) can be expanded at first order. The fluctuations of the electric field $\delta\tilde{E}^{(+)}_{\text{pulse}}(\Omega)$ are retrieved by subtracting the unperturbed single pulse field

$$\begin{aligned}\delta\tilde{E}^{(+)}_{\text{pulse}}(\Omega) &= \tilde{E}^{(+)}_{\text{pulse}}(\Omega,\overrightarrow{p}) - \tilde{E}^{(+)}_{\text{pulse}}(\Omega)\\ &\simeq \mathcal{E}_0\alpha_0\left[\delta\epsilon\tilde{u}(\Omega)-\delta\omega_0\frac{\partial\tilde{u}(\Omega)}{\partial\Omega}+i\omega_0\delta\tau_{ceo}\tilde{u}(\Omega)+i\Omega\delta\tau_r\tilde{u}(\Omega)\right].\end{aligned} \tag{4.6}$$

Note that the notation δ as in $\delta\tilde{E}^{(+)}_{\text{pulse}}(\Omega)$ implies the dependency in $\overrightarrow{p}$, i.e. $\delta\tilde{E}^{(+)}_{\text{pulse}}(\Omega)=\delta\tilde{E}^{(+)}_{\text{pulse}}(\Omega,\overrightarrow{p})$.

Using equation (4.6), we will show that the perturbed field can be decomposed in four noise modes. Thus, measuring the electric field in a given spectral mode allows to measure the noise on the corresponding parameter.

4.1.2 Field quadrature fluctuations

In the rest of the study the representation in terms of quadratures of the electric field $\tilde{x}(\Omega)$ and $\tilde{p}(\Omega)$ is used. Those quantities correspond to physical properties of the electric field accessible in an experiment, using for example a homodyne detection as described in section 3.3.

As introduced in section 1.2.3, the quadratures are related to the electric field according to

$$\tilde{E}^{(+)}_{\text{pulse}}(\Omega) = \frac{\mathcal{E}_0}{2}\left[\tilde{x}(\Omega)+i\tilde{p}(\Omega)\right], \tag{4.7}$$

where $\tilde{x}(\Omega)$ is proportional to the real part of the field and $\tilde{p}(\Omega)$ to its imaginary part. As seen in section 1.4.2.1, using this representation, the fluctuating electric field can be written

$$2\delta\tilde{E}^{(+)}_{\text{pulse}}(\Omega) = \mathcal{E}_0\left[\delta\tilde{x}(\Omega) + i\delta\tilde{p}(\Omega)\right], \tag{4.8}$$

with $\delta\tilde{x}(\Omega) = 2\delta\alpha_0\tilde{u}(\Omega)$, proportional to the amplitude fluctuations, and $\delta\tilde{p}(\Omega) = 2\alpha_0\delta\varphi\tilde{u}(\Omega)$, proportional to the phase fluctuations. By identification with equation (4.6) we find

$$\begin{aligned} \delta\tilde{x}(\Omega) &= 2\alpha_0\left[\delta\epsilon\tilde{u}(\Omega) - \delta\omega_0\frac{\partial\tilde{u}(\Omega)}{\partial\Omega}\right], && (4.9)\\ \delta\tilde{p}(\Omega) &= 2\alpha_0\left[\omega_0\delta\tau_{ceo}\tilde{u}(\Omega) + \Omega\delta\tau_r\tilde{u}(\Omega)\right]. && (4.10) \end{aligned}$$

In the expressions above, each of the four parameters is associated to a particular spectral mode related to the mean field one $\tilde{u}(\Omega)$. To normalize those modes, the mean field spectral mode can be approximated by a Gaussian centered on ω_0 according to

$$\tilde{u}(\Omega) = \frac{1}{\sqrt[4]{2\pi\Delta^2\omega}}\exp\left(-\frac{\Omega^2}{4\Delta^2\omega}\right), \tag{4.11}$$

where $\Delta\omega = \sqrt{\Delta^2\omega}$ is the spectral width of the field given by $\Delta^2\omega = \int\Omega^2|\tilde{u}(\Omega)|^2\,\mathrm{d}\Omega$. Using this definition, we have

$$\begin{aligned} \delta\tilde{x}(\Omega) &= 2\alpha_0\left[\delta\epsilon\tilde{u}_{amp}(\Omega) - \frac{\delta\omega_0}{2\Delta\omega}\tilde{u}_{cent-freq}(\Omega)\right], && (4.12)\\ \delta\tilde{p}(\Omega) &= 2\alpha_0\left[\omega_0\delta\tau_{ceo}\tilde{u}_{ceo}(\Omega) + \Delta\omega\delta\tau_r\tilde{u}_{rep-rate}(\Omega)\right], && (4.13) \end{aligned}$$

The normalized modes defined in expressions (4.12) and (4.13) are called detection modes and are given by

$$\begin{aligned} \tilde{u}_{amp}(\Omega) \equiv \tilde{u}_{ceo}(\Omega) &= \tilde{u}(\Omega)\\ \tilde{u}_{cent-freq}(\Omega) &= -2\Delta\omega\frac{\partial\tilde{u}(\Omega)}{\partial\Omega}\\ \tilde{u}_{rep-rate}(\Omega) &= \frac{\Omega\tilde{u}(\Omega)}{\Delta\omega} \end{aligned}$$

The dynamics of the laser can be characterized by measuring the electric field in the spectral modes associated to each parameter of the laser. It can be achieved by a spectrally resolved detection. The setup used to perform this measurement is described in the next section.

4.2 Measuring the multimode field

In order to characterize the laser dynamics, the experimental setup presented in Figure 4.1 is used. The beam under study is first split in two: an intense beam, and a weak

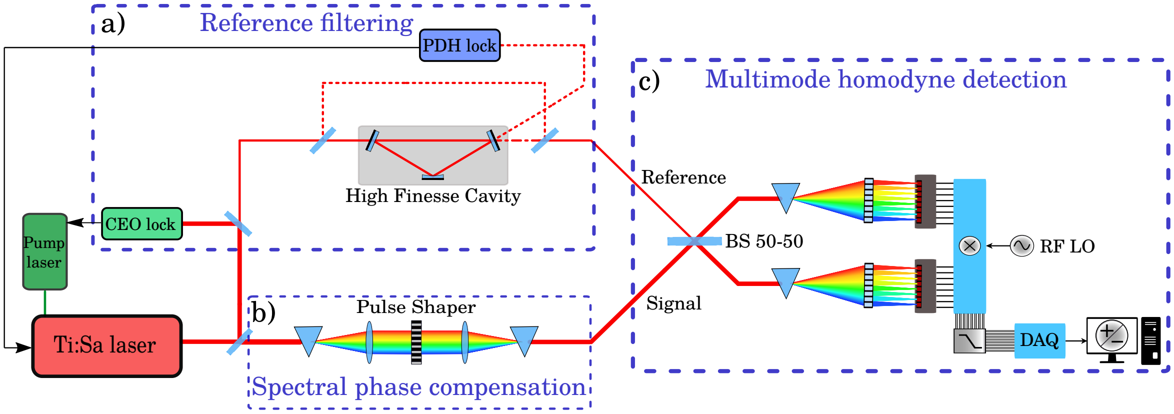

Figure 4.1 – **Experimental setup:** The experiment is composed of three parts. a) Reference filtering, to generate the reference beam via a high finesse cavity on which the repetition rate of the laser is locked. The CEO is also locked thanks to a f-2f interferometer to ensure maximum transmission through the cavity. The laser is free running above the locking bandwidth of a few kHz. b) Spectral phase compensation with a pulse shaper to ensure a flat phase for all spectral bands. That way, the homodyne is locked on the phase quadrature for all the spectral bands. c) Multipixel homodyne detection to measure the amplitude and phase noise in 8 different spectral bands. A demodulation stage is used to acquire noise at a given offset frequency selected by the radio-frequency local oscillator (RF LO) whose frequency can be swept. All the data are acquired by an acquisition card (DAQ) and are post processed on a computer to recover the covariance matrices.

one. The aim of this experiment is to perform a spectrally resolved measurement on the intense beam. Hence, we call this beam the signal. The setup can be decomposed in three different parts. The first one is the reference beam preparation. As a matter of fact, a phase measurement requires a phase reference to compare the field under study to. This is achieved by filtering the phase fluctuations of one of the beams, in this case the weak one, with a high finesse cavity. We call this beam the reference. The second part of the experiment, involving a pulse shaper, is used to properly control the relative phase between the beams across the spectrum for the homodyne detection. Finally, a multipixel homodyne detection is implemented to perform the spectrally resolved detection of the quadratures of the field. In the following we present each part in more details.

4.2.1 Reference beam

The first building block of the experiment is the preparation of the reference beam. Indeed, the phase measurement in the experiment relies on a homodyne detection.

More precisely, the variation of the homodyne detection described in section 3.3.3 is used to characterize the noise of the most intense of the two beams, the signal. We saw that this scheme gives access to a measurement of the amplitude noise of the signal and to a measurement of the relative phase noise between the signal and the reference. To retrieve the phase noise of the signal beam only, the reference beam needs to have lower phase noise than the signal beam. This is achieved by filtering the phase fluctuations of the reference. In principle other techniques can also be used such as an unbalanced Mach-Zehnder interferometer as seen in section 3.2. However, this is not the approach used in this experiment. Instead, a high finesse cavity ($F \simeq 1200$) has been designed to filter the phase noise. The technical description of this cavity can be found in [66] and a picture can be seen in Figure 4.3. This cavity acts as a low pass filter for the phase fluctuations with a bandwidth of approximately 125 kHz. This cavity is synchronized with the laser cavity [68]. Indeed, to ensure maximum transmission through this filtering cavity, a pulse circulating inside the cavity must overlap, after one round-trip, with the next pulse, from the train of pulses, injected. In the frequency domain, a frequency comb can be associated to the high finesse cavity. The separation between spectral lines is given by the length of the cavity. It defines the repetition rate of the cavity. Its CEO frequency is set by the intra-cavity dispersion. Hence, the laser spectrum is entirely transmitted, and thus the cavity are synchronized, if both repetition rates and CEO frequencies of the laser and the cavity are identical. Consequently, those quantities need to be locked. In principle, we lock the repetition rate and the CEO of the laser as the cavity is designed to be more stable. In the following parts we briefly discuss the technical aspects of those locking.

4.2.1.1 CEO locking

The first parameter that needs to be locked is the carrier-envelope offset (CEO) of the laser. As previously explained, this offset is due to the intra-cavity dispersion. Controlling the dispersion allows to control this parameter. This is usually ensured by a control of the pump laser intensity [69]. To lock the CEO, its value has to be measured first. This is achieved using a f-2f interferometer. A scheme of this interferometer is reproduced in Figure 4.2. Its principle is to use a photonic crystal fibre (PCF) to expand the pulse spectrum. This spectrum must be expanded enough to reach 532 nm and 1064 nm. Once done, a dichroic mirror separates the spectrum into two components. We write the frequencies of the two components as

$$f_{1064} = f_0 + n_{1064} f_r \quad \text{and} \quad f_{532} = f_0 + n_{532} f_r, \tag{4.14}$$

where f_0 is the CEO frequency, f_r the repetition rate and n_λ the index of the spectral line corresponding to the wavelength λ. The 1064 nm component is frequency doubled in a nonlinear crystal to reach 532 nm according to

$$f''_{532} = 2f_0 + 2n_{1064} f_r \tag{4.15}$$

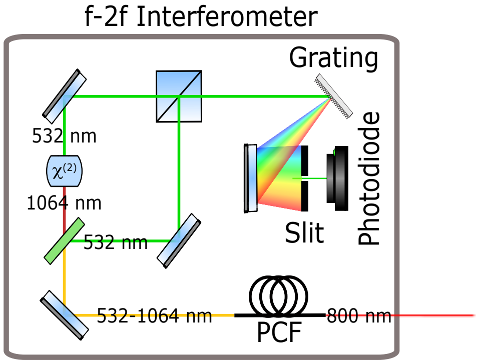

Figure 4.2 – **Drawing of the f-2f interferometer.** The initial spectrum is expanded thanks to a photonic crystal fibre to have a span of an octave. The signal at 532 nm is mixed with the one at 1064 nm but frequency doubled to measure the CEO of the laser.

Both beams at 532 nm are then recombined on a beam-splitter. Because $n_{532} = 2n_{1064}$, the beat signal between the two beams, measured with a photodiode, gives access to the CEO according to

$$f_{beat} = |f''_{532} - f_{532}| = f_0. \tag{4.16}$$

This value is then locked by mixing the beat signal with a stable radio-frequency (RF) reference which value is chosen in order to maximize the transmission of the filtering cavity. The error signal is sent, via a commercial PI servo controller from New Focus, with a bandwidth of 3 kHz, to the pump laser to act on its current. It results in a modulation of the pump laser intensity which modulates the intra-cavity dispersion of the laser and thus the CEO.

4.2.1.2 Repetition rate locking

Once the CEO is locked, the repetition rate of the laser, i.e. the length of the cavity, can also be locked to match the filtering cavity one. To this end, a Pound-Drever-Hall (PDH) method is used. To implement this locking, a counter-propagating beam is sent to the filtering cavity as illustrated in Figure 4.3. The phase of this field is modulated via a mirror mounted on a piezoelectric. The PDH signal is derived from the reflected beam at the output of the cavity. This scheme is used to avoid any modulation on the reference beam, in transmission, sent to the homodyne detection. The error signal is fed to another mirror mounted on a piezoelectric actuator in the laser cavity via another PI servo controller with a bandwidth of 1 kHz. A detailed description of this locking scheme can be found in [66].

4.2.2 Spectral phase compensation

The second building block of the experiment is the spectral phase compensation. It is based on a pulse shaper and is used to ensure a flat spectral phase across the spectrum of the signal beam with respect to the reference. This compensation is needed to satisfy the

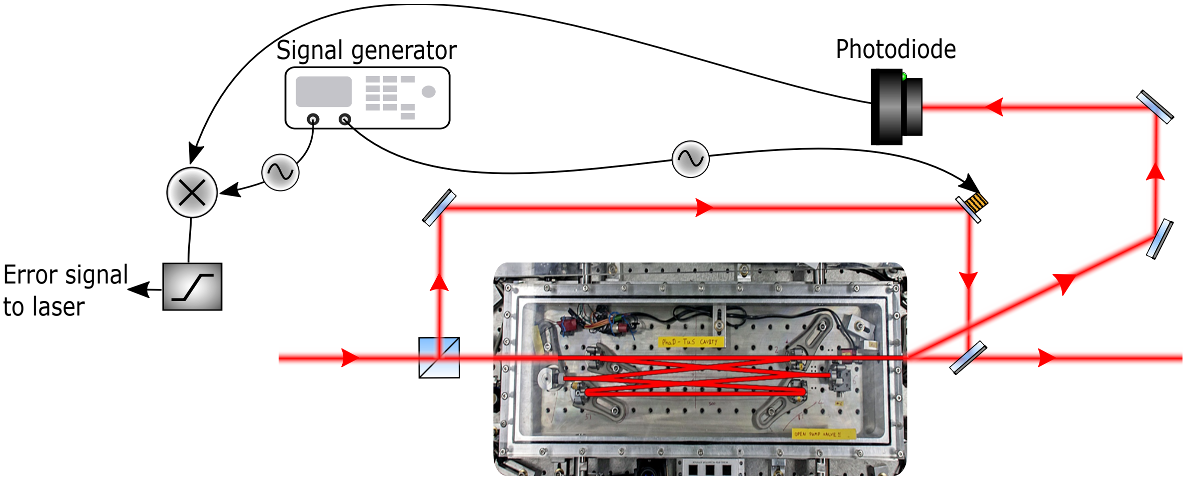

Figure 4.3 – **Drawing of the filtering cavity and the repetition rate locking.** The locking is realized with the reflection of a counter-propagating beam at the output of the cavity. The beam is modulated by a mirror mounted on a piezo and the reflected signal detected by a photodiode. This signal is mixed with a stable reference which creates the error signal. It is then send to another mirror mounted on a piezo in the laser cavity to stabilize the cavity length.

assumption made in section 4.1.1, namely that $\varphi(\Omega)$ is constant over Ω. This condition is important as with a non-flat phase the nature of the measured quadratures would evolve throughout the optical spectrum. In this section, the spectral interferometry technique used to measure the relative phase between the signal and reference beams is presented. Then, the working principle of a pulse shaper used to correct the spectral phase is briefly introduced.

4.2.2.1 Spectral phase measurement

The spectral interferometry technique is used to measure the spectral phase between the signal and reference beams. To this end, a delay τ is introduced on one of the arm of the homodyne detection. The signal and the reference beams are then combined on the homodyne BS. A spectrometer is placed at one of the outputs so that the spectrally resolved intensity is detected. Using the definitions of the electric field in the spectral domain 1.18: $\tilde{E}_j^{(+)} = \mathcal{E}_0\alpha_j|\tilde{u}_j(\Omega)|e^{i\varphi_j(\Omega)}$, the intensity reads

$$\begin{aligned} I(\Omega) &\propto |\tilde{E}_s^{(+)}(\Omega) + \tilde{E}_{ref}^{(+)}(\Omega)e^{i\Omega\tau}|^2 \\ &\propto I_s(\Omega) + I_{ref}(\Omega) + 2\mathcal{E}_0^2\alpha_s\alpha_{ref}|\tilde{u}_s(\Omega)||\tilde{u}_{ref}(\Omega)|\cos\left(\Omega\tau + \varphi_s(\Omega) - \varphi_{ref}(\Omega)\right), \end{aligned} \tag{4.17}$$

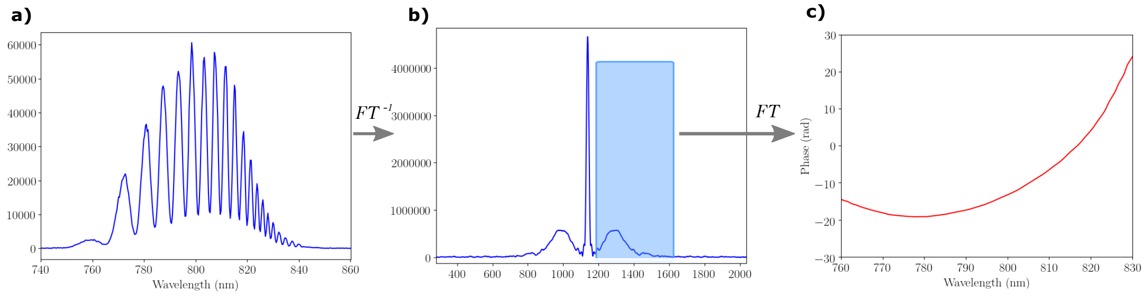

Figure 4.4 – **Representation of the spectral phase measurement.** A spectrum is first acquired (a) when a constant delay is introduced between the signal and the reference. The inverse Fourier transform of this spectrum is calculated (b). This signal is composed of a central peak and two sidebands at $\pm\tau$ due to the delay. The Fourier transform of one sideband is taken and the phase of the signal is plotted (c) to retrieve the spectral phase.

where $\Omega = \omega - \omega_0$. We write $\varphi(\Omega) = \varphi_s(\Omega) - \varphi_{ref}(\Omega)$ the spectral phase we aim to measure. It can be seen that the spectrum is composed of an oscillating term as a function of Ω due to the delay τ. This term is responsible for the fringes in the spectrum reproduced in Figure 4.4a. Those fringes are modulated across the spectrum by the spectral phase $\varphi(\Omega)$ changing locally their period. For simplicity, only the interference part is considered in what follows. The spectral phase can be determined by first taking the inverse Fourier Transform of the intensity (4.17). The signal reads

$$\begin{aligned}\mathrm{TF}^{-1}\{I(\Omega)\} \;\propto\; & \int_{\mathbb{R}} \alpha_s\alpha_{ref}|\tilde{u}_s(\Omega)||\tilde{u}_{ref}(\Omega)|e^{i\Omega(t+\tau)}e^{i\varphi(\Omega)}\mathrm{d}\Omega \\ + & \int_{\mathbb{R}} \alpha_s\alpha_{ref}|\tilde{u}_s(\Omega)||\tilde{u}_{ref}(\Omega)|e^{i\Omega(t-\tau)}e^{i\varphi(\Omega)}\mathrm{d}\Omega. \end{aligned} \tag{4.18}$$

The signal corresponding to the expression above is represented in Figure 4.4b. It is composed of a central peak (due to the DC term $I_s(\Omega) + I_{ref}(\Omega)$ not written in (4.18)) and two sidebands at delays $-\tau$ and $+\tau$ from the central peak.

A time window is applied to keep only the positive sideband at $+\tau$ which is then shifted back to $\tau = 0$. The Fourier transform of this filtered signal is then taken. The retrieved signal is:

$$s(\Omega) \propto \alpha_s\alpha_{ref}|\tilde{u}_s(\Omega)||\tilde{u}_{ref}(\Omega)|e^{i\varphi(\Omega)} \tag{4.19}$$

Therefore, taking the argument of the signal above gives the spectral phase $\varphi(\Omega)$. An example of measured spectral phase is represented in Figure 4.4c. This spectral phase can be controlled using a pulse shaper as described in the next section.

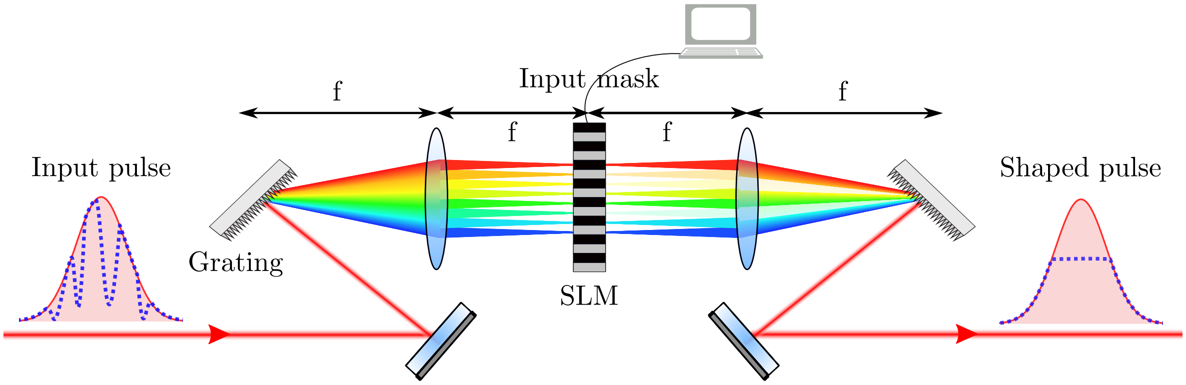

Figure 4.5 – **Working principle of a pulse shaper.** A pulse shaper is composed of a zero-dispersion line and a spatial-light modulator. The input beam is spectrally spread with a grating. The spectral phase of the input beam is shaped by applying different voltage values on the SLM. The output shaped beam is then recombined in frequency with another grating.

4.2.2.2 Pulse shaper

A pulse shaper can be used to shape the amplitude or the phase of the spectrum of a laser beam. A very detailed review of pulse shaping techniques can be found in [70]. In our experiment, the pulse shaper is mainly used as a phase modulator and is composed of a 4f line, also called zero-dispersion line, and a Spatial Light Modulator (SLM) placed in the Fourier plane as displayed in Figure 4.5.

Zero-dispersion line: It is composed of a first grating to angularly disperse the spectral components of the pulse. Each component is then focalized on a different spot in space by a first lens placed at a distance f from the grating, f being its focal distance. The second lens is placed at $2f$ from the first one. The SLM is placed in between the lenses. A second grating, at a distance f from the second lens, recombines all the spectral components in a single beam at the output of the pulse shaper. In the experiment this line is implemented in a folded configuration meaning that the SLM acts as a mirror and thus only one lens and one grating are used. A small vertical angle is set on the SLM so that the input and output beams can be separated.

Spatial Light Modulator: The SLM used in the experiment is based on liquid crystals (Hamamastsu LCOS-SLM X10468). It is placed between the two lenses at equal distance from each one. It is composed of a screen of 792 × 600 pixels acting as independent programmable waveplates depending on the voltage applied to each one of them [71]. As the spectrum is spread across the screen of the SLM, the spectral phase can be tuned by applying different voltage values to different pixels.

4.2.2.3 Compensation

For our analysis we use the pulse shaper combined with the spectral interferometry technique to ensure a flat relative phase across the spectrum. The spectral phase is first measured using the spectral interferometry. It can then be inverted and sent to the pulse shaper, placed on the signal path, to flatten the relative phase between the two beams. In practice only the quadratic phase is corrected in the experiment as it is the dominant contribution. Typically, a quadratic phase of - 2200 fs^2 is applied on the pulse shaper. In addition to ensure a flat spectral phase across the spectrum, this procedure enables to rise the homodyne contrast for the entire signal as it improves the overlap between the two fields. Before spectral phase compensation the contrast is about 35 %. Once corrected, almost 90 % contrast can be reached.

4.2.3 Multipixel homodyne detection

Finally, the most important building block of the experiment is the multipixel detection. After the homodyne beam-splitter (BS), the laser spectrum is spatially spread with a diffractive element, a grating in our case. This spectrum is sliced in spectral bands thanks to an array of microlenses. Each part of the spectrum is then detected by a photodiode from an array of 16 photodiodes from which only 8 are used. The reason for this choice will be explained later. As a homodyne detection is a projective measurement, this configuration is equivalent to performing 8 homodyne detections in the different spectral bands. In this section, the technical implementation of such measurement is discussed. Then, a new basis is introduced to model this measurement: the pixel basis.

4.2.3.1 Detectors alignement and calibration

As said previously, each detector (respectively called Harmony and Chaos) is composed of 16 photodiodes from which 8 only are used. The detectors have two outputs for each pixel: a low frequency one (DC signal), mainly used for alignment, and a high frequency one (AC signal), used for the acquisition. The cutting frequency between the two outputs is 200 kHz.
Each channel must be properly aligned and calibrated. In this section, the alignment as well as the calibration procedures are exposed. Note that all the procedures are realized using only the signal beam (the reference being blocked), as it is the most intense of the two beams and the one we wish to characterize.

Space wavelength mapping The first calibration step is the space-wavelength mapping. It consists in associating a wavelength to each pixel of the detectors. To realize this calibration, a spectral filter is used to select a very narrow spectral band ($\simeq$ 1 nm).

This spectral filtering is performed by the pulse shaper presented in section 4.2.2. By shutting down all the pixels from the SLM screen expect a very narrow line, only a small portion of the signal optical spectrum is reflected and sent to the detection. The central wavelength of the filter is shifted from 760 nm to 830 nm by shifting the position of the switched-on pixels on the screen. At each step, the wavelength corresponding to the light going through the spectral filter is measured with a spectrometer. Then, an acquisition of the DC signal of every pixels from each detector is taken during 100 ms. This signal is averaged over the acquisition time to retrieve the mean power seen by each pixel depending on the wavelength of the spectral filter. The experimental data are reproduced in Figure 4.6.
To find the correspondence between pixel and wavelength, the data of each pixel are fitted by a Gaussian and the central wavelength of each fit is plotted as a function of the pixel number as shown in Figure 4.7. Those data are then also fitted, using a linear fit. This linear curve allows to map each pixel to a wavelength[1].

Detector alignment The second step in the calibration is to ensure a good alignment of the two detectors, i.e. that a pixel of one detector receive the same power as the same one of the other detector. Because the space wavelength mapping has been done before, this is equivalent to making sure that both detectors see the same optical spectrum. To this end, the optical spectrum as seen by each detector is monitored by taking the average photo-current measured at the low frequency output of each photodiode. A real time measurement of the spectra allows to properly align the detectors. This alignment is done by tuning the longitudinal translation stages on which the detectors are mounted, the ones of the lens arrays as well as the position of the mirrors before and after the grating used to expand the spectrum. A good alignment is obtained when both detectors see the same average power (given by the sum of the power seen by each pixel) and when the two spectra perfectly overlap as can be seen in Figure 4.8. By doing so, we ensure that the homodyne detection is balanced for all the pixels.

Gain calibration Once the same optical spectrum is sent to each detector, the detectors high frequency outputs can be calibrated. Each high frequency output has a variable gain that can be modified. It is important to set the same gain for all pixels from one detector. Indeed, if the same modulated signal is sent to each pixel individually, the same modulation amplitude needs to be measured by each pixel. Furthermore, it is critical to set the same gain for the pixels detecting the same wavelength in both detectors. Indeed, if the gain is different, the situation is equivalent to an unbalanced homodyne measurement. To calibrate this gain, a stable reference is needed. This

---

[1] Note that in Figure 4.7, the pixels are numbered from 1 to 16 but only 8 are detected as explained before.

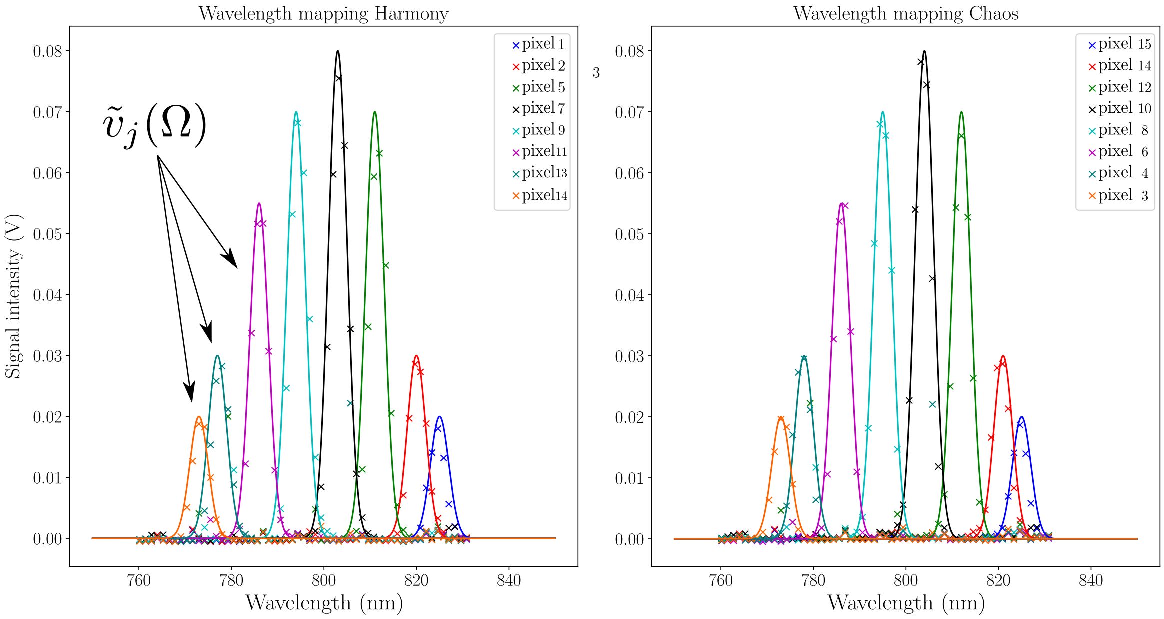

Figure 4.6 – **Experimental data and Gaussian fit of the light seen by each pixel depending on the incident wavelength**. Each point corresponds to a value of central wavelength of the spectral filter. Each color represents the signal measured by one pixel from 1 to 8. The mapping is done for the two detectors (called Harmony and Chaos). The Gaussian fit allows to determine the wavelength corresponding to the maximum detected signal for each pixel. In addition, each Gaussian corresponds to a pixel mode $\tilde{v}_j(\Omega)$

.

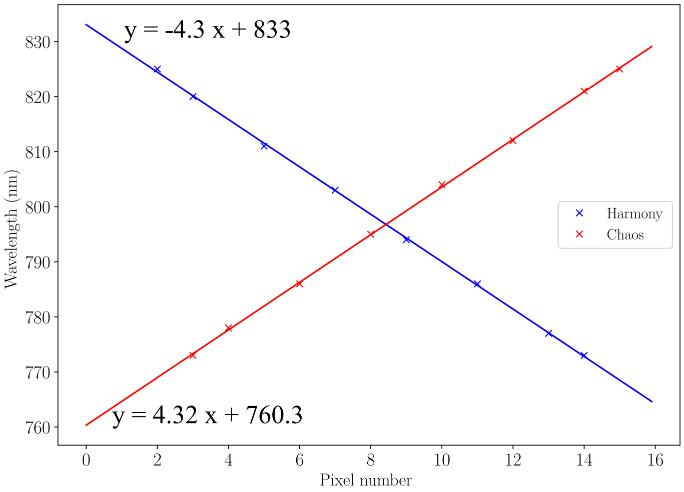

Figure 4.7 – **Mapping of the pixel number to the wavelength of the incident beam.** Each point corresponds to the maximum of the Gaussian from Figure 4.6 for each pixel. The two detectors have an opposite slope because of the mirror symmetry of the setup. Note that here the pixels are numbered from 1 to 16 but one pixel is left undetected between each pixel except in the wings.

reference is provided by an acousto-optic modulator (AOM) placed in the signal path. The full procedure can be summarized as follow:

- The position of the AOM on the signal path is adjusted. In particular, the angle between the incident field and the AOM surface is tuned to put maximum power in the diffracted order while keeping the detected optical spectra identical, to stay in a balanced configuration.
- The radio-frequency (RF) signal sent to the AOM is modulated in amplitude at 500 kHz resulting in a modulation of the optical power in the diffracted order.
- The laser field is measured by the detectors so that the modulation power seen by each detector can be plotted in real time.
- The gain of all the pixels of a single detectors is adjusted. It is achieved by illuminating one pixel at a time using once again the pulse shaper as a spectral filter. For this procedure, the wavelength of the filter is kept fixed and each pixel is successively placed in the beam by using the translation of the detector. The gain is adjusted by setting the same modulation power for every pixel.
- Finally, with the first detector calibrated, the gains of the second one can be be adjusted by setting the difference of the signals from both detectors to zero, pixel by pixel.

Gain verification, shot noise measurement: Once this calibration is done, it can be tested by removing the AOM and acquiring data from the high frequency channels of the detectors. Taking the difference of the photo-currents pixel by pixel leads to a measurement of the optical spectrum as seen by the AC outputs. Indeed, the homodyne detection, if only the signal beam is sent to the detectors, leads to a measurement of the shot noise, as all the correlated noises are subtracted. Because the shot noise depends on the number of photons and thus the optical power in each pixel, it allows to measure the optical spectrum as seen by the high frequency outputs of the detectors. This spectrum can be compared with the one acquired using the low frequency outputs. If the calibration is perfectly completed, both DC and AC spectra must overlap as can be seen in Figure 4.8.

Clearance: The last step is to ensure that any noise at any frequency of the noise spectrum (from a hundred kilohertz to a few megahertz) can be detected. As previously mentioned, the shot noise is the fundamental limit in an experiment, set aside the noise coming from the detection electronic, called electronic noise (or dark noise). To be certain to detect noises down to the shot noise level, the gain of the detectors must be high enough so that this fundamental noise is higher than the electronic noise. To

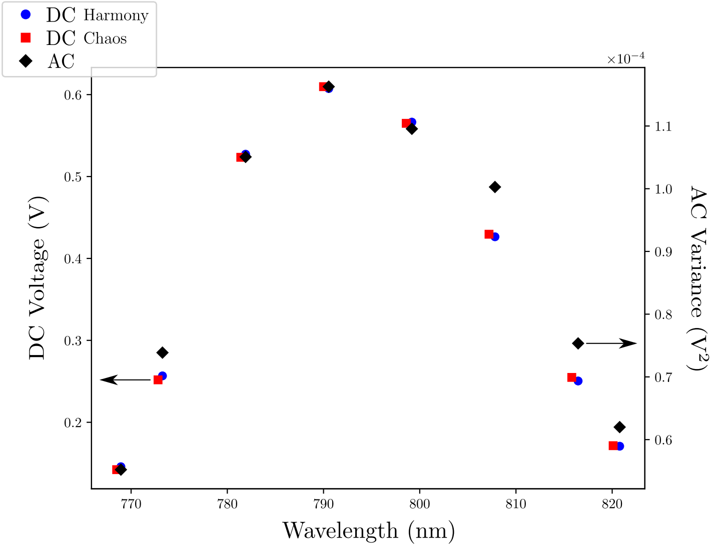

Figure 4.8 – **DC and AC optical spectra.** Left axis, blue dots and red squares: spectra acquired with the low frequency outputs of both detectors. Right axis, black diamond: variance of the difference of the signal acquired by the high frequency outputs of the detectors leading to a measurement of the shot noise. The three spectra overlap indicating a correct alignment and calibration.

quantify how different the shot noise is, compared to the electronic noise, the clearance is often used. The clearance is defined as the ratio between the shot noise, measured by the differential photo-current when only the signal illuminates the detectors, as explained in the previous paragraph, and the electronic noise, obtained when no light is going into the detectors. To recover those quantities, the noise spectra pixel by pixel, with and without light, are measured. The procedure to recover those noise spectra will be presented in section 4.3. Note that this technique is very convenient as it allows to characterize all the acquisition chain. The experimental data are reproduced in Figure 4.9. Each pixel has a clearance of at least a few dB, which is high enough to perform the measurements, even on the side-pixels for which the optical power is low due to the Gaussian shape of the spectrum, as can be seen in Figure 4.8.

4.2.3.2 The pixel basis

In the previous section, the technical implementation of the multipixel detection has been discussed. To pursue our investigations, a new basis needs to be introduced to properly describe the multipixel measurements. The decomposition in noise modes from equations (4.12) and (4.13) is given in a basis composed of continuous modes $u(\Omega)$, which are the detection modes. However, in the experiment, the spectrum is sliced in 8 spectral bands, using arrays of microlenses and photodiodes. Consequently, the acquisition must be expressed in a discrete basis composed of the 8 spectral bands. We consider an array of 8 pixels slicing the Gaussian mean field mode $\tilde{u}(\Omega)$ given by equation (4.11). We define the pixel basis $\{\tilde{v}_j(\Omega)\}$, $j \in \{1:8\}$ where each mode from the basis corresponds to a pixel. The particular shape of those pixel modes as a function of Ω is set by the geometry of the experiment [72]. Experimentally, the shape of those

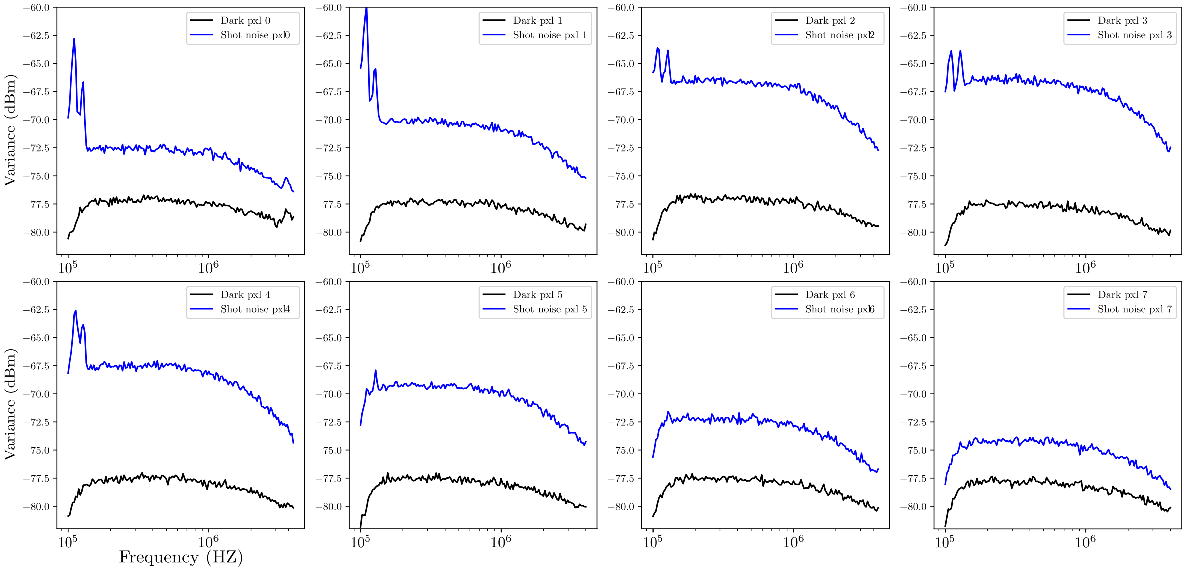

Figure 4.9 – **Clearance of each pixel.** Electronic (or dark) noise (black) and shot noise (blue) calculated by taking the variance of the difference of the AC outputs of the detectors for each pixel. The electronic noise is measured when no light is sent to the detectors. The shot noise is measured by sending the signal beam only to the homodyne detection. A good clearance is achieved even for the side-pixels which receive less light.

pixels can be determined via the space-wavelength mapping presented in the previous section. Each mode associated to a pixel j is given by the corresponding Gaussian function represented in Figure 4.6, as it defines the optical spectrum measured by each pixel. The fact that only 8 pixels from the 16 are used becomes clear by looking at the modes represented. To ensure that the pixel modes are orthogonal, their overlap should be minimized. This is made possible by leaving one pixel undetected between each pixel, hence the gap between each pixel mode. However, this procedure cannot be used for the side pixels. Indeed, the optical power is too low in the wings of the optical spectrum. Thus, two pixels side by side are taken, making those modes not perfectly orthogonal.

In this basis, each continuous mode $\tilde{u}(\Omega)$ can be redefined by a vector $\overrightarrow{u} = (u_1, \dots u_8)$ with

$$u_j = \int_{\mathbb{R}} \tilde{v}_j(\Omega)\tilde{u}(\Omega)\mathrm{d}\Omega. \tag{4.20}$$

In the remaining of this chapter we will express all the quantities is this discrete basis. Experimentally, the components u_j from, e.g. the amplitude mode (or the CEO one) $\tilde{u}_{amp}(\Omega) = \tilde{u}(\Omega)$, defined in section 4.1.2, are determined by measuring the DC level from the pixels when the signal beam is sent to the detectors. This measure directly gives access to the overlap between the laser spectrum and the pixel modes $\tilde{v}_j(\Omega)$. Hence, the pixelized amplitude mode coefficients $\tilde{u}_{amp,j}$, correspond to the data in red (or in blue) represented in Figure 4.8. Additionally, the other detection modes ($\tilde{u}_{cent-freq}(\Omega)$ and $\tilde{u}_{rep-rate}(\Omega)$) are determined by fitting the pixelised mode $\tilde{u}_{amp}(\Omega)$ and calculating its derivative.

4.2.3.3 Quadrature detection

Once the detectors aligned and calibrated, the field quadratures can be measured pixel by pixel in the new basis previously introduced. As seen in section 3.3, phase and amplitude fluctuations of an electric field lead to quadrature fluctuations, which can be retrieved via a measurement of the fluctuations of the homodyne signal. Indeed, as seen in equation (3.30), the sum of the photo-currents of the two outputs of the homodyne leads to a measurement of the quadrature $x_{s,j}$ of the intense beam for the j^{th} pixel, according to

$$\delta i_{+,j} \propto \alpha_{s,j} \delta x_{s,j}, \tag{4.21}$$

where the index j represents the pixel number ranging from 1 to 8. $\alpha_{s,j} = \sqrt{N_{s,j}}$ is the number of photons in the signal arm for the pixel number j.

On the other hand, a measurement of the difference of the photo-currents, provided that the relative phase between the two arms of the homodyne is set to $\pi/2$, leads to a measurement of the difference between the reference phase fluctuations and the signal ones as seen in equation 3.28:

$$\delta i_{-,j} = 2\alpha_{s,j}\alpha_{ref,j}(\delta\varphi_s - \delta\varphi_{ref}). \tag{4.22}$$

As previously explained in section 4.2.1, the phase fluctuations of the reference beam are filtered as we are interested in the fluctuations of the signal beam. Thus, the differential photo-current reads

$$\delta i_{-,j} = 2\alpha_{s,j}\alpha_{ref,j}\delta\varphi_s. \tag{4.23}$$

We saw in section 1.4.2.1 that $\delta p_s = \alpha_s \delta\varphi_s$. Consequently, measuring $\delta i_{-,j}$ is equivalent to measuring $\delta p_{s,j}$ but for a reduced number of photons due to the presence of the term $\alpha_{ref,j}$ in equation (4.23). The procedure to properly extract $\delta p_{s,j}$ and its consequences on the sensitivity of the phase measurement are discussed in section 4.3.2.

In this section we reviewed the most critical parts of the experimental setup. The three building blocks are a multimode homodyne detection, a reference beam and a pulse shaper. In the next sections the results obtained thanks to this experimental setup to characterize the dynamics of a Titanium Sapphire based frequency comb are presented.

4.3 Extracting the noise spectra

In the previous sections we introduced the decomposition in noise modes of a noisy electric field from an optical frequency comb and the experimental setup used to access those modes. From this measurement, it is possible to measure the fluctuations of the different parameters of the laser ($\delta\epsilon,\ \delta\omega_0,\ \delta\tau_{ceo},\ \delta\tau_r$). To characterize the dynamics of the laser, the noise spectrum of each laser parameter needs to be measured. Experimentally, a spectrum analyzer is usually used to calculate the power spectral density to characterize the noise on a given quantity. However, in this experiment this measurement is not possible since too many signals need to be acquired at the same time. Consequently, we present the technique used to recover the spectrum of all the laser parameters simultaneously. It is based on the previously mentioned mode decomposition and the spectrally resolved detection associated to a demodulation procedure introduced in this section. Because the acquisition is composed of many electronic components, relating the signal measured to physical quantities is not straightforward. Hence, we also present a normalization procedure to compare the noise to the shot noise as it is directly accessible by the homodyne detection. This normalization allows to remove the influence of the electronic acquisition chain from our measurements.

4.3.1 Measuring the noise spectrum: the sideband picture

In this work we are interested in noises affecting the frequency range from a hundred kilohertz to a few megahertz. As a matter of fact, the dynamics at frequencies lower than a hundred kilohertz, dominated by the environmental perturbations, such as temperature or air fluctuations, is not accessible with the current setup due to the bandwidth of the detectors and the filtering cavity. We focus our investigation on noises intrinsic to the laser, arising e.g. from the pump laser. Moreover we want to access the lowest noise level, the shot noise. From previous measurements [66], the laser is expected to reach it above a few MHz. In this configuration the light emitted by the laser is close to be a coherent state which is crucial for precision measurements.

As said previously, a spectrum analyzer cannot be used in this experiment as we wish to measure the signals from the 16 photodiodes of the two detectors simultaneously. Consequently, those signals are collected on a computer via acquisition cards. For many technical reasons, a demodulation stage is used in the experiment to investigate the noise in the frequency range of interest. The first reason is the limited sampling rate of the acquisition card used, which is 1 MHz. In addition, the laser is expected to be very noisy at low frequencies due to technical noises. Thus, acquiring all the noise spectrum in a single measurement would degrade the resolution of the spectrum at high frequencies where the noise is much lower. Consequently, before the acquisition, the noise measured is mixed with a radio frequency (RF) reference signal, delivered by a frequency generator, whose frequency is swept. The resulting signal is then low pass filtered. From a formal point a view this procedure is equivalent to measuring noises in the sidebands of the optical carrier at a given offset frequency. In what follows we present the concept of noise sidebands. Then, the general principle of the demodulation procedure and how it is used to retrieve the power spectral density of the laser parameters is described.

4.3.1.1 Noise sidebands

To begin, let us consider two modulating signals: amplitude modulation $m(t)$, and phase modulation $p(t)$, assumed to be sinusoidal at a given frequency f_{RF}:

$$m(t) = m\cos(2\pi f_{RF} t), \qquad p(t) = p\cos(2\pi f_{RF} t), \tag{4.24}$$

where m and p are the amplitude of the modulations, which are usually the quantities that need to be extracted. In the case of the experiment, they correspond to the strength of the amplitude and the phase noise at the frequency f_{RF}.
Those modulations are applied to the electric field leading to an amplitude modulated field, $E^{(+)}_{AM}(t)$, and a phase modulated one, $E^{(+)}_{PM}(t)$. Hence, the modulated fields can be written:

$$\begin{aligned} E^{(+)}_{AM}(t) &= \mathcal{E}_0 a(t)(1+m(t))e^{-i\omega_0 t}, && (4.25)\\ E^{(+)}_{PM}(t) &= \mathcal{E}_0 a(t)e^{ip(t)}e^{-i\omega_0 t}, && (4.26)\end{aligned}$$

By taking the Fourier transform of the expression (4.25), the amplitude modulation is given in the frequency domain by

$$E^{(+)}_{AM}(\Omega) = \mathcal{E}_0\left[\tilde{a}(\Omega) + \frac{m}{2}\tilde{a}(\Omega+f_{RF}) + \frac{m}{2}\tilde{a}(\Omega-f_{RF})\right]. \tag{4.27}$$

The same treatment can be done for the phase fluctuations. Assuming small fluctuations we can write: $E^{(+)}_{PM}(t) \simeq \mathcal{E}_0 a(t)(1+ip(t))e^{-i\omega_0 t}$. Consequently, the phase modulation is given in the frequency domain by

$$E^{(+)}_{PM}(\Omega) = \mathcal{E}_0\left[\tilde{a}(\Omega) + \frac{p}{2}\tilde{a}(\Omega+f_{RF}) + \frac{p}{2}\tilde{a}(\Omega-f_{RF})\right] \tag{4.28}$$

It can be seen that the modulations create two sidebands $\Omega \pm f_{RF}$ at offset frequencies $\pm f_{RF}$ from the central frequency. Those sideband amplitudes are driven by the modulation amplitudes m and p. In the framework of this experiment, as those modulations are assumed to be noise, those sidebands are called noise sidebands.

4.3.1.2 Demodulation procedure

In the previous section, we saw that amplitude and phase fluctuations create sidebands in the electric field. Ultimately, those fluctuations lead to fluctuations of the field quadratures, as described in section 3.3. Those quadratures are retrieved from the homodyne signal according to (4.21) and (4.23). Consequently, to access those sidebands, and thus the modulation amplitudes, a demodulation is applied to the homodyne signal. In this section, we briefly describe this procedure.

To illustrate the demodulation, we consider the signal corresponding to the sum of the photo-currents in the pixel basis, $i_{+,j}$ for the pixel j of the multipixel detection. The fluctuating photo-current can be written

$$i_{+,j}(t_n) = i_{+,j} + \delta i_{+,j}(t_n), \tag{4.29}$$

where, $i_{+,j}$ is the mean value of the photo-current and $\delta i_{+,j}(t_n)$ its fluctuations coming, e.g. from amplitude or phase modulations as defined in equations (4.25) and (4.26). t_n represents the fluctuations of the quadratures at the time scale of the noises under study, thus much slower than the timescale of the pulse duration. For clarity, only the fluctuating part of the signal is kept, which according to equation (4.21) is given by $\delta i_{+,j}(t_n) = \alpha_{s,j}\delta x_{s,j}(t_n)$, where $\alpha_{s,j} = \sqrt{N_{s,j}}$ is the number of photons in the signal arm for the pixel number j.

In order to retrieve the amplitude of the fluctuations at a frequency f_{RF}, the signal $\delta i_{+,j}(t_n)$ is mixed with a reference signal $s(t_n) = \cos(2\pi f_{RF} t_n)$, delivered by a frequency generator, so that

$$\begin{aligned}
\delta I_{+,j}(t_n) &= \delta i_{+,j}(t_n)s(t_n) = \alpha_{s,j}\delta x_{s,j}(t_n)\cos(2\pi f_{RF} t_n) \\
&\propto \alpha_{s,j}\left[\int_{\mathbb{R}} \delta x_{s,j}(f) e^{-2\pi i (f-f_{RF})t_n}\,\mathrm{d}f + \int_{\mathbb{R}} \delta x_{s,j}(f) e^{-2\pi i (f+f_{RF})t_n}\,\mathrm{d}f\right] \\
&\propto \alpha_{s,j}\left[\int_{\mathbb{R}} \delta x_{s,j}(f+f_{RF}) e^{-2\pi i f t_n}\,\mathrm{d}f + \int_{\mathbb{R}} \delta x_{s,j}(f-f_{RF}) e^{-2\pi i f t_n}\,\mathrm{d}f\right].
\end{aligned} \tag{4.30}$$

This signal is low pass filtered using a filter whose transfer function is $h(f)$. This transfer function is defined such that it is null for frequencies above the bandwidth of the filter Δf. Hence, the demodulated and filtered signal $\delta I^{LP}_{+,j}(t_n)$ can be written

$$\delta I^{LP}_{+,j}(t_n) \propto \alpha_{s,j}\left[\int_{-\Delta f}^{+\Delta f} h(f)\delta x_{s,j}(f+f_{RF}) e^{-2\pi i f t_n}\,\mathrm{d}f + \int_{-\Delta f}^{+\Delta f} h(f)\delta x_{s,j}(f-f_{RF}) e^{-2\pi i f t_n}\,\mathrm{d}f\right]. \tag{4.31}$$

If the filter is narrow enough compared to the acquisition rate, $\delta x_{s,j}(f)$ can be considered constant over its frequency band Δf. Hence, the signal (4.31) allows to retrieve the component of $\delta x_{s,j}(f)$ at the frequency f_{RF} according to

$$\delta I_{+,j}^{LP}(t_n) \simeq \alpha_{s,j}\left[\delta x_{s,j}(f_{RF})\int_{-\Delta f}^{+\Delta f} h(f)e^{-2\pi i f t_n}\,\mathrm{d}f + \delta x_{s,j}(-f_{RF})\int_{-\Delta f}^{+\Delta f} h(f)e^{-2\pi i f t_n}\,\mathrm{d}f\right]. \tag{4.32}$$

The same procedure can be applied to the differential photo-current fluctuations given by equation (4.23). This demodulation recovers the strength of a quadrature at an offset frequency set by the signal generator in a bandwidth fixed by the low pass filter of the demodulation stage. Thus, it can be used to measure the sidebands introduced in the previous paragraph. Note that the integral terms in equation (4.32) depend on the shape of the filter. To simplify the calculations, in the experiment the filter is assumed to be a step function of width Δf.

4.3.1.3 Demodulated covariance matrices and noise spectrum

Demodulated covariance matrices: To characterize each frequency channel, the 16 signals from the two detectors AC channels are demodulated and measured simultaneously via acquisition cards connected to a computer. Such simultaneous measurement allows the investigation of the noise in each spectral band as well as their correlations at a given frequency f_{RF} fixed by the frequency generator in the demodulation stage. To this end, the covariance matrix, as introduced in section 1.3.4, at the offset frequency f_{RF}, noted $\Gamma_{x,p}(f_{RF})$, is calculated. We first restrict our analysis to the amplitude and phase covariance matrices. The correlations between amplitude and phase will be studied in the next chapter. From the demodulated quadratures in the pixel basis, we define the spectral covariance matrices in amplitude and in phase according to

$$[\Gamma_x(f_{RF})]_{j,k} = \langle \delta x_j(t_n)\delta x_k(t_n)\rangle_{[f_{RF}:f_{RF}+\Delta f]}, \tag{4.33a}$$

$$[\Gamma_p(f_{RF})]_{j,k} = \langle \delta p_j(t_n)\delta p_k(t_n)\rangle_{[f_{RF}:f_{RF}+\Delta f]}, \tag{4.33b}$$

where $\langle\cdot\rangle_{[f_{RF}:f_{RF}+\Delta f]}$ corresponds to the average over the measurements of the demodulated quadratures at the offset frequency f_{RF} in the frequency band Δf described in the previous section.

The diagonal elements of those covariance matrices are the spectrally-resolved variances, meaning the noise in amplitude and in phase in each spectral band. The off-diagonal elements give the correlations between the spectral bands.

Laser parameters noise spectra: The noise on each mode will later be extracted from those matrices by projection on the detection modes introduced in section 4.1.2. Consequently, the variance of the laser parameters, e.g. the one of the repetition rate

$\mathrm{Var}\left[\tau_r(t_n)\right] = \langle|\delta\tau_r(t_n)|^2\rangle_{[f_{RF}:f_{RF}+\Delta f]}$, at the frequency f_{Rf} in the spectral band Δf, can be retrieved from the covariance matrices (4.33). Using the relation derived in section 1.4.1, the PSD can be related to the variance of a signal in a spectral bandwidth Δf according to

$$S_{\tau_r}(f_{RF}) = \frac{\langle|\delta\tau_r(t_n)|^2\rangle_{[f_{RF}:f_{RF}+\Delta f]}}{\Delta f}. \tag{4.34}$$

Therefore, sweeping the frequency of the RF signal allows to retrieve the PSD of the fluctuating parameters of the laser. This procedure is implemented in this experiment to measure the dynamics of the laser between 200 kHz and 4 MHz. Note that we make the assumption that measuring the covariance matrix is enough to recover all the information on the dynamics. This is true when the noises under study are Gaussian, which is a reasonable assumption in our experiment.

4.3.2 Normalization of the measurements

As seen in the previous parts, the acquisition channel is composed of many electronic components. They are used for the amplification as well as the demodulation. Thus, relating the signal measured to a physical quantity is not straightforward. To circumvent this issue, we normalize all our measurements to the shot noise. All the quantities are then given in units of shot noise (noise relative to shot noise, NRSN), which is the standard quantum limit in sensitivity for amplitude and phase noise as seen in section 1.4.2. The shot noise is a white and uncorrelated noise corresponding to the level of noise associated to a coherent state. Therefore, the level of noise displayed must be understood as an excess of noise compared to a coherent state of same mean power.

Amplitude normalization: According to equation (4.21) and taking into account the dark noise coming from the electronics, as well as a pixel dependent gain, the sum of the photo-currents from the pixels j of both detectors can be expressed as

$$\delta i_{+,j} = g_j \delta x_{s,j} + d_j \tag{4.35}$$

Where g_j is a variable gain, d_j the dark noise. Taking the covariance of the measured photo-current, assuming no correlations between the signal and the dark noise, leads to

$$\mathrm{Cov}\left[\delta i_+\right]_{j,k} = g_j g_k \mathrm{cov}\left[\delta x_s\right]_{j,k} + \mathrm{cov}\left[d\right]_{j,k} \tag{4.36}$$

To determine the gain factor, a shot noise measurement is taken, using the procedure described in section 4.2.3.1, and the variance of the signal is calculated. In this configuration, the variance of the quadrature is equal to one, i.e $\mathrm{Var}\left[\delta x_s\right]_j^{shot} = 1$. Thus, g_j is given by

$$g_j = \sqrt{\mathrm{Var}\left[\delta i_+\right]_j^{shot} - \mathrm{Var}\left[d\right]_j} \tag{4.37}$$

Finally, the amplitude quadrature is given by

$$\mathrm{Cov}\left[\delta x_s\right]_{j,k} = \frac{\mathrm{Cov}\left[\delta i_+\right]_{j,k} - \mathrm{Cov}\left[d\right]_{j,k}}{g_j g_k} \tag{4.38}$$

With this normalization, all the quantities are expressed in units of shot noise. We expect the covariance matrices to display only diagonal elements equal to one when the laser is shot noise limited.

Phase normalization: The normalization is slightly more complicated for the phase quadrature. As seen in equation (4.23), the phase fluctuations are measured via the difference of the photo-currents from pixel j of both detectors: $\delta i_{-,j} \propto \alpha_{s,j}\alpha_{ref,j}\delta\varphi_{s,j}$. This signal is proportional to the number of photons in the reference field, which is weaker than the signal ($\frac{\alpha_s^2}{\alpha_{ref}^2} \simeq 50$). Consequently, the phase fluctuations measured $\delta p_{mes,j}$, are the signal fluctuations for a reduced number of photons which can be modeled by adding losses. Those losses can easily be modeled by a beam-splitter where one input is the signal and the other one the vacuum. This BS would have a reflectivity $r_j = \frac{\alpha_{ref,j}}{\alpha_{s,j}}$ and a transmission $t_j = \sqrt{1 - \frac{\alpha_{ref,j}^2}{\alpha_{s,j}^2}}$. Thus, the measured phase fluctuations and signal ones are related by

$$\delta p_{mes,j} = \frac{\alpha_{ref,j}}{\alpha_{s,j}}\delta p_{s,j} + \sqrt{1 - \frac{\alpha_{ref,j}^2}{\alpha_{s,j}^2}}\delta p_{v,j} = r_j \delta p_{s,j} + t_j \delta p_{v,j} \tag{4.39}$$

Where δp_v are the vacuum fluctuations.
As previously, the photo-current fluctuations are related to the phase ones by

$$\delta i_{-,j} = g_j \delta p_{mes,j} + d_j \tag{4.40}$$

Where here again, g_j is a variable gain and d_j the dark noise. They are not necessarily the same as the ones of the amplitude fluctuations but the same notation is used for simplicity.
Using the expression (4.39) for δp_{mes}, the photo-current fluctuations can be written as

$$\delta i_{-,j} = g_j r_j \delta p_{s,j} + g_j t_j \delta p_{v,j} + d_j \tag{4.41}$$

As none of those contributions are correlated, the covariance is given by

$$\mathrm{Cov}\left[\delta i_-\right]_{j,k} = g_j g_k r_j r_k \mathrm{Cov}\left[\delta p_s\right]_{j,k} + g_j g_k t_j t_k \mathrm{Cov}\left[\delta p_v\right]_{j,k} + \mathrm{Cov}\left[d\right]_{j,k} \tag{4.42}$$

Once again, to determine the gain factor, the variance of the signal is measured for the shot noise so that $\mathrm{var}[\delta p_s]_j^{shot} = 1$. Furthermore, $\mathrm{Var}[\delta p_v]_j = 1$, as there is no correlations in vacuum. Finally, knowing that $r_j^2 + t_j^2 = 1$, the same equation as (4.37) is found for the gain:

$$g_j = \sqrt{\mathrm{Var}\left[\delta i_-\right]_j^{shot} - \mathrm{Var}\left[d\right]_j} \tag{4.43}$$

Eventually, the covariance matrix for the signal phase fluctuations is given according to

$$\mathrm{Cov}\left[\delta p_s\right]_{j,k} = \frac{\mathrm{Cov}\left[\delta i_-\right]_{j,k} - \mathrm{Cov}\left[d\right]_{j,k}}{g_j g_k r_j r_k} - \frac{t_j t_k}{r_j r_k} Id \tag{4.44}$$

Where Id is the identity matrix. As a matter of fact, the covariance of the vacuum fluctuations is the identity matrix because no correlations exist between the different spectral bands.

The consequence of the losses is a slightly reduced sensitivity of the phase measurement. Nonetheless, this normalization will still be convenient in the next section to relate our measurements to physical quantities.

4.4 Results

We present now the results obtained by investigating the dynamics of a Titanium-Sapphire based femtosecond oscillator from Femtolasers company. This laser delivers 22 fs FWHM pulses at a repetition rate of 156 MHz, resulting in a 40 nm FWHM wide spectrum centered at 795 nm. The average power is of the order of 1 W. This laser is pumped by a 5W Finesse Pure CEP pump laser at 532 nm from Laser Quantum.

4.4.1 Covariance matrices

As discussed along this chapter, the reconstruction of the covariance matrices from the data is done on a computer from the 16 photo-current signals (8 for each detector). The amplitude fluctuations are retrieved by taking the sum of the photo-currents pixel by pixel and the phase fluctuations by taking the difference pixel by pixel. The covariance matrices are measured at offset frequencies from 200 kHz to 4 MHz by sweeping the frequency of the demodulating signal. We note $\Gamma_{x,p}(f)$ the amplitude and phase covariance matrices calculated at the offset frequency f. An example of matrices acquired is shown in Figure 4.10. Figures 4.10*a* and 4.10*b* display the covariance matrices for the amplitude and phase fluctuations, respectively, for an offset frequency of 500 kHz. The insets display the same matrices for an offset of 4 MHz. As expected, the amplitude covariance matrix is purely diagonal at 4 MHz, with elements equals to one. It implies that the laser is indeed shot noise limited at this frequency. On the other hand, the amplitude and phase covariance matrices at 500 kHz display correlations. This is a signature of the classical noise affecting the laser dynamics. Note that the phase matrix at 4 MHz is not purely diagonal as it is the case for the amplitude one. This is the

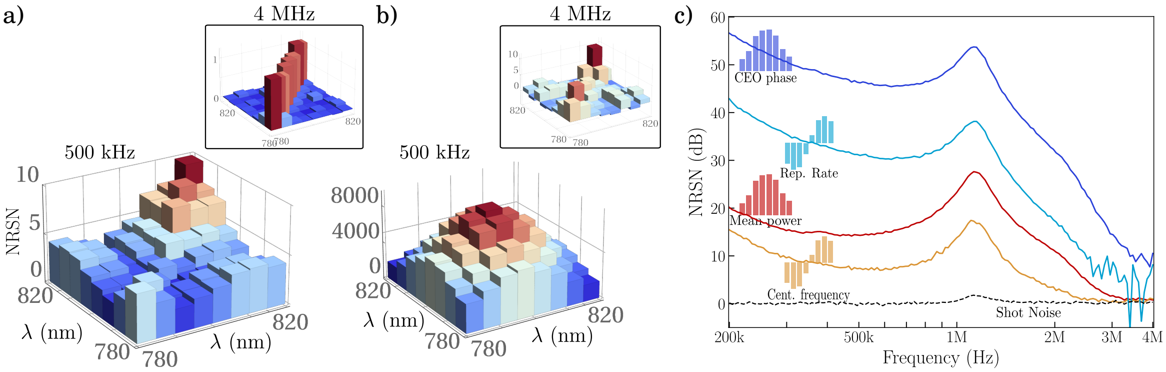

Figure 4.10 – **Experimental covariance matrices**. a) Amplitude and b): phase covariance matrices. The matrices are measured at 500 kHz. The noise is expressed as Noise Relative to the Shot Noise (NRSN) on a linear scale. Correlations can be seen between the different spectral bands. In inset, matrices for noises at 4 MHz. At that frequency, the laser is only affected by the shot noise. c): noise on the physical parameters relative to the shot noise. Projection of the covariance matrices on the modes corresponding to the noise on the CEO, central and repetition rate frequencies as well as the mean power. The noises are expressed in dB relative to the shot noise. The shot noise is measured by blocking the reference beam and taking the difference of the photocurrents.

consequence of the limited sensitivity of the detection for the phase noise due to the losses, as discussed in section 4.3.2.

4.4.2 Noise spectra

Once the covariance matrices measured, the noise on each parameter can be extracted by mathematically projecting those matrices on the corresponding spectral mode defined in section 4.1.2, after pixelisation using the procedure described in section 4.2.3.2. The resulting noise spectra are given by

$$\begin{aligned}
\delta\epsilon(f) &= \left[\overrightarrow{u}^T_{amp}\cdot\Gamma_x(f)\cdot\overrightarrow{u}_{amp}\right]^{1/2}, \\
\delta\omega_0(f) &= \left[\overrightarrow{u}^T_{cent-freq}\cdot\Gamma_x(f)\cdot\overrightarrow{u}_{cent-freq}\right]^{1/2}, \\
\delta\phi_{ceo}(f) &= \left[\overrightarrow{u}^T_{ceo}\cdot\Gamma_p(f)\cdot\overrightarrow{u}_{ceo}\right]^{1/2}, \\
\delta\tau_r(f) &= \left[\overrightarrow{u}^T_{rep-rate}\cdot\Gamma_p(f)\cdot\overrightarrow{u}_{rep-rate}\right]^{1/2},
\end{aligned} \tag{4.45}$$

where $\overrightarrow{u}_{mode}$ are the pixelised detection modes.
Figure 4.10*c* represents those fluctuations in dB relative to the shot noise as a function of

the offset frequency, thus corresponding to the spectrum of the noise of each parameter. It can be seen that the dominant noises in this frequency range are the phase ones and mainly the noise on the CEO phase. The laser reaches the shot noise level around 3 MHz meaning that technical noises are no longer affecting the laser. The peak around 1 MHz corresponds to the relaxation oscillations of the laser. One can notice a discrepancy with respect to the shot noise at high frequency for the phase noises even though the phase noise is expected to reach the shot noise level at high frequencies. It is again the consequence of the limited sensitivity of the measurement, as explained before.

To further investigate the dynamics of the laser, the noise spectra represented in Figure 4.10*c* can be converted into physical units. From equations (4.12, 4.13) and from the expressions of the noise relative to the shot noise (4.45), using the expression of the PSD (4.34), we obtain the following expressions for the power spectral densities of the Relative Intensity Noise ($RIN(f)$), the central frequency noise ($S_{\omega_0}(f)$), the CEO frequency noise ($S_{f_{CEO}}(f)$) and the timing phase noise ($S_{\phi_t}(f)$), with $\phi_t(f) = 2\pi f_r \delta\tau_r(f)$, together with their units:

$$\begin{aligned}
RIN(f) &= \left(\frac{\delta\epsilon(f)}{\sqrt{N_0}}\right)^2 T_m \quad \left[\mathrm{Hz}^{-1}\right], \\
S_{\omega_0}(f) &= \left(\frac{\Delta\omega}{\sqrt{N_0}}\delta\omega_0(f)\right)^2 T_m \quad \left[\mathrm{rad}^2.\mathrm{s}^{-2}/\mathrm{Hz}\right], \\
S_{f_{CEO}}(f) &= \left(\frac{f_r}{4\pi\sqrt{N_0}}\delta\phi_{ceo}(f)\right)^2 T_m \quad \left[\mathrm{Hz}^2/\mathrm{Hz}\right], \\
S_{\phi_t}(f) &= \left(\frac{\pi f_r}{\Delta\omega\sqrt{N_0}}\delta\tau_r(f)\right)^2 T_m \quad \left[\mathrm{rad}^2/\mathrm{Hz}\right],
\end{aligned} \tag{4.46}$$

where N_0 corresponds to the number of photons hitting the detector during the acquisition duration. It is given by $N_0 = PT_m/\hbar\omega_0$ where P is the optical power before the BS of the homodyne detection. Experimentally, the power sent to the detectors is $P = 11$ mW. However, to include the losses, mainly due to the pixels left undetected between each detected one, we take half of this power so that $P = 5.5$ mW. $T_m = 1/BW$ is the acquisition time with BW the bandwidth of the low-pass filter used in the detection chain after the demodulation ($BW = 10$ kHz). The spectra obtained are reproduced in Figure 4.11. As a comparison, the timing phase noise and the RIN of a mode-locked laser have been determined theoretically in [61] where similar noise levels have been found. Those spectra offer a quantitative measurement of the noise affecting the OFC, derived from a single measurement.

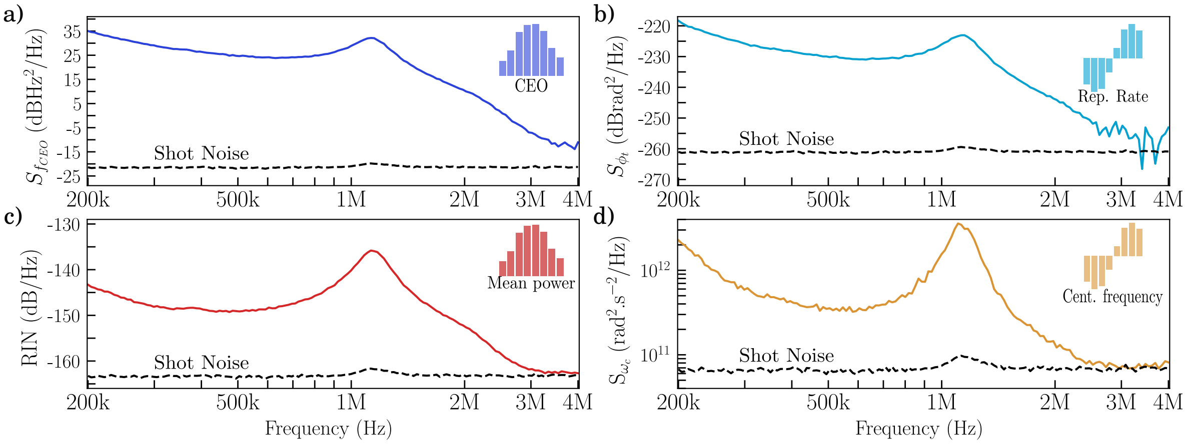

Figure 4.11 – **Noise in physical units** a) CEO frequency noise, b) timing jitter noise, c) mean power noise and d) spectrum center frequency noise. The spectral mode corresponding to each quantity is reproduced in each plot. The shot noise is plotted as a dashed black line.

4.4.3 RIN of the laser

To certify that our measurements allow to properly capture the dynamics of the laser, the RIN of the laser can be measured with a different setup. Indeed, the RIN is the easiest quantity to measure as a simple photodiode is sufficient. The other noises and specifically the CEO phase noise will be investigated in details in the next chapter.

The optical power of the laser can be described by its mean value $\overline{P}$ and its fluctuations $\delta P(t_n)$ according to $P(t_n) = \overline{P} + \delta P(t_n)$. The power spectral density of the RIN of the laser is defined by

$$RIN(f) = \frac{2}{\overline{P}^2} \int_{-\infty}^{+\infty} \langle \delta P(t_n) \delta P(t_n - \tau) \rangle e^{2i\pi f \tau} \mathrm{d}\tau \quad \left[\mathrm{Hz}^{-1}\right]. \tag{4.47}$$

To measure the RIN, a photodiode is connected to a spectrum analyzer. This photodiode is illuminated with 6 mW from the laser beam. The spectrum analyzer measurement, $S_{noise}(f)$, is expressed in dBm, corresponding to the level of electric power related to 1 mW. In order to translate this measurement into the RIN of the laser, we first express the noise in W/Hz by applying the transformation

$$P_{noise}(f) = \frac{1}{RBW} \left[10^{(S_{noise}(f)-30)/10} - 10^{(S_{dark}(f)-30)/10}\right] \quad [\mathrm{W/Hz}], \tag{4.48}$$

where RBW is the resolution bandwidth of the spectrum analyzer. $S_{dark}(f)$ corresponds to the electronic noise of the spectrum analyzer and the photodiode, measured when no light is sent to the detector. The expression above corresponds to the electric[2] power spectrum. This quantity is converted in optical power according to

$$P_{opt}(f) = \frac{\sqrt{P_{noise}(f) R_{res}}}{\mathcal{R} G} \quad \left[\mathrm{W}/\sqrt{\mathrm{Hz}}\right], \tag{4.49}$$

where R_{res} is the impedance of the spectrum analyzer (usually 50 Ω), G is the gain in V/A of the photodiode and $\mathcal{R}$ its responsivity in A/W. Finally, the RIN is given by

$$RIN(f) = 20 \log \left(\frac{P_{opt}(f)}{\overline{P}} \right) \quad [\mathrm{dB/Hz}], \tag{4.50}$$

where $\overline{P}$ is the mean optical power of the laser beam. The RIN of the laser measured using this procedure with 6 mW of optical power is reproduced in Figure 4.12. As a reference, it can be compared to the theoretical RIN corresponding to the shot noise given by

$$RIN_{SN} = \frac{2\hbar\omega}{\overline{P}} \quad \left[\mathrm{Hz}^{-1}\right]. \tag{4.51}$$

This RIN of an optical field limited by the shot noise is represented in Figure 4.12 in dashed black. It can be seen that the RIN of the laser reaches the shot noise around 3 MHz as identified in the previous section.

To compare this result to the measurement realized using the multipixel detection, we reproduce the RIN from Figure 4.11c in Figure 4.12, together with the shot noise measured experimentally. It can be seen that the level of noise measured with the multipixel is consistent with the one measured with the simple photodiode. This is a proof of the accuracy of our experimental setup. Still, it can be noted that the two RINs are not perfectly overlapping and that a small discrepancy is present between the two shot noises. The main reason is that the measurements were taken at two different times (in fact several years apart). Therefore, the optical powers were not exactly the same. Furthermore, the RIN measured with the photodiode corresponds to a period when our laser was working quite poorly, which explains the huge peak of relaxation oscillations.

Summary

We characterized the dynamics of an OFC using a modal approach. Each parameter of the laser can be associated to a spectral detection mode. The noise on each parameter can be recovered by projecting the covariance matrices, measured with a spectrally resolved homodyne detection, on the detection modes. To test the accuracy of the measurement, we measured the RIN of the laser with an independent experimental setup. Both measurements are in agreement.

---

[2] By electric we mean voltage measured by the spectrum analyzer.

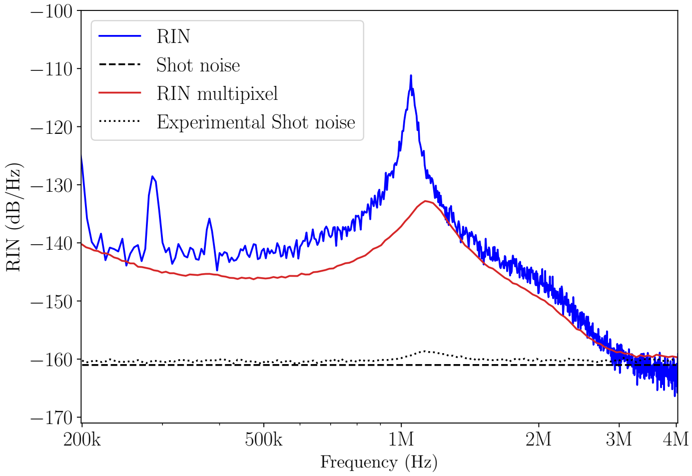

Figure 4.12 – **Comparison of the RIN.** In blue the RIN measured with a single photodiode. In red the one measured with the multipixel detection. In dashed black the theoretical RIN corresponding to the shot noise and in dotted black the one measured with the multipixel detection.

Chapter 5

Harnessing noises correlations

Contents

5.1 Amplitude-phases correlation matrices 101
5.2 Fixed point model 102
    5.2.1 General idea of the model 103
    5.2.2 Fixed point for laser pump noise 104
5.3 Unveiling the dynamics from XP correlations 109
    5.3.1 Singular value decomposition of the correlation matrix 110
    5.3.2 Intensity related dynamics: Model from J. Ye 111

In the previous chapter we saw how with a single setup it is possible to fully characterize the dynamics of a frequency comb. It is made possible by the measurement of the amplitude and phase covariance matrices and by projecting them on the spectral noise modes defined in section 4.1. One advantage of the simultaneous measurement of the noise on the four main parameters of the laser is the possibility to investigate their correlations. In this chapter we harness those correlations to gain insight on the dynamics of the laser and on the noise sources.

5.1 Amplitude-phases correlation matrices

As seen in section 4.2, the signals of the 16 photodiodes (8 for each detector) are collected on a computer to process the amplitude and phase covariance matrices simultaneously by taking the sum and difference of the photocurrents pixel by pixel. As a consequence, the correlations between amplitude and phase can also be investigated. Indeed in addition to Γ_x and Γ_p, the amplitude-phase correlation matrix can be calculated. It is given by

$$[\Gamma_{xp}(f)]_{ij} = \langle \delta x_i(t_n) \delta p_j(t_n) \rangle_{[f:f+\Delta f]}, \tag{5.1}$$

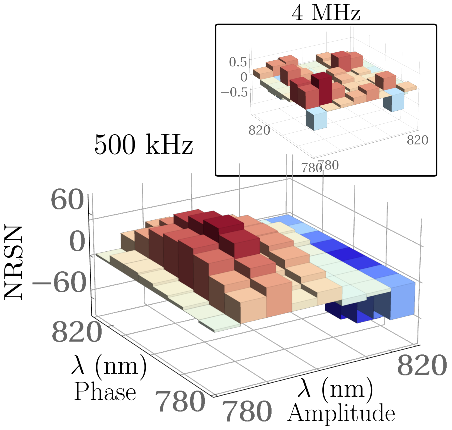

Figure 5.1 – **Phase and amplitude correlations:** Correlation matrix between amplitude and phase at an offset frequency of 500 kHz. A sign reversal indicates the presence of anti-correlations in the spectrum. In inset the same correlation matrix but at 4 MHz where the correlations vanish.

where f corresponds to the offset frequency and Δf the width of the filter given by the demodulation stage as explained in section 4.3.1.2.
An example of an amplitude-phase correlation matrix is represented in Figure 5.1 for an offset frequency of 500 kHz. As previously, the inset represents the same matrix but for an offset frequency of 4 MHz. It can be seen that no clear correlations are displayed at 4 MHz. This is indeed expected. We saw previously that the laser is shot noise limited beyond 3 MHz. Therefore, there is no correlations between the spectral components nor between amplitude and phase above that frequency. On the other hand, the matrix at 500 kHz displays a distinct structure. Along the phase axis the variation of the correlations is close to a Gaussian shape centered on the central wavelength of the laser. In contrast, the correlations along the amplitude axis present a sign reversal close to the center of the spectrum. It suggests that there are anti-correlations between the shorter-wavelength and the longer-wavelength part of the spectrum.

The possibility to access correlations, and especially amplitude-phase correlations, is a powerful tool to investigate the dynamics of optical frequency combs. Indeed, intensity related dynamics is one of the fundamental mechanisms that governs mode-locking. Consequently, those correlations can be exploited to find the noise sources and the coupling mechanisms. Thus, in the next sections we try to understand the amplitude-phase correlations and their origins, starting by the sign reversal in the middle of the correlation matrix.

5.2 Fixed point model

The first idea that came to our mind looking at the sign reversal is the presence of a fixed point close to the center of the spectrum. The idea is that there is a single frequency (or wavelength) in the spectrum which is not affected by the noise. More

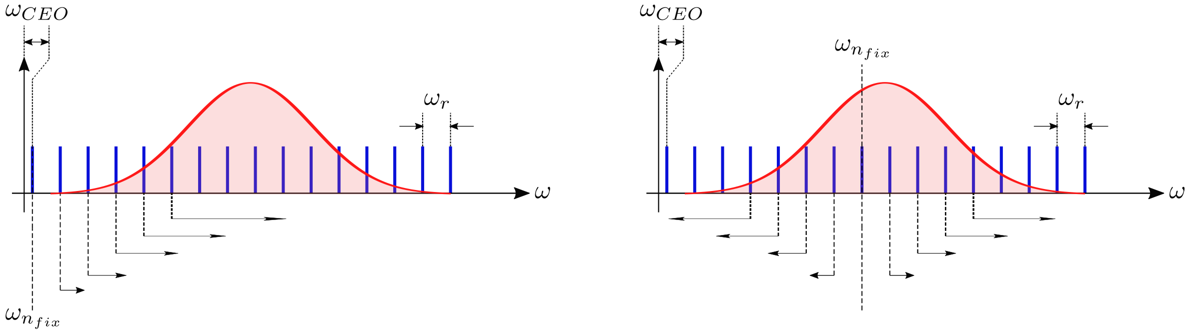

Figure 5.2 – **Fixed point model:** Illustration of the fixed point model. In the spectrum one frequency is fixed and does not fluctuate under a given perturbation. All the other lines will breath around that frequency with increasing strength. Left is the representation for a fixed point close to the zero frequency which is the case for cavity length fluctuations for example. Right is the representation for a fixed point close to the center of the spectrum. This is the case for fluctuations of pump power.

precisely, the different noise contributions cancel out for that particular frequency. All the other frequency lines will breath away from this point with increasing strength as we go farther from it [73, 74, 49]. This general concept is schematized in Figure 5.2. In the following sections we briefly review the model associated to this phenomenon and present the measurements performed to determine the fixed point for our laser.

5.2.1 General idea of the model

The fixed point model, or elastic tape model, is a phenomenological model describing how a noise source affects each frequency line of the comb. Starting from the frequency of one tooth of the comb

$$\omega_n = \omega_{CEO} + n\omega_r, \tag{5.2}$$

where ω_{CEO} is the CEO frequency and ω_r is the repetition rate, we assume that a noise source s, which can be pump intensity or cavity length fluctuations for example, induces CEO and repetition rate fluctuations. Thus, the resulting dynamics of the n^{th} tooth reads

$$\frac{\partial\omega_n}{\partial s} = \frac{\partial\omega_{CEO}}{\partial s} + n\frac{\partial\omega_r}{\partial s}. \tag{5.3}$$

We call fixed point the frequency line for which the fluctuations vanish i.e.

$$\frac{\partial\omega_{n_{fix}}}{\partial s} = \frac{\partial\omega_{CEO}}{\partial s} + n_{fix}\frac{\partial\omega_r}{\partial s} = 0 \quad \Rightarrow \quad n_{fix} = -\frac{\frac{\partial\omega_{CEO}}{\partial s}}{\frac{\partial\omega_r}{\partial s}}. \tag{5.4}$$

Consequently, by measuring the CEO frequency and the repetition rate fluctuations subjected to a perturbation, it is possible to find the line in the spectrum for which they both cancel out. It is then possible to extrapolate from this point to get the power spectral density of a given spectral line $S_\omega(f)$ according to [49]

$$S_\omega(f) \simeq \left(\omega - \omega_{n_{fix}}\right)^2 S_{\omega_r}(f), \tag{5.5}$$

where $S_{\omega_r}(f)$ is the power spectral density of the noise on the repetition rate induced by the noise sources.

The fixed points for various noise sources can be found in the literature. For example, the fixed points under cavity length fluctuations and pump power fluctuations have been measured in [49, 75]. The fixed point for cavity length fluctuations was found to be a few THz, i.e. close to the zero frequency of the spectrum. This can easily be explained by the fact that the cavity fluctuations have almost no impact on the CEO frequency, therefore the fixed point is close to this frequency. On the other hand, the fixed point for pump fluctuations was found to be close to the center of the spectrum of the laser, around 200 THz [49, 76, 75]. In the next section, an experiment to measure the fixed point is presented. This fixed point will be calculated for pump power fluctuations only. The reason for this choice will be explained in the next section. If the fixed point is found to be close to the center of the spectrum it would explain the sign reversal in the correlation matrix displayed in Figure 5.1.

5.2.2 Fixed point for laser pump noise

To determine the fixed point induced by the pump laser noise, the most straightforward approach is to apply a modulation at a given frequency f_{mod} to the pump laser intensity. This is usually achieved by modulating the pump laser current with a frequency generator. The fixed point is then determined by recovering the fluctuations of the CEO frequency and the repetition rate induced by this modulation, and applying the formula (5.4).

This technique was used in the aforementioned studies, and in particular in [66]. In this work, the fixed point for pump fluctuations for the Titanium Sapphire laser under study has been measured. It was found to be at 233 THz i.e. on the IR side of the spectrum. To perform this measurement, a slow modulation, typically 0.1 to 1 Hz was applied to the pump laser. The resulting fluctuations of the CEO and repetition rate frequencies were subsequently measured with frequency counters to determine the fixed point. Slow modulations were used to make the measurements with affordable frequency counters. However, the amplitude-phase correlation matrices in section 5.1 are measured at frequencies ranging from 200 kHz to 4 MHz. There is no a priori reason to believe that the fixed point is frequency independent. Consequently, to explain the sign reversal in the correlation matrix represented in Figure 5.1, we need to measure it for faster modulations, around a few hundred kilohertz. Note that, at those frequencies, the only noise source is expected to be the pump laser. The thermal or mechanical fluctuations are much slower (a few hundred Hertz). It explains why we only consider the fixed point induced by pump laser fluctuations.

Measuring the CEO frequency for fast pump power modulations is not an issue. However, one technical problem arises for the repetition rate. Indeed, the repetition rate, centered at 156 MHz, varies by only a few Hz when subjected to a modulation. It is then impossible to measure this deviation of a few Hz with modulations of the order of the kilohertz. To circumvent this issue, we can try to measure a multiple of the repetition rate. However, measuring the tenth or higher harmonic is still not enough and no electronics work for even higher harmonics. Consequently, the only solution is to measure the repetition rate in the optical domain by measuring one tooth of the laser spectrum. In this configuration, according to equation (5.2), the repetition rate will be multiplied by the number of the tooth under study n. For a frequency line close to the center of the spectrum n is roughly 10^6. Thus we are brought back to measuring a deviation of a few megahertz for modulations of a hundred kilohertz which is feasible. In this section, we describe the experimental setup to measure the repetition rate in the optical domain. This technique is then used to determine the fixed point.

5.2.2.1 Repetition rate measurement in the optical domain

To measure the repetition rate in the optical domain, we use a continuous wave (CW) stabilized laser at 780 nm brought in via a fiber optical link from Saïda Guellati-Khélifa and Pierre Cladé metrology laboratory next door. This laser is mixed on a BS with the frequency comb. It is then detected with a fast photodiode to produce a beat signal between the CW laser and the closest tooth to the CW laser frequency. This setup corresponds to a heterodyne detection as presented in section 3.1. The resulting beat signal is given by

$$f_{beat} = |f_{CEO} + n_{780} f_r - f_{780}|, \tag{5.6}$$

where f_{780} is the frequency of the CW laser and n_{780} is the number of the tooth closest to the frequency of the CW laser. It is given by

$$n_{780} = \left\lfloor \frac{1}{f_r} \left(\frac{c}{780 \cdot 10^{-9}} - f_{CEO} \right) \right\rfloor , \tag{5.7}$$

where $\lfloor \cdot \rfloor$ stands for the integer part. As can be seen in equation (5.6) the beat signal still depends on the CEO frequency and the repetition rate. To decouple those quantities, the CEO frequency is first measured with the f-2f interferometer presented in section 4.2.1.1. After proper amplification and filtering, we mix the measured CEO frequency with the beat signal. The result of this mixing can be sent to a spectrum analyzer to

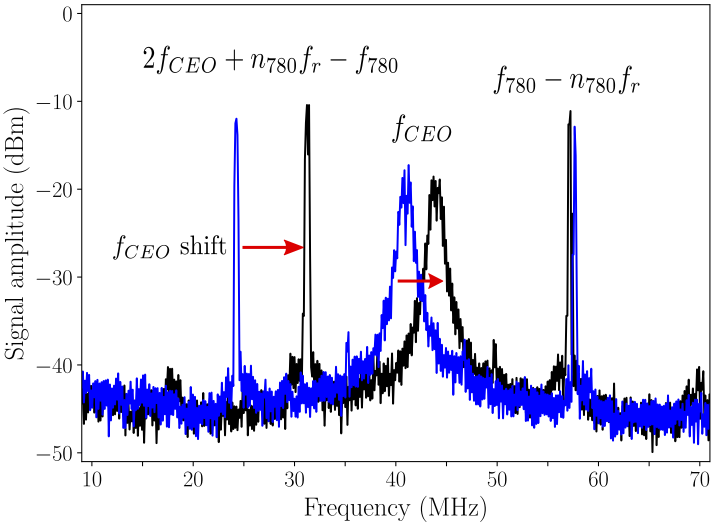

Figure 5.3 – **Spectrum of the beat signal**: Beat signal between the CW laser and the frequency comb measured at the spectrum analyzer. This signal is mixed with a RF signal at f_{CEO} to recover the components $f_{1,2,3}$. In order to identify the peaks, the CEO frequency is shifted (black curve). The unchanged peak corresponds to $f_3 = n_{780}f_r - f_{780}$.

recover the spectrum of the beat signal. A typical signal can be seen in Figure 5.3. Three peaks are present corresponding to oscillations at

$$f_1 = 2f_{CEO} + n_{780}f_r - f_{780}; \quad f_2 = f_{CEO}; \quad f_3 = n_{780}f_r - f_{780}. \tag{5.8}$$

The component f_2 can be used to measure the CEO frequency. On the other hand, the repetition rate of the comb can be recovered from f_3 since the wavelength of the CW is perfectly known. Nonetheless, it is not obvious to attribute a peak from the spectrum, to each component f_i. Hence, to identify each peak, we slightly shift the CEO frequency, as illustrated in Figure 5.3, by changing the pump power. The peak corresponding to f_3 should not be affected by the shift and can thus be identified. In Figure 5.3, f_3 corresponds to the peak on the right. Once each component identified, we have access to a measure of the CEO and the repetition rate of the laser. The fixed point can then be measured by applying a modulation on the pump laser and recording f_{CEO} and $n_{780}f_r - f_{780}$.

5.2.2.2 Fixed point measurement

To measure the fixed point, a sinusoidal modulation, of amplitude 1 Vpp and at the frequency f_{mod}, is applied directly to the pump laser current to modulate its intensity. The beat signal composed of the frequencies $f_{1,2,3}$ is recorded with an oscilloscope. Note that because the CW laser is a lot more stable than the frequency comb, measuring the fluctuations of f_3 really leads to a measurement of the fluctuations of f_r. The spectrogram of the signal is then computed using a short time Fourier transform (STFT). The STFT is calculated by computing the Fourier transform on a time window. The definition of this time window is important as it defines the resolution of the resulting spectrogram. If the time window is too small, the resolution in frequency is too coarse

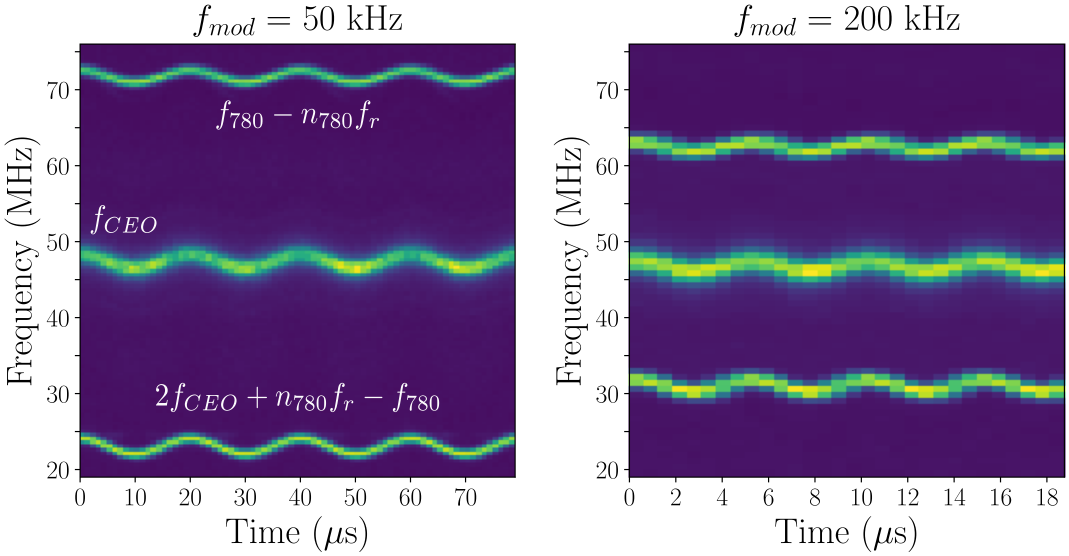

Figure 5.4 – **Averaged spectrograms of the modulated beat signal:** Left (right), averaged spectrogram of the beat signal for a modulation of the pump current at 50 kHz (200 kHz). The three components corresponding to $f_{1,2,3}$ deviates from their central frequency due to the modulation. The amplitude of the deviation allows to calculate the fixed point.

to resolve the modulation amplitude which is of the order of the megahertz. On the other hand, if the time window is too large, resolving fast oscillations, e.g. of a few hundred kilohertz, is not possible. As always, there is a trade-off between spectral and temporal resolution. To improve the signal to noise ratio, we average the spectrogram in time and keep only a restricted number of modulation periods. An example of two averaged spectrograms are shown in Figure 5.4 for modulation frequencies of 50 kHz and 200 kHz. We can clearly see the modulation of the three frequency components. This Figure illustrates the difficulties due to the trade-off for high frequency modulations. Indeed, for a modulation at 200 kHz, in order to have enough resolution in time, the spectral resolution is set to 800 kHz. On the other hand, the spectral resolution for the modulation at 50 kHz can be lowered to 500 kHz. Thus the signal is cleaner and the extraction of the information will be more accurate.

To retrieve the modulation amplitude of the repetition rate and CEO frequency, the most precise technique was found to be a 2D fit of the spectrogram around each component, assuming a Lorentzian peak with a time-varying central frequency, $f_{peak}(t)$, according to

$$\text{spectrogram}(f,t) = \frac{A}{1 + \left(\frac{f - f_{peak}(t)}{\sigma}\right)^2} \tag{5.9}$$

where A is the amplitude of the peak, σ is the full width at half maximum of the peak. In this experiment $f_{peak}(t)$ depends on time due to the modulation of the pump intensity. As the modulation is a sine function at the frequency f_{mod}, the expression of $f_{peak}(t)$ is given by

$$f_{peak}(t) = f_c + A_{mod} \sin\left(2\pi f_{mod} t\right), \tag{5.10}$$

where f_c is the frequency of the peak when no modulation is applied e.g. $f_c = f_{CEO} = 47MHz$ for the central peak; A_{mod} is the amplitude of the modulation of the peak that we want to measure.

This procedure allows to measure the response of the CEO frequency $\Delta_{f_{CEO}}(f)$ and the repetition rate $\Delta_{n_{780}f_r}(f)$ to the modulation of the pump laser current. A set of data for modulation frequencies going from 1 kHz to 500 kHz is reproduced in Figure 5.5. It can be noted that the variations are stronger for low frequency modulations than for higher frequencies. Two explanations can be considered. First, the laser cavity acts as a low pass filter for the modulation and thus tends to reduce its impact as its frequency increases. Another explanation may be related to thermal effects. When the pump laser intensity is changed, it changes the temperature of the crystal, which slightly modifies the lasing conditions. Since thermal effects occur on short time scales, those effects should be less significant at high modulation frequencies because the temperature change does not have time to take place. In any case, we can see that the modulation frequency has an impact on the dynamics of the parameter, hence the need to measure the fixed point around 500 kHz.

From the data reproduced in Figure 5.5, the fixed point can be computed according to

$$\lambda_{fix}(f) = c\left[f_{CEO} + \frac{\Delta_{f_{CEO}}(f)}{\Delta_{n_{780}f_r}(f)}\left(\frac{c}{780\cdot 10^{-9}} - f_{CEO}\right)\right]^{-1}. \tag{5.11}$$

Many data are taken to average over multiple runs. The resulting fixed point as a function of the modulation frequency is represented in Figure 5.6. One can see that the fixed point depends on the modulation frequency. This variation is stronger at low frequencies due to the variations of f_{CEO} and f_r which are diverging one away from the other as seen in Figure 5.5. The fixed point seems to stabilize after 50 kHz around 660 nm corresponding to 454 THz.

The fixed point measured at 660 nm is not in the spectrum and hence cannot explain the sign reversal seen in the correlation matrix represented in Figure 5.1. Although another explanation must be found for this sign reversal, this measurement still allowed us to accurately determine the fixed point due to pump fluctuations. In particular, we were able to study the frequency dependence of this fixed point by measuring it for

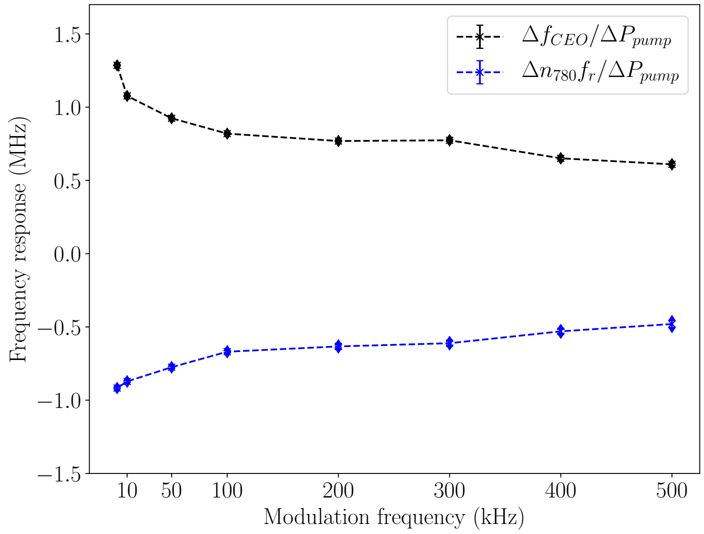

Figure 5.5 – **Frequency response of the CEO frequency $\Delta_{f_{CEO}}$ and the repetition rate $\Delta_{n_{780} f_r}$ as a function of the modulation frequency.** The fluctuations are less important at high frequencies due to the filtering of the cavity or due to thermal effects.

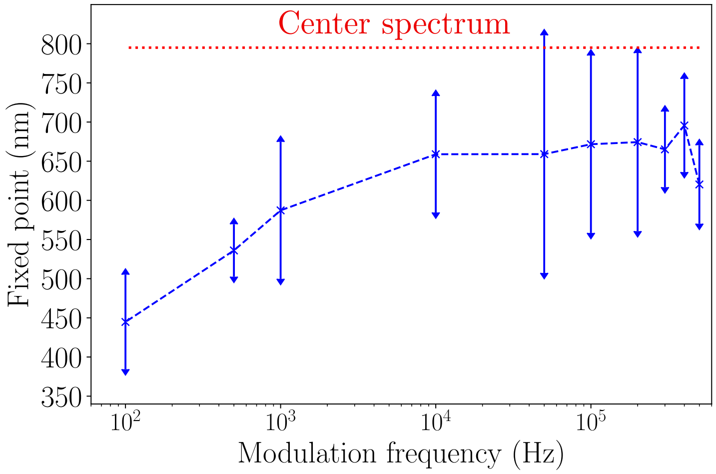

Figure 5.6 – **Fixed point as a function of the modulation frequency.** The fixed point slightly changes with the modulation frequency. Around a few hundred kHz the fixed point is found to be at 660 nm which is not in the optical spectrum.

different modulation frequencies, from 100 Hz to 500 kHz. This study shows that the fixed point is frequency dependent, which could be caused by filtering or thermal effects.

5.3 Unveiling the dynamics from XP correlations

As the fixed point model does not seem to explain the structure of the correlations, we decided to take a deeper look into their particular structure. To analyze this matrix, a singular value decomposition (SVD) is performed. The idea is to find spectral modes associated to the correlations, to connect them to a physical process.

5.3.1 Singular value decomposition of the correlation matrix

The singular value decomposition is a factorisation of a matrix, (real or complex) which generalize the eigendecomposition, to apply it to any matrix. More precisely it factorizes a matrix M, of dimension $m \times n$, into $M = U\Sigma V^{\star}$, where U and V are complex unitary matrices of dimension $m \times m$ and $n \times n$. Σ is a $m \times n$ rectangular diagonal matrix whose diagonal elements $\Sigma_{ii} = \lambda_i$ are the singular values. This decomposition is needed as the correlation matrix is the composition of two different spaces, the amplitude and the phase one. With this decomposition, the Schmidt number of the matrix can be calculated. This parameter provides information on the number of significant modes involved in the process. It is given by [77]

$$K = \left(\sum_n \lambda_n^2 \right)^2 / \sum_n \lambda_n^4. \tag{5.12}$$

This decomposition is applied to the correlation matrices for offset frequencies from 200 kHz to 4 MHz. The Schmidt number is represented in Figure 5.7a as a function of the offset frequency. It is equal to one up to 1 MHz indicating that only one pair of modes, one in phase and one in amplitude, is necessary to reconstruct the correlations. Those two modes, represented on the same Figure, are the singular modes. Before looking at those modes in details, it is interesting to note that this first quantity, the Schmidt number, already gives us information about the noise sources. As a matter of fact, because only one pair of modes is involved, we can assume that only one noise source is responsible for those correlations. As it has been shown in various papers [63, 65] it is expected to come from the fluctuations of the pump laser intensity. As said previously, the other noise sources such as thermal noise or vibrations are expected to affect the laser at lower frequencies (a few hundred Hertz). In the next section we will start from that hypothesis to derive a simple model to explain the correlations. Before doing so, let us have a closer look at the singular modes to try to extract physical meaning out of it.

A qualitative understanding of the underlying processes can be obtained through the projection of the singular modes on the detection modes introduced earlier in section 4.1.2. The projection of the amplitude singular mode on the mean power and spectrum center frequency detection modes and the projection of the phase singular mode on the CEO and repetition rate detection modes are represented in Figure 5.7b. It can be seen that mainly three modes are coupled. In phase, only the CEO detection mode is coupled to the amplitude ones. Indeed, this was expected as it is well-known that intensity fluctuations, induced by pump power fluctuations, have a huge impact on the CEO of the laser and are even used to control it [69] as it is the case in this study. In amplitude, the singular mode is a linear combination of the mean power and spectrum

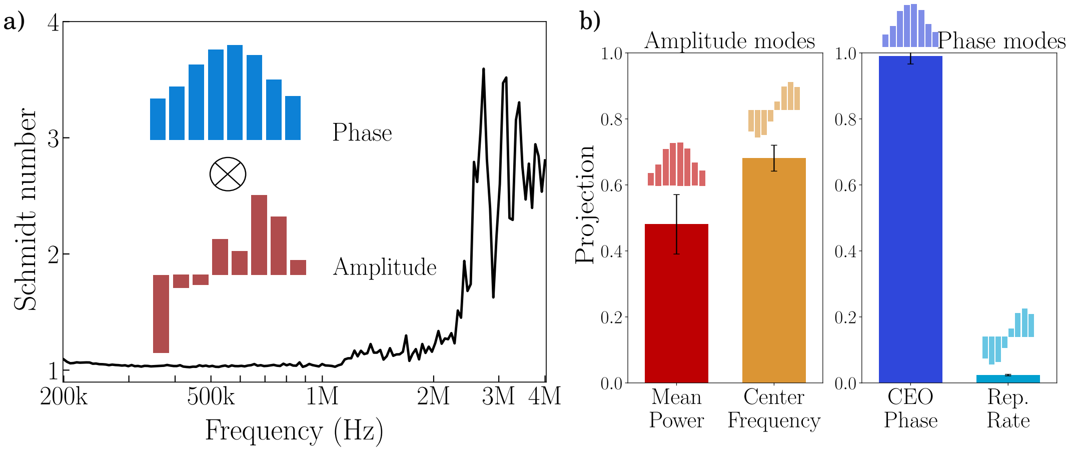

Figure 5.7 – **Phase and amplitude correlations:** a) Schmidt decomposition of the correlations matrices. The Schmidt number as a function of the offset frequency is plotted together with the amplitude and phase singular modes for the frequencies where it is equal to one. b) Projection of the amplitude and phase singular modes on the detection modes.

center frequency modes. The dominant contribution comes from the fluctuations of spectrum center frequency. Despite the fact that there is a strong coupling between the CEO and the mean power fluctuations due to the Kerr effect, this contribution seemed to be exceeded by the fluctuations of the spectrum center frequency. In the next section we investigate those correlations with a simple model describing the intensity related dynamics of the CEO fluctuations. We will see that the spectrum center frequency is indeed the bridge between pump laser fluctuations and CEO fluctuations when there is a non negligible residual group velocity dispersion inside the laser cavity [63].

5.3.2 Intensity related dynamics: Model from J. Ye

Our measurements from section 4.4 have shown that the dominant noise is the CEO frequency fluctuations. Moreover only one noise source is expected to induce correlations between amplitude and phase, as suggested by the SVD applied in the previous section. Finally, by projecting the singular modes on the detection modes, we saw that only the CEO is correlated to the amplitude fluctuations. As a consequence, following the idea developed in [63], we decided to investigate the intensity related dynamics of the CEO to explain the correlations and model the CEO noise.

5.3.2.1 Derivation of the model

In this section, only the intrinsic dynamics of the laser is considered. Consequently, all the effects described bellow take place inside the laser cavity. We start by reminding the definition of the CEO frequency. It is defined as

$$f_{CEO} = \frac{f_r}{2\pi}\Delta\phi_{CEO} = \frac{\omega_c}{2\pi}\left(1 - \frac{v_g}{v_\phi}\right), \tag{5.13}$$

where ω_c is the carrier frequency and v_g and v_ϕ the average group and phase velocities in the cavity defined by

$$\begin{aligned} \frac{c}{v_g} &= \overline{n} + \omega_c \frac{\mathrm{d}\overline{n}}{\mathrm{d}\omega}\ , & (5.14) \\ \frac{c}{v_\phi} &= \overline{n}\ . & (5.15) \end{aligned}$$

As there are many optics in the cavity, these velocities are averaged over the cavity length using the averaged refractive index over the cavity $\overline{n} = \overline{n}_0 + \overline{n}_2 I$, which also includes the Kerr effect via the non-linear refractive index $\overline{n}_2$ ($\overline{n}_0$ is the refractive index without the Kerr effect).

From equation (5.13), the intensity dependence of the CEO frequency is given by

$$\begin{aligned} \frac{\mathrm{d}f_{CEO}}{\mathrm{d}I} &= \frac{1}{2\pi}\left[\frac{\partial\omega_c}{\partial I}\left(1 - \frac{v_g}{v_\phi}\right) + \omega_c\frac{v_g}{v_\phi}\left(\frac{1}{v_\phi}\frac{\mathrm{d}v_\phi}{\mathrm{d}I} - \frac{1}{v_g}\frac{\mathrm{d}v_g}{\mathrm{d}I}\right)\right] \\ &= \frac{1}{2\pi}\left[\frac{\partial\omega_c}{\partial I}\left(1 - \frac{v_g}{v_\phi}\right) + \omega_c\frac{v_g}{v_\phi}\left(v_g\frac{\mathrm{d}}{\mathrm{d}I}\left(\frac{1}{v_g}\right) - v_\phi\frac{\mathrm{d}}{\mathrm{d}I}\left(\frac{1}{v_\phi}\right)\right)\right]. \end{aligned} \tag{5.16}$$

Before going any further, it is important to note that $\overline{n}$ depends on the intracavity intensity I, due to the Kerr effect, and on ω_c, due to the dispersion. In addition, ω_c itself also depends on I. Indeed, the central frequency can be affected by intensity fluctuations when an asymmetry between the gain and the loss profiles exists [59, 64]. In that configuration a change in the gain results in a frequency pulling effect due to a shift of the equilibrium frequency. Taking this into account, the derivative of the inverse of the group and phase velocities from equations (5.14) and (5.15) can be written

$$\begin{aligned} \frac{\mathrm{d}}{\mathrm{d}I}\left(\frac{1}{v_g}\right) &= \frac{\partial\omega_c}{\partial I}\cdot\frac{\partial}{\partial\omega}\left(\frac{1}{v_g}\right) + \frac{1}{c}\frac{\partial}{\partial I}\left(\overline{n}_0 + \overline{n}_2 I + \omega_c\frac{\mathrm{d}}{\mathrm{d}\omega}\left(\overline{n}_0 + \overline{n}_2 I\right)\right) \\ &= \frac{\partial\omega_c}{\partial I}\cdot\frac{\partial}{\partial\omega}\left(\frac{1}{v_g}\right) + \frac{1}{c}\left(\overline{n}_2 + \omega_c\frac{\mathrm{d}\overline{n}_2}{\mathrm{d}\omega}\right), \end{aligned} \tag{5.17}$$

$$\begin{aligned} \frac{\mathrm{d}}{\mathrm{d}I}\left(\frac{1}{v_\phi}\right) &= \frac{\partial\omega_c}{\partial I}\cdot\frac{\partial}{\partial\omega}\left(\frac{1}{v_\phi}\right) + \frac{1}{c}\frac{\partial}{\partial I}\left(\overline{n}_0 + \overline{n}_2 I\right) \\ &= \frac{1}{c}\frac{\partial\omega_c}{\partial I}\cdot\frac{\partial\overline{n}}{\partial\omega} + \frac{\overline{n}_2}{c}. \end{aligned} \tag{5.18}$$

Injecting equations (5.17) and (5.18) into equation (5.16) leads to

$$\begin{aligned}\frac{\mathrm{d}f_{CEO}}{\mathrm{d}I} &= \tfrac{1}{2\pi}\left[\tfrac{\partial\omega_c}{\partial I}\left[\left(1-\tfrac{v_g}{v_\phi}\right)+\omega_c\tfrac{v_g^2}{v_\phi}\mathrm{GVD}-\tfrac{\omega_c}{c}v_g\tfrac{\partial\overline{n}}{\partial\omega}\right]\right.\\ &\quad\left.+\tfrac{\omega_c v_g}{c}\left(\omega_c\tfrac{v_g}{v_\phi}\tfrac{\mathrm{d}\overline{n}_2}{\mathrm{d}\omega}-\overline{n}_2\left(1-\tfrac{v_g}{v_\phi}\right)\right)\right], \end{aligned}\tag{5.19}$$

where GVD is the average Group Velocity Dispersion inside the cavity given by GVD $= \frac{\partial}{\partial\omega}\left(\frac{1}{v_g}\right)$.

The model is derived with respect to the intra-cavity peak intensity I in the crystal, which we calculate for a Fourier transformed limited pulse (the effect of dispersion is included later). However, in practice, we measure the fluctuations of the parameters with respect to the laser mean output power P. The conversion from I to P is given by

$$\frac{\mathrm{d}I}{\mathrm{d}P}=\frac{2\times 0.88}{f_r T_{coupler}\Delta t_{pulse}\pi w^2}. \tag{5.20}$$

This quantity is determined from the parameters of the laser: $f_r = 156$ MHz, $T_{coupler} = 0.28$ the transmission of the output coupler, $\Delta t_{pulse} = 22$ fs the pulse duration and $w = 10$ μm the waist in the crystal. The factor 0.88 comes from the hyperbolic secant shape of the pulse. Given those data we find $\mathrm{d}I/\mathrm{d}P \simeq 5.8\times10^{-15}$ m^{-2}.

Using $\mathrm{d}I/\mathrm{d}P$ to get rid of the intensity in equation (5.19), the CEO frequency fluctuations can be written as

$$\begin{aligned}\delta f_{CEO} = \frac{1}{2\pi} &\left[\delta\omega_c\left(\left(1-\tfrac{v_g}{v_\phi}\right)+\omega_c\tfrac{v_g^2}{v_\phi}\mathrm{GVD}-\omega_c\tfrac{v_g}{c}\tfrac{\partial\overline{n}}{\partial\omega}\right)\right.\\ &\left.+\,\delta P\tfrac{\mathrm{d}I}{\mathrm{d}P}\tfrac{\omega_c v_g}{c}\left(\tfrac{v_g}{v_\phi}\omega_c\tfrac{\mathrm{d}\overline{n}_2}{\mathrm{d}\omega}-\overline{n}_2\left(1-\tfrac{v_g}{v_\phi}\right)\right)\right], \end{aligned}\tag{5.21}$$

From this expression, it is clear that the noise on the CEO frequency arises from the noise on the central frequency $\delta\omega_c$ and from the mean power fluctuations δP. The factor coupling the CEO frequency and the central frequency is composed of three terms. The first one comes from the dispersion in the laser, $\left(1-\frac{v_g}{v_\phi}\right)$, the second one from the group velocity dispersion, GVD, and the last one is due to the dispersion $\frac{\partial\overline{n}}{\partial\omega}$. On the other hand, the term coupling the CEO frequency to the intensity is mainly due to the Kerr effect, as expected, via $\overline{n}_2$ and its dispersion. We can now apply the formula (5.21) to our measurements to see if this simple model is sufficient to explain the main features of the noise and the correlations.

5.3.2.2 Laser parameters

To apply the model to our experiment, a few quantities need to be taken from the literature. We have $\overline{n} = 1.00116$, $\overline{n}_2 = 1.8\times10^{-23}$ m^{2}W^{-1}, $\frac{\mathrm{d}\overline{n}_0}{\mathrm{d}\omega} = 3.5\times10^{-21}$ s and $\frac{\mathrm{d}\overline{n}_2}{\mathrm{d}\omega}$

= 3×10^{-39} sm^{2}W^{-1} [63]. The last quantity needed to apply the formula is the GVD inside the cavity.

Estimation of the GVD: As constructor specifications are not available, we need to estimate the GVD from the geometry of the cavity and the properties of the laser directly at the output of the cavity. In section 2.3, we saw the effect of GVD on a pulse. In the presence of GVD, because the frequencies travel at different speeds, the pulse will be chirped. We remind that the electric field of a chirped pulse is given by

$$E^{(+)}(t) = E_0\mathrm{exp}\left(-\frac{1+i\beta_0}{2}\frac{t^2}{\Delta t_0^2}\right)\mathrm{exp}\left(-i\omega_c t\right), \tag{5.22}$$

where β_0 is the chirp parameter of the pulse and Δt_0 is the pulse duration. In addition, in section 2.2, we saw how the GVD inside a mode-locked laser cavity is related to the duration of the pulse emitted and its chirp. This relation is derived from equations (2.35) and is given by

$$GVD = D_g\frac{(3\beta_0-\delta t_{pn})}{2-\beta_0^2}, \tag{5.23}$$

where t_{pn} is the normalized pulse duration, δ the self phase modulation coefficient and D_g the gain normalized by the gain width. The parameters $\delta = 3\times10^{-6}$ rad/W and $D_g = 2.4\times10^{-30}$ s^2, are found in the literature [63]. Consequently, to estimate the GVD, the duration and the chirp of the pulse inside the laser cavity need to be determined.

The first step to determine the GVD is to determine the chirp of the pulse at the output of the laser. We use an auto-correlation technique to measure the duration of the pulse. Just after the output-coupler, the duration of the pulse is 36 fs FWHM. The spectrum is also measured with a spectrometer and found to be 40 nm FWHM, showing that the pulse is chirped. Indeed, a Fourier transform pulse whose spectrum has a FWHM of 40 nm has a duration of 22 fs. Thus, the chirp parameter at the output of the cavity is

$$\beta_0 = \sqrt{(36/22)^2-1} = 1.3. \tag{5.24}$$

Naturally, the chirp at the output of the laser is different from the chirp inside the laser cavity. First, the passage through the output-coupler needs to be taken into account. Note that in the following we go backward in propagation meaning that we remove dispersive elements from the optical path. To take into account the output-coupler, we estimate the chirp introduced by 4 mm of silica of dispersion $\beta_2 = 36$ fs^2/mm using equations (2.42) and (2.43). Before the output-coupler the pulse duration is found to be 24 fs and the chirp parameter 0.47. Then, the passage through the crystal also needs to be taken into account. Because the cavity is linear, each pulse before the output-coupler propagated twice in the crystal. This crystal is made of sapphire of

dispersion $\beta_2 = 58$ fs^2/mm and is roughly 2.5 mm long. In this configuration, if the dispersion from one trip through the crystal is removed, it leads to a pulse duration of 25 fs and a chirp parameter of -0.36. For two trips removed, we find a duration of 31 fs and a chirp parameter of - 1.2. Note that in both cases the chirp parameter is negative. A plot of the duration of the pulse and the chirp parameter as a function of the (negative) length of crystal crossed can be seen in Figure 5.8. Using equation (5.23) it is possible to determine the GVD inside the cavity as a function of the length of crystal crossed by the pulse. It is reproduced in Figure 5.9.
This calculation does not take into account the negatively chirped mirrors in the cavity. The main reason is that we do not have access to their characteristics as previously explained. Consequently, the GVD determined using this method is an upper bound on the intra-cavity dispersion. In addition, since we derived the expression (5.21) as the fluctuations averaged over the cavity, using the dispersion at a given point in the cavity is not entirely accurate. Indeed because the dispersion varies in the cavity, the noise level depends on where it arises in the cavity. Thus an uncertainty needs to be associated to the estimation of the dispersion. Therefore, we consider the dispersion for one trip in the crystal and calculate the uncertainty associated to a pulse which has not yet traveled through the crystal or which has done a double pass. Consequently, to have the dispersion and the uncertainty, we draw from a normal distribution centered at - 2.5 mm (one trip in the crystal) and with a variance of 2.5 mm (two trips or no trip) a set of path lengths. For each path length the duration of the pulse and the chirp parameter are calculated. From each set of data the GVD is determined according to (5.23). We then take the average of all the GVD values found and the variance to estimate the GVD and its uncertainty. The resulting calculated GVD is -280 fs^2 and the uncertainty is ± 50 fs^2.

5.3.2.3 Model applied to the experiment

The model can now be applied to our measurements. We use the fluctuations of the mean power, δP, and of the central frequency, $\delta\omega_c$, measured experimentally thanks to our setup, together with the GVD previously determined, to calculate the model (5.21). For each offset frequency f from 200 kHz to 4 MHz, the expected CEO frequency fluctuation δf_{CEO} is calculated. This gives a spectrum for the CEO frequency fluctuations, which can be compared to the one measured with the setup. The resulting trace is reproduced in Figure 5.10 alongside of the measured CEO frequency fluctuations given by $\delta f_{CEO} = \sqrt{S_{f_{CEO}}}$. A very good agreement is found between the model and the measured CEO fluctuations. The experimental data almost entirely fall in the uncertainty area up to 1 MHz. This agreement proves that the CEO dynamics is indeed related to the intensity fluctuations of the laser and that this feature is sufficient to explain it almost entirely. It confirms what was found with the SVD: the Schmidt number is equal to one as one noise source is responsible for the main dynamics. It also explains

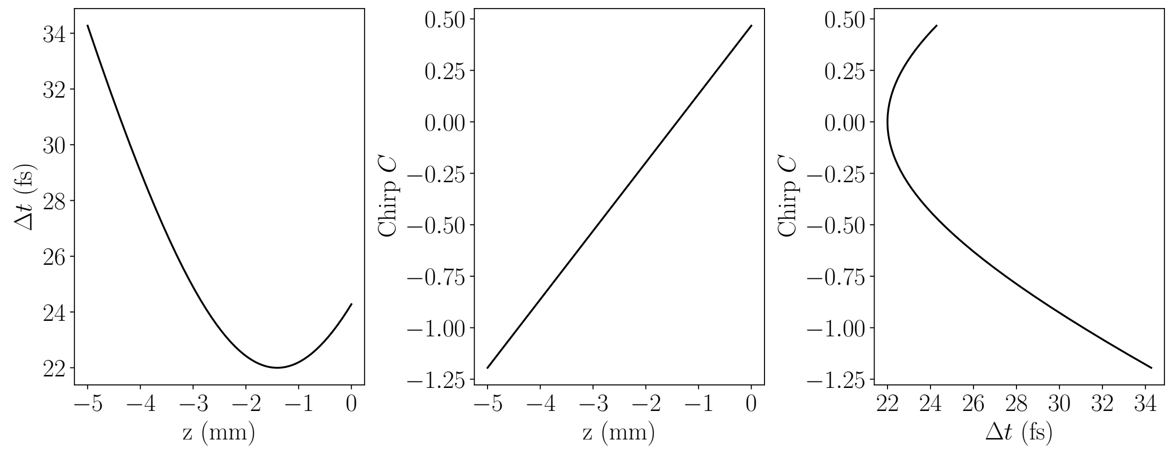

Figure 5.8 – **Evolution of the duration and the chirp through the crystal** From left to right, evolution of the duration of the pulse, evolution of the chirp parameter, and finally evolution of the chirp parameter as a function of the duration of the pulse. As we are removing optical path, -5 mm corresponds to the beam which has not yet crossed the crystal, -2.5 mm corresponds to one round-trip and 0 mm corresponds to two round-trips through the crystal. It can be noted that the duration of the pulse is the smallest between -1 and -2 mm of crystal. It roughly corresponds to the center of the crystal. This is consistent with the fact that the center of the crystal is the position in the cavity where the maximum non-linearity is desirable.

Figure 5.9 – **GVD as function of the crystal length.** The dispersion changes inside the cavity. Here again the minimum dispersion is found close to the center of the crystal around -1.5 mm.

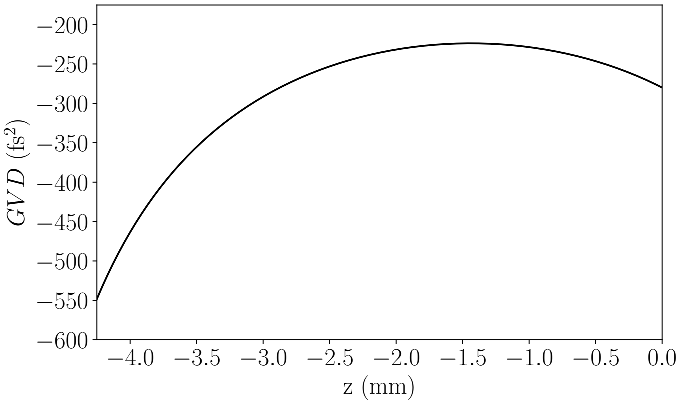

the coupling between the CEO and the central frequency fluctuations which was found by the projection of the singular modes. Nonetheless, the model does not seem accurate above 1 MHz. One explanation is that the model does not take into account the shot noise and describes only the correlations between the CEO and the amplitude modes. However, the amplitude noises are really close to the shot noise above 2 MHz. This is particularly true for the noise of the center spectrum which turns out to be the main contribution to the CEO fluctuations as discussed later. Hence, the model is no longer relevant above 2 MHz. This could also be due to some additional filtering coming from the laser cavity or the detection scheme not taken into account in the model.

To further explore the model, the ratio of the contributions of the center frequency and mean power fluctuations, calculated from the model, to the measured CEO fluctuations are reported in Table 5.1. It can be seen that the dominant contribution is the one coming from the spectrum center frequency. More precisely it is the spectrum center frequency via the GVD which seems to be the dominant contribution. This is in agreement with the results found in Section 5.3.1. The center spectrum detection mode has a higher contribution to the amplitude singular mode as it is directly coupled to the CEO frequency fluctuations via the GVD. This decomposition indicates that the mean power fluctuations has a really small direct effect on the CEO frequency. Note that in Figure 5.7*b* there is still a significant contribution to the amplitude singular mode from the mean power because the fluctuations of center frequency are also coupled to the intensity fluctuations due to the frequency pulling effect, as explained before.
With this study, it is possible to assert that the intensity has a significant impact on the CEO frequency only when there is a residual group velocity dispersion inside the laser cavity. This has also been identified in [63, 62]. The knowledge of this processes can help improving the performances of frequency combs. To achieve a lower CEO noise, the noise of the pump laser can be reduced or the GVD of the laser cavity can be reduced so that this intensity noise has a lower effect. In practice the first option is probably the easiest to implement. Alternately, a better lock of the CEO frequency can be achieved by using a laser cavity with an appreciable amount of group velocity dispersion.

Summary

In this chapter, we used a singular value decomposition to analyze the amplitude and phase correlations. We show that those correlations are mainly induced by a single noise source, the pump laser intensity fluctuations. Our analysis permits the identification of the coupling mechanisms. We determined that the fluctuations of the spectrum center frequency induced by the pump noise via frequency pulling is the main driving force of the CEO frequency noise. This is due to the group velocity dispersion of the laser cavity which was found to be -280 fs^2.

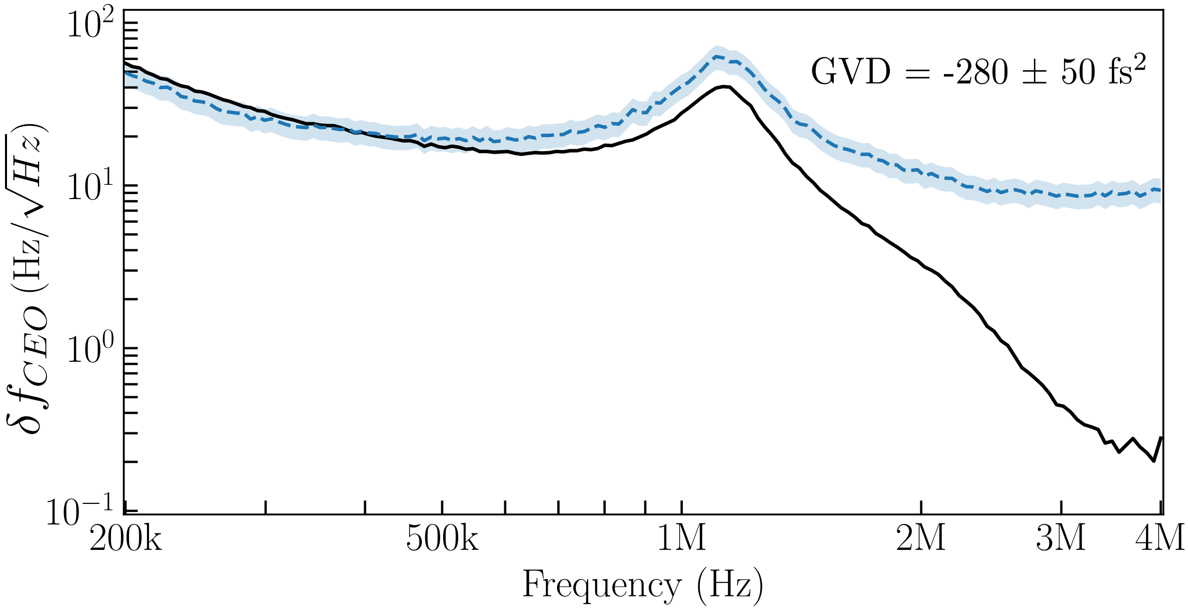

Figure 5.10 – **Experimental versus model for the CEO noise:** In dashed blue the model from (5.21), the shaded zone corresponds to the uncertainty on the GVD determined in the laser. Plain line: measured CEO frequency fluctuation given by $\delta f_{CEO} = \sqrt{S_{f_{CEO}}}$ from (4.46).

Contribution	Expression	ratio $\lvert c_j/\delta f_{CEO,exp}\rvert$
Group Velocity Dispersion	$c_1 = \frac{1}{2\pi}\delta\omega_c\left(\omega_c\frac{v_g^2}{v_\phi}\mathrm{GVD}\right)$	9×10^{-1}
Kerr Effect Dispersion	$c_2 = \frac{1}{2\pi}\delta\omega_c\left(\omega_c\frac{v_g}{c}\frac{\partial\overline{n}}{\partial\omega}\right)$	4×10^{-2}
Dispersion	$c_3 = \frac{1}{2\pi}\delta\omega_c\left(1-\frac{v_g}{v_\phi}\right)$	5×10^{-3}
Kerr Effect	$c_4 = \frac{1}{2\pi}\delta P\frac{\mathrm{d}I}{\mathrm{d}P}\frac{\omega_c v_g}{c}\left(\frac{v_g}{v_\phi}\omega_c\frac{\mathrm{d}\overline{n}_2}{\mathrm{d}\omega}-\overline{n}_2\left(1-\frac{v_g}{v_\phi}\right)\right)$	2×10^{-6}

Table 5.1 – **Expression and value of the ratio of the contributions of the model to the measured CEO fluctuations**. This ratio is averaged over the frequency range where the model is the most accurate, from 200 kHz to 500 kHz. The first three lines are the contributions from the spectrum center frequency and the last one the contribution from the power fluctuations.

Chapter 6

Menlo noise analysis

Contents

6.1 Unbalanced Mach-Zehnder for amplitude and phase measurement . . . 120
6.1.1 Reminder on self-heterodyne detection . . . 120
6.1.2 Amplitude and phase extraction . . . 122
6.1.3 Recovering the noise on the parameters . . . 124
6.2 Experimental setup . . . 125
6.3 Results . . . 126
6.3.1 Phase measurement . . . 126
6.3.2 Noise floors . . . 129

In this chapter the same approach as developed in section 4.1 is applied to a different laser source and a different experimental setup. This study was conducted at Thales Research & Technology (TRT) in Palaiseau. The laser investigated is a commercial fiber laser from MenloSystems. This laser emits at telecom wavelength and is expected to exhibit very different features from the previous one, as the mode-locking process is different. Contrary to the previous chapter, the noise measurement is performed with an optical bench developed at TRT, based on an unbalanced Mach-Zehnder interferometer (UMZI) similar to what was described in section 3.2.1. Our motivation is to show that our analysis can be applied to various sources of light pulses in different ranges of wavelength. In addition, the measurement bench developed by TRT is a lot more compact and thus versatile. In what follows, we present in details the experiment conducted to investigate the dynamics of the telecom laser and present the experimental results obtained.

6.1 Unbalanced Mach-Zehnder for amplitude and phase measurement

The experiment presented in this chapter relies on an unbalanced Mach-Zehnder interferometer (UMZI) to measure the amplitude and the phase of the laser. With this setup, the technique to extract the quadratures of the field is different from the homodyne detection. Consequently, in this section, we start by reminding the equations describing the field in the interferometer for a field undergoing amplitude and phase fluctuations. Secondly, the procedure to extract those fluctuations is presented. Finally, the covariance matrices are recovered from the amplitude and phase fluctuations.

6.1.1 Reminder on self-heterodyne detection

We first start by recalling the expression of the electric field

$$E^{(+)}(t) = \mathcal{E}_0 a(t) e^{-i(\omega_0 t+\varphi)}, \tag{6.1}$$

with ω_0 the carrier frequency, φ the phase of the field and $a(t)$ the slowly varying envelope. In this experiment, a spectrally resolved detection will be used similarly to the previous experiment. Hence, for simplicity, we directly write the field in the pixel basis introduced in section 4.2.3.2. The field detected by the pixel j reads

$$E_j^{(+)} = \mathcal{E}_0 \alpha_j e^{-i\varphi_j}, \tag{6.2}$$

with $\alpha_j = \sqrt{N_j}$ the amplitude of the field in the pixel mode u_j, and N_j the number of photons in this mode.
As usual, we are interested in measuring the amplitude and phase fluctuations of the electric field. Thus we introduce the amplitude fluctuations $\delta\epsilon_j(t_n)$ and the phase ones $\delta\varphi_j(t_n)$, where t_n stands for the slow fluctuations compared to the time scale of the pulse duration t. For simplicity we set $\varphi_j = 0$. The noisy electric field is written

$$E_j^{(+)}(t_n) = \mathcal{E}_0 \alpha_j (1+\delta\epsilon_j(t_n)) e^{-i\delta\varphi_j(t_n)}, \tag{6.3}$$

As illustrated in Figure 6.1, this electric field is split into two components, a zeroth order and a diffracted one, thanks to an acousto-optic modulator (AOM). Each order is connected to an arm of the interferometer. We assume that half of the total optical power goes in each arm. The electric field diffracted acquires a frequency shift f_{RF} corresponding to the driving frequency of the AOM. The other arm is delayed by introducing an optical fiber whose length is equivalent to a delay τ. Thus the two electric fields can be written

$$E_{j,0}^{(+)}(t_n) = \mathcal{E}_0 \frac{\alpha_j}{2}(1+\delta\epsilon_j(t_n-\tau)) \exp\left[-i\left(\omega_0\tau + \delta\varphi_j(t_n-\tau)\right)\right], \tag{6.4a}$$

$$E_{j,1}^{(+)}(t_n) = \mathcal{E}_0 \frac{\alpha_j}{2}(1+\delta\epsilon_j(t_n)) \exp\left[-i\left(-\omega_{RF} t_n + \delta\varphi_j(t_n)\right)\right], \tag{6.4b}$$

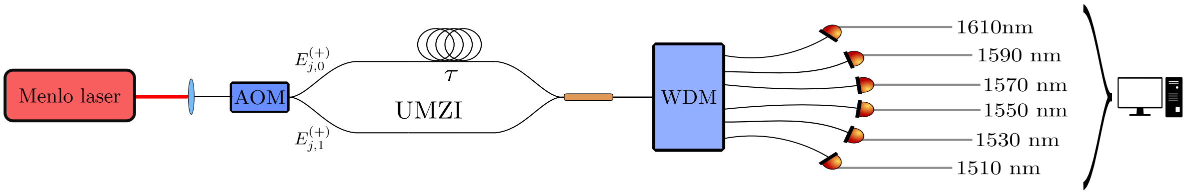

Figure 6.1 – **Experimental setup**. The laser is first split in two using an AOM to form the two arms of the interferometer. One of the arm is delayed using a long optical fiber (including dispersion compensated fiber). The two beams are recombined and sent to a WDM which separates the spectrum in six spectral bands. Each spectrum slice is then detected using a photodiode and the data are recorded by an oscilloscope.

where $\omega_{RF} = 2\pi f_{RF}$, $E^{(+)}_{j,0}$ is the field of the pixel j in the order 0 of the AOM and $E^{(+)}_{j,1}$ in the first order.

The two beams are recombined at the output of the interferometer and are detected by a photodiode whose photo-current reads

$$\begin{aligned} i_{out,j}(t_n) &\propto |E^{(+)}_{j,0}(t_n) + E^{(+)}_{j,1}(t_n)|^2 \\ &\propto |E^{(+)}_{j,0}(t_n)|^2 + |E^{(+)}_{j,1}(t_n)|^2 + E^{(-)}_{j,0}(t_n)E^{(+)}_{j,1}(t_n) + E^{(+)}_{j,0}(t_n)E^{(-)}_{j,1}(t_n), \end{aligned} \tag{6.5}$$

with $E^{(-)}(t_n) = \left(E^{(+)}(t_n)\right)^*$. Keeping only the two last terms corresponding to an oscillating signal at f_{RF} leads to

$$\begin{aligned} i_{out,j}(t_n) &= A\alpha_j^2\left[1+\delta\epsilon_j(t_n)\right]\left[1+\delta\epsilon_j(t_n-\tau)\right]\cos\left[\omega_0\tau - \omega_{RF}t_n + \delta\varphi_j(t_n) - \delta\varphi_j(t_n-\tau)\right] \\ &\simeq A\alpha_j^2\left[1+\Delta\epsilon_j(t_n,\tau)\right]\cos\left[\omega_0\tau - \omega_{RF}t_n + \Delta\varphi_j(t_n,\tau)\right], \end{aligned} \tag{6.6}$$

where A includes all constant terms, including the normalization constant $\mathcal{E}_0$ as well as the responsivity of the photodiodes $\mathcal{R}$ in A/W. In addition, the amplitude fluctuations have been developed at first order, and the relations

$$\begin{aligned} \Delta\varphi_j(t_n,\tau) &= \delta\varphi_j(t_n) - \delta\varphi_j(t_n-\tau), \\ \Delta\epsilon_j(t_n,\tau) &= \delta\epsilon_j(t_n) + \delta\epsilon_j(t_n-\tau), \end{aligned}$$

are introduced to simplify the expression.

After detection, the photo-current (6.6) is recorded on a oscilloscope. In the next section the procedure to extract the amplitude and the phase from this signal is presented.

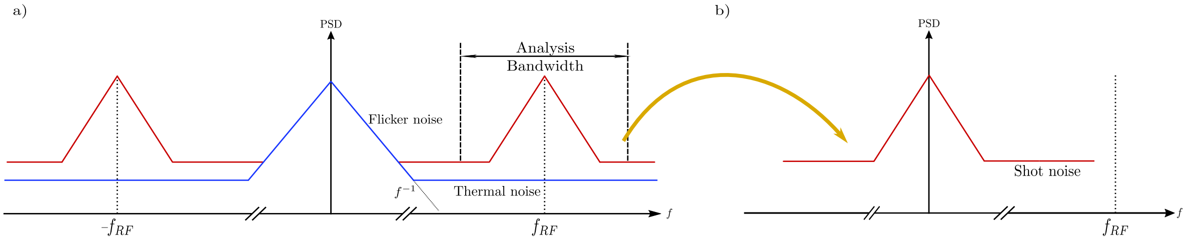

Figure 6.2 – **Numerical demodulation**. Scheme of the principle of the numerical demodulation. The laser noise is centered around the frequency f_{RF}. It is retrieved by applying a band-pass filter around this frequency, and shifting back the noise to the zero frequency. This procedure allows to get rid of the low frequency noise of the detection. This noise, called Flicker noise, occurs in electronic devices due to various effects such as impurities in transistors. It has a frequency dependence in f^{-1} and is often the dominant noise source at low frequency.

6.1.2 Amplitude and phase extraction

The AOM, used as the input port of the UMZI, also plays a role in the extraction of the amplitude and the phase. Because the field from one arm of the interferometer is shifted by f_{RF} with respect to the other, the beat signal between the two arms is centered around this frequency as can be seen from equation (6.6). It implies that the low frequency noise of the laser is translated around f_{RF}. This is schematized in Figure 6.2. This procedure allows to extract the signal of interest from the, generally high, low frequency detection noise coming from the detectors and the acquisition devices. To recover the amplitude and the phase separately from the signal, the following procedure is used [78].

We start from the measured photo-current described by equation (6.6). This signal can be rewritten

$$\begin{aligned} i_{out,j}(t_n) = A\alpha_j^2\left[1+\Delta\epsilon_j(t_n,\tau)\right]&\left[\cos\left(\omega_0\tau+\Delta\varphi_j(t_n,\tau)\right)\cos\left(\omega_{RF}t_n\right)\right.\\ &\left.+\sin\left(\omega_0\tau+\Delta\varphi_j(t_n,\tau)\right)\sin\left(\omega_{RF}t_n\right)\right]. \end{aligned} \tag{6.7}$$

The Fourier transform of the signal is then calculated and is given by

$$\begin{aligned} \mathrm{FT}\{i_{out,j}(t_n)\} = A\alpha_j^2 \times \mathrm{FT}\{1+\Delta\epsilon_j(t_n,\tau)\} * \Big[&\delta(f-f_{RF}) * \mathrm{FT}\{e^{-i(\omega_0\tau+\Delta\varphi_j(t_n,\tau))}\}\\ &+\delta(f+f_{RF}) * \mathrm{FT}\{e^{i(\omega_0\tau+\Delta\varphi_j(t_n,\tau))}\}\Big], \end{aligned} \tag{6.8}$$

where $*$ is the convolution product and $\delta(f)$ the Dirac function. To recover the amplitude and the phase, only the positive frequencies of the signal (6.8) are kept by applying a band-pass filter around f_{RF}. The width of the filter defines the analysis bandwidth in which the dynamics can be characterized. The filtered signal is shifted back to the zero frequency. This procedure is schematized in Figure 6.2. The resulting complex signal after inverse Fourier transform is given by

$$i_{out,j}(t_n) = A\alpha_j^2 \left[1 + \Delta\epsilon_j(t_n,\tau)\right] e^{i(\omega_0\tau + \Delta\varphi_j(t_n,\tau))}. \tag{6.9}$$

Phase extraction: The phase difference $\Delta\varphi_j(t_n,\tau)$ is retrieved by unwrapping the argument of the signal. Mathematically it consists in taking the arc-tangent of the ratio between the imaginary part and the real part of the signal. Thus we have

$$\omega_0\tau + \Delta\varphi_j(t_n,\tau) = \mathrm{Arctan}\left(\frac{\mathrm{Im}\left[i_{out,j}(t_n)\right]}{\mathrm{Re}\left[i_{out,j}(t_n)\right]}\right) \tag{6.10}$$

Here, we assume that $\omega_0\tau$ does not change during the measurement time. Thus, it corresponds only to a constant phase shift. Note that if the phase fluctuations are two high, i.e fluctuations are bigger than 2π between two measurement points, the unwrapping will introduce errors in the calculation as there will be ambiguity in unwrapping the phase.

The phase fluctuations can be retrieved by first computing its spectrum and applying the transfer function defined in section 3.2.2

$$h_{UMZI}(f,\tau) = \frac{1}{1 - \mathrm{e}^{-2i\pi\tau f}}. \tag{6.11}$$

Consequently, the spectrum of the phase fluctuations is given by

$$\delta\tilde{\varphi_j}(f) = h_{UMZI}(f,\tau)\Delta\tilde{\varphi_j}(f,\tau), \tag{6.12}$$

where $\Delta\tilde{\varphi_j}(f,\tau)$ is the Fourier transform of $\Delta\varphi_j(t_n,\tau)$, and $\delta\tilde{\varphi_j}(f)$ the one of $\delta\varphi_j(t_n)$ so that the phase fluctuations are given by $\delta\varphi_j(t_n) = \mathrm{FT}^{-1}\{\delta\tilde{\varphi_j}(f)\}$

Amplitude extraction: On the other hand, the amplitude fluctuations can be retrieved by first taking the modulus of the signal and removing the mean field according to

$$\Delta\epsilon_j(t_n,\tau) = \frac{|i_{out,j}(t_n)| - \langle |i_{out,j}(t_n)| \rangle_{t_n}}{\langle |i_{out,j}(t_n)| \rangle_{t_n}}, \tag{6.13}$$

where $\langle \cdot \rangle_{t_n}$ represents the time average value. The amplitude fluctuations $\delta\epsilon_j(t_n)$ are recovered by applying a transfer function in amplitude $h_{UMZI}^{Amp}(f,\tau)$ according to

$$\delta\epsilon_j(t_n) = \mathrm{FT}^{-1}\{h_{UMZI}^{Amp}(f,\tau)\Delta\tilde{\epsilon_j}(f,\tau)\}, \tag{6.14}$$

where $\Delta\tilde{\epsilon_j}(f,\tau)$ is the Fourier transform of $\Delta\epsilon_j(t_n,\tau)$ and $h_{UMZI}^{Amp}(f,\tau)$, is given by

$$h_{UMZI}^{Amp}(f,\tau) = \frac{1}{1 + \mathrm{e}^{-2i\pi\tau f}}. \tag{6.15}$$

This procedure to extract the amplitude and the phase is applied to all the pixels from the spectrally resolved detection represented in Figure 6.1. For each one, the amplitude fluctuations $\delta\epsilon_j(t_n)$ and the phase ones $\delta\varphi_j(t_n)$ are retrieved. They are then used to compute the quadratures of the field for each pixel and as well as the covariance matrices as detailed in the next section.

6.1.3 Recovering the noise on the parameters

Once the amplitude and the phase retrieved, they can be related to the quadratures of the field. For the pixel j, we have

$$\begin{aligned} \delta x_j(t_n) &= 2\alpha_j \delta\epsilon_j(t_n), && (6.16)\\ \delta p_j(t_n) &= 2\alpha_j \delta\varphi_j(t_n), && (6.17) \end{aligned}$$

with $\alpha_j = \sqrt{N_j}$, where N_j is the number of photons for the pixel j.
Finally, we use the decomposition in noise modes, introduced in section 4.1.2, to relate the quadrature fluctuations to the fluctuations of the parameters of the laser in the pixel basis according to

$$\begin{aligned} \delta\overrightarrow{x}(t_n) &= (\delta x_1(t_n), \ldots, \delta x_j(t_n), \ldots) = 2\alpha_0 \left[\delta\epsilon(t_n)\overrightarrow{u}_{amp} - \frac{\delta\omega_0(t_n)}{2\Delta\omega}\overrightarrow{u}_{cent-freq}\right], \\ \delta\overrightarrow{p}(t_n) &= (\delta p_1(t_n), \ldots, \delta p_j(t_n), \ldots) = 2\alpha_0 \left[\omega_0\delta\tau_{ceo}(t_n)\overrightarrow{u}_{ceo} + \Delta\omega\delta\tau_r(t_n)\overrightarrow{u}_{rep-rate}\right], \end{aligned}$$

where $\overrightarrow{u}_{mode}$ are the detection modes in the pixel basis introduced in section 4.1.2, and with $|\alpha_0|^2 = \sum_j |\alpha_j|^2 = N_0$ the total photon number detected. We remind that $\delta\epsilon(t_n)$ stands for the laser amplitude fluctuations, $\delta\omega_0(t_n)$ for carrier frequency fluctuations, $\delta\phi_{CEO}(t_n) = \omega_0\delta\tau_{ceo}(t_n)$ for CEO phase fluctuations and $\delta\tau_r(t_n)$ for timing jitter.

As in chapter 4, the noise on the laser parameters are recovered by projecting the covariance matrices on the associated modes. We remind that the covariance matrices in amplitude and phase are given in the pixel basis by

$$\begin{aligned} [\Gamma_x]_{j,k} &= \langle \delta x_j(t_n)\delta x_k(t_n)\rangle, && (6.18)\\ [\Gamma_p]_{j,k} &= \langle \delta p_j(t_n)\delta p_k(t_n)\rangle. && (6.19) \end{aligned}$$

Finally, to retrieve the noise spectra of each parameter, a demodulation procedure is employed similarly to the one described in section 4.3.1. Note that, in this experiment, the demodulation is performed numerically.

6.2 Experimental setup

The experimental setup is represented in Figure 6.1. The laser under study is a commercial fibered laser from MenloSystems (FC1500-250-ULN). It emits femtosecond pulses at 1550 nm at a repetition rate of 250 MHz resulting in a spectrum of approximately 100 nm. The field is first split in two paths thanks to an AOM driven at $f_{RF} = 110$ MHz, introducing at the same time a frequency shift f_{RF} in the diffracted beam. A fiber delay of roughly 60 m is introduced in the second arm. Both arms are finally recombined using a fiber-beam-splitter (BS). The recombined beams are sent into a commercial wavelength division multiplexer (WDM) from Edge Optical Solutions (DCMD-8H). This device splits the spectrum in 6 channels, each covering approximately 20 nm, whose central frequencies are $[1510, 1530, 1550, 1560, 1590, 1610]$ nm. Each channel is sent to a commercial fiber-coupled detector (Thorlabs DET01CFC). Finally, the detectors are connected to an 8 channels oscilloscope (Teledyne Lecroy HDO8038A) whose bandwidth is 300 MHz.

It can be noted that the setup is a lot more simple than the one used in the previous chapters. Because all the components are fibered, the experiment is more compact. No filtering cavity is used and thus no active locking of the repetition rate nor of the CEO is needed. In addition, all the elements are off-the-shelf components. Nonetheless, the construction of the delay is complicated by the wide spectrum of the laser. The delay needs to be properly set so that the pulses arrive at the same time on the recombining BS of the interferometer. To this end, a fiber-delay-line is used. When the delay is properly set, the contrast of the beat signal at f_{RF}, is maximal. The delay can also be adjusted by monitoring the spectrum of the beat signal and maximizing the height of the beat peak signal at f_{RF}. Similar to what was explained in section 4.2.2, the relative phase between the two arms needs to be flat across the spectrum to maximize the contrast in all the channels simultaneously. However, the delayed arm accumulates more dispersion than the other one. Hence, when the contrast of one frequency channel is maximized, the other ones are not due to the spectral phase variation across the spectrum. A lower contrast leads to a smaller signal to noise ratio of the beat signal which can be detrimental. Consequently, the relative dispersion between the two arms must be compensated. This is achieved using dispersion compensated fibers. Those fibers have negative dispersion, which at 1550 nm gives a positive GVD of the order of 5 fs^2/mm, while a normal fiber has a GVD of -25 fs^2/mm at 1550 nm. Nonetheless, as we need to find a configuration where the pulses from both arms arrive at the same time on the recombining BS, the path difference must be a multiple of the length separating two pulses which is approximately 1 m. Thus, finding the right configuration is a bit tricky and we did not manage to have a perfectly flat phase. The residual phase, measured with a spectral interferometry as described in section 4.2.2, is 3000 fs^2. The delay is then chosen in order get the maximum contrast as possible in all the channels at the same time.

6.3 Results

In this section we present the results obtained using the setup described above. First, the results of the phase measurement are presented, leading to the characterization of the CEO noise and timing jitter. Secondly, experimental limitations are discussed. As a matter of fact, for technical reasons that will be introduced, the amplitude cannot be accurately measured with the actual setup. Thus the RIN as well as the noise on the central frequency cannot be measured simultaneously to the phase noises.

6.3.1 Phase measurement

The amplitude and phase covariance matrices are calculated as described in section 6.1.3. An example of phase covariance matrices can be seen in Figure 6.3. Their shapes are similar to the ones measured with the titanium-sapphire laser. Correlations between spectral bands are present at low frequencies, indicating the presence of classical noise, and disappear at higher frequencies. Note that in this experiment, the matrices are not normalized with respect to the shot noise as the setup does not allow to measure it. Nevertheless, the procedure to extract the amplitude and the phase in section 6.1.2 directly gives the fluctuations in physical units, so that no additional normalization is needed[1].

From those matrices, the noise spectra of the CEO frequency f_{CEO} and the phase timing jitter ϕ_t can be recovered. They are reproduced in Figure 6.4. As a comparison, the timing jitter measured by the laser manufacturer using a different method can be seen in Figure 6.5. Note that this PSD is expressed in dBc/Hz which is 3 dB lower that the dBrad^2/Hz in Figure 6.4. Both curves display roughly the same level of noise, showing the ability of our technique to accurately characterize the phase noise of the laser. Comparing those curves with the ones represented in Figure 4.11, it appears that the phase noise of the menlo laser is a bit higher than the one of the Titanium-Sapphire. Nevertheless, the menlo laser does not present any relaxation oscillations peak as opposed to the Titanium-Sapphire.

We tried to apply the same analysis to the amplitude noise. However, we encountered an issue. Indeed, when looking at the amplitude covariance matrices as represented in Figure 6.6, only the diagonal elements are different from zero, even at low frequencies.

---

[1] However, if amplitude and phase correlations are analyzed using the correlation matrix, having the noises expressed in different units might be an issue.

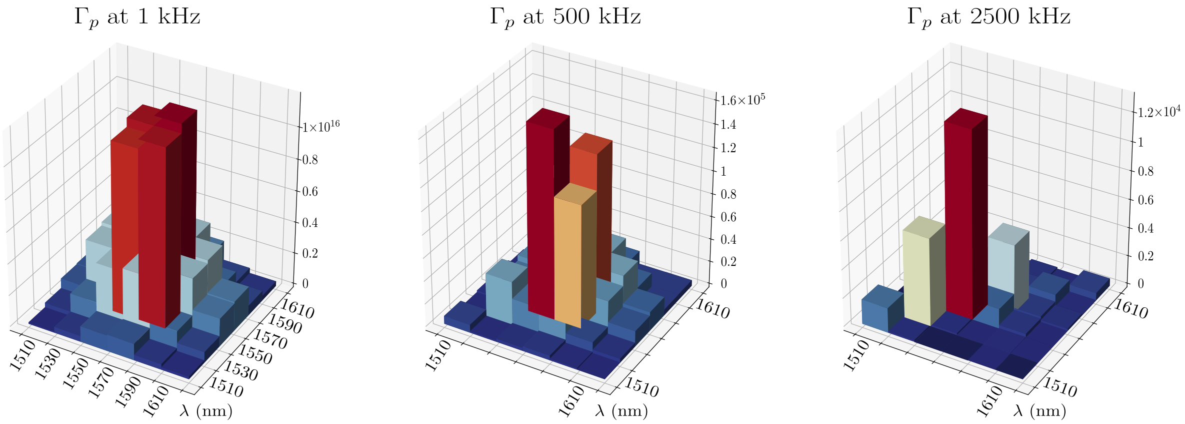

Figure 6.3 – **Phase covariance matrices**. The matrices are taken at three different analysis frequencies: 1 kHz, 500 kHz and 2500 kHz. As previously, the matrices display spectral correlations at low frequencies indicating the presence of classical noise. At higher frequencies, only the diagonal terms are present proving that the laser is shot noise limited.

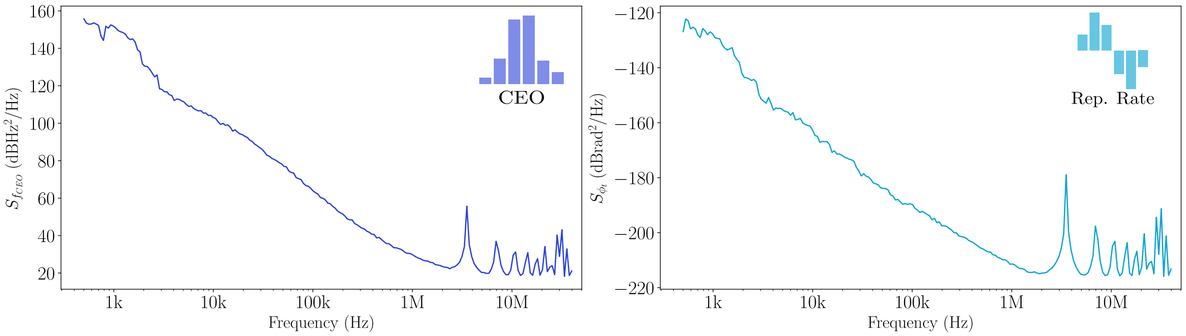

Figure 6.4 – **Phase noises**. Left: CEO frequency noise in physical units obtained by projecting the phase covariance matrix on the CEO mode represented on the same graph. Right: timing jitter obtained via projection of the corresponding spectral mode represented on the same graph.

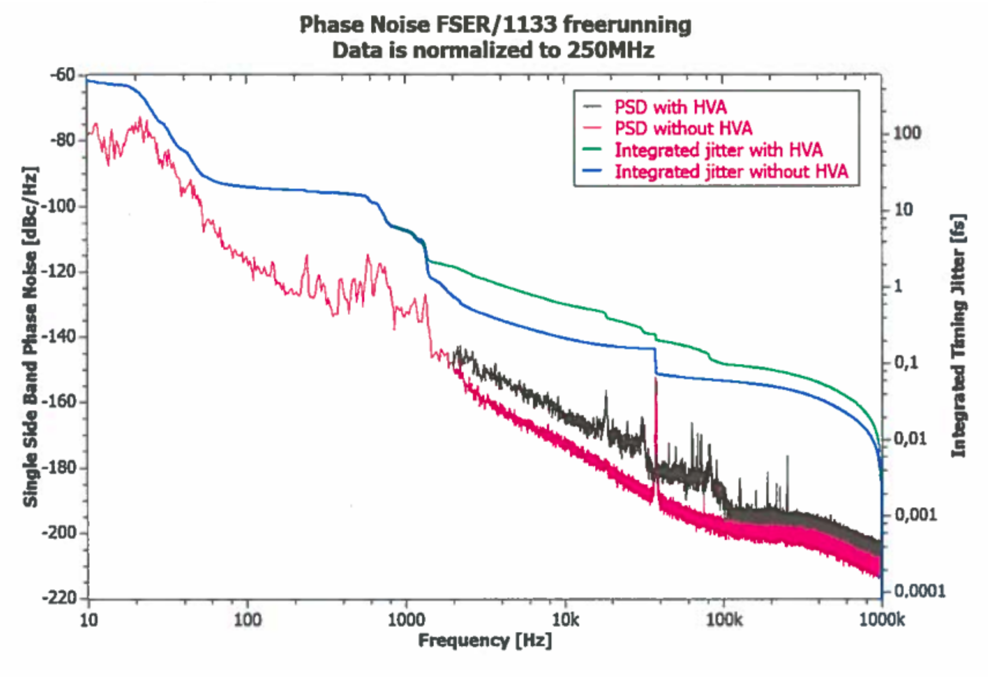

Figure 6.5 – **Timing jitter phase noise**. Figure taken from the laser datasheet. Noise of the repetition rate measured using two different measurement setups. The high frequency spectrum (>2 kHz) was measured by cross-correlating the optical pulses with a reference laser (Menlo M-Com, Serial Number FSER/0670). The low frequency spectrum (<1kHz) was measured using a Signal Source Analyzer at the 40^{th} harmonic of the laser. The timing phase noise is expressed in dBc/Hz which is 3 dB lower that the dBrad^2/Hz in Figure 6.4.

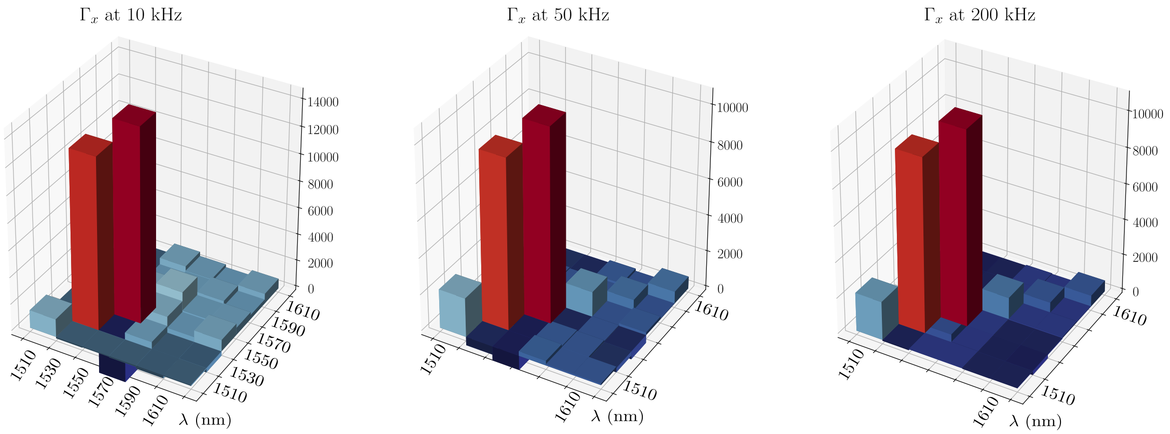

Figure 6.6 – **Amplitude covariance matrices**. The matrices are taken at three different analysis frequencies: 10 kHz, 50 kHz and 200 kHz. Those matrices do not display any spectral correlations even at low frequency. It suggests that the detection reaches a noise floor higher than the classical noises.

We saw that, in the presence of classical noises, spectral correlations appear in the covariance matrices. As we do not expect the laser to be free of classical noise at 10 kHz, it indicates that a detection noise floor higher than the classical noises is reached. To explain this effect, in the next section we briefly review the different sources of noise in the detection process and estimate their strengths.

6.3.2 Noise floors

The two important noises in a photodetection are the thermal noise and the shot noise. In this section we give the expression of those noises and evaluate their contributions.

Thermal noise: The thermal noise comes from the thermal agitation of the electrons in the detection circuit. It is a white noise whose power spectral density is given by [79]

$$S_{th}(f) = \frac{4k_B T}{Ri^2} \quad \left[\mathrm{Hz}^{-1}\right], \tag{6.20}$$

where, R is the resistance of the detectors (usually 50 Ω), i is the photo-current, k_B is the Boltzmann constant and T the temperature of the system.

Shot noise: The shot noise, as discussed previously, is also a white noise, which depends on the incident power. It is caused by the discrete nature of the photons. In a photodetection, this noise is translated in an electronic shot noise which corresponds to the discrete nature of the current composed of electrons. In principle both shot noises are related by the responsivity of the photodiode $\mathcal{R}$. If this responsivity is 1, it means that each photon creates one electron and thus both noises are identical. In terms of current, the shot noise power spectral density is given by [80]

$$S_{sn}(f) = \frac{2e}{i} \quad \left[\mathrm{Hz}^{-1}\right], \tag{6.21}$$

where i is the photo-current and e the elementary charge of an electron.

Detection floor: To try to understand the origin of the noise floor in the detection, the values of the thermal noise and the shot noise for each frequency channel of the experiment are calculated. The optical power measured at each output of the WDM is reproduced in Table 6.1. The photo-current generated by the detection of each optical channel is also given using the relation $i = \mathcal{R}P_{opt}$ with $\mathcal{R} = 0.85$, the responsivity of the photodiode. This photo-current allows to compute the value of the thermal and the shot noise using equations (6.20) and (6.21). The resulting noise power in dB/Hz are reproduced in Table 6.1.

	C1	C2	C3	C4	C5	C6
Optical power, P_{opt} (mW)	0.071	0.3	0.81	0.86	0.291	0.141
Photo-current, i (mA)	0.06	0.255	0.689	0.731	0.247	0.12
Thermal noise, $S_{th}(f)$ (dB/Hz)	-130	-143	-152	-152	-143	-136
Shot noise, $S_{sn}(f)$ (dB/Hz)	-143	-149	-153	-154	-149	-146

Table 6.1 – **Comparison of the optical power, photo-current and noise power for each frequency channel**. The photo-current is calculated according to $i = \mathcal{R}P_{opt}$ with $\mathcal{R} = 0.85$, the responsivity of the photodiode.

From Table 6.1 a first conclusion can be drawn. Because the optical power is low in all the frequency channels, the thermal noise is above the shot noise. Indeed, the thermal noise power varies as $1/i^2$ with respect to the photo-current while the shot noise varies as $1/i$. Hence, for low optical power, and thus low photo-current, the thermal noise can overcome the shot noise. This configuration is obviously not optimal as the detection is limited by noise independent from the properties of the source of light we wish to characterize.

To better understand the shape of the amplitude covariance matrices, the strength of the shot and thermal noises can be compared to the amplitude noise of the laser.

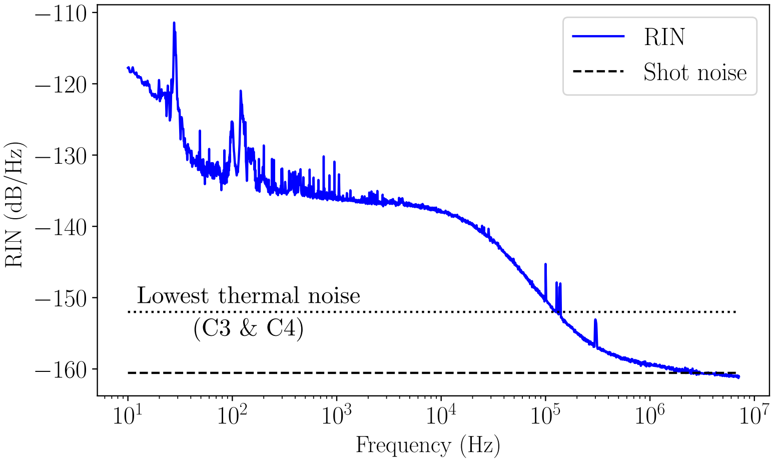

Figure 6.7 – **Relative Intensity Noise.** In blue the RIN of the menlo measured for an optical power of 3 mW. In dashed black the theoretical RIN of the shot noise for 3 mW. In dotted black the thermal noise for channels 3 and 4.

To this end, the relative intensity noise (RIN) of the laser is measured using a single photodiode as explained in section 4.4.3. It is reproduced in Figure 6.7. It can be seen that, even the lowest thermal noise power at -152 dB/Hz, corresponding to the two central frequency bands, is higher than the RIN above 100 kHz. It explains why the amplitude covariance matrices are diagonal even at low frequencies as the measurement is limited by the thermal noise of the detection which is uncorrelated.

To try to circumvent this issue, it would be necessary to put more power in the interferometer. However, this is not possible. Indeed, if the power at the beginning of the interferometer is increased, nonlinear effects start to occur. In particular, we noticed that, by increasing the power, self-phase modulation arises in the fibers. It results in a deformation of the optical spectrum of the laser, creating holes in it. Hence some channels receive no signal. Note that approximately 20mW are injected in the fiber before the interferometer. The power at the outputs is really low as losses are introduced due to the different components of the interferometer. Another way around would be to reduce those losses. However, we did not have the equipment nor the time to try doing so. In a last attempt to solve the issue, we decided to unplug the interferometer. By keeping only one arm with all the power in it, more power per channel is achievable at the expanse of the phase measurement. However, even with this configuration no significant results were found. Without the shift in frequency due to the AOM, the signal of interest lies in the low frequency part of the spectrum. Hence, the signal is drown into the electronic noise coming from the various detection components. As we did not have any low frequency amplifier, we where not able to extract any information from the signal.

Summary: The analysis technique developed in chapter 4 can be applied to different sources of light. As an improvement from the previous experiment, a different optical bench has been used. This setup, mainly based on commercial fiber components, is more compact and easy to handle than the one described in section 4.2. We managed to characterize the phase noise of the laser. However, due to the low optical power at the output of the interferometer, the amplitude measurement failed to give meaningful results. Many improvements can be maid to improve this experiment to apply the same investigation of the amplitude and phase correlations similarly to chapter 5.

Part III

PULSED APPROACH TO RESERVOIR COMPUTING

Introduction

In this part is presented a project started during the last year of my PhD. The idea is to take advantage of the tools presented along this manuscript for the implementation of a photonic machine learning protocol. Photonic computing is a recent development in the field of machine learning. It uses optical components to implement operations which are usually time and energy consuming on computers. By doing so, very efficient and fast information processing can be achieved [81, 82].

In this manuscript, we will concentrate on one particular type of machine learning protocol known as Reservoir Computing (RC). At the origin of RC are the recurrent neural networks [83]. Those networks are inspired from the brain mechanisms. They are composed of many interconnected artificial neurons. Because of the recurrent connections between the neurons, those networks possess a memory, making them suitable for processing time series such as speech recognition [84, 22]. Although very powerful, recurrent neural networks have proven to be hard to train. As a matter of fact, all the weights of the networks need to be trained using backpropagation in time [85], a time consuming and not always converging procedure [86]. To remediate to this drawback, new architectures of neural networks have been developed, classified under the common denomination of reservoir computing (RC). Those recurrent neural networks are composed of three elements: an input layer to inject the data into the system, a reservoir composed of a large amount of neurons (or nodes) randomly connected, and an output (or reading) layer to extract the information from the reservoir. The property that makes RC appealing is the possibility to only train the weights of the output layer to process information [21, 87]. Indeed, under certain conditions on the wiring of the reservoir, training the output layer with a simple linear regression can be sufficient.

As an example of application of reservoir computing, using the knowledge on the laser intensity dynamics gathered in the previous part of the manuscript, we implement a simulation to predict the evolution of the laser parameters from the pump power fluctuations.

The main challenge in reservoir computing is the design of the reservoir. However, once the reservoir set, its topology is left unchanged during all the processing. This feature makes reservoir computing a good candidate for hardware implementation, in particular in photonics. Many experimental realizations of reservoir can be found in the literature.

As an example, spatially distributed reservoir have been studied in [88, 89, 90]. In this work, a different approach is used, the delay-based reservoir. The general idea is to demultiplex in time the nodes of the reservoir so that one node is accessed at each time step. The nodes from the reservoir are connected in time via a feedback loop, conferring memory to the reservoir at the same time. The first experimental implementation of such reservoir was demonstrated in [23, 91] using opto-electronics. Reservoir have then be fully implemented optically using long delays in optical fibers as a distributed reservoir [92, 93]. This all-optical implementation makes the data processing faster than the opto-electronic one.

Consequently, in the following chapters, we present the design of a reservoir computing protocol using a single non-linear node as in [23]. In our setup, the idea is to use pulses from the OFC to perform time delayed-based reservoir computing. The information is encoded in the phase of each pulse and read using homodyne detection. The laser source used is the frequency comb studied in the previous chapters which emits femtosecond pulses at a repetition rate of 156 MHz.

The long-term objective is to go toward quantum reservoir computing. Quantum reservoir computing started to draw a lot of attention in the literature [94, 95, 96, 27]. The motivation to implement such quantum architecture is manifold. Among other, advantage can be taken from the high number of degrees of freedom associated to quantum systems. In addition, those platforms are naturally suited for quantum tasks. Hence, there is a real interest in exploring this particular topic. To that end, quantum resources need to be introduced in the protocol. One way to do so is to encode the information in a particular type of quantum states known as squeezed states. In this part, we present an experiment to produce such states. They are produced via spontaneous parametric down conversion in a PPKTP waveguide. It allows the creation of squeezing at the level of the laser's pulses, enabling their manipulation for the computation task.

Chapter 7

Time series processing with neural networks

Contents

7.1 Reservoir computing 137

7.1.1 General principle 138

7.1.2 Application of RC to noise analysis 141

7.2 Delayed-feedback reservoir computing 142

7.2.1 General description: memory and links 145

7.2.2 Experimental implementation 148

7.2.3 Capacity 153

In this chapter we are interested in studying a machine learning protocol called reservoir computing (RC). We start by introducing the general concept of reservoir computing. This protocol is then simulated on a computer in an attempt to predict the dynamics of the optical frequency comb investigated in the previous chapters. In a second time, the experimental implementation of an optical delay-based reservoir computing protocol is presented. It relies on an optical frequency comb and a homodyne detection. Using a quantity known as information processing capacity, we assess the ability of this architecture to reconstruct complex functions. We then compare the results to simulations.

7.1 Reservoir computing

As for many other machine learning protocols, the objective of reservoir computing is to process data in order to classify input data or recognize sequences of data. As reservoir computing is part of the recurrent neural networks, it is particularly suited for the processing of time series. In the following, we concentrate on this particular task.

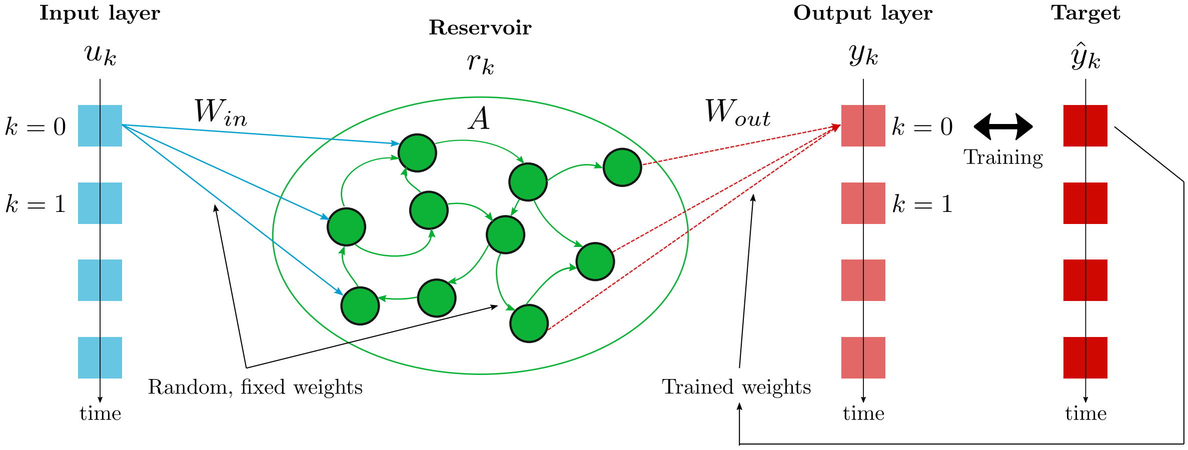

Figure 7.1 – **General scheme of a reservoir computing architecture**. It is composed of three parts: an input layer, a reservoir and an output layer. The input layer feeds the input data u_k into the reservoir at each time step. The reservoir is made of recurrent connections, providing memory to the protocol. The output layer is a linear combination of the values of the reservoir nodes. Only the weights W_{out} of this output layer are trained using a target function $\hat{y}(t_n)$.

The aim is, given an input signal, to recover a different signal which depends on the input. It can be, for example, a speech recognition task. In this case, a recording of spoken language is fed to the reservoir. The information to be retrieved is the written transcript of what was said.
To execute those tasks, a training procedure is first needed. A set of data, called training set, is used as input data. Those data are processed by the neuron network (the reservoir) and the output is compared to a target signal that we aim to recover. The parameters of the reservoir are tuned in order to get as close as possible to the target. After the training, a validation set of data is used to evaluate the performance of the training procedure. Once those steps achieved, the protocol is able to predict the output signal from any other input signal. In this section, the properties of the reservoir and the training procedure are first presented. Then, we introduce an application of such protocol. Our goal is to predict the laser dynamics studied in chapters 4 and 5 from a simulated reservoir on a computer.

7.1.1 General principle

A general reservoir computing architecture is represented in Figure 7.1. It is composed three main parts:

- **An input layer:** The data are injected in the network via this layer. It connects the input data u to the next layer via a vector W_{in} containing the weights of each connections.

- **A reservoir:** This reservoir layer is the recurrent layer. It is made of a large number N of neurons randomly connected in a graph. This graph is described by the adjacency matrix A.
- **An output layer:** This layer reads the state of the reservoir nodes to decode the information. It is connected to the reservoir via the vector W_{out}.

To process a time sequence $u(t_n)$[1], the signal is first sampled according to $u_k = u(t_n = kT_s)$ where T_s is the sampling time and $k \in [1 : L]$ with L the length of the input sequence. The aim of the protocol is to transform the input data u_k into an output y_k. This is achieved by first injecting u_k into the reservoir, using the input connectivity vector $\mathbf{W}_{in}$ of length N. Those data are then processed in the reservoir, described by the adjacency matrix A of dimension $(N \times N)$. Finally, the data are read from the reservoir via the output connectivity vector $\mathbf{W}_{out}$ of length N. The advantage of RC is the simplicity of the training procedure, as it exploits fixed input weights and fixed recurrent connections. $\mathbf{W}_{in}$ and A are in fact randomly distributed and do not evolve during all the procedure. Hence, the training of the network is performed by only training $\mathbf{W}_{out}$ using a target value $\hat{y}_k$ for each processed value y_k. The accuracy of the training is assessed by computing the normalized root mean squared error (NRMSE) defined by

$$\mathrm{NRMSE} = \sqrt{\frac{\langle (\hat{y}_k - y_k)^2 \rangle_k}{\langle (y_t - \langle y_t \rangle)^2 \rangle_k}}, \tag{7.1}$$

where $\langle\rangle_k$ is the average over the L data points.

A well-trained reservoir allows to reconstruct complex functions, which usually are non-linear combination of the input data. Nonetheless, this requires the reservoir to possess two key features [23]:

- It must be able to non-linearly transform the input signal into a high-dimensional state space. This can be achieved by using a reservoir composed of a large number of non-linear nodes.
- It must possess a fading memory (or short-term memory). It ensures that the current state of the reservoir depends on the recent past inputs and is not affected by inputs far in the past, and in particular is independent of initial conditions. This condition can be achieved by re-scaling the adjancy matrix, which defines the wiring of the reservoir, so that its spectral radius (its largest eigenvalue), ρ_A is smaller than one [87].

---

[1] Note that here we used the notation t_n for the time dependency. As in the previous chapters, it refers to slow variations in time, corresponding to the scale of the noise of the laser.

For a reservoir satisfying the previous conditions, the state of its N nodes is described by a vector r_k at the time step k given by

$$\mathbf{r}_k = f_{NL}\left[\mathbf{W}_{in} u_k + A\mathbf{r}_{k-1}\right], \tag{7.2}$$

where f_{NL} is a non-linear function which depends on the implementation of the reservoir. In the case of simulations, the hyperbolic tangent function is the most commonly used to introduce the non-linearity in the reservoir. $\mathbf{W}_{in}$, the input connectivity vector, is taken from a normal distribution centered at 0 and of variance σ^2. This variance as well as the spectral radius of the adjacency matrix are free parameters that can be tuned to improve the efficiency of the protocol depending on the task.
The output y_k is given by a simple linear combination of the reservoir neuron values:

$$y_k = \mathbf{W}_{out}^T \mathbf{r}_k, \tag{7.3}$$

where T stands for the transposition of the vector column.

As said previously, in RC, only the output weights from $\mathbf{W}_{out}$ need to be trained if the reservoir is designed to fulfill the two previously mentioned conditions. To perform this training, a full set of training data of length L_{train} is taken. The reservoir states $\mathbf{r}_k$ and the target data $\hat{y}_k$ for the full set of training data are regrouped in the vectors

$$R = \begin{pmatrix} \mathbf{r}_1 & \cdots & \mathbf{r}_{L_{train}} \end{pmatrix}, \qquad \hat{\mathbf{Y}} = \begin{pmatrix} \hat{y}_1 \\ \vdots \\ \hat{y}_{L_{train}} \end{pmatrix}. \tag{7.4}$$

The training procedure is performed using the so called ridge regression [97]. It allows to determine the output weights, as a function of the quantities defined above, according to

$$\mathbf{W}_{out}^{\star} = \hat{\mathbf{Y}} R^T \left(RR^T + \epsilon\mathbb{I}\right)^{-1}, \tag{7.5}$$

where $\mathbf{W}_{out}^{\star}$ is the trained set of output weights so that the output data $\mathbf{Y}$ (vector of the output data) approximates the best the target data $\hat{\mathbf{Y}}$. The ridge coefficient ϵ is a free parameter, and $\mathbb{I}$ is the identity matrix of dimension $(N \times N)$.
After the training, a new set of data, called validation set, is taken. Those data are injected in the network, and the output vector $\mathbf{Y}$ is calculated using the trained weights $\mathbf{W}_{out}^{\star}$. As previously stated, the NRMSE given by equation (7.1) is used to determine how close to the target the output signal is. The error, associated to this validation set, quantifies how well the protocol predicts a signal $y(t_n)$ given an input signal $u(t_n)$. The training procedure and the validation are repeated for different values of free parameters: σ the input scaling of the matrix $\mathbf{W}_{in}$, ρ_A the adjacency matrix spectral radius and ϵ the ridge coefficient. Once the best parameters (the ones achieving the lowest error) are found, the protocol can be used for predictions.

7.1.2 Application of RC to noise analysis

To give an example of application of such machine learning protocol, following the idea of [98, 99], we decided to take advantage of the knowledge gathered on the optical frequency comb studied in chapters 4 and 5, to try to predict its dynamics. In those chapters, we saw that the amplitude and phase noises are mainly induced by the pump laser intensity noise. Consequently, in this section, we try to predict the noise on the laser parameters, more precisely on the intensity, the center spectrum and the CEO frequency[2], from the intensity noise of the pump laser.

To perform this task, a simulation of a reservoir is designed on a computer by applying the equations derived in the previous section. As we aim to predict the intensity related dynamics, the intensity fluctuations of the pump power are used as input data. They are measured with a photodiode from a leak in the laser cavity. The output data, used as target, are the fluctuations of each laser parameter, measured using the experimental scheme described in chapter 4. In order to record the pump laser fluctuations simultaneously with the laser fluctuations, we unplug one pixel (one of the lowest on the side of the spectrum) from the acquisition card. We remind that, in chapter 4, a demodulation procedure is employed to measure the noise at a given offset frequency f. Hence, for each analysis frequency, a set of data is available, corresponding to the fluctuations in time of the parameters at the given sideband frequency. Each acquisition is composed of 10000 data points. We take 9000 data points to train the reservoir. The 1000 remaining points are used as a validation set to see how well the algorithm performs. The NRMSEs between the validation set and the target data for the three previously mentioned parameters as a function of the analysis frequency are reproduced in Figure 7.2 a, c, e. It can be seen that the performances depend on the frequency.

The dependency of the NRMSE as a function of the analysis frequency can be understood by determining the degree of correlation between pump intensity fluctuations and the laser parameters fluctuations as a function of the analysis frequency. To this aim, we first compute the cross-correlation, for every offset frequency f, between the measurements:

$$C(\tau)|_f = \int_{\mathbb{R}} \delta I_{pump}(t_n + \tau)|_f \times \delta param(t_n)|_f \, \mathrm{d}t_n, \tag{7.6}$$

where $\delta I_{pump}(t_n)|_f$ represents the pump intensity fluctuations at the offset frequency f and $\delta param(t_n)|_f$ the fluctuations of the laser parameters (which can be the intensity

---

[2] The noise on the repetition rate is lower than the other noises and is not expected to be highly correlated to the pump intensity noise. Thus we do not investigate it in this section.

$\delta\epsilon(t_n)|_f$, the spectrum center frequency $\delta\omega_c(t_n)|_f$ or the CEO frequency $\delta f_{CEO}(t_n)|_f$). Those quantities are taken to be real. The expression above allows to calculate the correlations as a function of the delay between the two quantities. To characterize the correlations between pump intensity fluctuations and the laser parameters fluctuations as a function of the analysis frequency, the maximum of the cross-correlation, from (7.6), as a function of the analysis frequency is calculated according to

$$\mathrm{Corr}(f) = \max_\tau \left[C(\tau)|_f \right]. \tag{7.7}$$

This quantity is calculated for the three laser parameters. The results are reproduced in Figure 7.2 b, d, f.
It can be seen that the frequencies for which the protocol performs the best, correspond to the ones where the quantities are highly correlated, which is understandable. It is worth mentioning that, this maximum happens close to the frequency of the relaxation oscillations, around 1.1 MHz. Again, this is not surprising as those oscillations are directly caused by the pump power fluctuations.

To visualize how well the protocol performs, we plot the mean power noise, the center spectrum and the CEO frequency, predicted after training from the pump laser fluctuations, together with the actual fluctuations of each quantity. We choose the frequency leading to the best prediction according to Figure 7.2. Those data are reproduced in Figure 7.3. It can be seen that, each time the predicted signal is close to the real noise measured experimentally.

As a conclusion, this protocol allows to predict the noise of at least three of the laser parameters, from the fluctuations of the pump laser. Even if this scheme is not perfect and needs refinement to improve the error, we could think of an active stabilization of the laser parameters using this technique. The optical bench, described in the previous chapters, would be used once to characterize all the noises simultaneously. Once the reservoir trained, only the pump intensity fluctuations need to be recorded using a simple photodiode. A feedback loop can then be used to stabilize each parameter.

7.2 Delayed-feedback reservoir computing

In the previous section we presented a numerical approach to the reservoir computing protocol. The aim of this second section is to implement a reservoir computing protocol on a photonic platform. The idea is to use photonic resources to speed up the protocol and make it energy-saving. This is of course the holy grail in this kind of experiment. In this work, we do not aim to be competitive with the state-of-the art protocols but to test the feasibility of an architecture and its possible advantages. Indeed, different

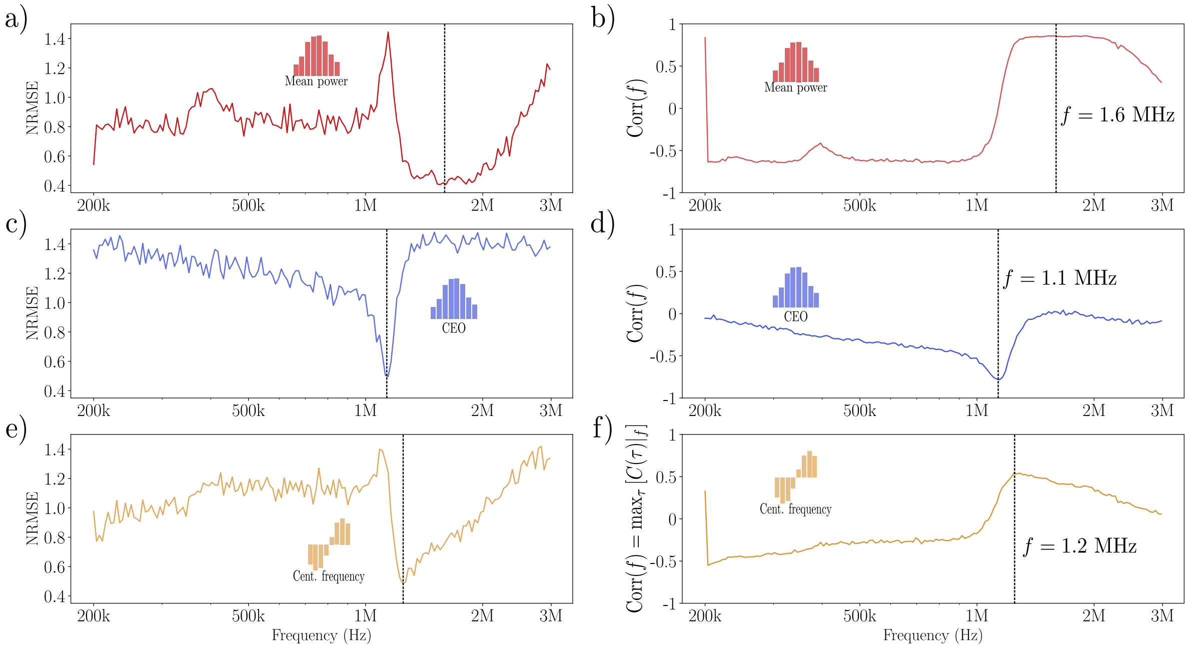

Figure 7.2 – **NRMSE and cross-correlations between pump noise and intensity, CEO frequency and center frequency noise**. Given the intensity noise of the pump laser as input data, we aim to teach the protocol to recover the noise on the laser parameters. a, c and e represent the NRMSE on the prediction of the noise on the intensity, CEO frequency and center spectrum of the laser depending on the analysis frequency. b, d and f represent the maximum of the cross-correlation from equation (7.7) as a function of the analysis frequency. The lowest error corresponds to the maximum correlation (or anti-correlation) which is achieved around the frequency of relaxation oscillations. The frequency at which this maximum is achieved is marked by the dashed black line.

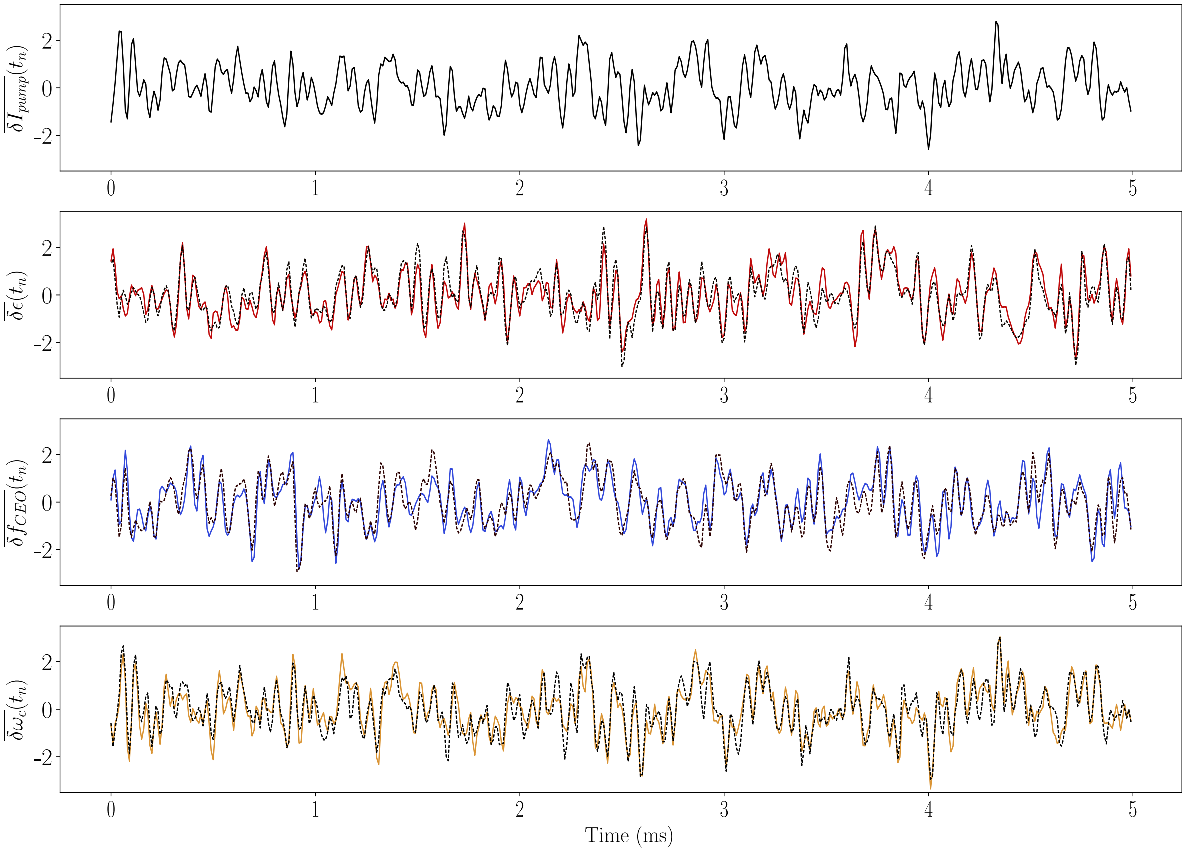

Figure 7.3 – **Prediction of the noise on the laser parameters from the pump intensity noise**. On top is represented the intensity fluctuations of the pump laser as a function of the time. Above are represented, from top to bottom, the intensity fluctuations $\delta\epsilon(t_n)$, the CEO frequency fluctuations $\delta f_{CEO}(t_n)$, and the center spectrum ones $\delta\omega_c(t_n)$. In dashed is represented the prediction of the noise of each parameter obtained from the pump intensity fluctuations after training of the reservoir. Each signal is normalized before processing (hence the line above) to be given as a z-score, i.e. we subtracted the mean value and divided by the variance of the signal. This procedure is used to increase the performances of the protocol. Each prediction is made for the frequency at which the lowest error is reached. For the intensity $f = 1.6$ MHz and NRMSE $= 0.4$, for the CEO frequency $f = 1.1$ MHz and NRMSE $= 0.5$, and for the center spectrum $f = 1.2$ MHz and NRMSE $= 0.5$.

photonic implementations of RC can be found in the literature [23, 91, 92, 93, 24]. We chose the approach known as delayed-feedback reservoir computing, similar to the one introduced in [23]. We implement the protocol via the tools used along this manuscript: the optical frequency comb and the homodyne detection. In particular, the pulses of the laser are used as nodes for the reservoir in which the input data are injected. The information is encoded in the phase of each pulse and decoded from their quadrature using a homodyne detection. In this section, we present the general idea of the delayed-feedback reservoir computing architecture. Then, the experimental implementation is detailed. Finally, the ability of the protocol to reconstruct complex functions is assessed using the information processing capacity.

7.2.1 General description: memory and links

We start by a general description of the delayed feedback reservoir computing architecture as well as the techniques used to create the reservoir and wire it. The scheme illustrating the principle of the protocol is represented in Figure 7.4. Contrary to the previous architecture, the reservoir is composed of virtual neurons distributed in time. It means that at a given time, only one neuron is accessible for encoding the information. Identically, only one neuron at a time is accessible for decoding the information. The reservoir is formed by using a delayed train of pulses corresponding to N neurons. Each neuron is separated from the others by a delay θ. In the following, the neurons are numerated from 1 to N and noted with the index j. The data points u are numerated by the index k, as previously. They are separated in time from the others by the time-span of the reservoir, τ, equivalent to its size, given by $\tau = N\theta$. Hence, the node $r_{j,k}$ corresponds to the time $t_n = k\tau + j\theta$.

In order to inject the data in the reservoir, each data point u_k must be distributed in time on every neuron in the delay-line. This is achieved by applying a mask function $m(t_n)$ to u_k. This mask is composed of N individual steps of duration θ so that $m_j = m(t_n = j\theta)$. The values of those steps are randomly taken from a normal distribution. This mask is similar to the input connectivity matrix W_{in} but distributed in time. Once the data injected, the reservoir can be built. More precisely, we need to provide memory to the reservoir and to wire it.

7.2.1.1 Memory

In order to provide memory to the reservoir, recurrent connections need to be made between the nodes. In the delayed-feedback architecture, this memory is implemented via a feedback. This feedback consists in injecting the data back into the reservoir after on delay round trip τ as illustrated in Figure 7.4. In these conditions, the state of the node j of the reservoir for the step k is described by the vector $r_{j,k}$ given by

$$r_{j,k} = f_{NL}\left[\beta m_j u_k + \alpha r_{j,k-1}\right], \tag{7.8}$$

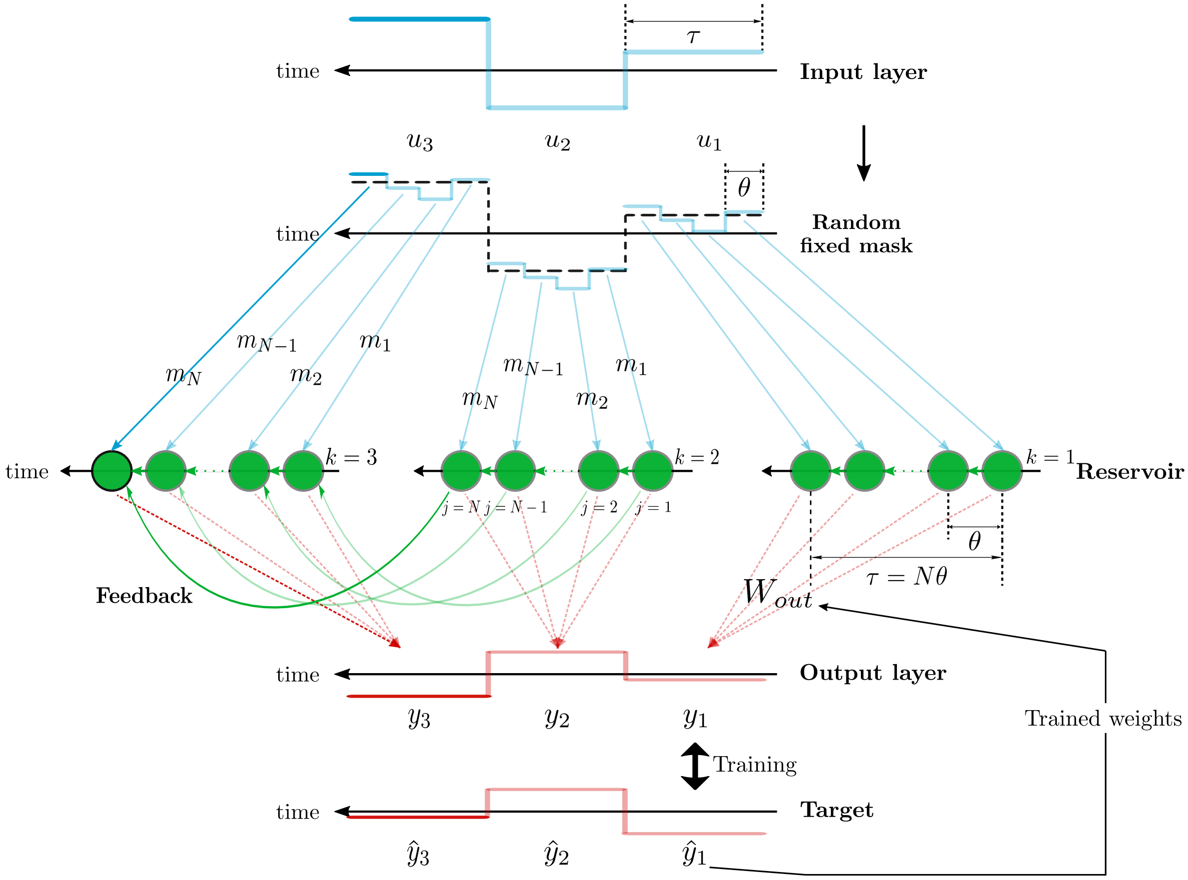

Figure 7.4 – **General scheme of a delay-based reservoir computing architecture.** In this configuration, the reservoir is demultiplexed in time so that at a given time, only one node is accessible (the other nodes, from the past, are drawn in transparency). This reservoir is composed of N nodes separated in time by θ. The injection of the data u_k is made possible by the application of a mask function $m(t_n)$ which plays the role of the input vector $\mathbf{W}_{in}$. The nodes are linked together (green arrows) in time using either a system with a finite bandwidth or using a shift between the delay and and injection of the data. The memory of the system is provided by the feedback of delay τ which plays the role of the recurrent connection. The training procedure is similar to the general configuration described in section 7.1.1.

where α and β are gain parameters that can be used to optimize the protocol; m_j is the value of the j^{th} step of the mask; f_{NL} is a non-linear function. In the simulation from the previous section, this function was a hyperbolic tangent. In this architecture, we will see that the non-linearity is introduced by the homodyne detection and thus is given by a sine function. The term $\alpha r_{j,k-1}$ corresponds to the data re-injected after the feedback. It connects two nodes j from two different time steps k and $k-1$. We can clearly see here that it provides memory to the system by re-injecting in the reservoir information depending on the input signal in the past.

7.2.1.2 Links

To create the network constituting the reservoir, links need to be created between the different nodes. Two approaches can be applied by either using the feedback loop or the system dynamics. The first approach consists in desynchronizing the injection of the data from the feedback [23, 92]. The other approach consists in using a system with a given response time, using for example a filter in the detection [91]. In this case, the network shape depends on the delay between two nodes and the characteristic time of the system. We briefly review the two approaches and the expressions describing the state of the reservoir in each case.

Unsynchronized regime: In this configuration, the time at which the data are injected back into the reservoir is shifted from the duration of the feedback delay τ. Thus, the delay after which the data are reinjected is $\tau' = \frac{N}{N+1}\tau$. This shift connects the node j at time $t_n = k\tau + j\theta$ (with $\tau = N\theta$) to the node $j+1$ at time $t_n = (k+1)\tau + (j+1)\theta$ as illustrated in figure 7.5. Using the same principle as equation (7.8), the state of the j^{th} node at the step k is given by

$$r_{j,k} = \begin{cases} f_{NL}\left[\beta m_j u_k + \alpha r_{j-1,k-1}\right] & \text{for } 2 \leq j \leq N \\ \\ f_{NL}\left[\beta m_j u_k + \alpha r_{N,k-2}\right] & \text{for } j = 1. \end{cases} \tag{7.9}$$

It can be seen that, in this configuration, the recurrent connections are created by the delay and the shift in time. At each time step k, one node j receive information from the node $j-1$ from time step $k-1$.

Non instantaneous system: In this configuration, the system is supposed to have a given response time to the injection of the data. To describe how connections can be made, let us assume a system with a characteristic time T_{BW}, given for example by the bandwidth of a filter at the detection. Because of the limited response time, the state of the j^{th} node of the reservoir can depend on the state of the previous node. Indeed, this system tends to reach its equilibrium after an exponential decay of the previous

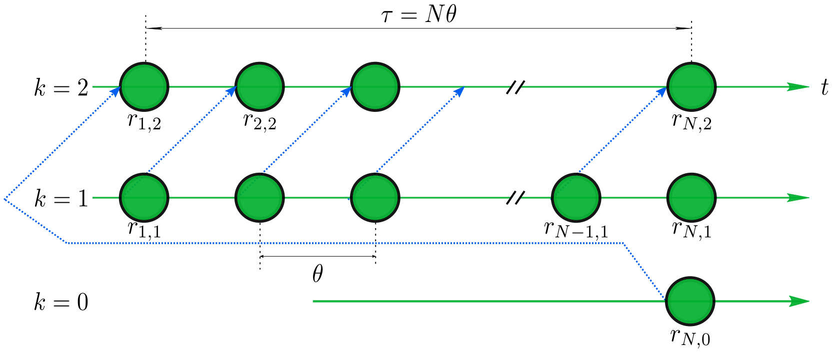

Figure 7.5 – **Graph representation of the unsynchronized configuration.** By shifting the time at which the data are re-injected with respect to the delayed feedback τ, connections are made between different nodes of successive time steps.

value and an exponential growth of the new one. The rate of the exponential is given by the ratio between the time separating the nodes θ and the characteristic time of the system T_{BW}. Consequently, the state of the j^{th} node for the time step k is given by

$$r_{j,k} = r_{j-1,k}e^{-\theta/T_{BW}} + \left(1 - e^{-\theta/T_{BW}}\right) f_{NL}\left[\beta m_j u_k + \alpha r_{j,k-1}\right]. \tag{7.10}$$

It can clearly be seen that the state of the node $r_{j,k}$ depends on the state of the previous node $r_{j-1,k}$ due to the response time of the system. In addition it depends, as in equation (7.8), on the input data u_k, as well as the state of the node $r_{j,k-1}$ from the previous time step due to the feedback. The graph created by this procedure is represented in Figure 7.6. Each node is connected to a few previous nodes with different strengths. Those connections depend on the ratio θ/T_{BW}. Changing this ratio modifies the influence of a given node on the future ones. Consequently, this parameter can be tuned to change the shape of the graph and optimize the protocol. In an experiment, this parameter is changed by either changing the delay between the nodes or by changing the response time of the system. In the next section we will see how, using this configuration, we can implement a reservoir computing protocol on our photonic platform. Note that both approaches can also be combined.

7.2.2 Experimental implementation

As previously mentioned, the implementation of this photonic reservoir computing relies on the use of an optical frequency comb and a homodyne detection. Note that a frequency comb is not required for the implementation of the pulsed approach of the reservoir computing. At no point of the experiment the pulses are temporally resolved. Therefore, lasers emitting longer pulses, with possibly higher repetition rates (to speed-up the process), could in principle be used. However, for this experiment we use the laser available in the lab, which happens to be a frequency comb. In addition, we will see in the next chapter that the spectral degree of freedom provided by the frequency

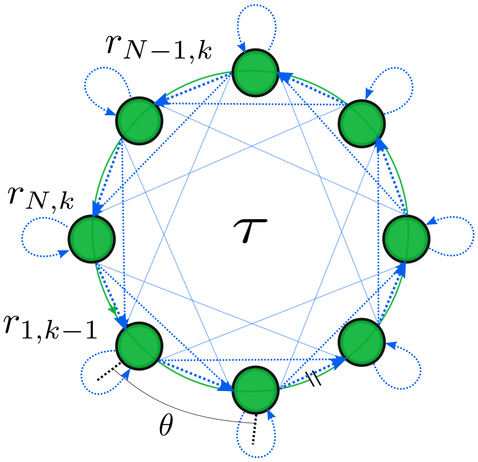

Figure 7.6 – **Graph representation of the system with a finite bandwidth.** Due to the finite response time of the system, each node from the reservoir is connected to the previous ones. The number of previous nodes influencing the current one depends on the ratio between the time separating two nodes, θ, and the bandwidth of the system T_{BW}.

comb could be exploited in a quantum version of the protocol.

In this experiment, each pulse from the laser is used as a neuron from the reservoir. Thus, the separation time θ is set by the separation in time between two successive pulses which is $\theta = T_r = 1/f_r \simeq 6.4$ ns, where $f_r = 156$ MHz is the repetition rate of the laser. The data are recovered by measuring each pulse individually. Each pulse counts as one data point corresponding to the state $r_{j,k}$ of the neuron which, multiplied by the output weight matrix $\mathbf{W}_{out}$, gives y_k. In order to introduce the non-linearity in the system, we choose to use a homodyne detection as a reading element of the nodes state. As we will see, by encoding the information in the phase of the pulses, the homodyne, which gives access to the quadratures of the electric field as seen in section 1.2.3, leads to a signal proportional to the sine (or cosine) of the injected data, introducing the non-linearity needed. In the following we describe the encoding of the data, the decoding and the wiring of the reservoir. The detailed experimental setup is then presented. Finally we test the architecture using a benchmark task known as NARMA5.

7.2.2.1 Encoding of the data

To describe the experiment, let us remind the expression of the electric field of one pulse given by equation (2.13): $E^{(+)}_{\text{pulse}}(t) = \mathcal{E}_0 a(t) e^{-i\omega_0 t}$. Even though a high bandwidth detector is used to measure the field pulse by pulse, this detector is not fast enough to resolve the pulse shape. In addition, one data point is taken for each pulse. Thus, we consider that each pulse has a constant amplitude a. The information, i.e the input data, can be encoded in the two degrees of freedom of the pulses, their amplitude or their phase. In [95], Nokkala et. al. investigated several RC protocol architectures with different encoding for the input data. In particular, the encoding into the amplitude or the phase of a coherent state was studied. They demonstrated that the phase encoding leads to better performances. Therefore, using the fact that under certain conditions the laser field can be assimilated to a coherent state, we choose to encode the information in the phase of the pulses. Hence, the field of the j^{th} pulse at the time step k, is multiplied by a phase term containing the injected data according to

$$E_{j,k}^{(+)} = \mathcal{E}_0 a \exp\left[2i\pi\left(\beta m_j u_k + \alpha r_{j,k-1}\right)\right],^{3} \tag{7.11}$$

where $E_{j,k}^{(+)}$ corresponds to the pulse at time $t_n = k\tau + j\theta$.

7.2.2.2 Extracting the information

In order to read the information encoded in the phase, the quadratures of each pulse are measured with a high bandwidth homodyne detection. If the homodyne is set to measure the p quadrature, the signal measured is proportional to the argument of expression (7.11). Consequently, we define the state of one node $r_{j,k}$ of the reservoir as the p quadrature of the pulse $E_{j,k}^{(+)}$ given by equation (7.11) i.e

$$r_{j,k} = a \sin\left[2\pi\left(\beta m_j u_k + \alpha r_{j,k-1}\right)\right]. \tag{7.12}$$

It is now clear why a phase encoding has been chosen. This encoding provides non-linearity to the protocol via the homodyne detection, which would not have been the case with an amplitude encoding.

7.2.2.3 Wiring the reservoir

Concerning the wiring of the reservoir, the most natural configuration is the non-instantaneous one. Indeed, the homodyne detector has a finite bandwidth of a few hundred MHz, which is a bit slower than the pulse repetition rate corresponding to the node separation ($\theta = T_r$). This bandwidth corresponds to the parameter T_{BW} of the protocol. In addition, low-pass filters can be added after the detector to reduce even more the bandwidth and tune the parameter θ/T_{BW} to change the graph shape. Consequently, the state of the node j at time step k is given by

$$r_{j,k} = r_{j-1,k} e^{-T_r/T_{BW}} + \left(1 - e^{-T_r/T_{BW}}\right) a \sin\left[2\pi\left(\beta m_j u_k + \alpha r_{j,k-1}\right)\right]. \tag{7.13}$$

7.2.2.4 Experimental setup

The scheme of the experimental setup is represented in Figure 7.7. As in a classical homodyne detection, the field from the laser is separated in two, a weak beam, the signal and a strong one, the local oscillator (LO). The phase encoding is achieved using an electro-optic modulator (EOM, iXblue NIR-800-LN-0.1) on the signal arm. By

---

[3] We omitted the term $e^{-i\omega_0 t}$ as it does not appear in the quadrature definition next (see section 1.2.3).

applying a voltage to this modulator, the phase of each pulse can be modified to encode the information. This EOM is driven from a computer using an arbitrary waveform generator (AWG, Teledyne SDR14). Regarding the delay, for simplicity, we decided to implement the feedback electronically as in [23] and not optically as in [93]. In fact, an optical feedback is hard to implement in this experiment as it requires an optical loop. These loops are usually built using fiber elements, which is not recommended with femtosecond pulses mainly due to chromatic dispersion. As long delays are difficult to handle in free space, we have chosen the electronic feedback. This is achieved by first, detecting the electric field after the encoding, with a homodyne detection, which is equivalent to measuring the nodes of the reservoir. The detection is assured by a home made high bandwidth balanced detector. Its bandwidth is approximately 100 MHz, details about this detector can be found in [71]. To create the links between the nodes, a low pass filter is introduced after the detection. The cutoff frequency can be changed to optimize the protocol. After detection, the signal measured by the detector is then split in two. A small part is gathered for processing and the other part is sent in a long coaxial cable to create the reservoir. It is finally mixed with the input signal from the AWG to be sent to the EOM, creating the feedback loop. At the time of the experiment, the longer cable in the lab was approximately 40 m, corresponding to only 35 nodes in the reservoir which is not a lot. As a comparison, the predictions in section 7.1 have been made with a reservoir made of 700 nodes.

7.2.2.5 Test of the architecture

Even though the experiment is not perfect, due to the limited number of nodes in the reservoir, we tested it using a benchmark task known as NARMA5 (derived from the NARMA10 introduced in [100]). The task consist in drawing the input data u_k from a uniform distribution in the interval $[0, 0.5]$ and use as a target the function

$$\hat{y}_k = 0.3\hat{y}_{k-1} + 0.05\hat{y}_{k-1}\left(\sum_{j=1}^{5}\hat{y}_{k-j}\right) + 1.5u_{k-1}u_{k-5} + 0.1. \tag{7.14}$$

This function is non-linear and depends on the five previous data points. Hence it allows to test the memory and the non-linearity of the protocol. A set of reconstructed data can be seen in Figure 7.8. The best error achieved with this experiment is a NRMSE of 0.44 for a system bandwidth of 22 MHz. The error is far from the best experimental realizations found in the literature where the NRMSE can reach at least 0.1. Many different elements can be improved to try to reach a lower error. For example, a longer cable can be used for the delay to create a larger reservoir. Another direction to explore is the implementation of the delay between the injection of the data and the feedback, as presented previously. As we will see in the next section, this configuration may lead to better performances.

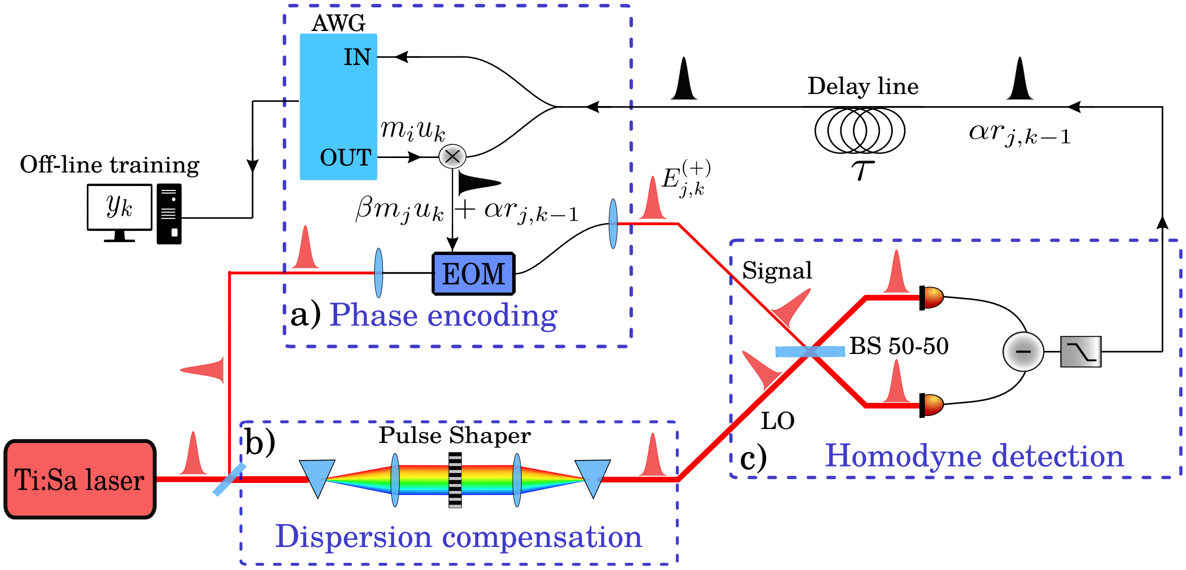

Figure 7.7 – **Experimental scheme of the delay-based reservoir computing architecture**. The field of the same Ti:Sa laser from the previous chapters is separated in two. The weak beam, the signal, is sent into an electro-optic modulator (EOM) controlled by an arbitrary waveform generator (AWG). Information is encoded in the phase of each pulse by applying a voltage to the EOM. The strong beam, the local oscillator, is sent into a pulse shaper to match the dispersion introduced by the EOM on the other arm. Both beams are combined on a 50-50 beam-splitter and detected by a high bandwidth balanced detector. After low pass filtering, to control the parameter T_{BW}, the signal is sent into a long coaxial cable to create a delay. A part of this signal is then mixed with the input data to create the feedback. The other part of the signal is acquired by the AWG to proceed to the off-line training of the output weights.

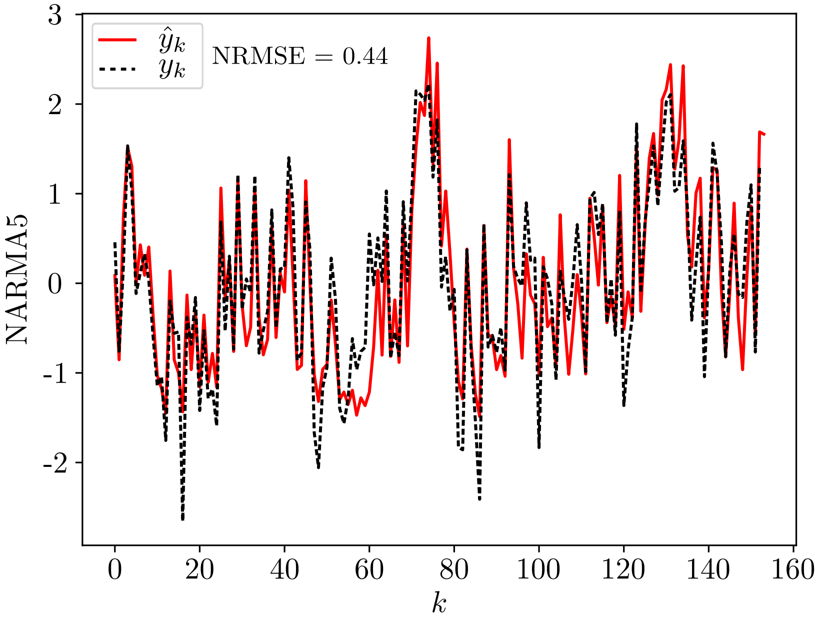

Figure 7.8 – **Narma 5 benchmark task.** In plain red, the target function given by equation (7.14). In dashed black, the predicted function after a learning procedure over 2500 data points. The bandwidth of the system is set to 22 MHz by using a low pass filter.

7.2.3 Capacity

Other tasks can be used to benchmark the protocol as well. Alternatively, a quantity known as information processing capacity (or capacity for short) can be used to characterize the protocol, task independently. Initially introduced by Dambre et. al. [25], the capacity quantifies the ability of a system to retain past input samples, generally given by the linear capacity, and to perform non-linear transformation of the data, given by the non-linear capacity. Those two quantities will be presented later. Many studies have been conducted in the literature using the capacity as a quantifier of the performances of the protocol. In [101], different input encoding, non-linearity and output decoding are compared by calculating the capacity of each scheme. In this section, we present the procedure to calculate the capacity. Then, the capacity of the experimental architecture is calculated and finally compared to simulations.

7.2.3.1 Calculation of the capacity

To compute the information processing capacity of a protocol, the input data u_k are taken from a random uniform distribution between -1 and 1. In order to properly calculate this capacity, a set of orthogonal functions must be chosen as targets functions $\hat{y}$ [25]. For this reason, as in other studies, we chose the Legendre polynomials as target functions so that

$$\hat{y}_k = \mathcal{P}_{deg}(u_k), \tag{7.15}$$

where *deg* is the degree of the polynomial. As an example, the four first polynomials are given by

$$\mathcal{P}_1(u_k) = u_k \qquad \mathcal{P}_3(u_k) = \frac{1}{2}(5u_k^3 - 3u_k)$$
$$\mathcal{P}_2(u_k) = \frac{1}{2}(3u_k^2 - 1) \qquad \mathcal{P}_4(u_k) = \frac{1}{8}(3u_k^4 - 30u_k^2 + 3)$$

After training, the reservoir is fed with another set, the validation set, of input data u_k. The capacity is derived from the NMSE when trying to predict the corresponding polynomials of different degrees. Mathematically, the capacity is given by

$$c = 1 - \frac{\langle(\hat{y}_k - y_k)^2\rangle_k}{\langle(\hat{y}_k - \langle y_k\rangle)^2\rangle_k} = 1 - \text{NMSE}^2. \tag{7.16}$$

It is important to note that the capacity is an additive quantity. Because it is calculated using orthogonal functions, the capacity of each degree brings independent information about the system. In particular, the capacity is usually separated into two contributions, the linear and non-linear contributions. The total capacity of the system is then the sum of both contributions. In what follows we define each of these contributions and briefly introduce the method to calculate it.

Linear capacity: The linear capacity allows to characterize the memory of the protocol. Its aim is to characterize how many past inputs the reservoir can retain. The more inputs the reservoir retains, the higher the memory. This linear capacity is computed by taking as a target function the delayed Legendre polynomial of first degree. More precisely, if the input data is u_k, the target function is $\hat{y}_k = \mathcal{P}_1(u_{k-\mathcal{T}_d}) = u_{k-\mathcal{T}_d}$ where $\mathcal{T}_d \in [0 : L]$ with L the length of the input sequence. The total linear capacity is given by the sum of the capacities given by equation (7.16) over all the delays $\mathcal{T}_d$ possible i.e

$$C_{lin} = \sum_{\mathcal{T}_d}\left(1 - \frac{\langle(\mathcal{P}_1(u_{k-\mathcal{T}_d}) - y_k)^2\rangle_k}{\langle(\mathcal{P}_1(u_{k-\mathcal{T}_d}) - \langle y_k\rangle)^2\rangle_k}\right). \tag{7.17}$$

Non-linear capacity: The non-linear capacity informs on the ability of the protocol to reconstruct highly non-linear functions. Similarly to the linear capacity, it is calculated by using as a target function $\hat{y}_k = \mathcal{P}_{deg}(u_{k-\mathcal{T}_d})$ with $deg > 1$, and summing over all possible delays $\mathcal{T}_d$. The total non-linear capacity is the sum over all degrees *deg*. It is important to note that products of polynomials must also be considered when computing the capacity. As an example, the capacity for the degree 2 is given by calculating first the sum of the individual capacities over the delays

$$C'_{NL2} = \sum_{\mathcal{T}_d}\left(1 - \frac{\langle(\mathcal{P}_2(u_{k-\mathcal{T}_d}) - y_k)^2\rangle_k}{\langle(\mathcal{P}_2(u_{k-\mathcal{T}_d}) - \langle y_k\rangle)^2\rangle_k}\right). \tag{7.18}$$

To this contribution must be added the contributions of the product of polynomial of first degree

$$C''_{NL2} = \sum_{\mathcal{T}_{d1}} \sum_{\mathcal{T}_{d2}>\mathcal{T}_{d1}} \left(1 - \frac{\langle (\mathcal{P}_1(u_{k-\mathcal{T}_{d1}})\mathcal{P}_1(u_{k-\mathcal{T}_{d2}}) - y_k)^2 \rangle_k}{\langle (\mathcal{P}_1(u_{k-\mathcal{T}_{d1}})\mathcal{P}_1(u_{k-\mathcal{T}_{d2}}) - \langle y_k \rangle)^2 \rangle_k} \right). \tag{7.19}$$

The total capacity of degree 2 is given by the sum of the two contributions $C_{NL2} = C'_{NL2} + C''_{NL2}$. Note that the higher the degree, the more complicated the calculation of the contributions. In fact, the calculation would be infinitely long if no conditions were applied on the values of the capacity, since all the delays and degrees possible would need to be computed. Consequently, as in [25, 95], we apply a threshold to the contributions of the capacity. This threshold is set for a NRMSE of 0.3. Above this value, the capacity is set to 0. This threshold allows to reduce the time needed for the calculation and prevent any over-estimation of the capacity.

The total information processing capacity is given by the sum of the linear and non-linear capacities. It has been demonstrated that this capacity is bounded by the total number of linearly independent variables of the system [25] which is usually given by the number of neurons of the reservoir. If a protocol reaches this bound, it implies that the dynamical system has fading memory [25], fulfilling the condition introduced in section 7.1.1. Note that because the capacity is bounded by the total number of neurons of the system considered, it can be normalized by this number so as to compare different protocols. In the following sections, we calculate the capacity of the protocol presented in section 7.2.2. At first we use a simulation of the experiment. It allows us to compare the two approaches developed in section 7.2.1, the unsynchronized and the non instantaneous system. In a second time, the experimental capacity is calculated.

7.2.3.2 Simulated capacity

In this section, we simulate the experiment by using the expressions (7.12) and (7.10) to mimic the evolution of the state of the reservoir for a system with a finite response time for a phase encoding and a decoding ensured by a homodyne detection with a bandwidth given by T_{BW}. The aim is to compare two wiring configurations of the reservoir. First, only the bandwidth of the system is used to create links in the reservoir. Secondly, we consider the configuration where a time shift is introduced between the feedback and the injection of the data (the unsynchronized configuration), in addition to the limited bandwidth. As a matter of fact, Ortin and Pesquera demonstrated that the capacity depends on the system response given by the ratio $\theta/T_{BW} = T_r/T_{BW}$. Furthermore, they demonstrated that combining this approach to a desynchronization of the injection of the data can lead to better performances [102]. Finally, we calculate the full capacity of the protocol.

Capacity vs bandwidth: As seen in section 7.2.2, the experimental implementation of the reservoir corresponds to the non-instantaneous configuration. The time response is given by the ratio between the nodes separation and the detection bandwidth: T_r/T_{BW}. In order to determine the best parameter to use in the experiment, we simulate the protocol for various values of this ratio. In Figure 7.9 a and b in black, are represented the linear capacity, and non-linear capacity of degree 3, respectively, as a function of the ratio T_r/T_{BW}. The same result as in [102] is found. Increasing the detection bandwidth changes the capacity, which ultimately leads to its deterioration. This is due to a decrease of the links strength as the bandwidth increases. In our simulations, performed with 200 nodes, the best performances are achieved for a ratio $T_r/T_{BW} \simeq 0.1$. Since the only free parameter in the experiment is the detection bandwidth T_{BW} (the separation between pulses cannot be changed), it corresponds to a detection bandwidth of $0.1T_r$. Thus, in order to achieve the best performances, a low-pass filter with a cut-off frequency of 15 MHz seems to be the most appropriate.
Alternatively, as in [102], the desynchronization of the input and the output data can be combined to the limited bandwidth detection. The capacities of this hybrid configuration are also represented in Figure 7.9 a and b in blue, for the linear capacity, and non-linear one of degree three. It can be seen that, if the delay τ is longer than the data injection time τ', the capacity can be improved, even when the full bandwidth of the system is used. Consequently, it seems that the wiring of the reservoir based on the hybrid configuration provides more memory than the one based on the bandwidth of the system only.

Full capacity of the protocol: The full capacity is calculated using the same principle as described in equations (7.17), (7.18) and (7.19) for all the degrees of the polynomial. We apply it for the two previously mentioned configurations. The total capacities are represented in Figure 7.10. These capacities are normalized to the number of neurons used (200 for the simulations). It can be noted that, as expected from Figure 7.9, the hybrid configuration leads to a higher capacity and even seems to saturate the bound.

7.2.3.3 Experimental capacity

To test our experimental implementation of reservoir computing, we calculate the experimental capacity. To this aim, the input data are drawn from a uniform distribution and sent to the EOM via the AWG. The data, once encoded in the phase of the pulses, are extracted using the homodyne detection. The protocol is trained to reconstruct the polynomials of various degrees for different delays between the input data and the target data. As said previously, at the time, the delay introduced to form the reservoir was really short. It implies that the reservoir is composed of only 35 neurons. Consequently a lower capacity is expected compared to the simulations. In addition, the

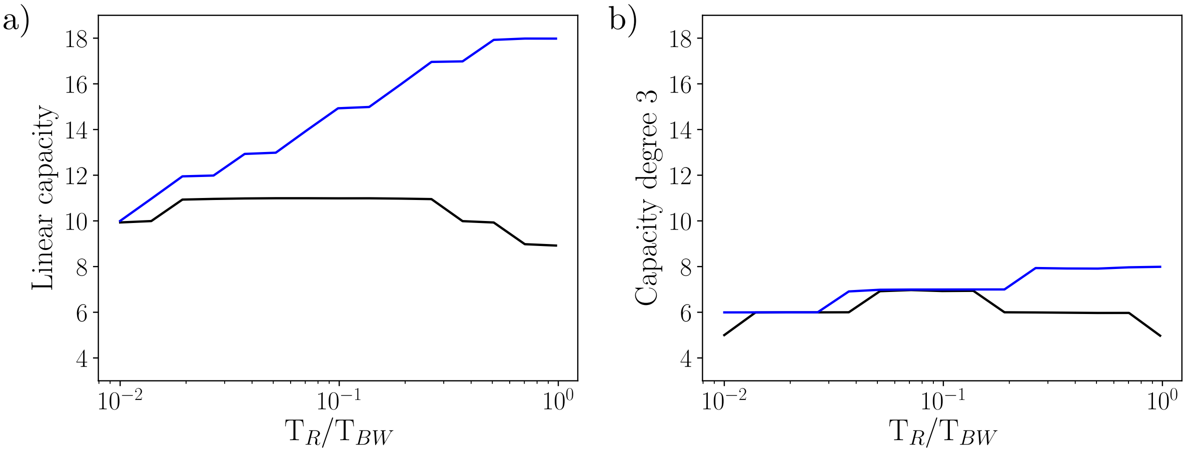

Figure 7.9 – **Linear capacity and non-linear capacity of degree 3 vs bandwidth.** a) Linear capacity as a function of the response time of the system T_r/T_{BW}. b) Non-linear capacity for a polynomial of degree 3. In black the configuration where the links between the nodes are created by the bandwidth of the system. In blue the hybrid configuration where a shift is introduced between the data injection time and the delay. The hybrid configuration leads to higher capacities. The simulations are done using 200 nodes for the reservoir.

hybrid configuration has not been implemented, so only the dependency of the capacity on the detection bandwidth is investigated. Low-pass filters are placed after the detectors to change the response time of the system. The capacity is calculated for T_{BW} = [10 MHz, 22 MHz, 48 MHz, 98 MHz]. The capacity values are reproduced in Figure 7.10. It can be noted that the capacity depends on the bandwidth of the detection, as expected from the simulations. The higher capacity is achieved for a bandwidth of 48 MHz (so $\simeq 0.3T_r$), which is a bit different from the value of 15 MHz found using the simulations. This can be explained by the fact that the number of neurons between the simulations and the experiment is really different (200 vs 35). In addition, not all the parameters can yet be tuned experimentally. This is the case, for example, of the feedback strength α which requires a variable electronic attenuator.

Summary

In this chapter we introduced a machine learning protocol called reservoir computing. This protocol can be used to process time series. Consequently, using a simulation of a reservoir, we predicted the intensity related dynamics of a frequency comb. Furthermore, this protocol is well suited for photonic implementations. We proposed an architecture based on a pulsed laser and a homodyne detection. This scheme seems to

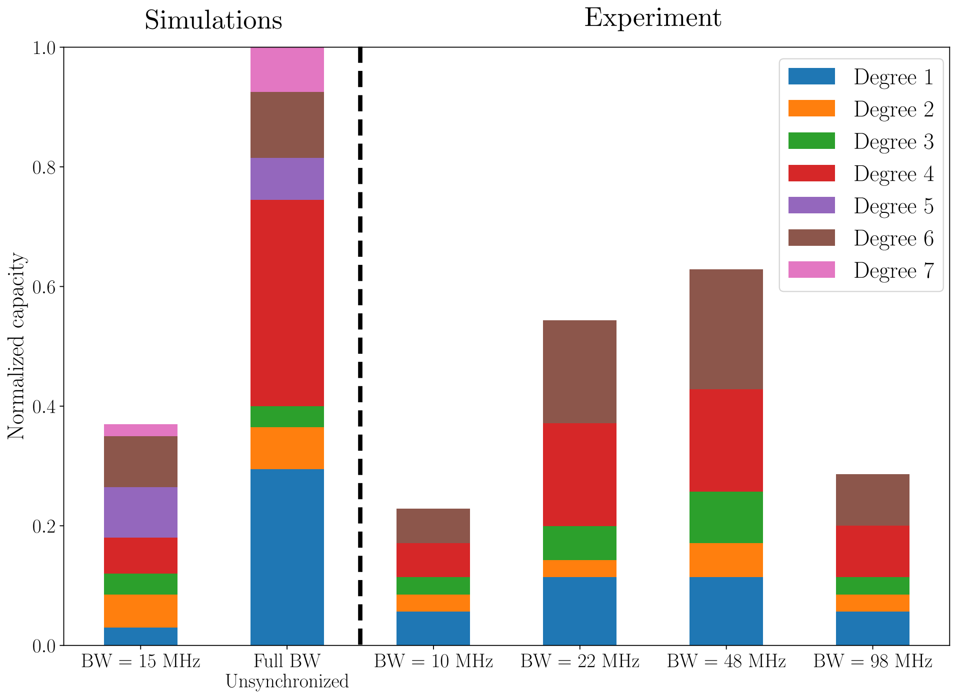

Figure 7.10 – **Simulated and experimental capacity.** On the left are represented the capacity of the simulated protocol without and with a time shift between feedback and data injection. On the right, the capacity calculated experimentally for different detection bandwidths. To each color corresponds a degree of capacity from 1 to 7. Experimentally, the highest total capacity is achieved for a system bandwidth of 48 MHz which is different from the 15 MHz found using the simulations. This is mainly due to the difference between the parameters of the protocols, and particularly the number of neurons (200 vs 35).

be able to process non-linear functions. However, the number of nodes in the reservoir is small which limits the capacity of the protocol. As an improvement, a longer cable in the feedback can be used in order to increase the size of the reservoir. In addition, the hybrid configuration should be implemented as it seems to lead to an important increase of the capacity, as demonstrated by our simulations.

Chapter 8

Toward quantum reservoir computing

Contents

8.1 Single mode squeezing 161
- 8.1.1 Parametric down conversion 162
- 8.1.2 Quantum correlations 163

8.2 Multimode squeezing 165

8.3 Single pass squeezing 166
- 8.3.1 Experimental scheme 166
- 8.3.2 Results 168

In the previous chapter we introduced a reservoir computing protocol based on photonic resources. As mentioned in the introduction, the long term objective of the project is to implement a quantum version of this protocol. To this end, a source of quantum states is needed to be used as a platform for the reservoir. In this chapter we present such a source based on a non-linear process, the parametric down conversion. Using a particular configuration of this process, the so called squeezed states of light can be produced. We will see that, combining two sources of squeezed states allows to create quantum correlations between laser pulses. Those quantum links can be used in the reservoir to replace the classical links created by the bandwidth of the detector. Note that this project was the main project of another PhD student and I mainly took part in the design of the experiment and the measurements. Consequently, this chapter is kept as succinct as possible.

8.1 Single mode squeezing

In section 1.3.2, we introduced the coherent states. We saw that those states saturate the Heisenberg inequality, i.e $\mathrm{Var}\left[\hat{x}\right]\mathrm{Var}\left[\hat{p}\right] \geq 1$. In this section, we present another family of states that saturates this inequality, the squeezed states.

8.1.1 Parametric down conversion

Squeezed states of light can be created using parametric down conversion (PDC), a non-linear process occurring when light with a high intensity propagates in a birefringent medium with a non-zero second order susceptibility χ^2. In the visible[1], this process is commonly achieved using, for example, BBO (β-Barium Borate) non-linear crystals or KTP (Potassium Titanyl Phosphate) waveguides. In this process, one photon from an incident field, called pump, at frequency ω_p and wavevector k_p, is converted into two photons of lower frequencies, the signal, at frequency ω_s and wavevector k_s, and the idler, at ω_i and k_i. This process is governed by the energy conservation, $\omega_p = \omega_s + \omega_i$, as well as the phase-matching condition $k_p = k_s + k_i$. In this study, we consider the degenerate case where the signal and the idler have the same frequency, i.e. $\omega_s = \omega_i$, and same wavevector, i.e. $k_s = k_i$. In addition, we consider the so called type 0 PDC, where all the fields have the same polarization. The single mode degenerate PDC process can be described by the Hamiltonian[2] [30]

$$\hat{H}_{PDC} = ig\left(\hat{a}_s^{\dagger 2} - \hat{a}_s^2\right), \tag{8.1}$$

where g is the gain of the non-linear process, and $\hat{a}_s$ the creation operator of the signal (identical to the idler one in the degenerate configuration). The unitary evolution operator associated to this Hamiltonian is given by

$$\hat{U} = \exp\left[-\frac{i}{\hbar}\hat{H}_{PDC}\; t_{int}\right] = \exp\left[\frac{g}{\hbar}\left(\hat{a}_s^{\dagger 2} - \hat{a}_s^2\right) t_{int}\right], \tag{8.2}$$

where t_{int} is the interaction time with the non-linear crystal. This operator is called squeezing operator. This name becomes clear by considering the evolution of the quadratures of the electric field under this operator. Assuming that the signal field of frequency ω_s propagates inside a non-linear crystal, it can be shown that its quadratures $\hat{x}_0$ and $\hat{p}_0$ are transformed according to [30]

$$\begin{aligned} \hat{x}_s &= e^{-r}\hat{x}_0, \\ \hat{p}_s &= e^{r}\hat{p}_0, \end{aligned}$$

where $r = 2gt_{int}/\hbar$ is the squeezing parameter. It can be seen that, depending on the sign of r, one quadrature is amplified while the other is deamplified. As a consequence, the variance of the quadratures after the crystal are given by

$$\begin{aligned} \mathrm{Var}\left[\hat{x}_s\right] &= e^{-2r}\mathrm{Var}\left[\hat{x}_0\right], \\ \mathrm{Var}\left[\hat{p}_s\right] &= e^{2r}\mathrm{Var}\left[\hat{p}_0\right]. \end{aligned}$$

---

[1] Our laser sources operate at 800 nm.

[2] The pump is considered as a classical field.

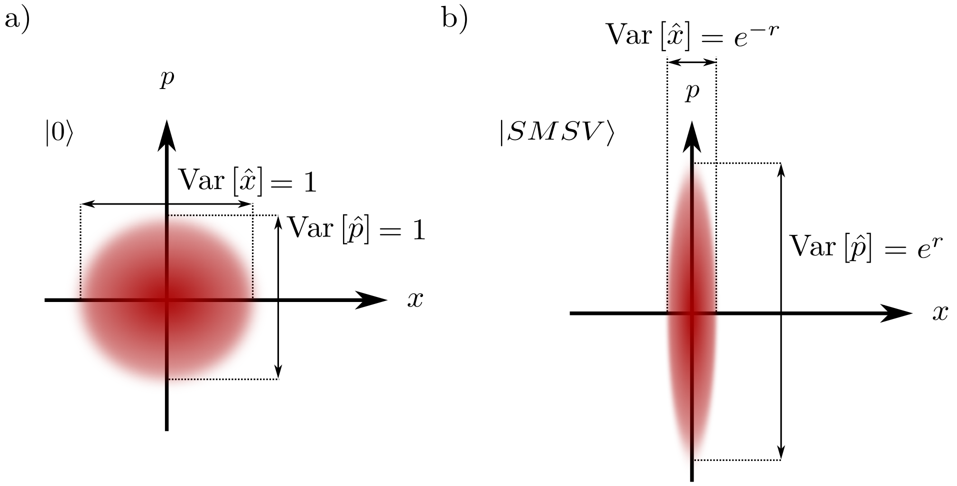

Figure 8.1 – **Phasor representation of a vacuum and a single mode squeezed vacuum state**. a) vacuum state and b) squeezed state. The variance of the quadratures of the single mode squeezed state (SMSV) are squeezed in one direction and spread in the other.

Here again, depending on the sign of the squeezing parameter r, the variance of one quadrature is increased while the other one is reduced, hence the name squeezing. From the expressions above, it is also clear that the Heisenberg inequality is indeed saturated by the squeezed quadratures. Their phasor representation is reproduced in Figure 8.1 alongside the one of a vacuum state as a comparison. Those squeezed states are of great interest in metrology, for example in gravitational interferometer [103], as they allow to perform measurements bellow the standard quantum limit.

8.1.2 Quantum correlations

The process described above allows to create a single-mode squeezed state. In order to create quantum correlations, namely entanglement, a second identical source can be used.
We consider two single-mode squeezed states, squeezed along opposite directions. Their quadratures are given by

$$\hat{x}_{in,1} = e^{r}\hat{x}_0 \qquad \hat{x}_{in,2} = e^{-r}\hat{x}_0$$
$$\hat{p}_{in,1} = e^{-r}\hat{p}_0 \qquad \hat{p}_{in,2} = e^{r}\hat{p}_0$$

Assuming that those states are mixed on a 50-50 beam-splitter, the quadratures at

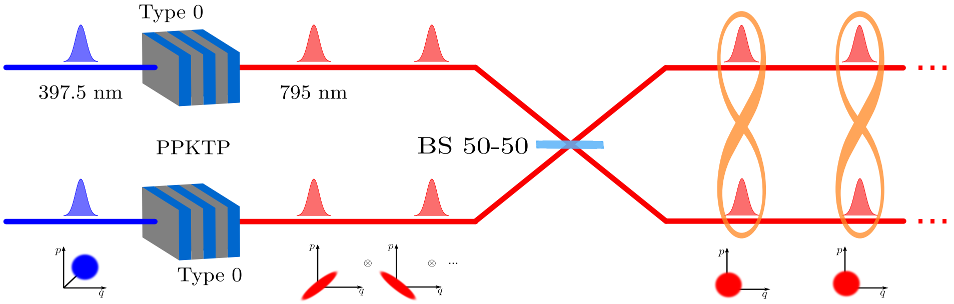

Figure 8.2 – **Experimental setup for the production of entangled states**. Two sources of pulsed squeezed states allow to produce quantum correlated pulses by mixing two squeezed pulses on a 50-50 BS. Those correlated pulses can be used as nodes for a quantum reservoir computing architecture.

the output ports are given by

$$\hat{x}_{out,1} = \frac{1}{\sqrt{2}}\hat{x}_0\left(e^{r} + e^{-r}\right) \qquad \hat{x}_{out,2} = \frac{1}{\sqrt{2}}\hat{x}_0\left(e^{r} - e^{-r}\right)$$

$$\hat{p}_{out,1} = \frac{1}{\sqrt{2}}\hat{p}_0\left(e^{-r} + e^{r}\right) \qquad \hat{p}_{out,2} = \frac{1}{\sqrt{2}}\hat{p}_0\left(e^{-r} - e^{r}\right)$$

By taking the variance of the difference or the sum of the quadratures, it can be seen that the output fields described by the quadratures above are entangled. Indeed, we have

$$\mathrm{Var}\left[\hat{x}_{out,1} - \hat{x}_{out,2}\right] = 2e^{-2r}\mathrm{Var}\left[\hat{x}_0\right] \tag{8.3}$$

$$\mathrm{Var}\left[\hat{p}_{out,1} + \hat{p}_{out,2}\right] = 2e^{-2r}\mathrm{Var}\left[\hat{p}_0\right] \tag{8.4}$$

Assuming that the initial state is either the vacuum or a coherent state, we have $\mathrm{Var}\left[\hat{x}_0\right] = \mathrm{Var}\left[\hat{p}_0\right] = 1$. It can be seen that if r tends to infinity, which implies that the states are infinitely squeezed, we obtain perfect correlations between the quadratures $x_{out,1}$ and $x_{out,2}$, and anti-correlations between $p_{out,1}$ and $p_{out,2}$. These states are often referred as EPR states [104]. Those correlations can be used in the reservoir to replace the classical links in order to implement a quantum version of the reservoir computing protocol[3]. A scheme of the system that can be used to produce those correlations is represented in Figure 8.2.

---

[3] Of course more complex graph should be constructed in this case, see for example the dual-rail cluster state [105].

8.2 Multimode squeezing

The description above is valid for a single-mode squeezed state. However, in this work, the experiment is performed with an optical frequency comb. The advantage of such laser is that very high intensities can be achieved in the non-linear medium due to the ultra-short pulses produced by the laser. In addition, as we saw previously, the frequency comb is composed of many individual spectral lines whose frequencies are given by $\omega_m = \omega_{CEO} + m\omega_r$, with ω_{CEO} the CEO frequency and ω_r the repetition rate. Hence, when the light from an OFC propagates in a non-linear medium, each individual tooth can undergo parametric down conversion. Thus, the pump photons at $\omega_{p,m} = 2\omega_{CEO} + m\omega_r$[4] can be converted into signal ω_s and idler at ω_i so that $\omega_s + \omega_i = \omega_{p,m}$. Consequently, this process is highly multimode. Those additional degrees of freedom can be used to increase the performances of the reservoir computing protocol.

To describe this multimode process, the Hamiltonian (8.1) must be rewritten, so that the multimode PDC Hamiltonian is given by [106, 107, 108]

$$\hat{H}_{PDC} = ig\sum_{n,k} \Phi_{n,k}\hat{a}^\dagger_{s,n}\hat{a}^\dagger_{i,k} + hc, \tag{8.5}$$

where $\Phi_{n,k}$, the joint spectral distribution, governs the process and depends on the parameters of the system: the phase matching condition in the crystal and the pump field. It can be shown that this Hamiltonian can be simplified by diagonalizing the joint spectral distribution using a Bloch-Messiah decomposition [109]. It can then be written as

$$\hat{H}_{PDC} = ig\sum_{j} \Lambda_j \hat{S}_j^{\dagger 2} + hc, \tag{8.6}$$

where $\hat{S}_j^{\dagger 2}$ represents the creation operators associated to the eigenmodes s_j of $\Phi_{n,k}$, and Λ_j the eigenvalues associated to those modes.
This Hamiltonian represents an assembly of independent single-mode squeezing operators, as described in section 8.1, acting on the modes s_j. Those modes are called the supermodes of the system [110]. Assuming that the pump spectrum has a Gaussian shape and that the phase matching is also approximated by a Gaussian, it can be shown that those squeezed eigenmodes can be approximated by Hermite-Gauss modes in the spectral domain [106], given by

$$HG_m(\omega) = \frac{1}{\sqrt{\pi 2^{m+1} m!}} H_m\left(\frac{\omega-\omega_0}{\sigma_\omega}\right) e^{-\frac{(\omega-\omega_0)^2}{2\sigma_\omega^2}}, \tag{8.7}$$

---

[4] The factor 2 here is used because the spectrum of the laser is frequency doubles to obtain the pump at 397.5 nm.

where ω_0 is the carrier frequency, and σ_ω^2 the spectral width of the modes. $H_m(x)$ is the Hermite polynomial of degree m given by $H_m(x) = (-1)^m e^{x^2} \frac{\mathrm{d}^m e^{-x^2}}{\mathrm{d}x^m}$. The first mode, leading to the highest value of squeezing, is the Hermite-Gauss of order 0 (HG0), which corresponds to a Gaussian spectrum, centered at ω_0, and whose spectral width, σ_ω^2, is given by the parameters of the process (typically around 15 nm FWHM in our experiment).

8.3 Single pass squeezing

Such multimode process usually occurs in a cavity. Indeed, higly multimode squeezed states can be obtained using, for example, a synchronously pumped optical parametric oscillator (SPOPO) [111, 72]. In such systems, a non-linear crystal is placed in a cavity designed to be resonant at the wavelength of the signal. Hence, the photons created by the PDC undergo many round-trips, increasing the gain of the process. In such experimental setup, the bandwidth of the squeezed states produced is limited by the bandwidth of the cavity (usually around a few MHz, depending on the finesse of the cavity). However, in our experiment, we wish to create correlations, and thus squeezing, between laser pulses (i.e. at a rate of 156 MHz), to harness those correlations in a reservoir computing architecture. Hence no cavity can be used to enhance the efficiency of the non-linear process. Alternatively, we decided to use a periodically poled KTP waveguide instead of bulk crystal to produce the squeezed states. The benefit of waveguides is their ability to confine the light in a very small cross section (typically 4 μm) for a long propagation distance, increasing the gain of the non-linear process [71, 108].

8.3.1 Experimental scheme

To produce squeezed pulses, the laser at 795 nm, is first frequency doubled with a non-linear crystal to obtain the pump field at 397.5 nm. This pump field is sent to a PPKTP type 0 waveguide, manufactured by AdvR, using the injection setup represented in Figure 8.3. Two lenses, with very short focal lengths, focus the light inside the waveguide mounted on a 6-axis stage (3 translations and 3 rotations) for fine alignment. The alignment is first done with a seed beam at 795 nm. This procedure is quite complex and many parameters must be taken into account. Among others, the numerical aperture of the lenses[5], the size of the beam at the input of the waveguide, as well as the overall alignment, are critical parameters that need attention for proper injection. The field at the output of the waveguide is detected using a homodyne detection, similarly to almost all experiments in this thesis. The field is mixed on a 50-50 BS with a strong beam, the

---

[5] and their orientation...

local oscillator (LO). Here again, precise alignment is needed. This alignment is also performed using the seed beam, injected in the waveguide. In order to limit the losses, the spatial and spectral overlap of the seed and the LO must be carefully optimized. The spatial overlap is tuned by using telescopes on the LO path in order to match the LO spatial mode to the spatial mode of the waveguide. The spectral overlap can be tuned using a pulse-shaper on the LO path, as presented in section 4.2.2. In addition, the pulse shaper is used to shape the LO spectral mode into Hermite-Gauss modes of various order, to measure the squeezing in the eigenmodes defined in equation (8.6). At first, the LO is shaped into a HG0 mode as it is the mode with the highest squeezing value. The quality of the total overlap is assessed by computing the contrast between the LO and the seed. The temporal overlap, between the seed and the LO as well as the seed and the pump, is also a critical parameter as we are working with ultra-short pulses. Note that all the optimization procedure is realized with the seed, which is not exactly identical to the signal we want to measure. In particular, the signal is usually multimode while the seed is single mode. Nevertheless, it allows to be as close as possible to the measurement conditions and thus gives an estimation of the real contrast.

Once the waveguide aligned, the seed is blocked. Therefore only the pump is injected in the waveguide. At the output, a dichroic mirror is used to remove the pump light to keep only the signal field produced via the parametric down conversion. When no seed light is sent at the input of the waveguide along with the pump, the parametric process is called spontaneous (SPDC). It means that the signal field at the input of the waveguide is in a vacuum state. Consequently, the signal at the output of the waveguide is a squeezed vacuum state.

The light at the output of the homodyne BS is measured with the same high-bandwidth balanced detector as in chapter 7. A ramp is applied on a piezo on which a mirror is mounted on the LO path, to scan the relative phase of the LO and the signal. This detection measures the quadratures of the signal beam and allows to characterize the signal state produced after propagation in the waveguide. Since we are using a high-bandwidth detector, a quadrature measurement of each pulse can be taken using the procedure described in the next section. Note that the alignment of the high bandwidth detector is another critical point of the experiment. Since the detector has a high-bandwidth, it detects a strong component at 156 MHz, corresponding to the repetition rate of the laser. To prevent any saturation of the detector, the two arms of the detection must be carefully balanced in power. In addition, the response in time of both photodiodes must be matched by changing their bias current. A good alignment is obtained when the repetition rate peak is minimized. Temporally it corresponds to having a homodyne signal as flat as possible.

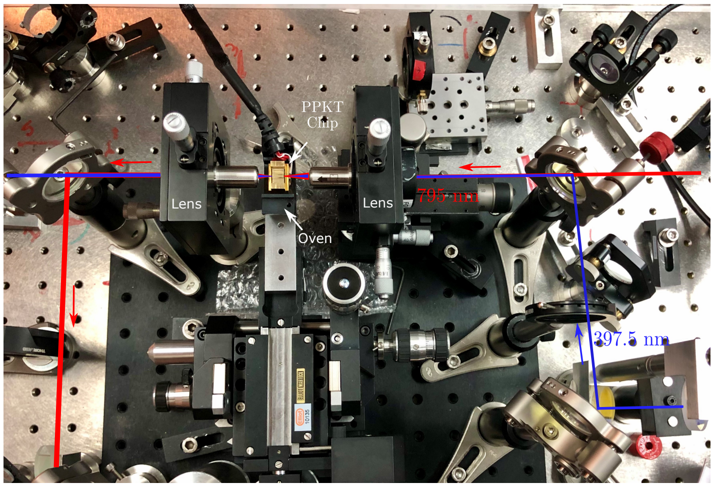

Figure 8.3 – **Experimental setup of the injection of the waveguide**. The PPKTP waveguide is placed on a 6 axis stage (3 rotations and 3 translations) and on an oven, to control its temperature. The light is injected and collected using two lenses with very short focal lengths. The seed, at 795 nm, is injected in the waveguide for alignment. The pump, at 397.5 nm, is separated from the signal using a dichroic mirror after the waveguide.

8.3.2 Results

In this section are presented the preliminary results obtained during my PhD. The setup described in the previous section is used to record the signal measured by the high-bandwidth balanced detector. In order to reveal the squeezing, two measurement devices can be used. The first one is a spectrum analyzer. This device allows to measure the variance of a signal. Using proper settings, it is possible to measure the time evolution of this variance in a given bandwidth around a central frequency. This measurement leads to traces similar to the one reproduced in Figure 8.5a. It represents the evolution of the variance of the quadrature measurements as a function of time. In black is represented the shot noise. It is measured by blocking the signal beam and measuring the variance of the LO. In red is represented the variance measured when the signal beam (and thus squeezed states) is sent with the LO, on the detector. Oscillations of the variance appear due to the ramp applied on the piezo on the LO path. This ramp changes the relative phase between the signal and the LO and allows to explore the different field quadratures. It can be seen that the variance goes below the shot noise, corresponding to the squeezed quadrature, and above it, corresponding to the anti-squeezed quadrature. Even though convenient to witness squeezing and measure its value, this device is not the most practical to demonstrate that squeezing is created at the level of each pulse. As a matter of fact, each point corresponds to the variance calculated over the resolution bandwidth of the instrument (usually a few kHz) and thus over many pulses. Hence, an oscilloscope can be used to measure the evolution of the homodyne signal from pulse to pulse, and to determine the evolution of the quadratures of the signal beam. The aim is to recover the value of the quadrature $\hat{q}_s^{pulse}$ of each pulse detected. To this end, a particular treatment must be applied to the data.

Defining the time window: The first step is to define the time window, of duration T_{window}, corresponding to the detection of one laser pulse. As previously explained, once the balanced detector are properly aligned, because the signal corresponds to the difference of the two photodiodes, it is hard to identify the pulses on the recorded trace, as can be seen in red in Figure 8.4. In order to identify the portion corresponding to one pulse, an acquisition is taken by blocking one photodiode. The resulting trace is reproduced in blue in Figure 8.4. This signal allows to define the time window, centered on each peak of the single photodiode signal[6]. Once the time windows defined, we apply them on the homodyne signal. For each window, the integral of the signal is taken. Indeed, we remind that the homodyne signal in the temporal domain, derived in section 3.3.1 can be written as

$$\hat{q}_s^{pulse}(t_i) \propto \int_{t_i}^{t_i+T_{window}} \{\alpha_{LO}(t')\hat{a}_s^\dagger(t') + \alpha_{LO}^\star(t')\hat{a}_s(t')\} \, \mathrm{d}t', \tag{8.8}$$

where $\hat{q}_s^{pulse}(t_i)$ is the quadrature of one pulse from the signal field, α_{LO} is the LO field[7], and $\hat{a}_s$ is the annihilation operator for the signal field. Using this procedure, one quadrature value is recovered for each pulse. Many pulses are measured in order to recover the statistic of their quadratures. Two techniques can then be used to reveal the squeezing at the level of the laser pulses from those measurements.

Long acquisition: The first technique is to acquire data from the homodyne signal on the oscilloscope during a relatively long time (20 ms). At the same time, the ramp applied on the piezo, to scan the LO phase relative to the signal, is set to 10 Hz. Hence, during one acquisition, the homodyne will scan the different quadrature values of the signal beam. In addition, because the ramp is a lot slower than the repetition rate of the laser, several pulses are measured for the same relative phase between the signal and the LO. The quadrature values, corresponding to each pulse detected during this acquisition, are calculated using the previously defined time windows. By plotting those values as a function of time, it is possible to visualize their statistics and how it evolves while scanning the relative phase, as represented in Figure 8.5b. In this Figure,

---

[6] Note that we take the positive peak as a central reference as we are looking at the photodiode producing a positive photo-current while the other one produced a negative photo-current.

[7] As the LO is a lot stronger than the signal, it is considered classical.

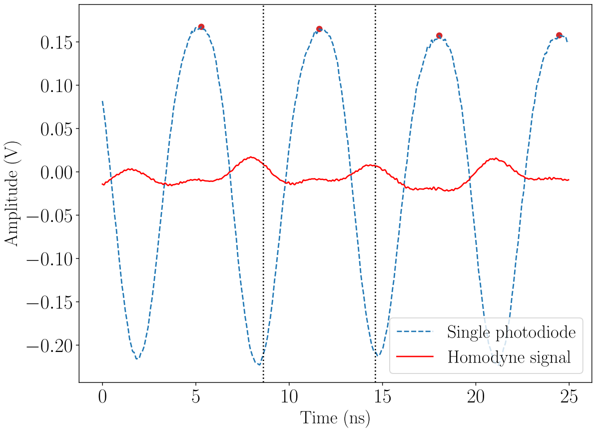

Figure 8.4 – **Definition of a time window.** The signal from one photodiode in blue is used to determine the window during which a pulse is detected. A value of quadrature is found by integrating the homodyne signal, in red, over each window.

each point represents a quadrature measurement from one pulse. As a comparison, the shot noise, measured using the same technique, is represented in Figure 8.5c. A trace is taken simultaneously using the spectrum analyzer. It is reproduced in Figure 8.5a. It can be seen that, contrary to the shot noise, the spreading (and thus the variance) of the quadrature values of the signal oscillates. They are sometimes less spread, corresponding to the squeezed quadrature, and sometimes more spread, corresponding to the anti-squeezed quadrature.

Single-shot measurement: Although this technique allows to visualize the squeezing, it is not the most practical to quantify it. In addition, long acquisitions are sensitive to the drifts of the experiment, which sometimes masks the squeezing. Consequently, another method has also been employed. Data are acquired from the oscilloscope during 50 μs to prevent any drift of the experiment. The ramp on the relative phase is set to 300 mHz, so that one acquisition corresponds to one phase value and thus one quadrature. The aim is to recover the statistic of the quadrature when the homodyne measures either the squeezed or the anti-squeezed quadrature. To determine which quadrature is being measured, this acquisition is triggered simultaneously with an acquisition from the spectrum analyzer. The acquisition from the spectrum analyzer spans one second. Thus, the data acquired from the oscilloscope correspond to the first few points of the acquisition from the spectrum analyzer. It allows us to distinguish data corresponding to the squeezed quadrature, when the variance is bellow the shot noise (Figure 8.6a), from the data corresponding to the anti-squeezed quadrature (Figure 8.6b). Many sets of data are taken for both squeezing and anti-squeezing from the oscilloscope. Once acquired, the same procedure as previously described allows to retrieve the values of the quadrature in both configurations. All the squeezing data are staked together on one side and all the anti-squeezing ones on the other side. The resulting distributions of the squeezed and anti-squeezed quadrature values are represented in Figure 8.6c, with the shot noise as a reference. Because the squeezing is low, it is not easy to see, but the

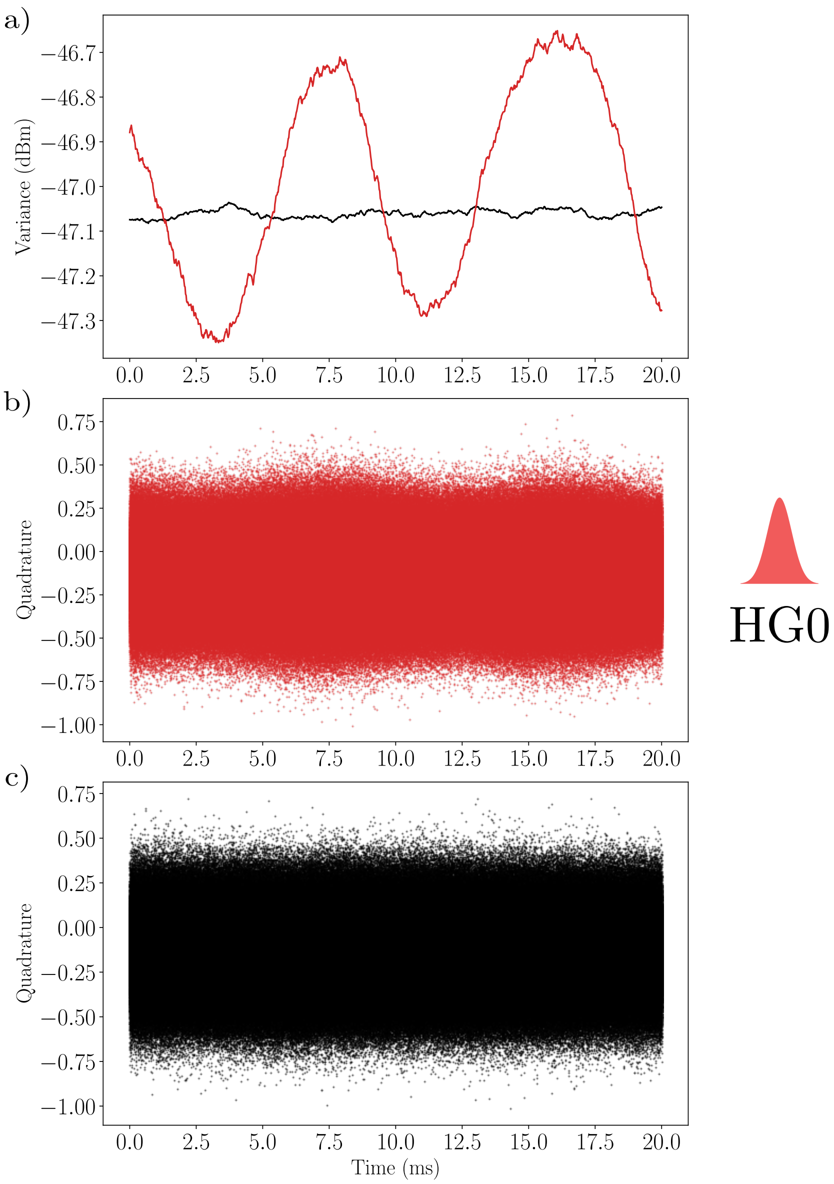

Figure 8.5 – **Long acquisition of the quadratures**. a) in red, measurement of the variance of the signal from a spectrum analyzer. In black, the shot noise variance. The measurements are performed with a LO shaped as a HG0 mode. The acquisition is done around a central frequency of 10 MHz using a resolution bandwidth of 240 Hz and a video bandwidth of 30 Hz. b) Distribution of the quadrature values while the relative phase between LO and signal is scanned. Each point corresponds to the quadrature value of one pulse. The variance is reduced when the squeezed quadrature is measured and increased for the anti-squeezed quadrature. c) Distribution of the quadrature values of the shot noise.

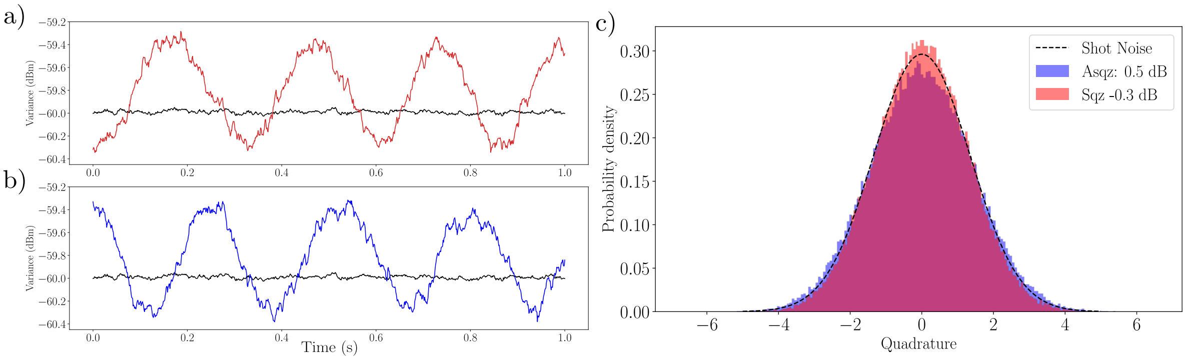

Figure 8.6 – **Single-shot acquisition**. a) and b) traces from the spectrum analyzer measured around 10 MHz using a resolution bandwidth of 240 kHz and a video bandwidth of 15 Hz. In red, the first few points correspond to the squeezed quadrature and in blue the anti-squeezed one. c) distribution of the squeezed (red) and anti-squeezed (blue) quadrature values. In black the fit of the distribution of the shot noise. It can be seen that the squeezing distribution is narrower and leads to a value of -0.3 dB.

distribution corresponding the the squeezed quadrature is narrower than the one corresponding to the anti-squeezing and the shot noise. The variance of each distribution leads to the squeezing value of -0.3 dB and anti-squeezing value of 0.5 dB with respect to the shot noise.

Multimode structure: This experiment does not allow to produce highly squeezed states. Many elements need to be optimized in order to increase the squeezing value such as the coupling of the pump in the waveguide. Nevertheless, as explained in section 8.2, this process is multimode. Hence, squeezing can be measured in the different eigenmodes of the joint spectral amplitude. As previously mentionned, the pulse-shaper is used to shape the LO spectral mode into Hermite-Gauss modes. Hence, by shaping it into modes of higher order, the multimode aspect of the process can be revealed. Similarly to the previous measurements, the distribution of the squeezed and anti-squeezed quadratures are measured for the Hermite-Gauss mode 1 and 2. It leads to a value of -0.27 dB of squeezing and 0.46 dB of anti-squeezing in the Hermite-Gauss mode of first order (HG1), and a value of -0.18 dB of squeezing and 0.3 dB of anti-squeezing in the second Hermite-Gauss mode (HG2). The data measured with the spectrum analyzer for those two spectral modes are represented in Figure 8.7.

Summary

The experiment presented in this chapter allows to produce squeezed states at the level of the laser pulses i.e. with a bandwidth corresponding to the repetition rate of

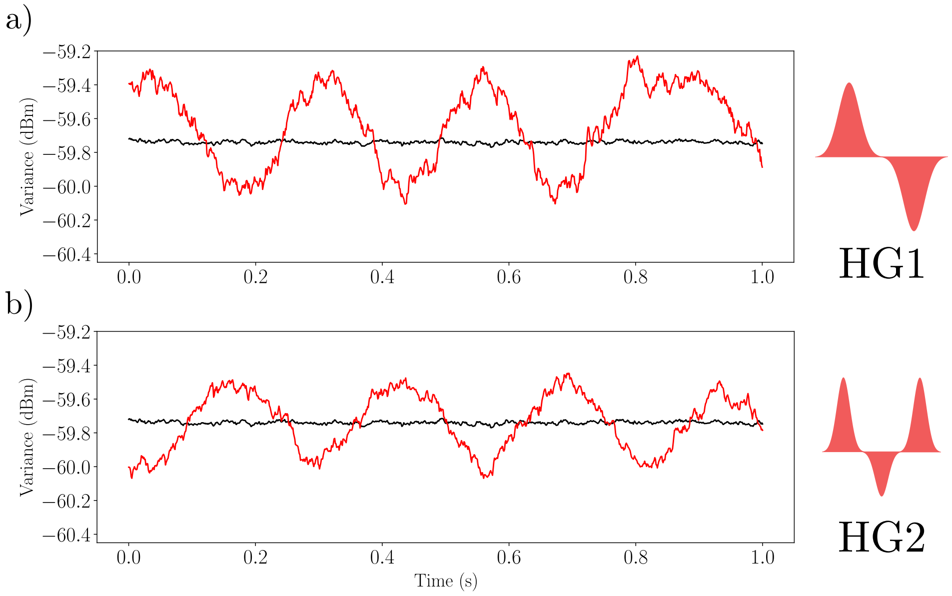

Figure 8.7 – **Variance of the spectral modes HG1 and HG2**. a) In red, variance of the signal with a LO shaped into a HG1 mode and b) into a HG2 mode. In black, the shot noise variance. The acquisition is done around a central frequency of 10 MHz using a resolution bandwidth of 240 kHz and a video bandwidth of 15 Hz. The level of squeezing in the HG1 mode is found to be -0.27 dB and -0.18 dB in the HG2 mode.

the laser. Such source of single pulse squeezed states can be duplicated to produce entanglement. Our aim is to use the entanglement as link between nodes in a reservoir computing architecture. Even though the level of squeezing is low, it is still interesting to implement it, and study whether any advantage can be gained over the classical architecture. Furthermore, the states produced are highly multimodes. Those spectral modes bring an additional degree of freedom to the protocol, which can be an advantage in terms of capacity.

Conclusion

The main focus of this manuscript was the investigation of optical frequency combs dynamics. Based on a spectral modal decomposition of the electric field, a full characterization of the laser dynamics was achieved by measuring the fluctuations of the four main laser parameters: the intensity, the carrier-envelope offset (CEO), the central frequency and the repetition rate. This characterization was performed using two different setups.

The first experimental setup, based on a multipixel homodyne detection, allowed the simultaneous measurement of the four laser parameters. Consequently, their correlations were exploited to gain insight on the mode-locking mechanism at the origin of the production of frequency combs. Particularly, the intensity related dynamics was investigated. Based on a simple model, we demonstrated that, in the frequency range studied, the main source of noise is the pump laser via its intensity fluctuations. This noise induces phase noise, and especially CEO noise, via the fluctuations of the center of the spectrum. The coupling parameter between both quantities is the residual group velocity dispersion of the laser which was evaluated experimentally.

The second experimental setup was developed in collaboration with Thales Research and Technology. This optical bench, built from off-the-shelf components, is based on an unbalanced Mach-Zehnder interferometer (UMZI). It is more compact and easier to handle than the previous one. With this setup, the same spectrally resolved analysis was applied to a fiber-based frequency comb. This analysis seemed, to a certain limit, to be able to accurately capture the laser dynamics, proving the versatility of our technique which can be applied to different sources of laser pulses in various ranges of wavelengths. Nonetheless, this experiment did not lead to results as successful as the previous ones. This was mainly due to technical limitations, and in particular the limited amount of optical power in the interferometer.

To complete our investigation, both setups were compared in terms of sensitivity. Using the Fisher information, we demonstrated that the first experiment leads to an optimal measurement. The sensitivity is limited only by the standard quantum limit. On the other hand, the study of the UMZI sensitivity lead to a different result. In the case of an optimal estimator, the standard quantum limit can be reached under certain circumstances. However, experimentally, this optimal estimator is not accessible. Hence, the actual sensitivity of the measurement is decreased.

After studying the laser dynamics, we used the experimental techniques and the knowledge acquired so far to investigate the use and the implementation of a machine learning protocol called reservoir computing (RC). Reservoir computing is a powerful protocol for the processing of time series due to the simplicity of the training procedure. As an application example, a simulated RC algorithm was designed to predict the intensity related dynamics of the laser investigated in the previous part. The fluctuations of three of the laser parameters were predicted from the pump laser fluctuations.
Experimentally, a delayed-feedback-based photonic reservoir computing protocol was implemented. A frequency comb, and more precisely a train of pulses, was used as a hardware to implement the RC protocol. It relied on the encoding of the information in the phase of the laser pulses, and the extraction was ensured by a homodyne detection. This experiment, although still preliminary, seemed to be able to process data, as demonstrated by the calculation of the information processing capacity.
The long term objective of this experiment is to go toward quantum reservoir computing. Consequently, a source of quantum states was developed. Based on a PPKTP waveguide, multimode squeezed states were produced at the scale of the laser pulses.

This work opens some (more or less long-term) perspectives. First, the optical bench developed in collaboration with Thales can be improved by reducing the losses and properly compensating the dispersion in the interferometer. Combined with an appropriate work on the design of the experiment, it should provide an efficient and compact way to characterize the dynamics of various sources of light pulses.
Second, combining the laser characterization with an improved version of the reservoir computing algorithm could lead to active stabilization of the laser.
Finally, as already mentioned, using the quantum resource in the reservoir computing protocol would allow us to investigate experimentally whether this architecture brings any advantage over its classical counterpart.

Bibliography

[1] Benjamin P Abbott, Richard Abbott, TD Abbott, MR Abernathy, Fausto Acernese, Kendall Ackley, Carl Adams, Thomas Adams, Paolo Addesso, RX Adhikari, et al. Observation of gravitational waves from a binary black hole merger. *Physical review letters*, 116(6):061102, 2016. (Cited on page 1.)

[2] Arthur Ashkin, James M Dziedzic, and T Yamane. Optical trapping and manipulation of single cells using infrared laser beams. *Nature*, 330(6150):769–771, 1987. (Cited on page 1.)

[3] TW Murphy Jr, Eric G Adelberger, JBR Battat, LN Carey, Charles D Hoyle, P LeBlanc, EL Michelsen, K Nordtvedt, AE Orin, Jana D Strasburg, et al. The apache point observatory lunar laser-ranging operation: instrument description and first detections. *Publications of the Astronomical Society of the Pacific*, 120(863):20, 2008. (Cited on page 1.)

[4] Theodore H Maiman et al. Stimulated optical radiation in ruby. 1960. (Cited on page 1.)

[5] Th W Hänsch, MD Levenson, and AL Schawlow. Complete hyperfine structure of a molecular iodine line. *Physical Review Letters*, 26(16):946, 1971. (Cited on page 1.)

[6] David E Spence, P Np Kean, and Wilson Sibbett. 60-fsec pulse generation from a self-mode-locked ti: sapphire laser. *Optics letters*, 16(1):42–44, 1991. (Cited on page 1.)

[7] Scott A Diddams, David J Jones, Jun Ye, Steven T Cundiff, John L Hall, Jinendra K Ranka, Robert S Windeler, Ronald Holzwarth, Thomas Udem, and Theodor W Hänsch. Direct link between microwave and optical frequencies with a 300 thz femtosecond laser comb. *Physical review letters*, 84(22):5102, 2000. (Cited on page 1.)

[8] Th Udem, R Holzwarth, and T W Hänsch. Optical frequency metrology. 416:5, 2002. (Cited on page 1.)

[9] Th. Udem, S. A. Diddams, K. R. Vogel, C. W. Oates, E. A. Curtis, W. D. Lee, W. M. Itano, R. E. Drullinger, J. C. Bergquist, and L. Hollberg. Absolute frequency measurements of the hg$^+$ and ca optical clock transitions with a femtosecond laser. *Phys. Rev. Lett.*, 86:4996–4999, May 2001. (Cited on page 1.)

[10] A. Shelkovnikov, R. J. Butcher, C. Chardonnet, and A. Amy-Klein. Stability of the proton-to-electron mass ratio. *Phys. Rev. Lett.*, 100:150801, Apr 2008. (Cited on page 1.)

[11] Hélène Fleurbaey, Sandrine Galtier, Simon Thomas, Marie Bonnaud, Lucile Julien, Fran çois Biraben, Fran çois Nez, Michel Abgrall, and Jocelyne Guéna. New measurement of the $1s - 3s$ transition frequency of hydrogen: Contribution to the proton charge radius puzzle. *Phys. Rev. Lett.*, 120:183001, May 2018. (Cited on page 1.)

[12] Alexey Grinin, Arthur Matveev, Dylan C. Yost, Lothar Maisenbacher, Vitaly Wirthl, Randolf Pohl, Theodor W. Hänsch, and Thomas Udem. Two-photon frequency comb spectroscopy of atomic hydrogen. *Science*, 370(6520):1061–1066, 2020. (Cited on page 1.)

[13] Scott A. Diddams, Leo Hollberg, and Vela Mbele. Molecular fingerprinting with the resolved modes of a femtosecond laser frequency comb. *Nature*, 445(7128):627–630, Feb 2007. (Cited on page 1.)

[14] Nathalie Picqué and Theodor W. Hänsch. Frequency comb spectroscopy. *Nature Photonics*, 13(3):146–157, Mar 2019. (Cited on page 1.)

[15] Fabrizio R. Giorgetta, William C. Swann, Laura C. Sinclair, Esther Baumann, Ian Coddington, and Nathan R. Newbury. Optical two-way time and frequency transfer over free space. 7(6):434–438, 2013. (Cited on page 1.)

[16] J Guéna, S Weyers, M Abgrall, C Grebing, V Gerginov, P Rosenbusch, S Bize, B Lipphardt, H Denker, N Quintin, S M F Raupach, D Nicolodi, F Stefani, N Chiodo, S Koke, A Kuhl, F Wiotte, F Meynadier, E Camisard, C Chardonnet, Y Le Coq, M Lours, G Santarelli, A Amy-Klein, R Le Targat, O Lopez, P E Pottie, and G Grosche. First international comparison of fountain primary frequency standards via a long distance optical fiber link. *Metrologia*, 54(3):348–354, may 2017. (Cited on page 1.)

[17] K. Predehl, G. Grosche, S. M. F. Raupach, S. Droste, O. Terra, J. Alnis, Th. Legero, T. W. Hänsch, Th. Udem, R. Holzwarth, and H. Schnatz. A 920-kilometer optical fiber link for frequency metrology at the 19th decimal place. *Science*, 336(6080):441–444, 2012. (Cited on page 1.)

[18] I Coddington, William C Swann, Ljerka Nenadovic, and Nathan R Newbury. Rapid and precise absolute distance measurements at long range. *Nature photonics*, 3(6):351–356, 2009. (Cited on page 1.)

[19] Pu Jian, Olivier Pinel, Claude Fabre, Brahim Lamine, and Nicolas Treps. Real-time displacement measurement immune from atmospheric parameters using optical frequency combs. *Optics Express*, 20(24):27133–27146, 2012. (Cited on page 1.)

[20] Richard A. McCracken, Jake M. Charsley, and Derryck T. Reid. A decade of astrocombs: recent advances in frequency combs for astronomy. *Opt. Express*, 25(13):15058–15078, Jun 2017. (Cited on page 1.)

[21] H. Jaeger. Harnessing Nonlinearity: Predicting Chaotic Systems and Saving Energy in Wireless Communication. *Science*, 304(5667):78–80, April 2004. (Cited on pages 2 and 135.)

[22] Laurent Larger, Antonio Baylón-Fuentes, Romain Martinenghi, Vladimir S. Udaltsov, Yanne K. Chembo, and Maxime Jacquot. High-Speed Photonic Reservoir Computing Using a Time-Delay-Based Architecture: Million Words per Second Classification. *Physical Review X*, 7(1):011015, February 2017. (Cited on pages 2 and 135.)

[23] L. Appeltant, M.C. Soriano, G. Van der Sande, J. Danckaert, S. Massar, J. Dambre, B. Schrauwen, C.R. Mirasso, and I. Fischer. Information processing using a single dynamical node as complex system. *Nature Communications*, 2(1):468, September 2011. (Cited on pages 2, 136, 139, 145, 147, and 151.)

[24] Guy Van der Sande, Daniel Brunner, and Miguel C. Soriano. Advances in photonic reservoir computing. *Nanophotonics*, 6(3), January 2017. (Cited on pages 2 and 145.)

[25] Joni Dambre, David Verstraeten, Benjamin Schrauwen, and Serge Massar. Information Processing Capacity of Dynamical Systems. *Scientific Reports*, 2(1):514, December 2012. (Cited on pages 2, 153, and 155.)

[26] Jonathan Roslund, Renné Medeiros De Araujo, Shifeng Jiang, Claude Fabre, and Nicolas Treps. Wavelength-multiplexed quantum networks with ultrafast frequency combs. *Nature Photonics*, 8(2):109–112, 2014. (Cited on page 3.)

[27] P. Mujal, R. Martínez-Peña, J. Nokkala, J. García-Beni, G. L. Giorgi, M. C. Soriano, and R Zambrini. Opportunities in quantum reservoir computing and extreme learning machines. *arXiv 2102.11831*, 2021. (Cited on pages 3 and 136.)

[28] Matthieu Ansquer, Valérian Thiel, Syamsundar De, Bérengère Argence, Gregory Gredat, Fabien Bretenaker, and Nicolas Treps. Unveiling the dynamics of optical

frequency combs from phase-amplitude correlations. *Physical Review Research*, 3(3):033092, 2021. (Cited on page 3.)

[29] Claude Fabre and Nicolas Treps. Modes and states in quantum optics. *Reviews of Modern Physics*, 92(3):035005, 2020. (Cited on page 10.)

[30] Gilbert Grynberg, Alain Aspect, and Claude Fabre. *Introduction to quantum optics: from the semi-classical approach to quantized light*. Cambridge university press, Cambridge, CB2 8BS, UK, 2010. (Cited on pages 13, 72, and 162.)

[31] Roy J Glauber. Coherent and incoherent states of the radiation field. *Physical Review*, 131(6):2766, 1963. (Cited on page 14.)

[32] Nicolas Treps, Vincent Delaubert, Agnès Maître, Jean-Michel Courty, and Claude Fabre. Quantum noise in multipixel image processing. *Physical Review A*, 71(1):013820, 2005. (Cited on page 15.)

[33] Rodney Loudon. *The quantum theory of light*. OUP Oxford, 2000. (Cited on page 15.)

[34] Ulf Leonhardt and H Paul. Measuring the quantum state of light. *Progress in Quantum Electronics*, 19(2):89–130, 1995. (Cited on page 16.)

[35] Anatole Kenfack and Karol Życzkowski. Negativity of the wigner function as an indicator of non-classicality. *Journal of Optics B: Quantum and Semiclassical Optics*, 6(10):396, 2004. (Cited on page 16.)

[36] Alessandro Ferraro, Stefano Olivares, and Matteo GA Paris. Gaussian states in continuous variable quantum information. *arXiv preprint quant-ph/0503237*, 2005. (Cited on page 16.)

[37] C Radhakrishna Rao. Information and the accuracy attainable in the estimation of statistical parameters. *Reson. J. Sci. Educ*, 20:78–90, 1945. (Cited on page 22.)

[38] Olivier Pinel. *Optique quantique multimode avec des peignes de fréquence*. PhD thesis, 2010. Thèse de doctorat dirigée par Nicolas Treps, Paris 6 2010. (Cited on page 23.)

[39] Pu Jian. *Limites quantiques dans les mesures de distance à l'aide de peignes de fréquences*. PhD thesis, 2014. Thèse de doctorat dirigée par Nicolas Treps, Paris 6 2014. (Cited on page 23.)

[40] Carlton M Caves. Quantum-mechanical noise in an interferometer. *Physical Review D*, 23(8):1693, 1981. (Cited on page 24.)

[41] Marc Thierry Jaekel and Serge Reynaud. Quantum limits in interferometric measurements. *EPL (Europhysics Letters)*, 13(4):301, 1990. (Cited on page 24.)

[42] Andrew Weiner. *Ultrafast optics*, volume 72. John Wiley & Sons, Hoboken, New Jersey, USA, 2011. (Cited on pages 27, 32, 33, and 34.)

[43] H. A. Haus, J. G. Fujimoto, and E. P. Ippen. Structures for additive pulse mode locking. 8(10):2068, 1991. (Cited on pages 32 and 33.)

[44] Fabien Bretenaker. *Laser Physics Lecture.* 2015. (Cited on page 38.)

[45] Evgeni Sorokin, Gabriel Tempea, and Thomas Brabec. Measurement of the root-mean-square width and the root-mean-square chirp in ultrafast optics. *J. Opt. Soc. Am. B*, 17(1):146–150, Jan 2000. (Cited on page 39.)

[46] JA Armstrong. Measurement of picosecond laser pulse widths. *Applied Physics Letters*, 10(1):16–18, 1967. (Cited on page 41.)

[47] S. Kameyama, T. Ando, K. Asaka, Y. Hirano, and S. Wadaka. Compact all-fiber pulsed coherent doppler lidar system for wind sensing. *Appl. Opt.*, 46(11):1953–1962, Apr 2007. (Cited on page 45.)

[48] Christopher V. Poulton, Ami Yaacobi, David B. Cole, Matthew J. Byrd, Manan Raval, Diedrik Vermeulen, and Michael R. Watts. Coherent solid-state lidar with silicon photonic optical phased arrays. *Opt. Lett.*, 42(20):4091–4094, Oct 2017. (Cited on page 45.)

[49] Nathan R. Newbury and William C. Swann. Low-noise fiber-laser frequency combs (invited). 24(8):1756, 2007. (Cited on pages 45, 69, 103, and 104.)

[50] D. Hou, C.-C. Lee, Z. Yang, and T. R. Schibli. Timing jitter characterization of mode-locked lasers with 1 zs/$\sqrt{\text{hz}}$ resolution using a simple optical heterodyne technique. 40(13):2985, 2015. (Cited on page 45.)

[51] Takanori Okoshi, Kazuro Kikuchi, and Akira Nakayama. Novel method for high resolution measurement of laser output spectrum. *Electronics letters*, 16(16):630–631, 1980. (Cited on page 45.)

[52] Olivier Llopis, Pierre-Henri Merrer, Houda Brahimi, Khaldoun Saleh, and Pierre Lacroix. Phase noise measurement of a narrow linewidth cw laser using delay line approaches. *Optics letters*, 36(14):2713–2715, 2011. (Cited on page 49.)

[53] Haochen Tian, Wenkai Yang, Dohyeon Kwon, Runmin Li, Yuwei Zhao, Jungwon Kim, Youjian Song, and Minglie Hu. Optical frequency comb noise spectra analysis using an asymmetric fiber delay line interferometer. *Optics express*, 28(7):9232–9243, 2020. (Cited on page 49.)

[54] Horace P Yuen and Vincent WS Chan. Noise in homodyne and heterodyne detection. *Optics letters*, 8(3):177–179, 1983. (Cited on page 49.)

[55] Giacomo Sorelli, Manuel Gessner, Mattia Walschaers, and Nicolas Treps. Moment-based superresolution: Formalism and applications. *arXiv:2105.12396 [quant-ph]*, 2021. (Cited on pages 58 and 59.)

[56] Vincent Michaud-Belleau, Jérôme Genest, and Jean-Daniel Deschênes. Optimal detection scheme for shot-noise-limited phase estimation in passive classical-light interferometry. *Physical Review Applied*, 10(2):024025, 2018. (Cited on page 61.)

[57] Stefan Ataman, Anca Preda, and Radu Ionicioiu. Phase sensitivity of a mach-zehnder interferometer with single-intensity and difference-intensity detection. *Physical Review A*, 98(4):043856, 2018. (Cited on page 61.)

[58] H. A. Haus and Y. Lai. Quantum theory of soliton squeezing: a linearized approach. 7(3):386–392, 1990. (Cited on page 69.)

[59] H. A. Haus and A. Mecozzi. Noise of mode-locked lasers. 29(3):983–996, 1993. (Cited on pages 69 and 112.)

[60] R. Paschotta. Noise of mode-locked lasers (part II): timing jitter and other fluctuations. 79(2):163–173, 2004. (Cited on page 69.)

[61] R. Paschotta. Noise of mode-locked lasers (part i): numerical model. 79(2):153–162, 2004. (Cited on pages 69 and 96.)

[62] N. R. Newbury and B. R. Washburn. Theory of the frequency comb output from a femtosecond fiber laser. 41(11):1388–1402, 2005. (Cited on pages 69 and 117.)

[63] K.W. Holman, R.J. Jones, A. Marian, S.T. Cundiff, and Jun Ye. Detailed studies and control of intensity-related dynamics of femtosecond frequency combs from mode-locked ti:sapphire lasers. 9(4):1018–1024, 2003. (Cited on pages 69, 110, 111, 114, and 117.)

[64] Curtis R. Menyuk, Jared K. Wahlstrand, John Willits, Ryan P. Smith, Thomas R. Schibli, and Steven T. Cundiff. Pulse dynamics in mode-locked lasers: relaxation oscillations and frequency pulling. 15(11):6677, 2007. (Cited on pages 69 and 112.)

[65] J. K. Wahlstrand, J. T. Willits, T. R. Schibli, C. R. Menyuk, and S. T. Cundiff. Quantitative measurement of timing and phase dynamics in a mode-locked laser. 32(23):3426, 2007. (Cited on pages 69 and 110.)

[66] Roman Schmeissner. Frequency combs at the quantum limit. page 187, 2014. (Cited on pages 69, 76, 77, 88, and 104.)

[67] Valerian Thiel. Modal analysis of an ultrafast frequency comb : from classical to quantum spectral correlations. page 256, 2017. (Cited on page 69.)

[68] Renné Medeiros De Araujo. Génération et manipulation de peignes de fréquences quantiques multimodes. November 2012. (Cited on page 76.)

[69] L. Xu, T. W. Hänsch, Ch. Spielmann, A. Poppe, T. Brabec, and F. Krausz. Route to phase control of ultrashort light pulses. 21(24):2008, 1996. (Cited on pages 76 and 110.)

[70] Antoine Monmayrant, Sébastien Weber, and Béatrice Chatel. A newcomer's guide to ultrashort pulse shaping and characterization. 43(10):103001, 2010. (Cited on page 80.)

[71] Tiphaine Kouadou. Single-pass generation and detection of ultrafast multimode squeezed light. page 187, 2021. (Cited on pages 80, 151, and 166.)

[72] Thibault Michel. Optimisation of the pump spectral shape in a parametric down conversion process to generate multimode entangled states. 2021. (Cited on pages 85 and 166.)

[73] H.R. Telle, B. Lipphardt, and J. Stenger. Kerr-lens, mode-locked lasers as transfer oscillators for optical frequency measurements. 74(1):1–6, 2002. (Cited on page 103.)

[74] Erik Benkler, Harald R. Telle, Armin Zach, and Florian Tauser. Circumvention of noise contributions in fiber laser based frequency combs. 13(15):5662, 2005. (Cited on page 103.)

[75] D.V. Sutyrin, N. Poli, N. Beverini, S.V. Chepurov, M. Prevedelli, M. Schioppo, F. Sorrentino, M.G. Tarallo, and G.M. Tino. Frequency noise performances of a ti:sapphire optical frequency comb stabilized to an optical reference. 291:291–298, 2013. (Cited on page 104.)

[76] D.R. Walker, Th. Udem, Ch. Gohle, B. Stein, and T.W. Hänsch. Frequency dependence of the fixed point in a fluctuating frequency comb. 89(4):535–538, 2007. (Cited on page 104.)

[77] Andreas Christ, Kaisa Laiho, Andreas Eckstein, Katiúscia N Cassemiro, and Christine Silberhorn. Probing multimode squeezing with correlation functions. *New Journal of Physics*, 13(3):033027, 2011. (Cited on page 110.)

[78] Max Schiemangk, Stefan Spießberger, Andreas Wicht, Götz Erbert, Günther Tränkle, and Achim Peters. Accurate frequency noise measurement of free-running lasers. *Applied optics*, 53(30):7138–7143, 2014. (Cited on page 122.)

[79] H. Nyquist. Thermal agitation of electric charge in conductors. *Phys. Rev.*, 32:110–113, Jul 1928. (Cited on page 129.)

[80] Ya M. Blanter and M. Büttiker. Shot noise in mesoscopic conductors. 336(1):1–166, 2000. (Cited on page 130.)

[81] H.J. Caulfield, J. Kinser, and S.K. Rogers. Optical neural networks. *Proceedings of the IEEE*, 77(10):1573–1583, 1989. (Cited on page 135.)

[82] Ying Zuo, Bohan Li, Yujun Zhao, Yue Jiang, You-Chiuan Chen, Peng Chen, Gyu-Boong Jo, Junwei Liu, and Shengwang Du. All-optical neural network with nonlinear activation functions. *Optica*, 6(9):1132–1137, Sep 2019. (Cited on page 135.)

[83] Mantas Lukoševicˇius and Herbert Jaeger. Reservoir computing approaches to recurrent neural network training. *COMPUTER SCIENCE REVIEW*, page 23, 2009. (Cited on page 135.)

[84] David Verstraeten, Benjamin Schrauwen, and Dirk Stroobandt. Reservoir-based techniques for speech recognition. pages 1050–1053, 2006. (Cited on page 135.)

[85] Paul J Werbos. Backpropagation through time: what it does and how to do it. *Proceedings of the IEEE*, 78(10):1550–1560, 1990. (Cited on page 135.)

[86] Kenji Doya et al. Bifurcations in the learning of recurrent neural networks 3. *learning (RTRL)*, 3:17, 1992. (Cited on page 135.)

[87] Herbert Jaeger. The "echo state" approach to analysing and training recurrent neural networks – with an Erratum note. page 48. 2010. (Cited on pages 135 and 139.)

[88] Jonathan Dong, Mushegh Rafayelyan, Florent Krzakala, and Sylvain Gigan. Optical Reservoir Computing using multiple light scattering for chaotic systems prediction. *IEEE Journal of Selected Topics in Quantum Electronics*, 26(1):1–12, January 2020. arXiv: 1907.00657. (Cited on page 136.)

[89] Jonathan Dong, Ruben Ohana, Mushegh Rafayelyan, and Florent Krzakala. Reservoir Computing meets Recurrent Kernels and Structured Transforms. *arXiv:2006.07310 [cs, eess, stat]*, October 2020. arXiv: 2006.07310. (Cited on page 136.)

[90] Mushegh Rafayelyan, Jonathan Dong, Yongqi Tan, Florent Krzakala, and Sylvain Gigan. Large-Scale Optical Reservoir Computing for Spatiotemporal Chaotic Systems Prediction. *arXiv:2001.09131 [physics]*, January 2020. arXiv: 2001.09131. (Cited on page 136.)

[91] Y. Paquot, F. Duport, A. Smerieri, J. Dambre, B. Schrauwen, M. Haelterman, and S. Massar. Optoelectronic Reservoir Computing. *Scientific Reports*, 2(1):287, December 2012. (Cited on pages 136, 145, and 147.)

[92] François Duport, Bendix Schneider, Anteo Smerieri, Marc Haelterman, and Serge Massar. All-optical reservoir computing. *Optics Express*, 20(20):22783, September 2012. (Cited on pages 136, 145, and 147.)

[93] Daniel Brunner, Miguel C. Soriano, Claudio R. Mirasso, and Ingo Fischer. Parallel photonic information processing at gigabyte per second data rates using transient states. *Nature Communications*, 4(1):1364, June 2013. (Cited on pages 136, 145, and 151.)

[94] Jiayin Chen, Hendra I. Nurdin, and Naoki Yamamoto. Temporal Information Processing on Noisy Quantum Computers. *arXiv:2001.09498 [quant-ph, stat]*, July 2020. arXiv: 2001.09498. (Cited on page 136.)

[95] Johannes Nokkala, Rodrigo Martínez-Peña, Gian Luca Giorgi, Valentina Parigi, Miguel C. Soriano, and Roberta Zambrini. Gaussian states provide universal and versatile quantum reservoir computing. *arXiv:2006.04821 [quant-ph]*, June 2020. arXiv: 2006.04821. (Cited on pages 136, 149, and 155.)

[96] L. C. G. Govia, G. J. Ribeill, G. E. Rowlands, H. K. Krovi, and T. A. Ohki. Quantum reservoir computing with a single nonlinear oscillator. *Physical Review Research*, 3(1):013077, January 2021. (Cited on page 136.)

[97] Arthur E Hoerl and Robert W Kennard. Ridge regression: applications to nonorthogonal problems. *Technometrics*, 12(1):69–82, 1970. (Cited on page 140.)

[98] Pablo Amil, Miguel C. Soriano, and Cristina Masoller. Machine learning algorithms for predicting the amplitude of chaotic laser pulses. *Chaos: An Interdisciplinary Journal of Nonlinear Science*, 29(11):113111, November 2019. arXiv: 1911.04815. (Cited on page 141.)

[99] A. Cunillera, M. C. Soriano, and I. Fischer. Cross-predicting the dynamics of an optically injected single-mode semiconductor laser using reservoir computing. *Chaos: An Interdisciplinary Journal of Nonlinear Science*, 29(11):113113, November 2019. (Cited on page 141.)

[100] Herbert Jaeger. Adaptive nonlinear system identification with echo state networks. *Advances in neural information processing systems*, 15:609–616, 2002. (Cited on page 151.)

[101] Jaël Pauwels, Guy Verschaffelt, Serge Massar, and Guy Van der Sande. Distributed Kerr Non-linearity in a Coherent All-Optical Fiber-Ring Reservoir Computer. *Frontiers in Physics*, 7:138, October 2019. (Cited on page 153.)

[102] Silvia Ortín and Luis Pesquera. Tackling the Trade-Off Between Information Processing Capacity and Rate in Delay-Based Reservoir Computers. *Frontiers in Physics*, 7:210, December 2019. (Cited on pages 155 and 156.)

[103] Junaid Aasi, J Abadie, BP Abbott, Richard Abbott, TD Abbott, MR Abernathy, Carl Adams, Thomas Adams, Paolo Addesso, RX Adhikari, et al. Enhanced sensitivity of the ligo gravitational wave detector by using squeezed states of light. *Nature Photonics*, 7(8):613–619, 2013. (Cited on page 163.)

[104] A. Einstein, B. Podolsky, and N. Rosen. Can quantum-mechanical description of physical reality be considered complete? *Phys. Rev.*, 47:777–780, May 1935. (Cited on page 164.)

[105] Shota Yokoyama, Ryuji Ukai, Seiji C. Armstrong, Chanond Sornphiphatphong, Toshiyuki Kaji, Shigenari Suzuki, Jun-ichi Yoshikawa, Hidehiro Yonezawa, Nicolas C. Menicucci, and Akira Furusawa. Ultra-large-scale continuous-variable cluster states multiplexed in the time domain. 7(12):982–986, 2013. (Cited on page 164.)

[106] Giuseppe Patera. *Quantum properties of ultra-short pulses generated by SPOPOs: multi-mode squeezing and entanglement*. PhD thesis, Université Pierre et Marie Curie-Paris VI, 2008. (Cited on page 165.)

[107] Shifeng Jiang, Nicolas Treps, and Claude Fabre. A time/frequency quantum analysis of the light generated by synchronously pumped optical parametric oscillators. *New Journal of Physics*, 14(4):043006, apr 2012. (Cited on page 165.)

[108] V Roman-Rodriguez, B Brecht, Srinivasan K, C Silberhorn, N Treps, E Diamanti, and V Parigi. Continuous variable multimode quantum states via symmetric group velocity matching. *New Journal of Physics*, 23(4):043012, apr 2021. (Cited on pages 165 and 166.)

[109] Samuel L. Braunstein. Squeezing as an irreducible resource. *Phys. Rev. A*, 71:055801, May 2005. (Cited on page 165.)

[110] Giuseppe Patera, Nicolas Treps, Claude Fabre, and German J De Valcarcel. Quantum theory of synchronously pumped type i optical parametric oscillators: characterization of the squeezed supermodes. *The European Physical Journal D*, 56(1):123–140, 2010. (Cited on page 165.)

[111] Renné Medeiros De Araujo. *Génération et manipulation de peignes de fréquences quantiques multimodes.* PhD thesis, Université Pierre et Marie Curie-Paris VI, 2012. (Cited on page 166.)